EXPERIMENTAL INVESTIGATION OF ALPHA-GAS STATES USING HIGH-MULTIPLICITY PARTICLE SPECTROSCOPY

by

JACK EDWARD BISHOP

A thesis submitted to the University of Birmingham for the degree of DOCTOR OF PHILOSOPHY

School of Physics and Astronomy
College of Engineering and Physical Sciences
University of Birmingham
United Kingdom

April 2018

Abstract

The onset of a new state of matter in the nucleus, whereby the system can be described as a dilute gas of α-particles, represents a fantastic probe of the nuclear force. The observables from such an α-gas state are discussed here in tandem with a discussion of traditional α-cluster structure. An experiment, utilising a high energy compound nucleus reaction to study the $^{12}\mathrm{C}(^{16}\mathrm{O}, 7\alpha)$ reaction was performed at LNS Catania to search for the signatures of such a state of matter. Direct evidence of near-threshold α-gas states was found to be impeded by the effect of the Coulomb barrier. The break-up of the system into α-particles was seen to exceed the predictions from a statistical decay model of the compound nucleus which was performed. These results were instead compared with the Fermi break-up model which showed a greater agreement with the data but the limitations of the model meant an exact agreement was not achieved. No evidence of α-condensation was found in this experiment however an improved experiment where the effect of the Coulomb barrier is no longer important is presented as a future probe of this structure.

Dedicated to my family

Acknowledgements

I would first like to thank everyone who ever graced us with their presence at lunchtimes: Dan, Joe, Sam, Robin, Chris, Nima, Hurry, Tony, Stuart, Marianna, Ollie, Jakub, Håkan, Pedro, Beckie, Yi Ming and Neil. The words "from my perspective" will never be heard the same way again. Neither will "data", "fewer" or "bang!". In addition to "extra-curricular" activities, I would like to thank everyone in CHARISSA who has joined me on a plethora of experiments whether at the Tron or somewhere more exotic. In particular, I would like to thank my nuclear partner-in-crime Robin without whom I wouldn't have learnt so much about experimental physics or the tensile strength of glass.

I am also extremely grateful for the knowledge imparted from many other people: Neil, Carl, Domenico and finally Giuseppe Cardella who talked me through the minutiae of CHIMERA.

Any thesis is of course impossible without the tireless efforts of supervisors. I am extremely fortunate to have received expert input from both Martin and Tzany over the course of my thesis. I would especially like to thank Tzany for her tireless efforts to keep me sane, happy and on track throughout. I appreciate your dedication more than words can say.

Finally, I would like to thank my family who have supported me over many years and have endured my many sarcastic comments. It is to you therefore, that I dedicate this thesis.

"Time is an illusion. Lunchtime doubly so."

Douglas Adams

List of Figures

List of Tables

Contents

Chapter 1

Introduction

Our current theories of physics aim to explain the physical phenomena in our universe via the rules set forward by the four fundamental forces of nature. These are; the strong nuclear force, the weak nuclear force, the electromagnetic force and gravity. The least well understood (especially in the low energy region the majority of the universe exists in), is the nuclear strong force. One of the major scientific achievements of the 20^{th} century was the development of Quantum ChromoDynamics (QCD) which described the interaction of gluons and quarks to form hadrons via the SU(3) symmetry group [1]. This was later developed further with the theoretical foundations for asymptotic freedom by David Gross, Frank Wilczek and David Politzer [2][3] allowing the calculation of strong coupling strengths using Feynmann diagrams. The energy scale associated with asymptotic freedom however is of the order of GeV to TeV, well in excess of the MeV scales associated with the nucleus.

The problem of describing the strong force is not only due to the failure of perturbative approaches at low energy but also due to the fact that in the nuclear force, the underlying degrees of freedom do not come from quarks but from protons and neutrons. The protons and neutrons cannot be described as (uud) and (udd) quarks respectively. Deep Inelastic Scattering shows that as well as these valence quarks, as one probes the proton and neutron deeper, the effect of additional components called "sea quarks" and gluons become increasingly important, meaning a precise description of the nuclear force as a remnant of the strong force is a lot more complicated than initially suggested [4]. This fundamental understanding of the proton is also exemplified by measurements which generate vastly difference radii [5] as well as initial confusion regarding the origin of the proton's spin. Experiments in the 1980s showed that the valence quarks account

for only around 30% of the proton's spin [6] demonstrating the added complexities inherent within even the simplest nucleus. These experiments show that an understanding of the nuclear force from QCD is an extremely difficult task. As such, one may well ask how well one can describe the nuclear force phenomenologically. By examining the predictions from our best models for the nuclear force, one can compare with experiment and use this to inform on its true form.

This is therefore one of the current aims of UK Experimental Nuclear Physics; by examining the residual interaction of the nuclear force, one can use this to generate an underlying understanding of this force (which is in-itself a residual interaction from the strong force) [7].

To generate a meaningful insight into the nuclear force, one must carefully design experiments which test the current nuclear models to improve our understanding. As an example of this insight, one can look at the area of nuclear structure where an attempt to study the intrinsic structure of the atomic nucleus allowed for great insights in both quantum mechanics and nuclear physics.

1.1 A brief history of the nucleus

As more experiments aimed to elucidate the structure of the nucleus, the models describing the atom and the nucleus also advanced. An early model of the atom, in an attempt to describe the positive and negative 'pieces' was proposed by J. Thomson in 1904 [8]. The electron had recently been discovered and was modelled to occupy a space inside a "soup" of positive charge (the proton having not yet been discovered) which spatially extended the entire size of the atom and generated a net neutral charge.

In 1911, Rutherford interpeted the results of the seminal Geiger-Marsden experiment [9] where a gold foil was irradiated with an α-particle source. By observing the angular dependence of the scattered α-particles [10], Rutherford deduced that the atom was consisted of an extremely small spherical nucleus at the centre precipitating the start of a new area of physics called Nuclear Physics, replacing the model proposed by Thomson. This small, dense, spherical description of the nucleus was continued with the liquid drop model which, combined with a knowledge of neutrons [11], allowed for a basic understanding of the nuclear force from a geometrical perspective. The semi-empirical mass formula [12] can calculate the binding energy (the energy require to dismantle a nucleus into its nucleon constituents) of a nuclear system by understanding a few

aspects of the nuclear force with the parameters matched to experimentally observed values. The basic form is shown in Equation 1.1.

$$E_B = a_V A - a_S A^{2/3} - a_C \frac{Z(Z-1)}{A^{1/3}} - a_A \frac{(A-2Z)^2}{A} + \delta(A,Z) \tag{1.1}$$

The first term corresponds to the volume term. Along with the surface, this describes how the nucleons feel an attractive short-range force to other nucleons (nearest neighbours). This short distance interaction can be explained using the ideas from the energy-time uncertainty principle. To mediate the nuclear force, one needs an exchange particle. The nuclear force differs here from the strong force (which is granted an infinite range by virtue of the zero mass of the gluon), as the nuclear force requires a colour-neutral force mediator, the exchange boson is instead the π meson which has a mass of 135 MeV/c^2 and 140 MeV/c^2 for the π^0 and $\pi^{\pm}$. The energy-time uncertainty principle tells us that one can "borrow" a small amount of energy ΔE with the proviso that one pays it back after a time Δt. The borrowing exchange-rate between the energy and time is then given by $\Delta E \Delta t \sim \hbar$. Borrowing the energy for a pi-meson then gives the range for the nuclear force as $\sim 10^{-15}$m, a value that matches with both the observed size of the nucleus and the skin thickness, as determined from a realistic model of the nucleus such as the Woods-Saxon potential [13]. The third term in the liquid drop model is the Coulomb term which demonstrates the importance of the electromagnetic force in the nucleus, as protons repel one another making the nucleus less bound. One may naïvely ask if proton-proton, neutron-neutron and proton-neutron interactions are all positive and proton-repulsion causes a less bound nucleus, why not build our nuclei solely out of neutrons? The final two terms allow for an understanding of why this is not the case. The asymmetry term is indicative of a system where an imbalance of protons or neutrons requires more energy than an equal spread between the two showing that the energy levels that can be occupied by the nucleons must fill increasingly higher energy levels due to the effect of the Pauli Exclusion Principle (PEP). This situation is discussed later in Section 2.2.1 where this asymmetry term can be understood better in subseqent models of the nucleus.

The final component is the pairing term which shows that pairs of protons or neutrons are much more stable than a single nucleon suggesting a two-fold degenerate energy level. A double occupation of a single energy level increases the overlap between the two particles filling it, therefore increasing their attraction. This hints at the two-fold degeneracy which is a feature of future nuclear models. This understanding of

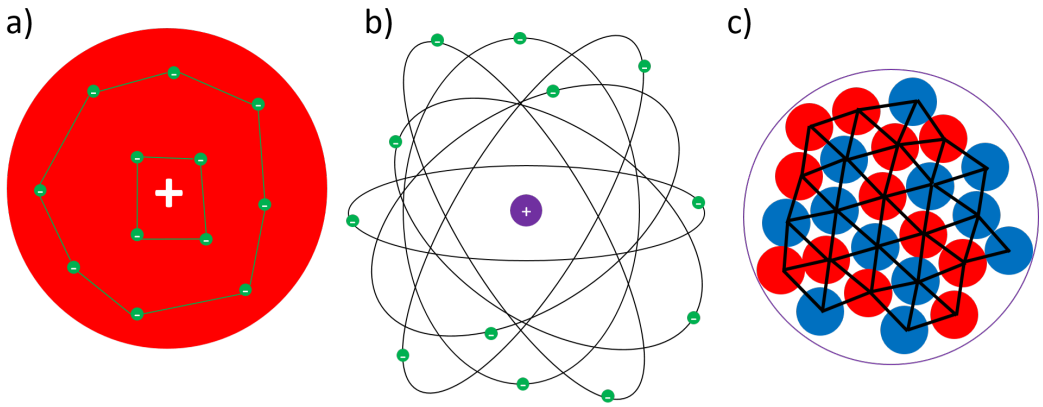

Figure 1.1: Development of nuclear theory from a) Thomson's plum pudding description, to b) Rutherford's nuclear orbits followed by c) the liquid drop model. The initial plum pudding model in a) relied on electrons being interspersed inside a spatially extended positive charge. Rutherford developed this model to be comprised of electrons orbiting a nucleus significantly smaller than the size of the atom. Further development into the liquid drop model as seen in c) created an understanding of the energetics of the nucleus via short-range and long-range interactions. The short-range interactions between neighbouring nuclei are shown in black for the liquid drop model.

the nuclear energy levels and degeneracies further developed with the formation of the nuclear shell model (SM) [14]. Following the ideas from atomic physics, where electron energy levels are generated from a simple harmonic oscillator, the nucleons can occupy a series of discrete energy levels. The key insight was in an ability to describe the so-called "magic numbers". These are a set of numbers of protons and neutrons which have an increased stability (binding energy). As will be discussed in Section 2.2.1 and shown in Figure 2.4, large gaps in the discrete energy levels appear at 2, 8, 20, 28 and 50 after a splitting occurs of the allowed states. This modification to the energy gaps is caused by a spin-orbit interaction. This is an interaction between the spin of a nucleon and the angular momentum it has while in a particular orbit. The addition of this term allows the model to reproduce the experimentally observed magic numbers. The measurement of the binding energies (and therefore calculating the magic numbers) has demonstrated the importance of a spin-orbit term in the nuclear force.

This shows the importance of experimental nuclear physics to understand the strongest of the four fundamental forces and in particular the emergence of the nuclear force from its residual interactions.

1.2 Thesis work

In this thesis, data from a high energy compound nucleus reaction ^{12}C(^{16}O,^{28} Si) performed at LNS, Catania, Italy is presented. This experiment aims to study how highly excited states in ^{28}Si decay into a system of 7 α-particles. Examination of this process and comparison with current theoretical models can provide an insight into to what degree certain states of matter can be described as a dilute gas of α-particles known as an α-gas. In particular, the analysis focuses on whether the break-up to 7 α-particles is enhanced in comparison to a traditionally clustered system. The measurement or refutation of such an exotic states can provide important insights into the nuclear force. In particular, how the nuclear force behaves at low densities.

Chapter 2

Theory

The interpretation of experimental data often requires a large amount of theoretical input. As often as possible, this is done in a model independent way or by making an appropriate approximation. This can then be compared to the results obtained via experiments. Broadly speaking, experimental nuclear physics can be divided into two main topics: nuclear reactions and nuclear structure. **Nuclear reactions** rely on different methods of interaction between nuclei and by studying the various experimental observables (cross section, energy, angle etc.) one can extract information about the physics occurring by understanding the perturbation to the system. **Nuclear structure** mainly relies on the measurement of the discrete energy levels in a given nucleus. The information from these states (branching ratios, excitation energies, spin-parity etc.) can provide an insight into the structure of the populated nucleus. These discrete states, which are solutions to the Schrödinger equation, should then uniquely describe the potential felt by the nucleons, from which the nuclear force properties can be extracted.

2.1 Nuclear Reactions

In order to study the nuclear structure, one can use a variety of mechanisms which probe different features and give alternate experimental observables. The most widely occurring reactions for a nucleus-nucleus interaction are shown in Figure 2.1a. A selection of these methods will briefly be discussed here:

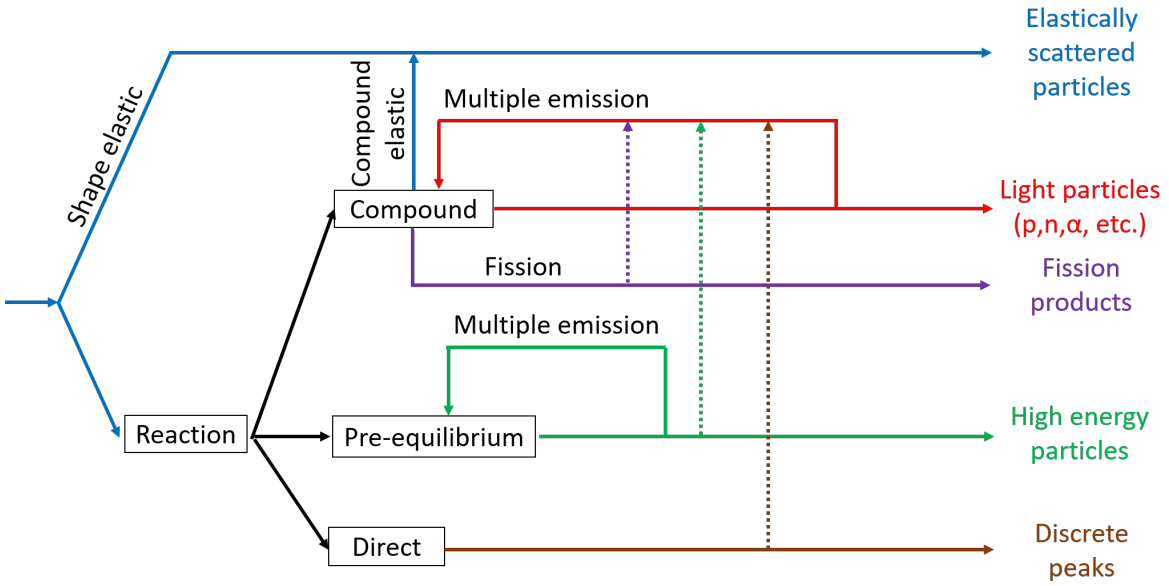

(a) Figure adapted from [15] showing the different reaction mechanisms and the products generated from these decay paths.

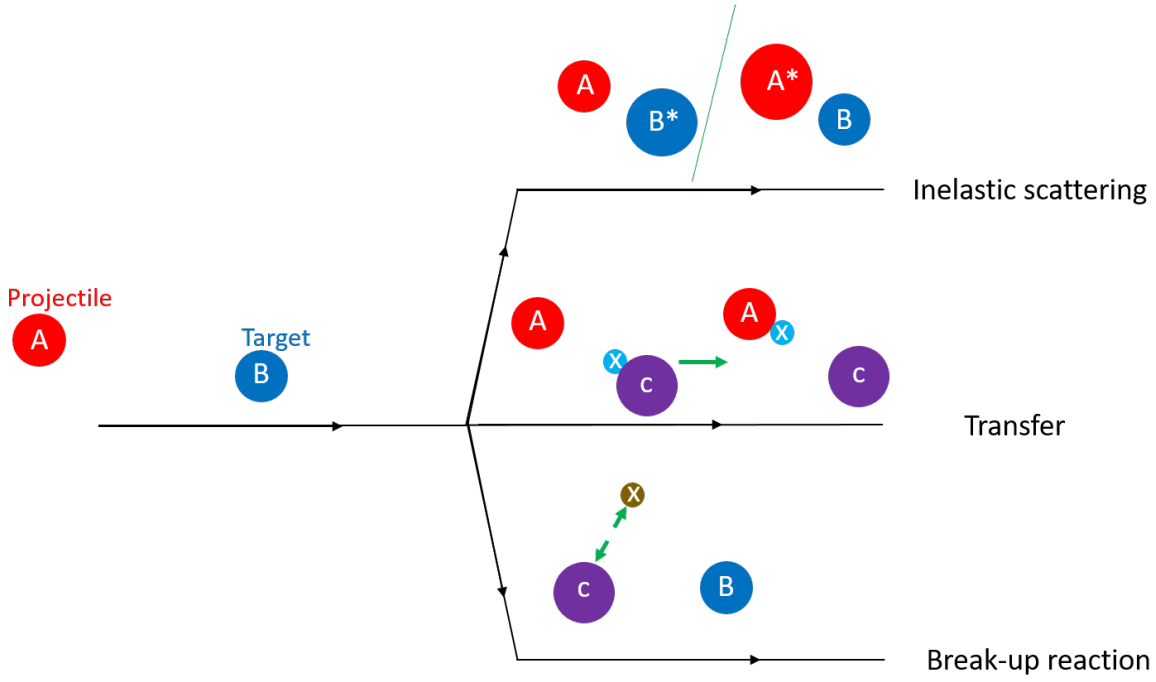

(b) Direct reactions.

Figure 2.1: Schematic explanation of the reaction mechanisms for particle-particle reactions (Figure 2.1a). Figure 2.1b shows three different direct reaction mechanisms.

2.1.1 Direct reactions

One can describe the interaction between two nuclei as direct if the interaction between the projectile and target is sufficiently weak to be treated only to the first order in perturbation theory. In order to excite the nucleus, one can bombard it with another, where the incident nucleus maintains its original form. For example, one can bombard a ^{12}C nucleus with a proton. If the proton has an energy of $\sim$ 10 MeV, it will have sufficient energy to overcome the Coulomb barrier (which in this reaction is 2 MeV) and transfer some energy to the ^{12}C nucleus via an inelastic interaction. In such scenarios, the proton is then scattered and leaves the system with its internal structure unperturbed. The energy in the excited ^{12}C* allows for a movement of the protons and neutrons to higher energy levels. Measuring the differential cross section, $\frac{d^2\sigma}{d\Omega dE}$, for the proton can give information about the existence of the resonances in the ^{12}C system as the momentum-vector uniquely defines the excitation energy of the ^{12}C. This reaction is known as **inelastic scattering**.

Another technique involves **particle transfer**. This mechanism involves one or several nucleons from the target/beam being transferred. For instance, one can populate states in ^{16}O by bombarding a ^{12}C target with a ^{6}Li beam. In the ^{12}C(^{6}Li,d) reaction, an α-particle from the beam is transferred to the ^{12}C to form ^{16}O. From measurement of the residual deuteron momentum, one can infer which energy level has been populated.

Finally, the direct dissociation of the projectile/target as it feels the influence of the bombarding particle can be observed. The electromagnetic/nuclear field can break up the particle and yield a 3 (or more) particle final state without going through an intermediate excited state. This is known as a **break-up reaction**. An example of this is where a ^{12}C target is bombarded with a ^{6}Li beam (as with the particle transfer reaction) although the interaction of the ^{6}Li with the ^{12}C causes the direct break-up of ^{6}Li$\rightarrow$ d+α.

In summary, one uses direct reactions to populate a state in the nucleus of interest or cause a re-arrangement of the nucleons in the system. Analysing the residual particles or measuring the decay of the state of interest can then give information about the energy levels populated.

2.1.2 Compound nucleus formation

Another way to probe the nucleus is via **compound nucleus formation**. In this reaction mechanism, two nuclei are collided together (usually one is stationary in the

lab frame) and fuse completely. The system lives long enough that the original incoming channel for this reaction is forgotten, (independence hypothesis), [16] [17], as the nucleons in the compound system have sufficient time to effectively thermalise and share the energy from the reaction between all the constituents. The cross section and the decay mechanism for a given energy can then give information about resonances in the system. Once the system has fused, it can dissociate if it has sufficient energy. The compound system may prefer to return back to the original entrance channel or instead **fission** into two lighter reaction products. This mechanism is driven predominantly by the tunneling probability and Q-value of the final state and does not yield useful information about the nuclear force. At lower excitation energies (above the particle decay threshold but below the continuum), measuring the cross section as a function of the incoming beam energy allows for the examination of resonances in the compound nucleus. The subsequent decay of this compound state can be described using the very successful R-matrix formulation in a region where there are a series of resonances, sufficiently spaced, such that their average separation is smaller than the average width.

R-matrix theory [18][19] allows for a good description of multiple resonances via a solution of the Schrödinger equation by separating the nucleus into two regions. The internal region ($r < a$) is where the effects of the nuclear (given by V(r)) and Coulomb forces are felt and the Schrödinger equation is that given by Equation 2.1. The external region ($r > a$) is chosen to be sufficiently far away from the nucleus such that the only force left is that of Coulomb. This is shown in Figure 2.2. The Schrödinger equation in this external region is given by Equation 2.2. The wave function for a system with angular momentum ℓ which solves the Schrödinger equation is given by χ_ℓ with $k = p/\hbar$ and $\eta = \frac{Z_1 Z_2 e^2}{4\pi\epsilon_0 \hbar v}$.

$$r < a \qquad \left(\frac{\partial^2}{\partial r^2} - \frac{\ell(\ell+1)}{r^2} - \frac{2\mu}{\hbar^2}\left(V(r) + \frac{Z_1 Z_2 e^2}{r} - E\right)\right)\chi_\ell^{int}(r) = 0 \tag{2.1}$$

$$r > a \qquad \chi_\ell^{ext}(k,r) = \frac{1}{kr}\left(H_\ell^{(-)}(\eta,kr) - S_\ell H_\ell^{(+)}(\eta,kr)\right) \tag{2.2}$$

$$H_\ell^{\pm} = G_\ell \pm iF_\ell, \tag{2.3}$$

with F_ℓ and G_ℓ corresponding to the regular and irregular Coulomb wave functions respectively. For $r < a$, the Schrödinger equation must be solved numerically. The

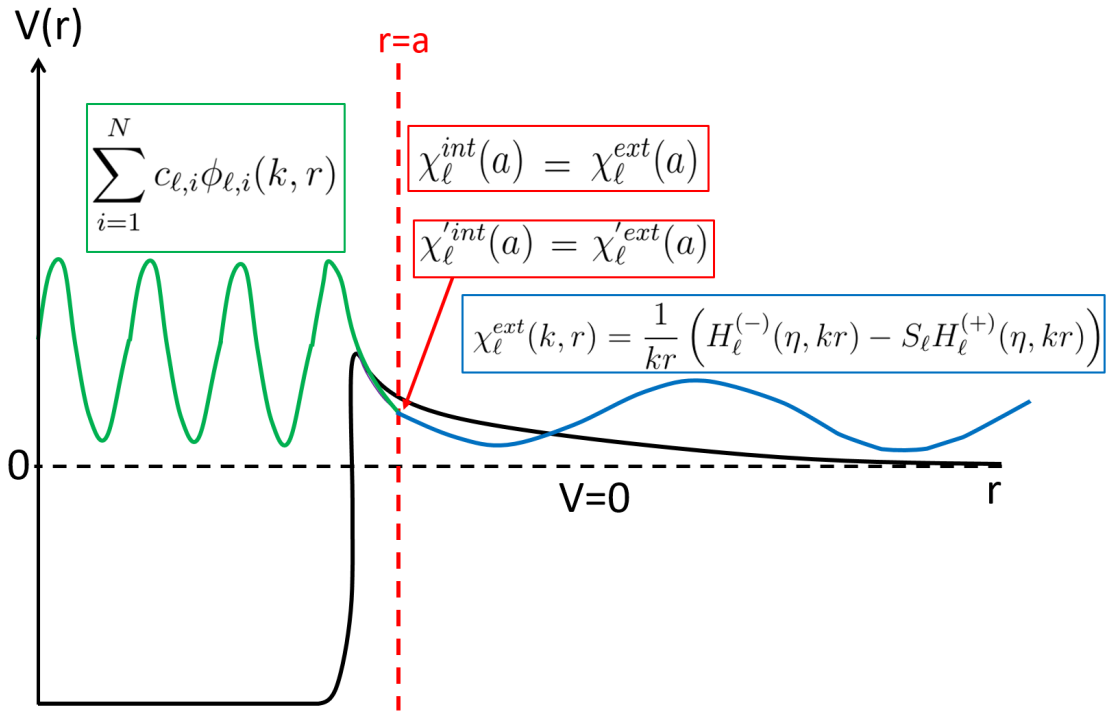

Figure 2.2: R-Matrix formulation for the compound nucleus which relies on dividing the nuclear potential into two regions. The external region $r > a$ is where the nuclear force is no longer felt and the potential is driven by the Coulomb (and centrifugal) force. In the internal region $r < a$, the wave function (green) is not explicitly solved but is denoted as a sum over a generic basis set.

general basis $\phi_{\ell,i}$(k,r) can then be expanded over with the coefficients $c_{\ell,i}$:

$$\chi_\ell^{int}(k,r) = \sum_{i=1}^{N} c_{\ell,i}\phi_{\ell,i}(k,r) \tag{2.4}$$

This equation is solved in R-Matrix theory using the Bloch-Schrödinger equation:

$$(H - E + \mathcal{L})\chi_\ell^{\text{int}} = \mathcal{L}\chi_\ell^{\text{ext}} \text{ where the Bloch operator } \mathcal{L} = \frac{\hbar^2}{2\mu}\delta(r-a)\frac{d}{dr} \tag{2.5}$$

The Bloch operator then ensures that both the wave function and its derivative are continuous at the matching radius a, and also solves the Schrödinger equation in this internal region. Rather than extracting the values χ_ℓ^{int}, one may instead use a series of mathematical "tricks" which allow us to extract the scattering-matrix elements.

To do this, one can look at the wave function at the border region divided by its derivative.

$$\frac{\chi_\ell^{int}(a)}{\chi_\ell'^{int}(a)} = \frac{\chi_\ell^{ext}(a)}{\chi_\ell'^{ext}(a)} = \frac{H_\ell^{(-)}(\eta,ka) - S_\ell H_\ell^{(+)}(\eta,ka)}{\frac{d}{dr}\left(H_\ell^{(-)}(\eta,ka) - S_\ell H_\ell^{(+)}(\eta,ka)\right)} = aR_\ell(E), \tag{2.6}$$

where we equate this ratio to the matching radius a multiplied by a new matrix R_ℓ which we define as the R-matrix. This matrix changes for different entrance and exit channels, different orbital angular momenta, ℓ, and also with energy, E. Calculation of the S-matrix is then required which allows for a formulation of the differential cross section, $d\sigma/d\Omega$, which is given by:

$$\frac{d\sigma}{d\Omega} = \left|\frac{1}{2ik}\sum_{L=0}^{\infty}(2L+1)P_L(\cos(\theta))(S_L - 1)\right|^2 \tag{2.7}$$

$$S_\ell = \frac{H_\ell^{(-)}(\eta,ka)}{H_\ell^{(+)}(\eta,ka)}\frac{1 - L_\ell^\star R_\ell(E)}{1 - L_\ell R_\ell(E)} \text{ where } L_\ell = ka\frac{\frac{d}{d(ka)}H_\ell^{(+)}(\eta,ka)}{H_\ell^{(+)}(\eta,ka)}, \tag{2.8}$$

with P_L being the Legendre polynomial of order L. The collision matrix, U_ℓ, is then formulated which gives an idea of the phase change, δ_ℓ, in the system:

$$U_\ell = -\text{atan}\left(\frac{F_\ell(ka)}{G_\ell(ka)}\right)\text{atan}\left(\frac{P_\ell R_\ell}{ka}\right) = e^{2i\delta_\ell} \tag{2.9}$$

The system is then parameterised in terms of poles with an energy E_i and a reduced

width $\gamma^2_{\ell,i}$.

$$R_{\ell,i}(E) = \sum_{i=1}^{N} \frac{\gamma^2_{\ell,i}}{E_i - E} \tag{2.10}$$

It can clearly be seen here that when $E = E_i$ the R-matrix elements becomes infinite, the collision matrix and therefore the phase change passes through 90°, where the cross section becomes maximal which corresponds to a resonance. The parameters E_i and $\gamma_{\ell,i}$ are then varied to match the differential cross section data for the different channels present. Once these parameters have been optimised to fit the data, they can be related to the experimental observables, the resonance energy, E_R, and decay width, Γ_i, using the equations:

$$E_R = E_i - \mathrm{Re}(L_\ell) \tag{2.11}$$

$$\Gamma = 2\mathrm{Im}(L_\ell)\gamma^2_{\ell,i} = 2P_\ell\gamma^2_{\ell,i}, \tag{2.12}$$

with P_ℓ being the penetrability.

2.1.3 Photodissociation/Coulomb excitation

Another emerging probe of nuclear structure is via the use of nuclear photodissociation. In order to populate the nucleus, a high luminosity and energy electron beam is used to Compton backscatter off a laser, which generates a narrow energy gamma "beam". This gamma "beam" is then diverted into a Time Projection Chamber (TPC) where it interacts with a target exciting the target above the particle decay threshold. By measuring the subsequent decay of the excited nucleus and the angular correlations, one can extract the contribution of the E1 and E2 transitions. This allows for a good selectivity of populated states, the higher J states are less well populated, since they have no E1 or E2 strength to the ground state. A recent success using this technique allowed the measurement of a 2^+ rotational band member in ^{12}C which had previously been obscured by the strongly populated 3^- state [20]. This result will be discussed later.

A related technique which also depends on the break-up of a nucleus via electromagnetic interaction is Coulomb excitation (Coulex) as shown in Figure 2.3. Coulex differs from photodissociation as the photon, used to precipitate the excitation of the nucleus, is a virtual photon mediated during the Coulomb repulsion between the target

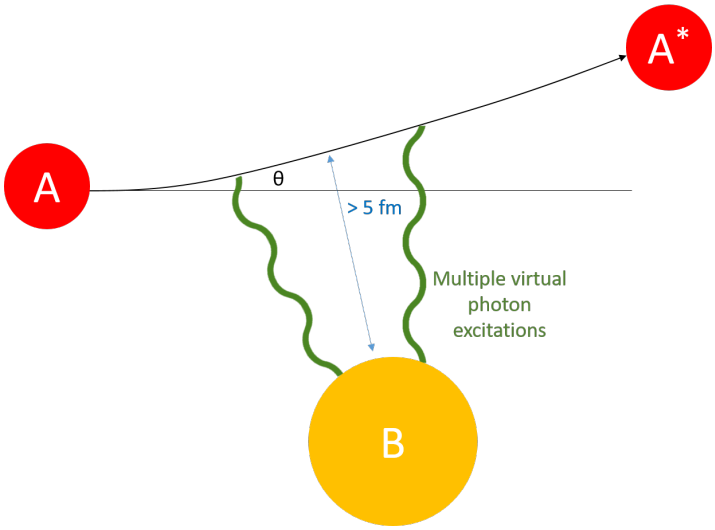

Figure 2.3: Coulomb excitation (Coulex) occurs when two nuclei approach one another and virtual photons are exchanged to mediate the electromagnetic interaction. This can excite the incident nucleus to an higher energy state. Many such interactions can occur allowing higher excitation energies to be reached.

and the beam. To ensure a purely electromagnetic interaction, the experiment parameters are chosen such that the smallest distance between the target and beam always exceeds 5 fm (safe distance criterion) [21]. The Coulex process is shown in Figure 2.3 where the nucleus of study is the beam and impinges on a very heavy (and therefore highly charged) nucleus, which gives a large electromagnetic interaction. This technique is particularly useful for studying short-lived isotopes produced at a radioactive beam facility. Additionally, the nature of the interaction means that high energy states with low angular momentum can be populated, as will be discussed in Section 8.

2.2 Nuclear Structure

As previously discussed, an understanding of the nuclear structure of a state can be instructive about the underlying physics. If the nature of the nuclear force is such that different structures are energetically preferred/forbidden this can then yield information about the form of the nuclear potential. This area is particularly prevalent when using gamma-rays to investigate low-lying energy levels in the nucleus. By looking at energy-spin dependence, one can infer information about the nucleus such as its deformation. These low energy excitations are well described by the shell model [22].

2.2.1 Shell Model

As a very basic model to solve the interaction of the nucleons, one can approximate the form of the nuclear + Coulomb potentials as a simple harmonic oscillator (SHO) potential $V(r) = \frac{1}{2}m_0\omega^2 r^2$, with m_0 being the reduced mass, ω the angular frequency (which changes the strength of the potential) and r the distance from the centre of the system. The potential for the nucleons therefore depends only on position, an idea known as the mean-field approximation, where the dynamics of the system are ignored. While this is a major simplification, it produces equations which are much easier to solve and still capture the overall behaviour of the system. The SHO is a reasonable choice for a potential despite its apparent differences with the Woods-Saxon (WS) type potential [13], which provides a good description of the observed nuclear densities. The Woods-Saxon form is given by:

$$V_{WS}(r) = \frac{-V_0}{1 + \exp(\frac{r-R}{a})}, \tag{2.13}$$

with r being the distance from the centre of the potential, V_0 the strength of the potential, a the diffuseness parameter which describes the range of the strong force and R the radius of the nucleus, usually described in the liquid-drop model as $R = r_0 A^{1/3}$ with r_0 varying from $1.2 \rightarrow 1.4$ fm. The Woods-Saxon describes the measured nuclear potential extremely well, but has a form which must be solved computationally when inserted into the Schrödinger equation. As $r \rightarrow \infty$, $V \rightarrow \infty$ for the SHO potential, whereas for the WS potential, $V \rightarrow 0$. This makes a negligible difference to the solution of the Schrödinger equation since outside the nuclear region the wave function rapidly tends to 0, therefore, the action of the potential operator on the wave function makes a very small difference. Inside the nuclear region, the potential is smooth and a quadratic description is a good approximation. The form of the Schrödinger equation in spherical polar co-ordinates (r, θ, ϕ) one must then solve is as follows:

$$\hat{H}\Psi = (\hat{T} + \hat{V})\Psi \tag{2.14}$$

$$\Psi = Y_{lm}(\theta, \phi)R(r) \tag{2.15}$$

$$\left(-\frac{\hbar^2}{2m_0 r^2}\frac{d}{dr}\left(r^2\frac{d}{dr}\right) + \frac{\hbar\ell(\ell+1)}{2m_0 r^2} + \frac{1}{2}m_0\omega^2 r^2\right)R(r) = ER(r), \tag{2.16}$$

with Y_{lm} being the spherical harmonic functions and m_0 describing the reduced mass. This relies on the separation of the solution into the radial component $R(r)$ and the angular dependence $Y_{lm}(\theta, \phi)$. This can be solved via a power series which gives discrete eigenvalues of energy:

$$E = \left(2n + \ell + \frac{3}{2}\right)\hbar\omega, \tag{2.17}$$

with a degeneracy of $2(2\ell + 1)$ states for each ℓ (as m_ℓ varies from $-\ell, -\ell + 1, -\ell + 2, ... - 1, 0, 1, ...\ell - 1, \ell$). Each harmonic oscillator also has an additional two-fold spin degeneracy. Examination of the first energy levels $\frac{3}{2}\hbar\omega$, $\frac{5}{2}\hbar\omega$, $\frac{7}{2}\hbar\omega$ and $\frac{9}{2}\hbar\omega$ yield degeneracies of 2, 6, 12 and 20 respectively which give the first few magic numbers as 2, 8, 20 and 40. While the first three magic numbers are well reproduced, the magicity of 28 is replaced by 40 which is incorrect. By applying a spin-orbit interaction to the simple harmonic oscillator (SHO) as discussed in Chapter 1.1, the degeneracy of the system is modified to $2j + 1$ with $\vec{j} = \vec{l} + \vec{s}$. The magic numbers then correspond to 2, 8, 20, 28, 50, 82, 126 and 184 (shown in Figure 2.4). All apart from the last of these have been experimentally observed. This simple model based on a crude approximation of the nuclear potential is exceedingly good at predicting the ground states across the nuclear chart. Excitations can be understood as protons and neutrons moving to higher nuclear levels leaving an unoccupied shell space known as a hole. While these simple excitations can describe some low-lying states, many states are incorrect in their energy ordering due to the fact that the simple shell model assumes an independent particle description, whereas in reality the particles interact with one another. This is best illustrated by observing the non-zero quadrupole moment of ^{17}O. In comparison, ^{16}O is a doubly-magic nucleus, therefore has an electric quadrupole moment of Q ~ 0, this being an intrinsic prediction of the shell model as it is spherically symmetric. The addition of a neutron behaving independently should not affect this spherical charge distribution as it is electrically neutral. The proton-neutron coupling however deforms the nucleus creating a quadrupole moment of Q$= -2.6$ e(fm)^2 (compared to a naïve SM estimate of -0.1) [23].

Modern shell model codes therefore solve this residual interaction as a perturbation to the initial Hamiltonian. The nucleon-nucleon (NN) interaction comes from extensive experimental investigation of NN phase shifts (e.g. Argonne v18 potential [24]). Performing such a full calculation however is a computationally intensive task which

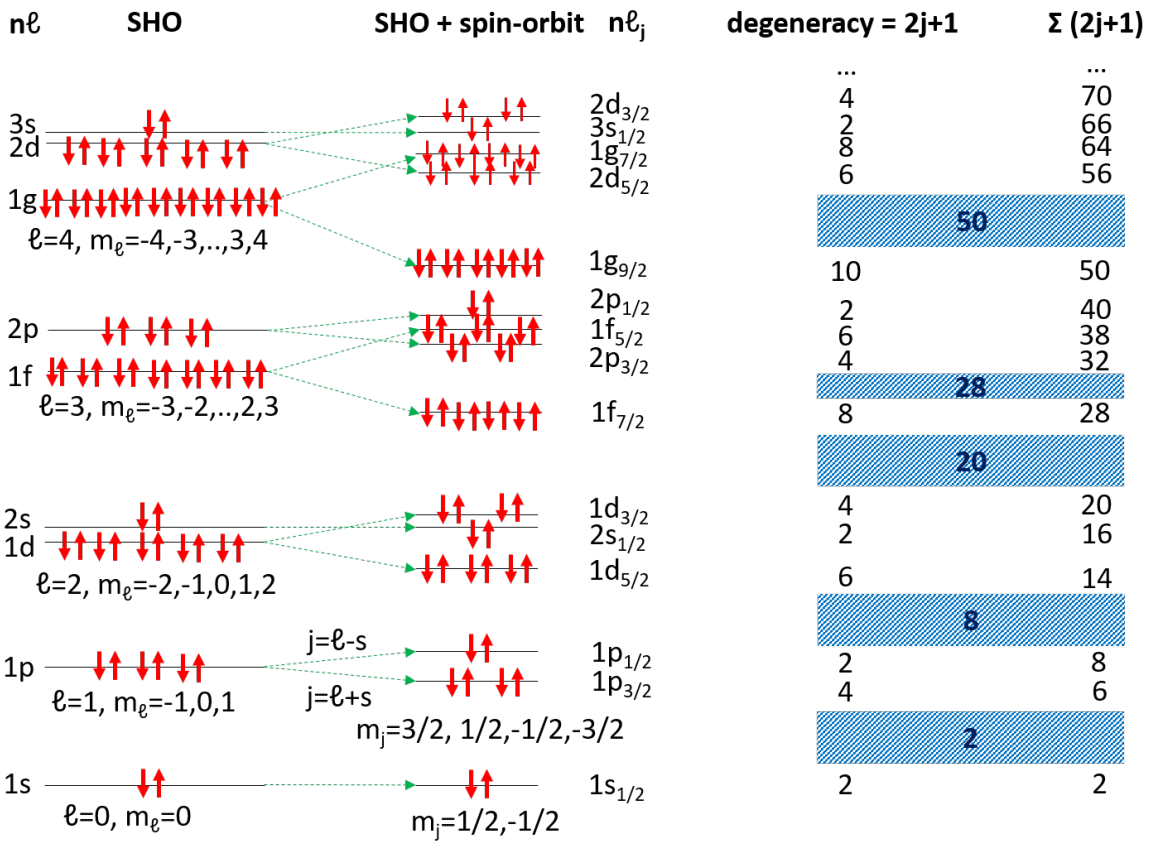

Figure 2.4: Solutions of the simple harmonic oscillator (SHO) potential of the nuclear system and their corresponding degeneracies (left). As the spin-orbit coupling is applied the energy levels are perturbed depending on whether the angular momentum and spin are aligned or anti-aligned. This then modifies the location of the energy gaps corresponding to nuclear magic numbers. These magic numbers are seen on the right, as the blue shaded regions, where no single-particle levels exist.

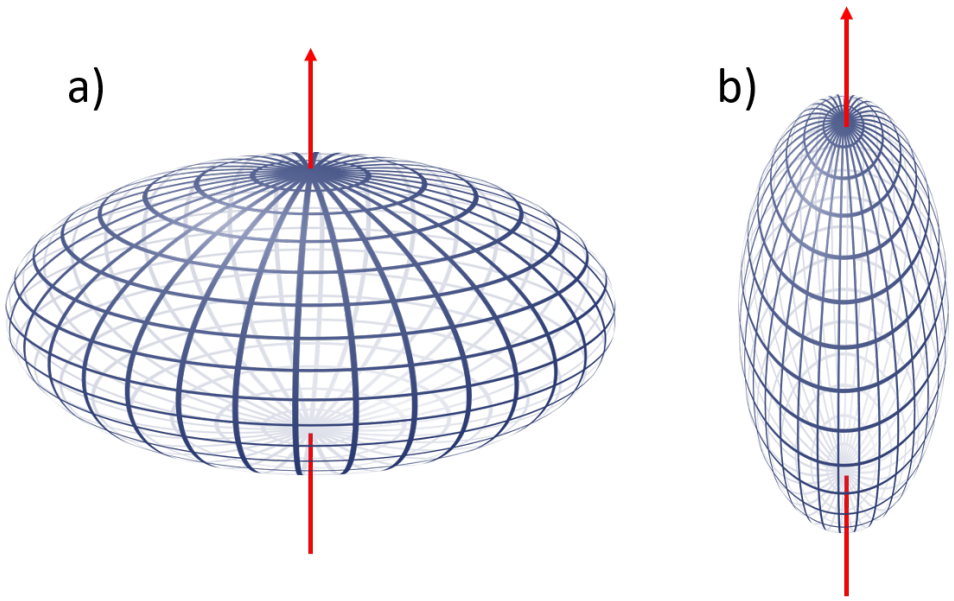

Figure 2.5: Different deformations for an ellipsoid nucleus. a) shows oblate while b) corresponds to prolate deformation.

requires the diagonalising of extremely large matrices. Therefore the maximum oscillator quanta are often truncated to limit the computation time required but sufficiently large to allow for the convergence of a solution. These calculations have been very successful in describing many shell model phenomena however for specific regions of the nuclear chart, this model is no longer a good treatment. This failure arises from the assumption that the nucleus is spherical. As discussed above, doubly-magic closed shell nuclei are spherical. When one examines nuclei far from closed shells, it can be seen that the nucleus changes shape from spherical to a deformed ellipsoid. The two extremities of this deformation are shown in Figure 2.5 where the symmetry axis defines whether the shape is oblate or prolate. This shape change has the effect of both splitting the single-particle solutions as well modifying the energy level as the deformation increases.

While this deformation expansion of the shell model increases the applicability of the mean-field description, there still remain a subset of states which cannot be described by the shell model and require a beyond mean-field extension.

2.2.2 Clustering

Clustering is the phenomena where it becomes energetically favourable for the structure of a nucleus to change from a spherical amorphous ball of protons and neutrons

into a system where in the intrinsic frame (i.e. before symmetry restoration), localised clusters of nucleons appear. This is a very dramatic structural change which cannot be well described by a mean-field approach where the force felt by an individual nucleon is the average it would feel over the entire nucleus. From experimental observations in the area of light nuclei, these clusters are very common and take many forms. The first attempts to model nuclear forces beyond a mean-field nucleon interaction relied on modeling clusters of α-particles. The importance of α-particles as a nuclear sub-unit was well understood both in terms of comprising a doubly-magic nucleus and when examining the binding energy per nucleon of the α-conjugate nuclei. Additionally, the first excitation in ^{4}He is above 20 MeV meaning it constitutes an inert sub-unit. ^{6}Li is often described as a α+d cluster structure, the reason for this is apparent from an understanding of the shell model energy levels. The additional proton and neutron, which are added to ^{4}He to form ^{6}Li cannot generate a large amount of overlap with the inert α core due to the Pauli exclusion exhibited because of their fermionic nature. This idea further extends to ^{8}Be which comprises two α clusters in its ground state and even the heavy ^{212}Po system exhibits a ^{208}Pb + ^{4}He structure [25]. Both of these clusters being doubly magic means that their residual inter-cluster attraction is limited allowing for a non-spherical structure.

This is therefore why the best examples of clustering are focused around α-particles (and α-conjugate nuclei). The Ikeda diagram in Figure 2.6 shows the predicted energies at which these cluster structures are expected to manifest themselves. This cluster-structure is theorised to manifest itself around the decay-threshold for the specific cluster type as the residual interaction is expected to be very weak. The most interesting type of clustering in this thesis is the **N-α clustering**. This is where the nucleus can be described solely as being constructed from α-particles. This type of clustering sits above the **N-α threshold**, the energy required to break-apart the nucleus into a system of N α-particles. As an example, in ^{12}C the 3-α structure is predicted to exist just above an energy of 7.27 MeV, the 3-α decay threshold. At 7.65 MeV, a 0^{+} state of extreme astrophysical and anthropic importance has been discovered [26] which shows a startling propensity for a 3-α cluster structure. This state is known as the Hoyle state.

When undergoing nucleosynthesis, helium-burning stars encounter a startling bottleneck. Despite the large abundance of hydrogen and helium, the fusion of two helium nuclei to form ^{8}Be generates only an extremely short lived nucleus of 10^{-16} s. This ^{8}Be decays rapidly back to 2 α particles as it is unbound by 92 keV. Upon examining the Segré chart, one sees that all mass 5 and 8 nuclei are unstable therefore one may ask

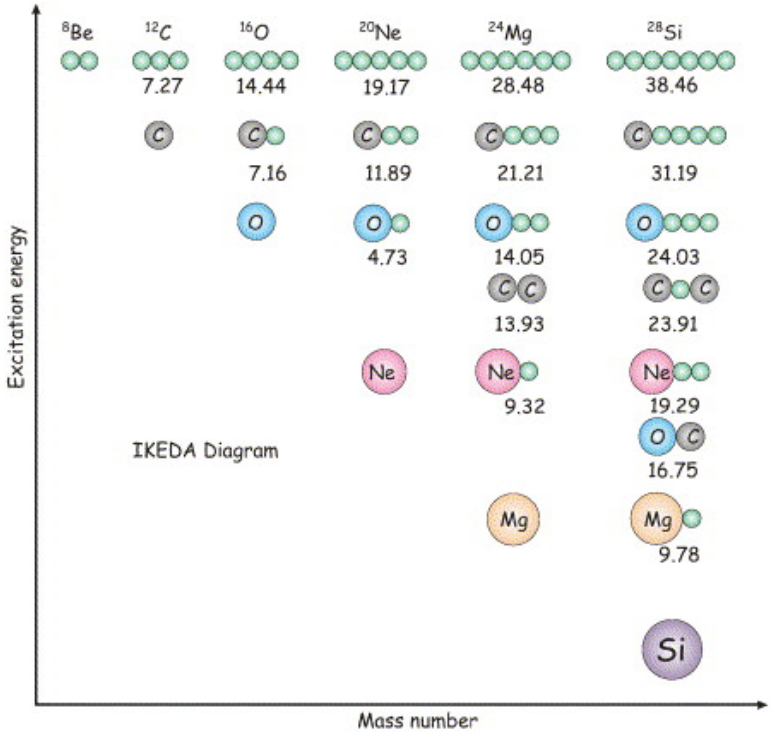

Figure 2.6: "Ikeda diagram" showing the prediction of different cluster configurations in the α-conjugate nuclei at different excitation energies. The $a \oplus b$ cluster structure is expected to appear just above the a+b decay threshold. From [27].

how to generate heavier elements. To overcome this bottleneck, it is possible (albeit improbable) for a third α-particle to fuse with the short lived ^{8}Be nucleus before it decays, to form ^{12}C, with a large amount of internal energy. If the ^{12}C can then release this energy via gamma-emission or pair-production, then ^{12}C decays to the ground-state and can then undergo further fusion to make heavier elements (which requires a higher temperature). This synthesis of ^{12}C is known as the triple-α reaction and is shown in Figure 2.7. This reaction rate was calculated to predict the relative abundances of ^{4}He, ^{12}C and ^{16}O in the universe and it was seen that the theory underestimated the expected reaction rate necessary to match the experimental data by several orders of magnitude. To alleviate this disparity, Fred Hoyle hypothesised the existence of a resonance lying close to the 3-α decay threshold which enhances the cross section for the triple-α reaction. The parameters of this state must be finely tuned to have a considerable 3-α structure in order to enhance the cross section sufficiently for heavier elements (^{12}C and ^{16}O) to be produced in comparison to the amount of ^{4}He [28].

The state was subsequently experimentally observed [29] and hailed as a great ex-

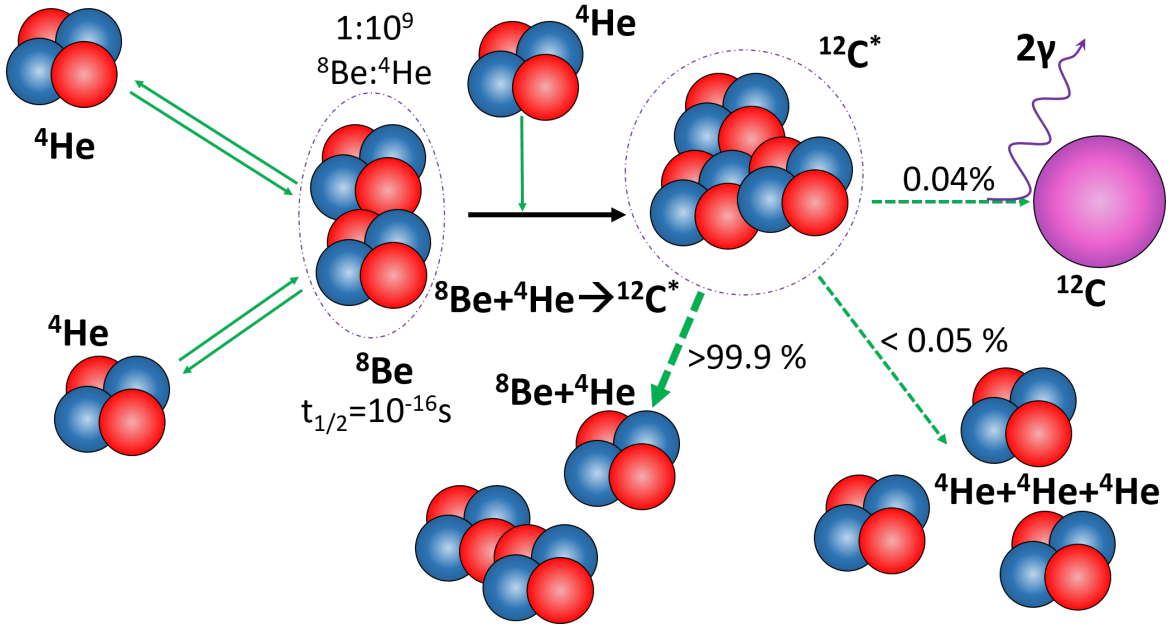

Figure 2.7: Two-step procedure for the triple-alpha process.

ample of fine-tuning of physical parameters in nature. This state was suitably placed to allow life to exist; a corresponding energy level existing in ^{16}O above the $^{12}\mathrm{C} + \alpha$ threshold is not found. This equivalent state in ^{16}O would destroy the large amount of ^{12}C generated to produce ^{16}O and subsequent heavier elements. While the 3-α structure of the state was understood early on in its discovery, the nature of this 3-α structure caused much debate (and indeed still does to today). In 1956, Morinaga [30] proposed a linear chain arrangement for the Hoyle state while others preferred a more compact geometric cluster structure [31]. These simple models have described the observed characteristics of light nuclear systems such as ^{8}Be extremely well. This basic description uses the Brink model which places the α-particles at specific points in space using the $\mathrm{Sp}(2, \mathbb{R})$ symmetry group [32]. The predicted energy-levels and electromagnetic transition strengths (B(E2)) agree well with experimental data.

More recent theories have had success in describing the Hoyle state as a equilateral triangle of α-particles [33] following the success of the simple geometric model in ^{8}Be, reproducing the rotational bands. An idea developed mainly over the last decade has succeeded in replicating the inelastic scattering form factor for the Hoyle state by treating the α-particles as an independent boson gas [34]. These ideas will be discussed in depth later in Chapter 3.

As an extension of the ideas of Ikeda, one can look at how the addition of neutrons

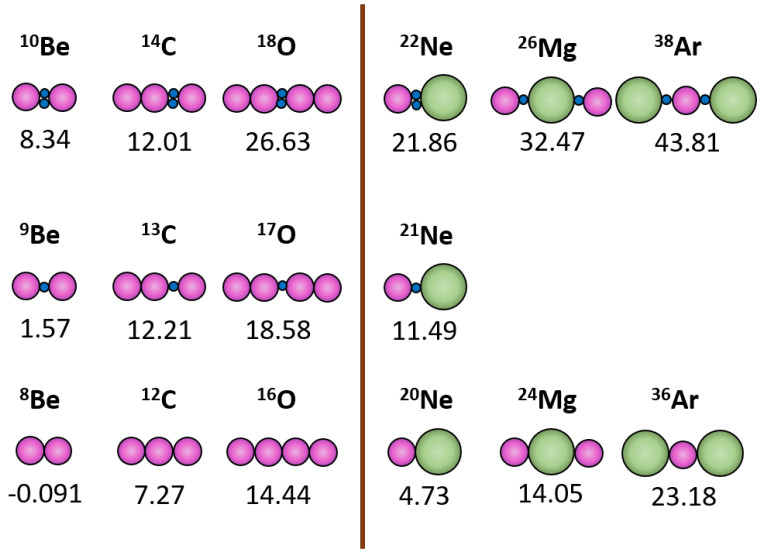

Figure 2.8: Extended Ikeda diagram showing the cluster structures possible when adding neutrons to the α-conjugate nuclei. Adapted from [35].

affects the expected cluster structures. In many cases, the neutrons are expected to behave like electrons in an atomic compound. These states are summarised in the extended Ikeda diagram seen in Figure 2.8. The neutrons occupy orbits in between the two clusters and generate an attractive force between them and can also act as a stabiliser to otherwise unstable configurations in α-conjugate nuclei. As an example, in ^{12}C, the linear chain state has been demonstrated to be unstable to bending motion [36]. In ^{14}C, the effect of two extra neutrons means that the stiffness of the linear chain configuration is increased and evidence of a linear chain has been seen [37]. In ^{9}Be(g.s), a similar feature is seen where the addition of an extra neutron stabilises ^{8}Be, making it bound. The behaviour of the neutron occupying the inter-cluster region shows that it behaves very similarly to an electron between two atoms where it can exhibit π or σ type bonding [38] [39]. This general idea of neutrons behaving like electrons in a covalent system is known as a **nuclear molecule**.

2.2.3 Alpha Cluster Model (ACM)

To go beyond the standard SM ideas, the harmonic oscillator was replaced with the deformed harmonic oscillator and the building blocks of nucleons were replaced with α-particles. The quadrupole deformation of the system changes the degeneracy, as oscillations along the deformation axis (denoted n_z) have a different energy contribution

from those perpendicular to the deformation (denoted $n_\perp$). At deformations of $j:1$ where $j \in \mathbb{N}$, degeneracies appear which can be seen in Figure 2.9. For a given $j:1$ deformation, the $1:1$ deformation degeneracies are repeated j times. This suggests that such a $j:1$ deformed system comprises of j interacting spherical potentials. The densities for 2:1, 3:1 and 4:1 deformations can be seen in Figure 2.10. These

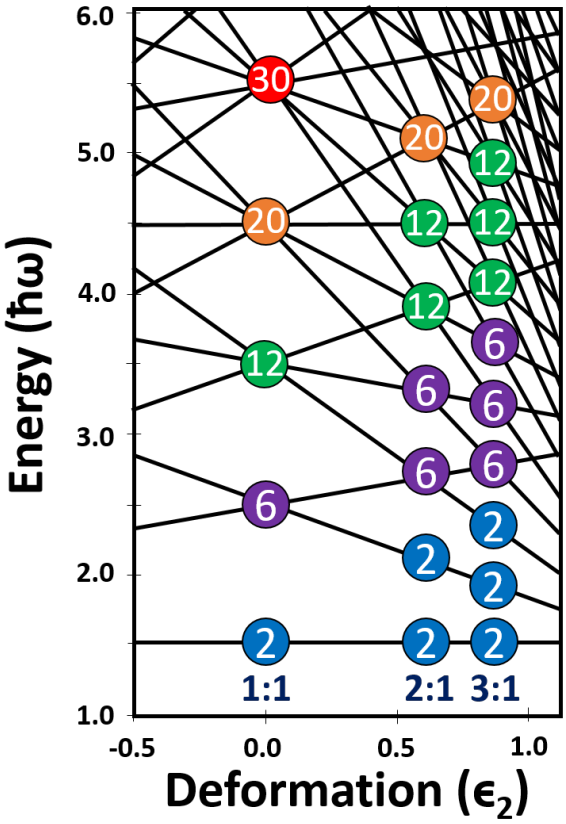

Figure 2.9: Development of degeneracies at deformations of 1:1, 2:1 and 3:1 in the deformed harmonic oscillator. Image adapted from [40].

ACM calculations demonstrate how one can describe linear chain configurations in α-conjugate nuclei.

Developments following this work on the deformed harmonic oscillator incorporate more sophisticated techniques to solving an N-body system. These rely on more realistic two-body forces as well as incorporating the antisymmetrisation properties needed to describe a fermionic system accurately. An example of a very successful method to incorporate these symmetries is that of Antisymmetrised Molecular Dynamics (AMD).

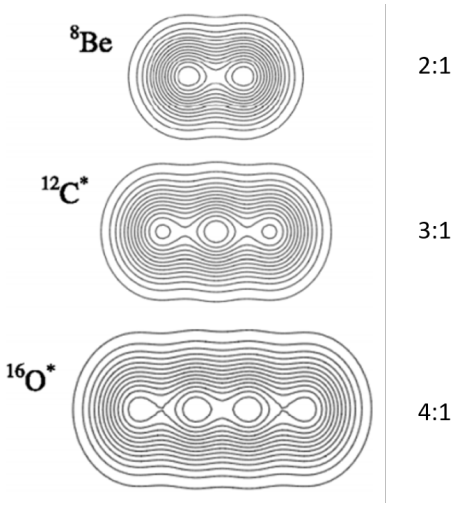

Figure 2.10: Density distributions of 2:1, 3:1 and 4:1 deformed harmonic oscillators showing the n interacting spherical harmonic oscillators for an $n:1$ deformed system [41].

2.2.4 Antisymmetrised Molecular Dynamics (AMD)

AMD relies on a very simple basis wave function which describes the fermionic system via the antisymmetrisation of Gaussian wave packets which describe the A nucleons in a system. The wave function is formulated best via the Slater determinant as follows [42]:

$$\Phi_{AMD}(Z) = \frac{1}{\sqrt{A!}}\mathcal{A}\{\varphi_1, \varphi_2 ..., \varphi_A\} \tag{2.18}$$

$$\varphi_i = \phi_{z_i}\chi_i\tau_i \tag{2.19}$$

$$\phi_{z_i}(\mathbf{r}_j) \propto \exp\left(-\nu\left(\mathbf{r}_j - \frac{\mathbf{Z}_i}{\sqrt{\nu}}\right)^2\right), \tag{2.20}$$

where χ_i and τ_i are the spin and isospin parts of the wave function and ν defines the diffuseness of the Gaussian. This wave function is then used to achieve an energy minimisation via the variation of the parameters $\mathbf{Z}$ (including the position of the Gaussian wave packets and the spin orientations) along with realistic finite-range two-body forces and zero-range three-body forces. After parity projection, the energy minimised wave function can be used to examine the features of a particular state, such as its structure in the intrinsic frame, and the energies and spin-parities of minima found. A great success of AMD in cluster physics is the fantastic agreement between the experimental evidence for clustering and the theoretical results obtained via AMD [43]. Figure 2.11

shows the results of an AMD density distribution for the first few excited states of ^{12}C, showing evidence of clustering (even small amounts below the break-up threshold) and a highly clustered Hoyle state without any assumption or preference for clustering inserted *a priori*. These calculations highly favour a ^{8}Be+α structure which will enhance the predicted branching ratio to this path.

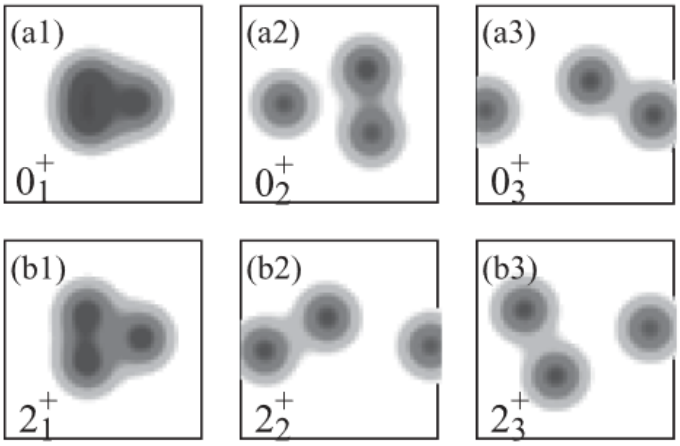

Figure 2.11: Density distribution from AMD calculations of the first few excited states in ^{12}C in the intrinsic frame - taken from [44]. The full spatial extent of the plot is 10 fm $\times$ 10 fm.

2.2.5 Group theory

As discussed in the introduction, it is the great success of modern physics that we can describe the majority of the observable universe via the four fundamental forces. Taking just three of the four (the strong, weak and electromagnetic forces), these forces are unified into the "standard model". The standard model takes a mathematical form described by the product group SU(3) $\times$ SU(2) $\times$ U(1)$_Y$. This product group represents the key features of the known fundamental particles. The first group SU(3) is used to describe the three colour charges inherent in the strong force (red, green, blue) and its generator describes the conversion between these colour charge combinations. The second group, SU(2), describes the weak isospin [45]. The final group U(1)$_Y$ [45] describes weak hypercharge.

These fundamental symmetry groups also appear in the nuclear force via the Interacting Boson Model (IBM) [46]. The SU(3) which is used in the standard model to describe the interplay of the colour charges of the strong force also has equal applica-

bility in describing an axially-symmetric prolate rotor [47]. The intrinsic symmetries of the group enter in the Hamiltonian which must be used to describe the system. The Bayman-Bohr theorem [48] describes how the shell model wave function is identical to a cluster-model wave function at zero separation between the clusters. As one inserts energy into the system, the evolution of the cluster-model wave function then corresponds to a breaking of the SU(3) symmetry.

In more complicated systems, the group becomes more interesting. To describe a system with ν degrees of freedom [49], one can describe the dynamics of the system with the U(ν+1) group. This can be used to describe a system of $N - \alpha$ particles where the degrees of freedom $\nu = 3(N-1)$. Previous studies [50] have described how these symmetries can be applied to ^{12}C. One can then formulate a Hamiltonian with the same symmetries as the U(7) which describes the dynamics of a triangular system. Taking a subgroup which describes an oblate equilateral triangle configuration (shown in Figure 2.12a), one is left with the D_{3h} symmetry group. This symmetry group has been used in chemistry to describe equilateral triangle molecules such as boron trifluoride as shown in Figure 2.12b. This symmetry can then be solved to second order in rotation-vibration interactions. This yields a series of states with different quantum numbers $(\nu_1, \nu_2, \ell_2, K, L, \pi)$. Figure 2.13 shows the comparison of the theoretically predicted against the experimental states in ^{12}C which shows a good agreement. This assignment therefore attributes the Hoyle state as a breathing mode vibration of the ground state (also known to have a very condensed 3-α structure). A description of the Hoyle state with this breathing mode requires a monopole excitation. Such monopole excitations are prohibited, the nuclear equation of state shows nuclear matter is incompressible [53]. This suggests a lower density of the nuclear equation of state is appropriate here where the compressibility of nuclear matter isn't excluded although this is an area which has not been sufficiently investigated.

This idea can be extended for the ^{16}O system where once again, one can analyse the U(10) symmetry properties and choose an appropriate subset which can be easily solved. This is done by assuming a tetrahedral symmetry of α-particles which manifests in the $\mathcal{T}_d$ symmetry group. In this formulation, summarised in Figure 2.14, a breathing mode assignment is also attributed to the first excited state, 0_2^+ in ^{16}O at 6.05 MeV. This designation may be worrying as this state is given a 4p-4h (4 particle + 4 hole) configuration [54][55] which is not expected to exhibit any condensation effects. Additionally, as admitted in the symmetry paper itself, the first excited state has recently been demonstrated to prefer a square configuration in *ab initio* lattice calculations [56]

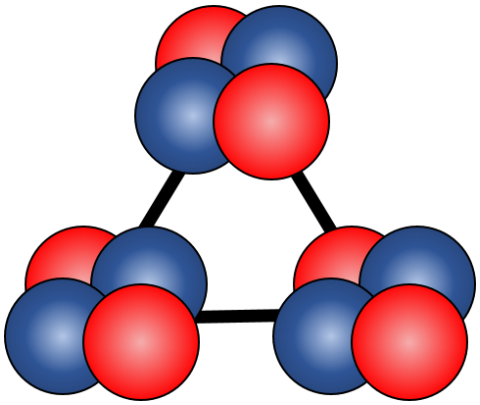

(a) With an α-particle placed at each vertex of an equilateral triangle, the nuclear system has the same intrinsic symmetries as that as in BF_3 and can then be described by the same mathematics - the D_{3h} symmetry group.

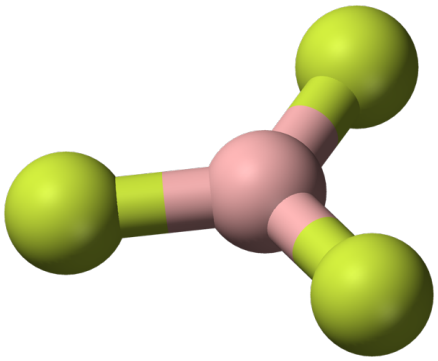

(b) BF_3 molecule displaying the same structure as the 3-α cluster structures in ^{12}C. From [51].

Figure 2.12: Symmetries employed for atomic molecular systems also provide a good description of nuclear structure states.

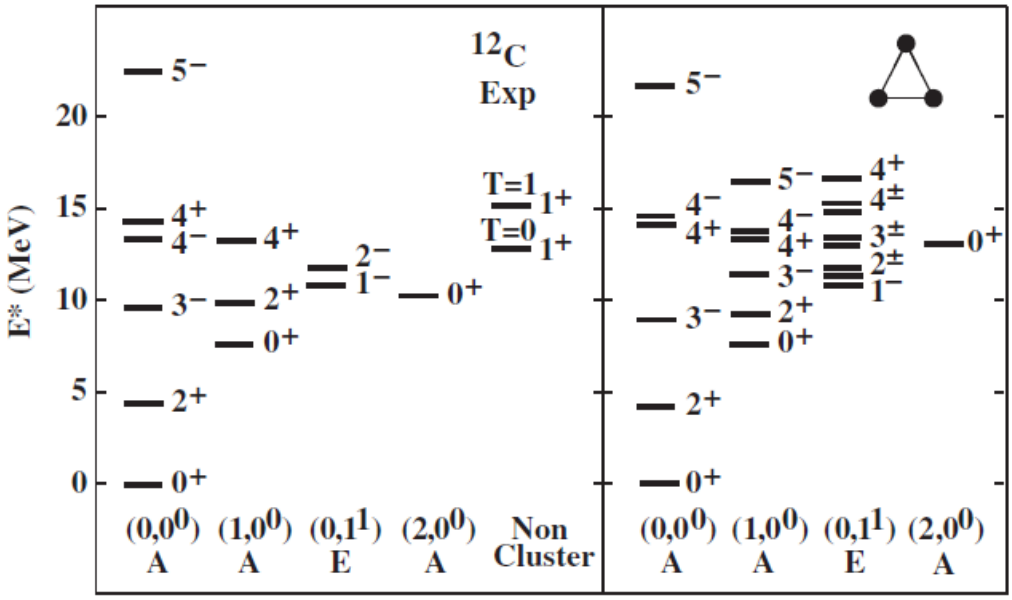

Figure 2.13: Comparison between experimentally measured states in ^{12}C (left) against those theoretically predicted by the D_{3h} group (right). From [52].

while the ground-state assignment agrees with a tetrahedral configuration (although the degree of separation of the α-particles is extremely limited) showing there is still much experimental work to be done here.

While the D_{3h} symmetry shows a remarkable predictive power in ^{12}C, one must ensure not to take the structural implications too strongly and instead understand these symmetry groups as a computational tool for describing the important parts of a state's subspace.

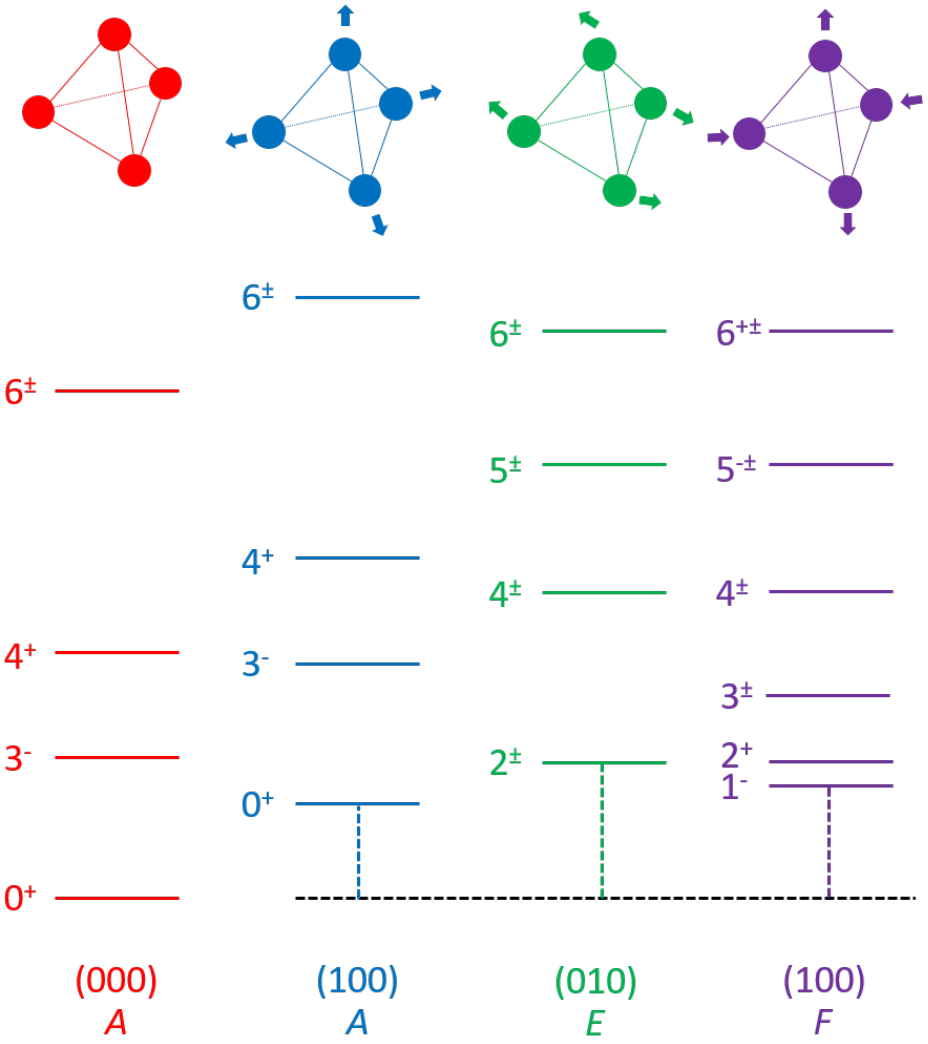

Figure 2.14: Prediction of states from a tetrahedral arrangement of α-particles described by the $\mathcal{T}_d$ symmetry group. The (000) rotational band denotes the ground-state band. The (100) band describes the symmetric breathing mode (analogous to the Hoyle breathing mode in D_{3h}). The movement of the α-particles corresponding to the different breathing/vibration modes are shown. Adapted from [57].

Chapter 3

Alpha-gas states

An extreme development of the cluster model is to treat the nucleus as composed entirely of interacting α-particles with no rigid structure. The highly inert nature of α-particles and their 0^+ spin-parity mean that they can behave like weakly interacting bosons. This constitutes a transition from a fermionic to a bosonic system where the Pauli Exclusion principle no longer affects the constituents. This results in a new state of matter called an **α-condensate** [34]. Quarteting of a two-neutron two-proton system into an α-condensed state in infinite matter has been well demonstrated [58] [59]. This corresponds to a phase transition with the α-particle scattering length as the order parameter. Where this reaches zero, the system exhibits a phase transition from a nuclear liquid to an α-condensate [60]. The nucleus exhibits this phase change when the density changes from ρ_0 to below the critical density of around $\frac{\rho_0}{5} \rightarrow \frac{\rho_0}{3}$ [61] [62] [63] [64].

3.1 THSR treatment

An analogue to this highly diffuse bosonic system is well studied in atomic systems where sufficiently cooled atoms can form a Bose-Einstein Condensate (BEC), whereby the bosons macroscopically occupy the lowest energy level [65] [66] [67]. This occurs at temperatures approaching absolute zero where a phase transition occurs, the effect this has on the system can be seen in Figure 3.1. This phenomena was first observed in ^{4}He, where a cooled liquid demonstrated the onset of superfluidity. New features of this low temperature state of matter are constantly being uncovered. Recent experiment efforts [68] have demonstrated exceptionally low densities of a BEC, whereby beyond mean

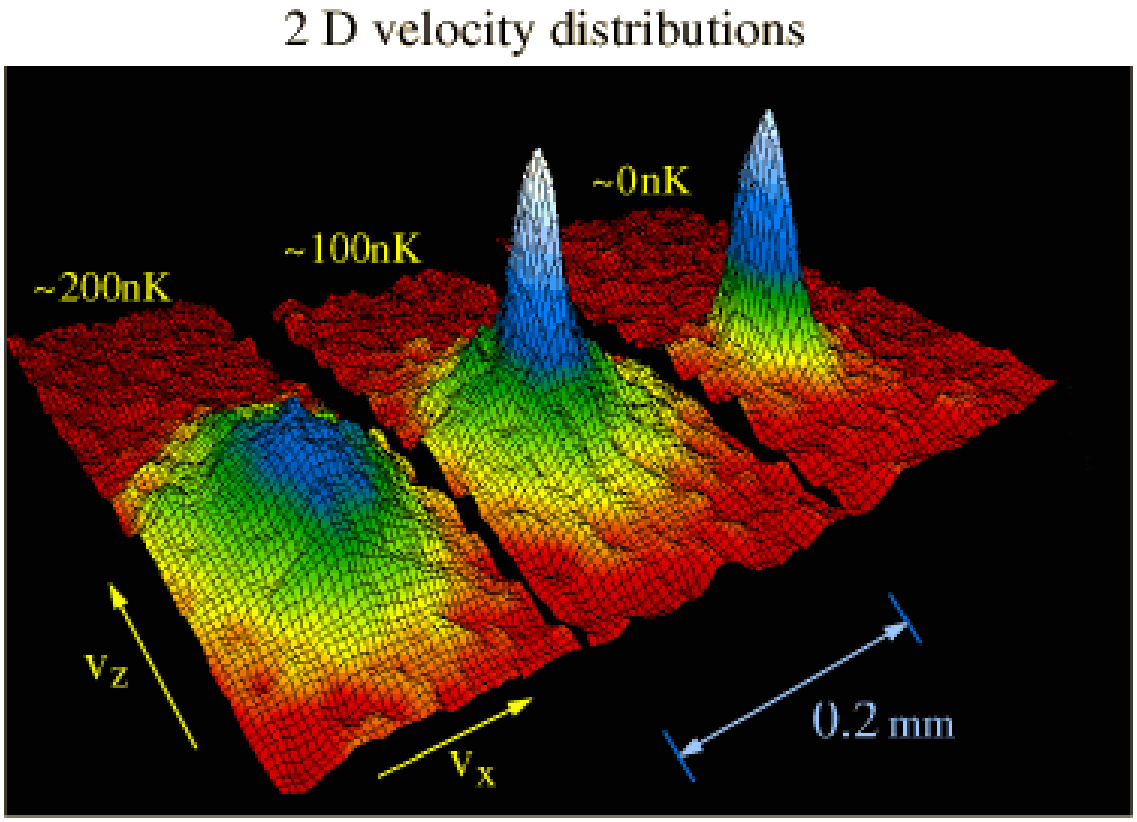

Figure 3.1: Velocity distributions for a cloud of ^{87}Rb undergoing a phase transition to a Bose-Einstein Condensate. As the critical temperature is achieved, the velocity spread becomes much smaller as the atoms macroscopically occupy the same state, the ground state. This smaller spread in momentum therefore corresponds to a larger spread in velocity as given by the position-momentum uncertainty principle. Image from [70].

field effects stabilise the liquid in an otherwise unstable configuration.

Fermionic systems can also undergo a similar phase transition although this differs from a BEC. ^{3}He exhibits a phase transition to a superfluid phase at 3 mK, whereby the fermionic ^{3}He atoms pair up to form pseudo-bosons [69]. This same phenomena is modeled to exist in the nuclear system with the quarteting of 2 protons and 2 neutrons and is parameterised using the THSR (Tohsaki-Horiuchi-Schuck-Röpke) wave function which describes the bosonic degrees of freedom of the α-particles [34].

The assumption of the THSR is based on a low overlapping of α-particles which allows for the bosonic nature of the state to be maintained as the fermionic sub-structure only becomes important at small distances. This is similar to how the quark degrees of freedom are unimportant for nuclear physics where the distances probed are large

enough that proton and neutron's substructure is not resolved. The $\alpha - \alpha$ potential as seen in Figure 3.2a shows why this idea is cogent, at small distances the $\alpha - \alpha$ potential becomes increasingly repulsive therefore the wave function overlap at small distances is prohibitively small. It is worth comparing this $\alpha - \alpha$ potential to atomic phenomenological potentials describing the effect of the Pauli exclusion principle from electron orbitals. A widely used potential is the Lennard-Jones 6-12 potential [71], whose form can be seen in Figure 3.2b and bears a striking similarity to the potential seen in Figure 3.2a. The Leonard-Jones 6-12 potential arises from a combination of the Pauli repulsion from overlapping electron orbitals and a van der Waals interaction arising from quantum fluctuations of the atoms which causes polarisations attracting atoms together. In the $\alpha - \alpha$ potential, this is replaced by the effect of the nuclear force. Utilising this $\alpha - \alpha$ potential allows for a description of this condensed system.

The THSR wave function for an $N - \alpha$ system is given by the following form [34]:

$$\Psi = \int d\vec{R}_1 d\vec{R}_2 d\vec{R}_3 ... d\vec{R}_n \mathcal{A} \left\{ G_1(\vec{R}_1) G_2(\vec{R}_2) ... G_n(\vec{R}_n) \times \exp -(R_1^2 + R_2^2 + ... R_n^2)/B^2 \right\}, \tag{3.1}$$

with the $G_n(\vec{R})$ being the α-particle wave function with a Gaussian-type spatial description. The entire wave function is antisymmetrised to maintain the effects of the underlying fermionic nature of the α-particles at small distances. This Gaussian-type wave function includes the spin, isospin and spatial components. The spatial component is a Gaussian with a diffuseness parameter b. The whole wave function is also contained in a Gaussian packet of diffuseness parameter B.

This wave function can be understood with the simple $N = 2$ case where the wave function is shown in Equation 3.2.

$$\Psi = \int d\vec{R}_1 d\vec{R}_2 \mathcal{A} \left\{ G_1(\vec{R}_1) G_2(\vec{R}_2) \times \exp\left(-(R_1^2 + R_2^2)/B^2\right) \right\} \tag{3.2}$$

This is an integral of the 3 + 3 dimensions for the 2 α-particles. If the region of this 6D space is examined where $\vec{R}_1 \approx \vec{R}_2$ then the antisymmetrisation term is as follows:

$$\begin{aligned} &\mathcal{A} \left\{ G_1(\vec{R}_1) G_2(\vec{R}_2) \times \exp -(R_1^2 + R_2^2)/B^2 \right\} \\ &= \exp -\frac{(R_1^2 + R_2^2)}{B^2} \left(G_1(\vec{R}_1) G_2(\vec{R}_2) - G_1(\vec{R}_2) G_2(\vec{R}_1) \right), \end{aligned}$$

with all the G_n being identical (representing the α-particle in the $(0s)^4$ configuration

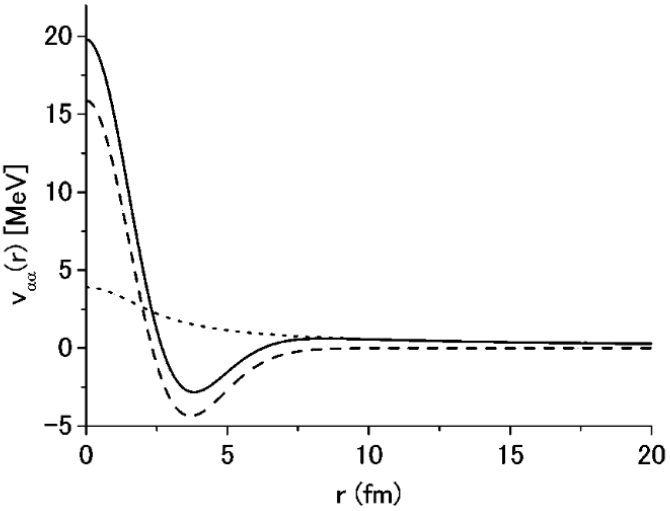

(a) Phenomenological potential felt by an $\alpha - \alpha$ interaction (solid). The contribution from the nuclear (dashed) and Coulomb (dotted) potentials are also shown separately. Figure taken from [72].

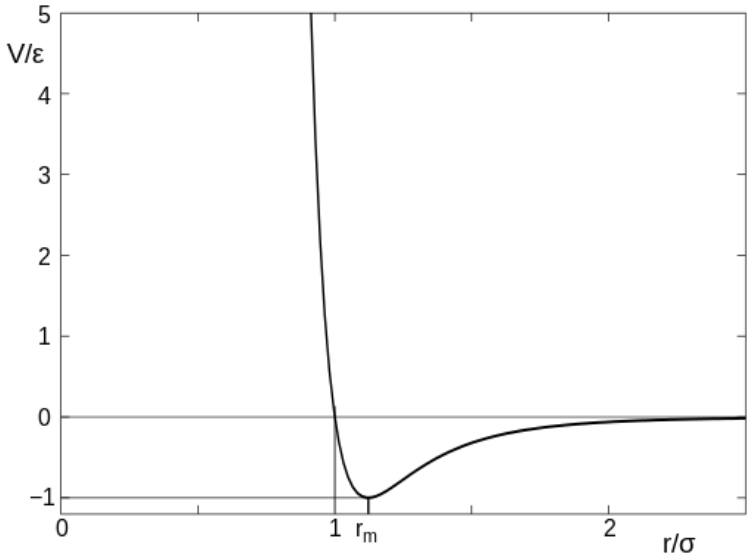

(b) Leonard-Jones 6-12 phenomenological potential, V, rescaled by the binding energy, ϵ. This describes the interaction between neutral atoms at a distance, r, as a combination of spontaneous Van-der-Waals interactions and the effect of the Pauli Exclusion Principle at short distances. The x-axis denotes the distance, r, scaled by the value at which the potential felt is zero. Figure taken from [73].

Figure 3.2: Comparison between the nuclear $\alpha - \alpha$ potential and an atom-atom interaction showing similarity between the two particularly pertaining to the effect of the PEP.

where all nucleons are in the lowest energy level) and $\vec{R_1} \approx \vec{R_2}$ then the antisymmetrisation causes this part of the wave function to go to zero very rapidly. This is solely the effect of the Pauli Exclusion Principle preventing multiple fermions occupying the same quantum mechanical state. If the value of the diffuseness parameter B is sufficiently small, the exponent is larger and therefore a more confined system ($\vec{R_i} \to 0$) is less inhibited. With a larger value of this parameter B, the system exhibits a larger $\vec{R_i}$ for the α-particles without the exponential term becoming prohibitively small. This oscillation parameter is then highly indicative of the size of the system.

When the size of the $0s^4$ wave function is much smaller than the size of the system (i.e. $b << |\vec{R_1} - \vec{R_2}|$), the effect of the diagonalisation becomes smaller and the N-α system behaves independently, much like a gas of α-particles. States in this regime can **then be described as α-gas states**. This is a more specific configuration that the α-condensate which, as shown above, can also describe a confined system. This condition can be seen to be well ensured by the potential seen in Figure 3.2a. In the opposite limit where $B \approx b$, the underlying fermionic nature of the constituents becomes dominant and one is left with the Slater determinant of the single-particles, the Hartree-Fock approximation. It can be demonstrated for the $N = 3$ α-particle system that as $B \to b$, the THSR wave function tends to the shell-model wave function [43]. This demonstrates the underlying features of the shell-model are contained within this model albeit with an additional degree of freedom by virtue of the breaking of the shell-model symmetry.

Studies of infinite nuclear matter properties have demonstrated that these forms of matter only become preferable at lower nuclear densities [74], a situation which is also seen in the form of the wave function. Following the Heisenberg position-momentum uncertainty principle, a smaller spread in momentum by virtue of a large occupation of a single energy level corresponds to a larger spatial spread. A good sign a given state is concordant with an α-gas is an extended radius. The two N-α states ascribed as α-condensate states both have anomalously large radii. This can be seen for ^{8}Be where the rotational band 0^+, 2^+, 4^+ shows a good rigid rotor, whereby the moment of inertia can be extracted (which is sensitive to r^2 rather than r). In order to describe these rotational band levels, the angular momentum projection must be carefully applied onto the THSR wave function. Despite the individual α-clusters being in a 0s state, the THSR wave function effectively solves the Schrödinger equation in a Gaussian basis where the weightings are physically motivated by the expected structure of the state. This can then still yield a non-spherical solution. To understand this, one can examine the deformation of ^{8}Be within this framework.

3.2 ^{8}Be

The 2^+ state in ^{8}Be is at 3.03 MeV [75]. With the energy relation for a rotational band:

$$E = E_0 + \frac{\hbar^2}{2\mathcal{I}} J(J+1), \tag{3.3}$$

with $\mathcal{I}$ being the momentum of inertia of the rigid rotor. This gives a value of an $\alpha - \alpha$ separation of 4.4 fm for ^{8}Be, which roughly corresponds to the two α-particles sitting at their touching distance ($r_\alpha \sim 2.2$ fm) demonstrating the reduction in density necessary to facilitate such a phase change. The results of the THSR calculation in comparison with the Brink model (which, as discussed previously, places α-particles at defined points in space) can be seen in Figure 3.3 which show similarity given the simplicity of the Brink model.

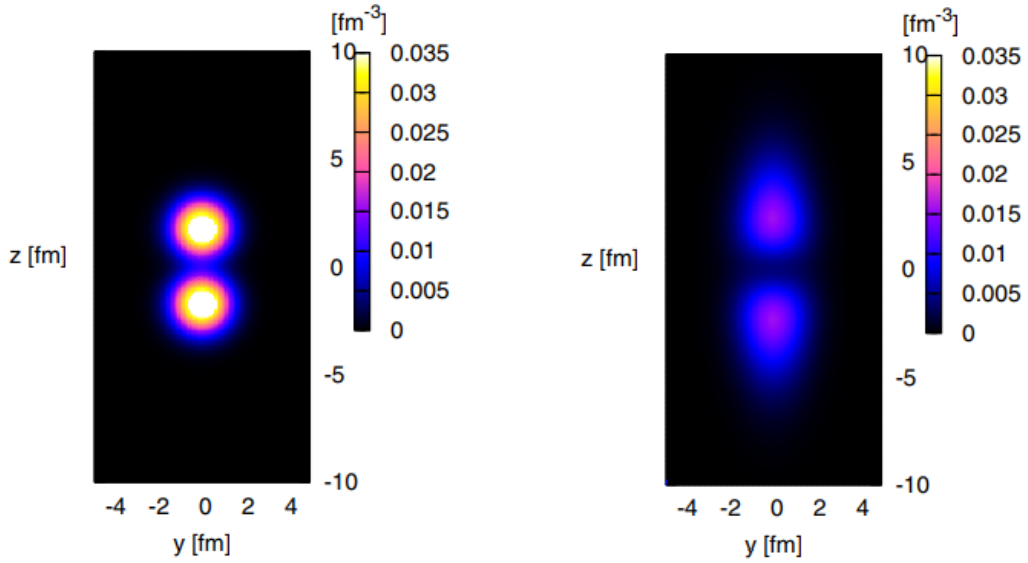

Figure 3.3: Comparison of single Brink (left) and THSR (right) intrinsic densities for ^{8}Be. Figure taken from [76].

The THSR naturally predicts the dumbbell structure and reproduces the inter α-particle distance well. Once again, this can be linked back to the $\alpha - \alpha$ potential where the demonstrated equilibrium position is around 4 fm. The stronger repulsion at shorter distances can also be seen in the intrinsic density plot, whereby the inter α-particle area has a lower density as the wave function is inhibited here and instead a broader tail at

higher distances is observed where the repulsion of the Coulomb barrier is weaker.

This demonstrates that developing a model of the nucleus as an α-condensate is not incongruous with certain traditional cluster models but merely describes the system within a physically motivated model space. This is seen in other situations, such as those mentioned above whereby cluster models also contain the zero-separation exact shell model solutions as part of their model space for certain systems.

3.3 $^{12}C(0_2^+)$

Naturally, one can also develop these tools further to applications of the N=3 system, ^{12}C. Analysis of the inelastic scattering form factor also demonstrates an extended radius for the Hoyle state, which indicates a larger volume by a factor of 2.5 to 4 [77]. This volume change is therefore sufficient to drop the density to the critical density for a phase change to an α-condensate making it an excellent candidate for an α-gas state. This structure is shown in Figure 3.4.

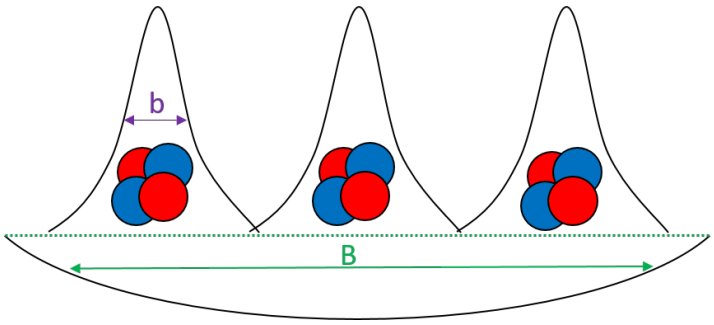

Figure 3.4: THSR description of a 3-α system showing the two diffuseness parameters b and B which define the α-diffuseness and the nuclear size respectively.

3.4 $^{16}O(0_6^+)$

While the Hoyle state is well established and has been studied for over 60 years, the Hoyle analogue state in ^{16}O is a more recent idea [78]. Calculations using the 4-body Orthogonality Condition Model (OCM) predict a series of 0^+ states in ^{16}O up to and above the 4-α threshold. The OCM model describes the relative motion between clusters which are subsequently antisymmetrised. These predicted states are visible in Figure 3.5 in comparison to experimentally observed states. The $0_{6\,\mathrm{OCM}}^+$ has a large radius of $\sqrt{< r^2 >} = 5$ fm and a 4-α occupation probability of 61% [79] (i.e. the wave

function is in the $(0s)^4$ state 61% of the time), suggesting this state reproduces the key parameters predicted by an α-condensate state.

These results can also be compared to calculations from the THSR wave function which also predicts a state with condensate characteristics above the 4-α threshold [80]. In the THSR framework, this state also has a large $^{12}C(0_2^+) + \alpha$ overlap suggesting a strong condensate nature to this state. This THSR state also has 64% occupation of the α-particles in the 0s orbital demonstrating a good agreement with the calculations in the OCM model.

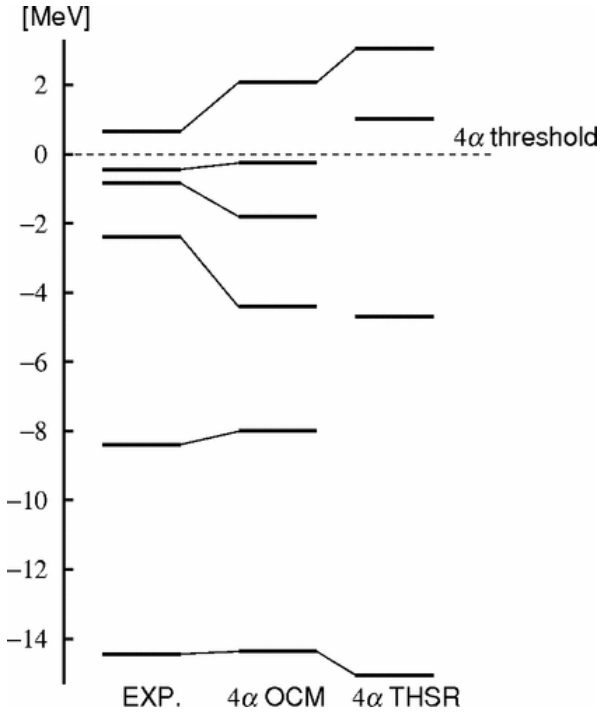

Figure 3.5: Comparison between experimentally observed 0^+ states, Orthogonality Condition Model predictions and THSR α-condensate predictions. Figure taken from [81].

A prediction of a condensed state at this energy (15.1 MeV) may be experimentally difficult to verify. As mentioned above, one can measure the strength of the decay of an N-α condensate to the (N-1)α condensate state. Examination of the predicted widths from the THSR wave function are tabulated in Table 3.1. These calculations demonstrate the proximity to the 4-α threshold is extremely prohibitive to the decay to the Hoyle state. To examine the degree of clustering for a state, the measured decay width Γ is examined. While this value is indicative of the structure of the system, the effect of penetrability can have a large influence on this value. Instead, the reduced

width amplitude γ^2 is more useful which is connected to the decay width Γ by:

$$\Gamma = 2\gamma^2 P_\ell(E), \tag{3.4}$$

with $P_\ell(E)$ being the penetrability. This is calculable by the R-matrix technique discussed in Section 2.1.2 via the regular and irregular Coulomb wave functions F_ℓ and G_ℓ and is given by:

$$P_\ell(E) = \frac{ka}{F_\ell^2 + G_\ell^2}, \tag{3.5}$$

where $k = p\hbar$ and with a choice of the matching radius a sufficiently far to not feel the effect of the nuclear force. This reduced width amplitude can then be compared to the Wigner limit which describes a theoretical maximum width in a system where the exit channel of interest has a constant probability density throughout the nucleus. The Wigner limit is then [82]:

$$\gamma_W^2 = \frac{3\hbar^2}{2m_0 a^2}, \tag{3.6}$$

with m_0 once again being the reduced mass. To determine the degree of clustering, this Wigner limit is compared to the reduced width amplitude as the Wigner ratio:

$$\theta_W^2 = \gamma^2/\gamma_W^2 \tag{3.7}$$

If this value is greater than ~ 0.1, the state can be considered to be well clustered and is therefore a useful observable to measure the degree of clustering.

Applying this to the $^{16}\mathrm{O}(0_6^+)$, despite a small Wigner ratio for the α_0 and α_1 decay, (where α_n corresponds to the decay path of $^A\mathrm{X}^\star + \alpha$ with the nucleus X in the n^{th} excited state), the absence of a prohibitive barrier for these decay paths means these become the dominant decay mode and the α_2 is experimentally almost impossible to measure (branching ratio (BR) $< 10^{-9}$). The change in the density of such an α-gas state must however be taken into account when considering the effect of tunneling.

Channel	θ_W^2 [83]	Γ (keV) [83]
α_0	0.024	104
α_1	0.016	32
α_2	0.6	8×10^{-7}

Table 3.1: Decay modes for the 0_6^+ state in ^{16}O as predicted from a THSR treatment of the state, with the penetrability calculated using R-Matrix (from [83]).

3.5 Coulomb barrier modification

The effect of this density change also has a drastic effect on the Coulomb potential [84] [85]. In order to describe the potential felt during the decay, one can use a single-folding potential. This is a convolution between the nucleon-nucleon potential and the density distribution of the decay product. In this single folding potential, one of the decay products is described as point-like. One can improve this potential by using a double-folding potential which is a double convolution of the nucleon-nucleon potential with the density distributions of both decay products. In situations where both decay products have a large spatial extent, the double-folding will differ to a larger degree from the single-folding potential.

In situations such as α-decay where one of the products is well described as point-like due to its small radius, the single-folding potential suffices and is given by:

$$V(\vec{R}) = \int d\vec{R}\, v(\vec{r} - \vec{R})\rho(\vec{R}) \tag{3.8}$$

The traditional nucleon-nucleon interaction is a combination of a Woods-Saxon potential to describe the nuclear force and a Coulomb term depending on the distance between the A_1 nucleons, $\vec{r'}$.

$$v(\vec{r'}) = \frac{-A_1 V_0}{1 + \exp((r' - R_0)/a)} + Z_1 Z_2 \frac{e^2}{r'}, \tag{3.9}$$

with V_0 describing the strength of the nuclear potential, R_0 the radius of the nucleus and a the diffuseness parameter. In order to describe the sparse and extended nature of an ejected α-particle condensate, a Gaussian with a tunable parameter b is used to describe the diffuseness of the system as shown in Eq. 3.1. The potential formed can describe the probability for this given decay particle pair using the WKB approximation [86]. The probability that an incident particle can tunnel through the barrier $V(r)$ with

an energy E is:

$$T = \exp\left(-\frac{2}{\hbar}\int_{r_1}^{r_2}\sqrt{2m(V(r)-E)}dr\right) \tag{3.10}$$

The decay rate, λ, is then given by the product of this decay probability, T, and the number of interactions with the barrier per second, f.

$$\lambda = fT = \frac{v}{r_1}T, \tag{3.11}$$

where v is the velocity of the pre-formed product inside the parent nucleus and r_1 is the distance to the classical turning point. Finally, the decay width, Γ, can be given by:

$$\Gamma = \hbar\lambda \tag{3.12}$$

An enhancement of the decay width for an α-condensate path against the predicted penetrability is also a signature of a condensate (by virtue of its extended radius). In addition, this reduced barrier for α, ^{8}Be and ^{12}C(0_2^+) (if the latter is indeed an α-condensate state) means that one would see an enhancement in the α-particle multiplicity as this decay channel is energetically favoured. This also manifests itself as a shift in the detected α-particle energy spectrum. The reduced barrier means that lower energy α-particles can overcome the Coulomb barrier as shown diagrammatically in Figure 3.6.

This technique is essentially equivalent to measuring a resonance in an α-clustered and a non α-clustered way, and attempting to find the energy of the peak, with the two different techniques. If the α-clustered decay gives a much lower excitation energy then this discrepancy can be explained via the modification of the Coulomb barrier for this decay mode.

3.6 Previous experiments

There have been previous investigations which have allowed for a partial insight into the propensity of α-particles to condense. A selection of results from different nuclei will briefly be presented here.

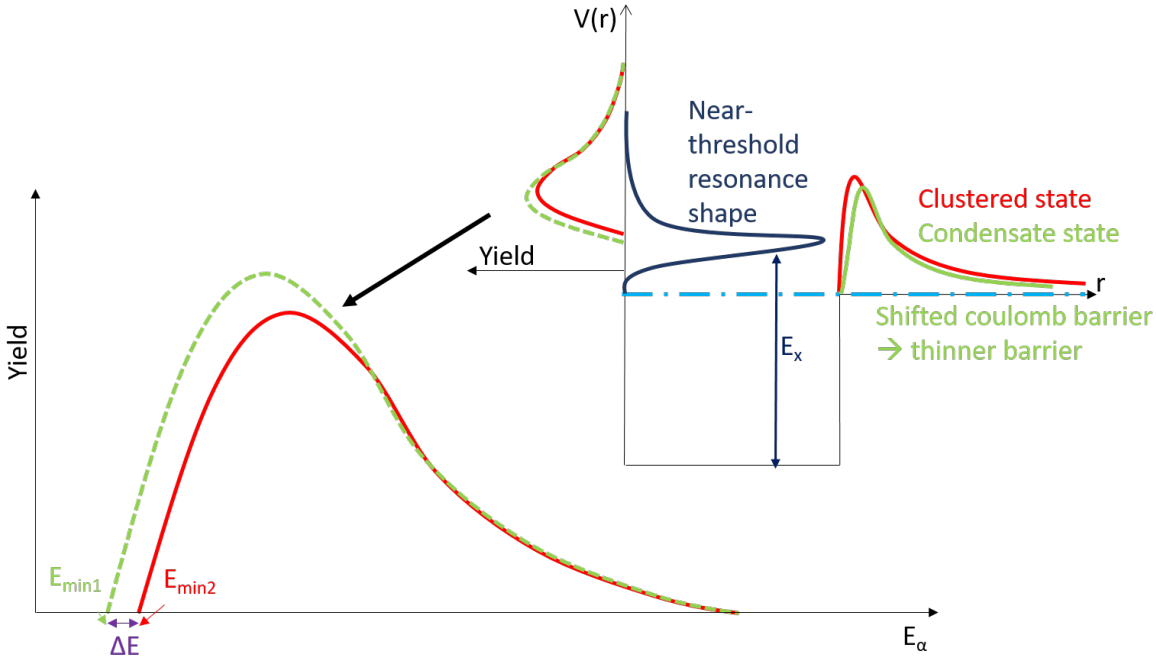

Figure 3.6: Diagrammatic explanation of the effect the reduced barrier has on the α-particle energy spectrum. In the top-right, one can see how the Coulomb barrier is different for a traditional clustered state (red) and an α-condensate state (green). The effect this has on the energy spectrum (bottom-left and to the left of the axis) is that the magnitude of the resonance multiplied by the penetrability through the Coulomb barrier gives the yield at a given excitation energy. For the condensed state, the width through the Coulomb barrier is reduced at low excitation energies in comparison to the traditional clustered state so the yield is increased here. The size of this effect can be inferred by analysing the minimum observed energy for a traditional clustered and an α-condensate state and calculating the difference between the two, ΔE.

Investigations of ^{12}C

As previously discussed, the N-α and α-condensate states are expected above the N-α threshold. For ^{12}C, this therefore corresponds to the Hoyle state. Given the interest in the Hoyle state and the ease of populating this resonance, there have already been experimental investigations which can elucidate to what degree the system can be described as a condensate. Two such contributions will shortly be discussed.

Measurement of the direct break-up of the Hoyle state

A key observable for the Hoyle state is a measurement of the branching ratio, whereby the decay does not proceed via the ^{8}Be(g.s) but instead decays directly to 3 α-particles. This value is useful for the astrophysical models of carbon burning and over many years, improved limits on this very small decay path have been measured. The latest of these was performed at Birmingham [87] and corroborated by an independent experiment at INFN, Napoli [88] at the same time.

These experiments demonstrated the direct branching ratio to 3 α-particles is $<$0.042% (95% confidence level). This value can be compared with predictions from a condensate which gives a value of around 0.06% by comparison of the two and three-body phase space and tunneling probabilities (from [87]).

A more recent study has focused on a more in-depth description of the decay mechanism (although omitting the important effects of the nuclear force) has predicted a direct decay component of $< 0.001\%$ [89]. This prediction is within current experimental reach albeit with a much greater amount of beam time required to reach the necessary statistics. Although further theoretical and experimental input is needed to determine to what degree the Hoyle state can be described as a condensate, the current results show no incongruity with the predictions.

Measurement of the rotational excitation of the Hoyle state

A traditional method of learning more about the structure of a given state is to investigate the rotational excitations of the resonance. The effect of introducing angular momentum to the system can give important information about the moment of inertia of the system, as discussed previously for ^{8}Be (Equation 3.3), as well allowing for a measurement of the electromagnetic transition rates. This is traditionally given as a B(E2) value, enhancements of which are indicative that the initial and final state

have a similar structure and as such belong to a rotational band. Different theoretical models can also predict different values for the size of this transition strength which can differentiate between alternate descriptions of a state's structure.

The rotational excitations of the Hoyle state are difficult to measure, mostly down to the strength of other states in the vicinity of the predicted energy region. The first rotational band candidate to be measured was a 4_1^+ state at 13.3 MeV [90]. Following the expected energy-spin systematics, this placed the 2_2^+ in close proximity to the 3_1^- at 9.64 MeV which is usually strongly populated and therefore would shroud a contribution from the 2_2^+. Several experiments had indirectly demonstrated an additional yield at around 9.7 MeV [91] [92] [93] however an experiment utilising a photodissocation reaction in an optical time projection chamber (TPC) proved this was due to a $J^\pi = 2^+$ resonance. The energy of the state was measured as 10.0 MeV (although a further calculation taking into consideration the effects on the non-resonant contribution gave a smaller value of 9.9 $\rightarrow$ 9.75 MeV for a radius of 5 fm $\rightarrow$ 6.5 fm accordingly [94]). Looking at the energy-spin systematics for the Hoyle rotational band, for the bandhead, 2^+ and 4^+, the curve deviates from the normal E $\propto$ J(J+1) line (see Figure 3.7).

As seen from the figure, the results from AMD calculations (discussed in detail in Chapter 2.2.4) are compared with the experimental observations. By extrapolating backwards to find the expected bandhead energy (E_0) from the measurement of the 2_2^+ and 4_1^+ (where an energy of 9.8 MeV is used for the 2_2^+), the expected E_0 energy is in-between the Hoyle state and the 0_3^+. This 0_3^+ state is extremely broad and was traditionally attributed as part of a very wide resonance at 10.3 MeV but has since been discovered to be composed of two broad 0^+ states [95]. The 0_3^+ was shown to have a large ^{8}Be(g.s)+α decay width therefore was assigned as a "higher nodal state" of the Hoyle resonance whereas the 0_4^+ was attributed to a quasi-linear chain arrangement. The AMD calculations [96] show a large transition amplitude between the 2_2^+ and the 0_3^+ suggesting that perhaps the "true" bandhead for this rotational band is that of this 0_3^+ rather than the Hoyle state. Alternatively, this strong transition strength could be indicative of a change of the moment of inertia of a rotational band built on the Hoyle state as the angular momentum increases. Further investigation of this rotational band is therefore required and experimental data measuring the transition strengths from $2_2^+ \rightarrow 0_3^+$ and $2_2^+ \rightarrow 0_2^+$ are required to confirm the AMD calculations. Different experimental groups are currently trying to measure them. For example, see [97].

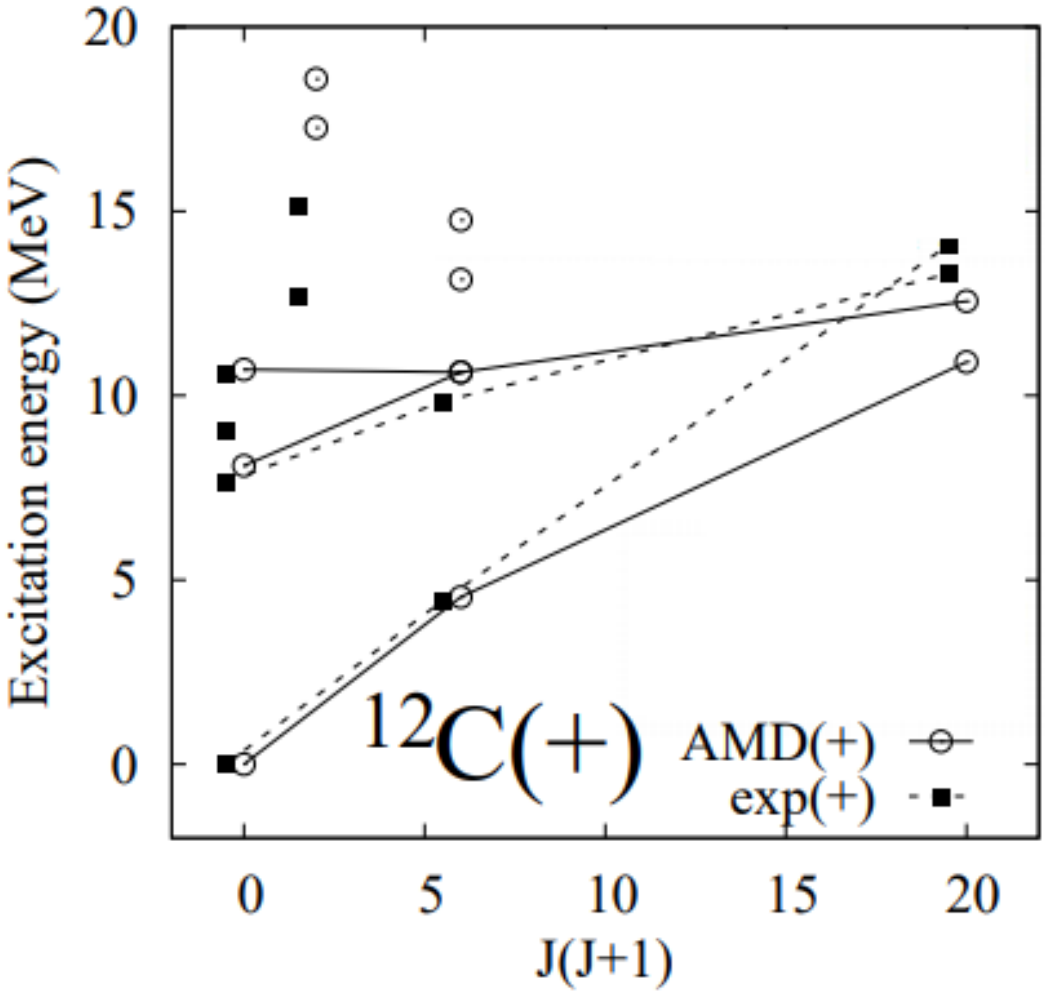

Figure 3.7: Energy spin-systematics for the resonances above the 3-α threshold in ^{12}C. The Hoyle rotational band can be seen to have a bent-arm structure from AMD calculations. Figure adapted from [43].

Investigations in ^{16}O

Research into 4-α structures has been developed since the 1960s with an experiment performed using the ^{12}C(α,^{8} Be)^{8}Be [98] compound nucleus reaction purporting to find a rotational band with an extremely large moment of inertia. Such a large moment of inertia was attributed to a linear chain arrangement, however further investigations failed to find evidence of either the bandhead or the 8^+ member of this band [99]. This idea still persisted until a more recent experiment [100] demonstrated these states do not constitute a rotational band and as such a 4-α linear chain structure cannot be seen around the 4-α threshold. Among these improved data are no rotational bands with a bandhead just above the 4-α decay threshold around the 15.1 MeV, where the predicted α-condensate state should be.

A recent experiment performed in Cape Town, South Africa [101], aimed to populate states in ^{16}O using an α inelastic scattering reaction in conjunction with an extremely high resolution spectrometer. A simultaneous measurement of the scattered beam and the scattered ^{16}O* products allowed for the differentiation between the α_0, α_1 and p_0 decay paths for the excited ^{16}O system (where α_n and p_n refer to a decay where an α-particle and proton are emitted in the ground-state and the residual nucleus is left in the n^{th} excited state). The main results from this experiment can be seen in Figure 3.8, where the decay path selection and overall excitation function are shown. In particular, there is a blown-up region showing the vicinity of the expected 15.1 MeV condensate state which can be seen to be comprised of a doublet of states separated by roughly the experimental resolution. Angular correlation measurements of the α_0 channel also demonstrated that this doublet of states is incompatible with a 0^+ and an $\ell = 0 \rightarrow 6$ contribution casting doubt on whether this narrow state in the α_0 channel corresponds to a 0^+ state and if it is therefore a strong candidate for the α-condensate system in ^{16}O.

Investigations in heavier systems

While experimental evidence for α-condensation in light nuclear systems is well developed (but has not demonstrated yet unequivocally the existence of these states), investigations in heavier systems have had less experimental focus. Two experiments have attempted to probe potential α-condensation structure in heavier systems; their results will briefly be discussed here.

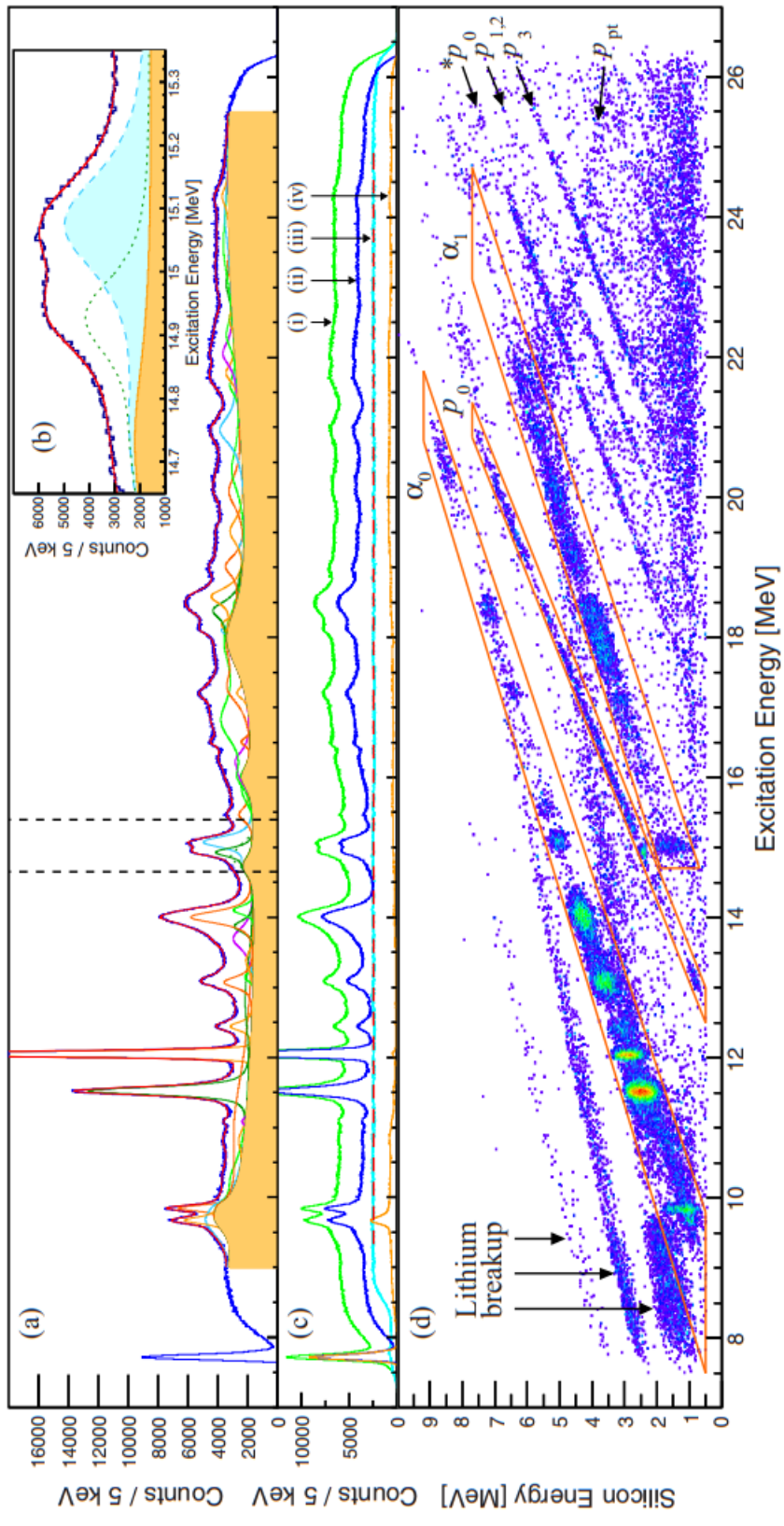

Figure 3.8: Results from a $^{16}O(\alpha,\alpha')^{16}O$ experiment showing the states populated in ^{16}O and their corresponding decay paths. Part a) shows the raw excitation function in contrast to Part c) which shows the effect of various background subtraction techniques from the raw spectrum (i) to removal of the background in (ii) which can be split into contributions from the primary target (iii) and the carbon backing (iv). Part d) shows how the coincident matrix between the silicon energy to measure the scattered target and the excitation energy from the spectrometer can identify the different decay paths. Part b) shows the region around 15.1 MeV where the α-condensate state is predicted to exist. Figure taken from [101].

^{18}O(^{13}C,^{23}Ne)2α and ^{28}Si(^{24}Mg,^{40}Ca)3α Two experiments were performed by Kokalova [102] [84] [85] using the GASP γ-detector array in conjunction with the ISIS silicon-ball which allowed for charged-particle spectroscopy in conjunction with γ-ray detection. The first experiment utilised an ^{18}O beam at 100 MeV impinging on a ^{13}C target. The channel selected was where two α-particles were measured in the ISIS array. A differentiation between those reactions whereby these α-particles originated from ^{8}Be(g.s) and from a direct emission was possible. The distinction between these two decay paths allows for a comparison of the γ-decay spectrum whereby additional reaction channels become open. This demonstrates that when observing the decay via ^{8}Be rather than 2α, the daughter nucleus is left in a higher excited state where more decay channels are open. Although this can be attributed to a kinematic effect (both in terms of angular momentum and sequential tunneling for a single step or double step reaction), this could be an indication of a lowering of the Coulomb barrier due to α-condensation. This lowering of the barrier means that a decay product with a lower overall energy can be emitted leaving the system in a higher excited state via the mechanism shown in Figure 3.6.

A similar analysis technique utilising a ^{24}Mg beam at an energy of 130 MeV impinging on a ^{28}Si target analysed the difference of 3 sequential α-particles versus the emission of ^{12}C(0_2^+) (the Hoyle state). Once again, additional channels remained open as evidenced by the γ-spectrum. In this case, this γ-decay from ^{36}Ar has been observed which corresponds to a 4$^{\text{th}}$ α-particle (unmeasured) being emitted which is not predicted by the statistical compound decay model (Hauser-Feshbach). A possible interpretation of this is the effect of condensation therefore lowering the barrier and allowing tunneling beyond that of the Hauser-Feshbach calculations performed by Kokalova. These investigations laid the basis for the current investigation in ^{28}Si. By examining both the effect of correlated versus uncorrelated emissions, one can infer whether the system is consistent with sequential decay models.

Nickel-56 More recent experiments have focused on the most extreme N=Z, α-conjugate nuclei by looking at ^{56}Ni [103]. By populating high excitations via an α inelastic scattering at 50AMeV, high multiplicity decays of α-particles were measured. Although the full m=14 events were not detected, multiplicities up to 7 were seen. This was then compared with predictions from Hauser-Feshbach calculations using CASCADE and was shown to exceed the predictions from the statistical decay model. This work is promising, however to demonstrate the effects of condensation in such a system,

the full multiplicity events are needed. The limits of the statistical decay model used may also be brought into question as examined in Chapter 5. Additionally, one may also question whether the ^{56}Ni is too heavy to form an α-condensate as discussed in Chapter 8.

Lessons learnt

Analysis of previous efforts to investigate α-condensation show a few common themes which will be briefly summarised.

- One particular area of interest is in demonstrating that via a **high multiplicity break-up**, additional mechanisms are observed above those predicted by statistical decay models.

- An understanding of the intrinsic symmetries of the condensate wave function and comparing it to other condensate wave functions shows that by **observing the decay modes of a particular condensed state to a lighter condensed system** can also give a signature of this type of matter.

- Using the ideas of the modification of the nuclear radius and the effect this has on the Coulomb barrier from condensation, this **modification to the Coulomb barrier** then means that α-condensed systems are less inhibited and correspondingly can undergo decays at a lower excitation than expected from a traditional clustered system [84]. This then corresponds to a measurement of the statistical decay energy spectrum, **a shift in the minimum measured energy between a condensed and a clustered state** is then a signature of condensation (as other phenomena cannot explain such a drastic modification of the penetrability).

- A direct examination of the ***α*-conjugate excitation functions** and their associated decay paths can also indicate the presence of states which are "Hoyle analogues" and can be considered as an α-condensed system by virtue of its proximity to the N-α barrier.

3.7 Summary

As elucidated in this Chapter, through the continuing comparison of experimental data with theory, making use of different models and reaction mechanisms, one can gain an insight into the nature of the nuclear force. In particular, the model of treating α-conjugate nuclei as an α-gas system of weakly interacting bosons is presented as a good probe of the nuances of the nuclear force. Here, care must be taken not to confuse the completeness of a particular model space with the system as being representative of the wave function basis used. In this case, the success of the THSR wave function in describing ^{8}Be and ^{12}C(0_2^+), as well as structures such as $^{16}\mathrm{O} \oplus \alpha$ cannot be taken as proof that those correspond to α-condensed states. Instead, the model space (albeit physically motivated by α-condensed states) is general enough to describe the $^{16}\mathrm{O} \oplus \alpha$ traditional cluster structure, which is not associated with a system comprised solely of weakly interacting α-particles. To find evidence of α-gas states, one must look to experimental observables which differ from the predictions of cluster calculations such as those listed in Chapter 3.

This new state of matter corresponds to a phase change from geometrical clustering which in itself is a breaking of the U(6) symmetry used to describe spherical nuclei. Perhaps future ideas on α-gas states can rely on the tools and techniques already developed in group theory (as discussed in Chapter 2.2.5, specifically for the D_{3h} group description of ^{12}C) to describe the phase change as an additional breaking of symmetry. These ideas are summarised in Figure 3.9 which show the evolution of the different symmetries for different descriptions of nuclei. In a similar way, Figure 3.10 shows how the deformation changes across the nuclear chart and, as such, the group used to describe the shape also changes.

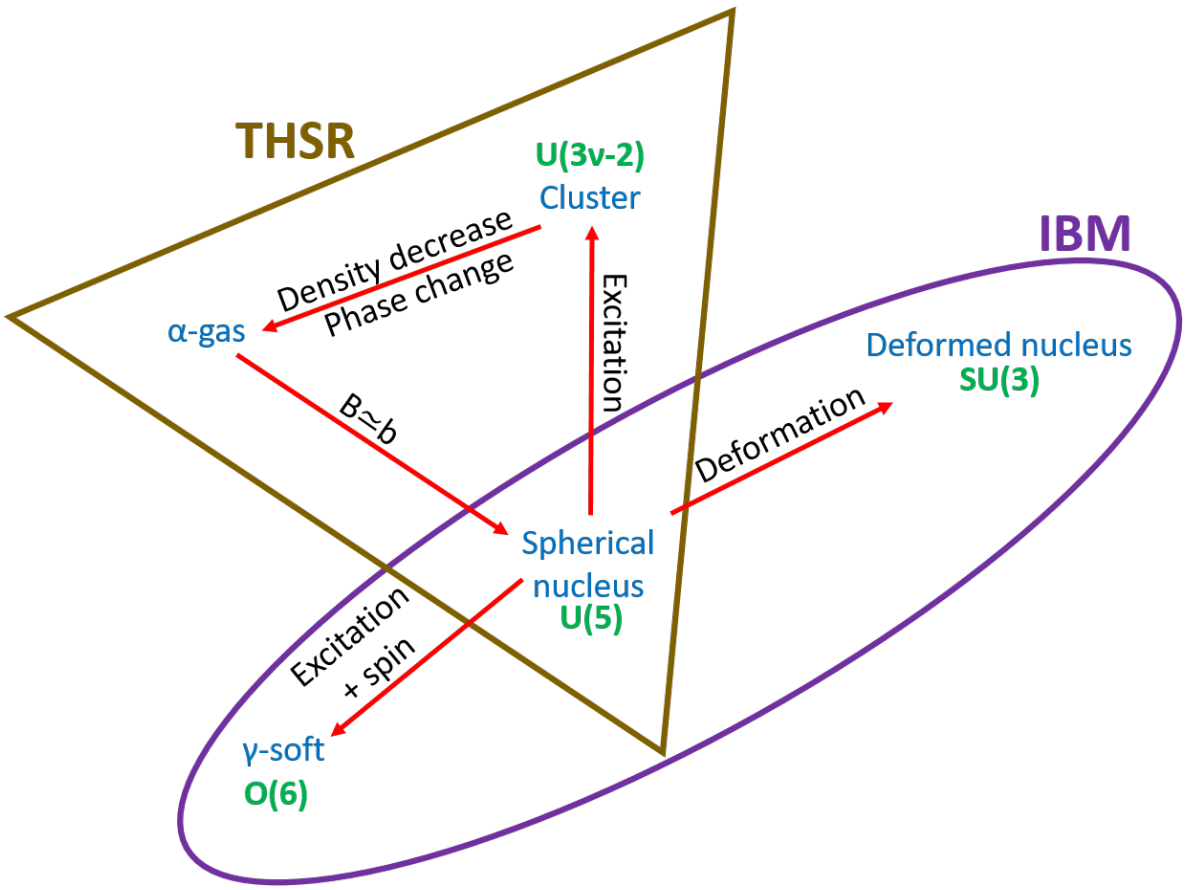

Figure 3.9: Diagram showing the connection between the different group symmetries. Starting with the U(5) model which describes spherical nuclei via the IBM, excitations can cause a breaking of this symmetry to a geometrical cluster structure (e.g. the D_{3h} group for a triangular arrangement of α-particles). This symmetry can then be further broken to form an α-condensate. Taking the appropriate limit of such a state ($B \approx b$) one can then regain the shell model-like solution. Alternatively, this symmetry can be broken by provoking deformation. These different deformation regions can also be seen in Figure 3.10. The region subtended by the yellow triangle can be described via the THSR treatment while the purple ellipse shows the extent of the IBM.

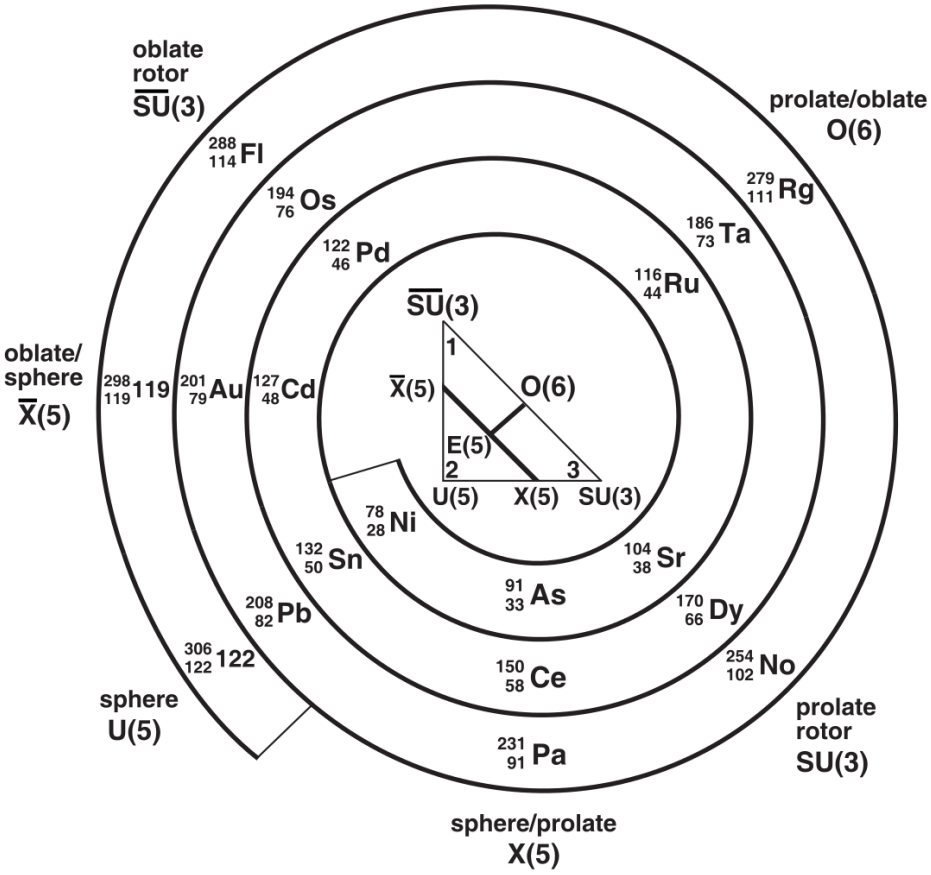

Figure 3.10: Different regions of the nuclear chart can be described by symmetry groups based on their deformation using the IBM. This chart shows how the appropriate symmetry group evolves periodically as one moves through closed shells. Taken from [104].

Chapter 4

Experiment

To investigate α-gas states, an ^{16}O beam at a lab energy of 160, 280 and 400 MeV from a K800 cyclotron was impinged on a natural carbon target of thickness 58 $\mu g/cm^2$ with an average beam current of 100pA. The decay of the compound nucleus ^{28}Si then allowed an analysis of the α-gas observables mentioned previously. Measuring a final state of 7 α-particles is therefore the main goal of the experiment. Such analysis relies on the careful measurement of several experimental observables.

4.1 Experimental requirements

As discussed in the previous chapter, in order to extract a signature for the α-condensate states, one must carefully measure the features mentioned in Chapter 3.6. To do this with sufficient statistics and resolution, a much more advanced charged particle detection set-up than traditionally used to study light clustering systems is required. For these traditional experiments, a series of particle detectors (i.e. silicon double-sided silicon strip detectors (DSSDs)) are placed in the chamber providing a small angular coverage in a position where the reaction products are expected to be produced. These experiments usually pick up 2 or 3 reaction products where the kinematics are rather rigorously set, so a more sophisticated output is needed for this investigation. This measurement requires a high angular coverage detector where the efficiency to pick up high multiplicity events is not inhibited by the detector array. Additionally, due to the high excitation energies which are to be employed in this investigation, a large range of energies are needed to be covered (from ~ 1 MeV $\rightarrow$ 400 MeV). Across this entire energy range, a good identification of the reaction products as well as a precise measurement

of their energy and corresponding direction is required. These key criteria are therefore summarised below:

- **Large solid-angle coverage**
- **High dynamic energy range coverage**
- **Good energy resolution**
- **Good α-particle identification** across the entire energy range
- **High granularity** of the detector array to give good position resolution

4.1.1 Accessibility of observables

With an experimental facility which possesses the required criteria, several of the key observables for an α-gas system are accessible.
The main observable which is to be examined in this experiment is the increased multiplicity when examining the break-up of the compound system into α-particles or a sub-system which is entirely composed of an α-gas (i.e. ^{8}Be $+^{12}$ C$(0_2^+) + \alpha + \alpha$). The combination of large solid-angle coverage and good particle identification means that on an event-by-event basis, the total number of α-particles can be counted. A good understanding of the detector response (particularly missing solid-angle coverage) means that the original decay multiplicity can be obtained (as performed in Chapter 5.4.2).
As well as observing the total α-multiplicity, a particular signature this experimental set-up is sensitive to is the comparison of the 7-α decay modes. As mentioned before, the decay modes to different α-gas states should have the same transition strength i.e. ^{12}C$(0_2^+) +^{12}$ C$(0_2^+) + \alpha$, ^{8}Be $+^{8}$ Be $+^{8}$ Be $+ \alpha$ and 7α all have the same probability to be populated from an α-gas state of 7 α-particles. With a modest detector coverage of 25%, if 7 α-particles are emitted isotropically then this gives an efficiency to detect 7 α-particles of 0.01%. With an estimated 7-α cross section of 10 mb, a carbon target of 92 μg/cm^2 and a beam current of 100pA, $\sim$ 170 7-α events should be measured over 7 days of beam time. This is sufficient to give a 10% total error. A comparison of the strength for the 8 different paths can then be achieved with a 20% error on each value. If these values are in agreement with one another, this is indicative that the compound system (and indeed the Hoyle state) can be described by an α-gas.
The final observable to be investigated with the given experimental set-up is the direct

observation of N-α states. In particular, a strong population of the suspected α-gas 15.1 MeV state in ^{16}O and/or near N-α threshold states in ^{20}Ne and ^{24}Mg are also highly indicative of an α-gas state where the inter α-particle binding is weak. Observation of the 15.1 MeV state via the highly suppressed 4-α decay mode to obtain a branching ratio also allows for a probe of whether this structure can be described as an α-gas system. An enhancement of this channel compared to the prediction made in Table 3.1 is also an observable signature with the current set-up. By choosing to study the decay of ^{28}Si therefore, the α-conjugate nuclei up to ^{24}Mg can be investigated simultaneously. Selecting a heavier nucleus to study however starts to become prohibitive as the probability for measuring all the α-particles decreases and the results are limited by statistics.

These array criteria are not readily satisfied for the study of light cluster physics however other experimental setups with these capabilities are available for use. To achieve the key criteria above, a search was performed to find a suitable location for this experiment. One such facility found was the Laboratori Nazionali del Sud (LNS), Catania, Italy, used for investigations in heavy ion physics. In particular, this setup is used to look at fragmentation and isospin effects of multifragmentation reactions to study the nuclear equation of state. This facility has not previously been used to study similar nuclear structure physics but gave the best fulfillment of the necessary criteria. An additional aim of this thesis was therefore to explore and demonstrate the feasibility of the use of this facility for light structure physics.

To improve the setup to meet the key criteria listed above, a smaller detector array which was newly commissioned was also implemented into the setup. These two detectors arrays were the CHIMERA [105] and FARCOS [106] systems.

4.2 Combined system

The combined CHIMERA+FARCOS system provides a good combination of high angular resolution at small angles and a high detector coverage. The working telescopes and overall coverage can be seen in Figure 4.1 and 4.2. An overall solid angle coverage of 28% was achieved (when excluding those which were excluded as discussed in this Chapter) demonstrating the advantages of utilising such an array. This combines 1192 telescopes in CHIMERA with 4 FARCOS detectors. Such a large number of detectors required a substantial amount of development of various calibration techniques and codes which will be covered during this chapter. The main analysis code was based on

the *CHIMERAUNPACKER* [107] decoder which allowed the CHIMERA and FARCOS ADC values to be read into C++/ROOT in a combined data stream.

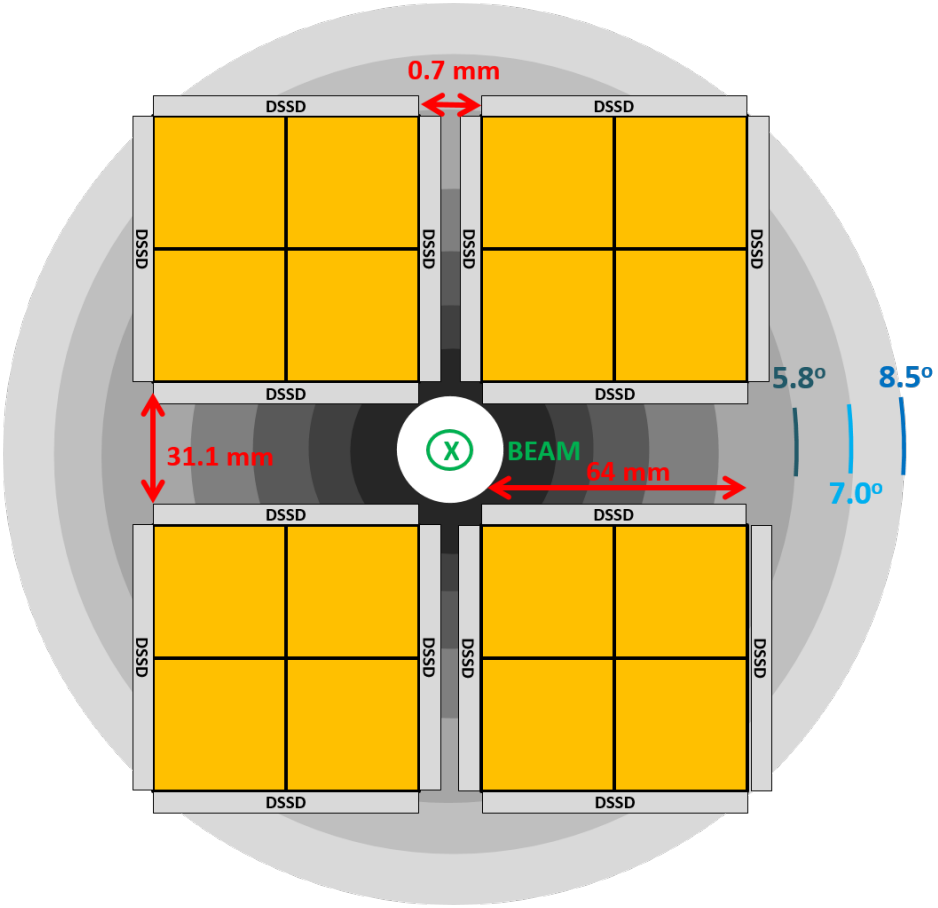

Figure 4.1: Schematic of the combined system when viewed from the target down the beam-line. FARCOS obscures several low angle CHIMERA rings (shown in grey) behind the four FARCOS modules. Not to scale. The lab scattering angle is shown for a few CHIMERA rings.

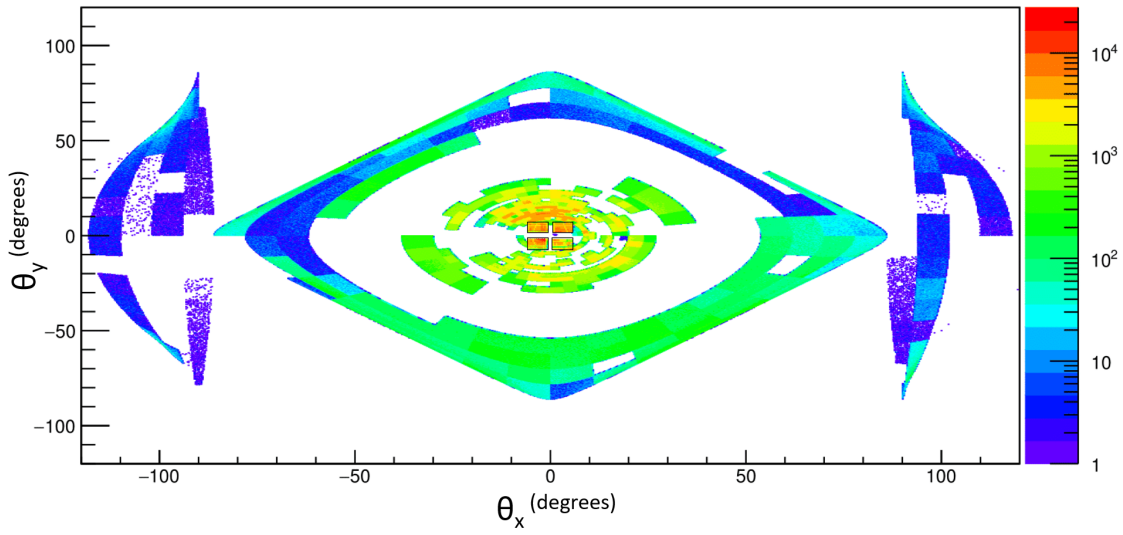

Figure 4.2: Hit patterns for the combined system with a projection in terms of the Cartesian angles θ_x and θ_y. The FARCOS detectors have been overlaid with black squares to show their location in the centre of the detector array.

4.3 CHIMERA

The CHIMERA (Charged Heavy Ion Mass and Energy Resolving Array) detector comprises two sections, the first being the forward rings. This section consists of 18 rings (i.e. full annular azimuthal coverage) of detectors covering lab scattering angles from $1^\circ \rightarrow 30^\circ$ at varying distances with the smallest angles the furthest away. The second section is the backwards ball component which has rings covering from $30^\circ \rightarrow 176^\circ$ at a constant distance from the target of 40 cm. This configuration can be seen in Figure 4.3 and the detector parameters are available in Table 4.1. The rings consist of a series of individual telescopes which allow for high dynamic-energy range particle-identification and momentum measurement.

Ring number	**No. of detectors**	**Working detectors**	$\theta_{\mathbf{low}}(^\circ)$	$\theta_{\mathbf{high}}(^\circ)$	**Distance (cm)**	$\mathbf{\Delta}\theta(^\circ)$	$\mathbf{\Delta}\phi(^\circ)$
1I	16	0	1	1.8	350	0.8	22.5
1E	16	0	1.8	2.6	350	0.8	22.5
2I	24	0	2.6	3.6	300	1.0	15.0
2E	24	0	3.6	4.6	300	1.0	15.0
3I	32	0	4.6	5.8	250	1.2	11.25
3E	32	2	5.8	7.0	250	1.2	11.25
4I	40	11	7.0	8.5	210	1.5	9.0
4E	40	18	8.5	10.0	210	1.5	9.0
5I	40	13	10.0	11.5	180	1.5	9.0
5E	40	12	11.5	13	180	1.5	9.0
6I	48	12	13.0	14.5	160	1.5	7.5
6E	48	17	14.5	16.0	160	1.5	7.5
7I	48	22	16.0	18.0	140	2.0	7.5
7E	48	12	18.0	20.0	140	2.0	7.5
8I	48	16	20.0	22.0	120	2.0	7.5
8E	48	21	22.0	24.0	120	2.0	7.5
9I	48	21	24.0	27.0	100	3.0	7.5
9E	48	11	27.0	30.0	100	3.0	7.5
10	32	0	30.0	38.0	40	8.0	22.5
11	32	0	38.0	46.0	40	8.0	22.5
12	32	0	46.0	54.0	40	8.0	22.5
13	32	14	54.0	62.0	40	8.0	22.5
14	32	10	62.0	70.0	40	8.0	22.5
15	32	14	70.0	78.0	40	8.0	22.5
16	32	19	78.0	86.0	40	8.0	22.5
17	32	1	86.0	94.0	40	8.0	22.5
18	32	10	94.0	102.0	40	8.0	22.5
19	32	7	102.0	110.0	40	8.0	22.5
20	32	15	110.0	118.0	40	8.0	22.5
21	32	0	118.0	126.0	40	8.0	22.5
22	32	0	126.0	134.0	40	8.0	22.5
23	32	0	134.0	142.0	40	8.0	22.5
24	32	0	142.0	150.0	40	8.0	22.5
25	32	0	150.0	163.0	40	8.0	22.5
26	32	0	163.0	176.0	40	8.0	22.5

Table 4.1: Parameters of CHIMERA rings. Those shaded darker blue correspond to the forward rings whereas those shaded in light blue correspond to the ball section of the CHIMERA detector.

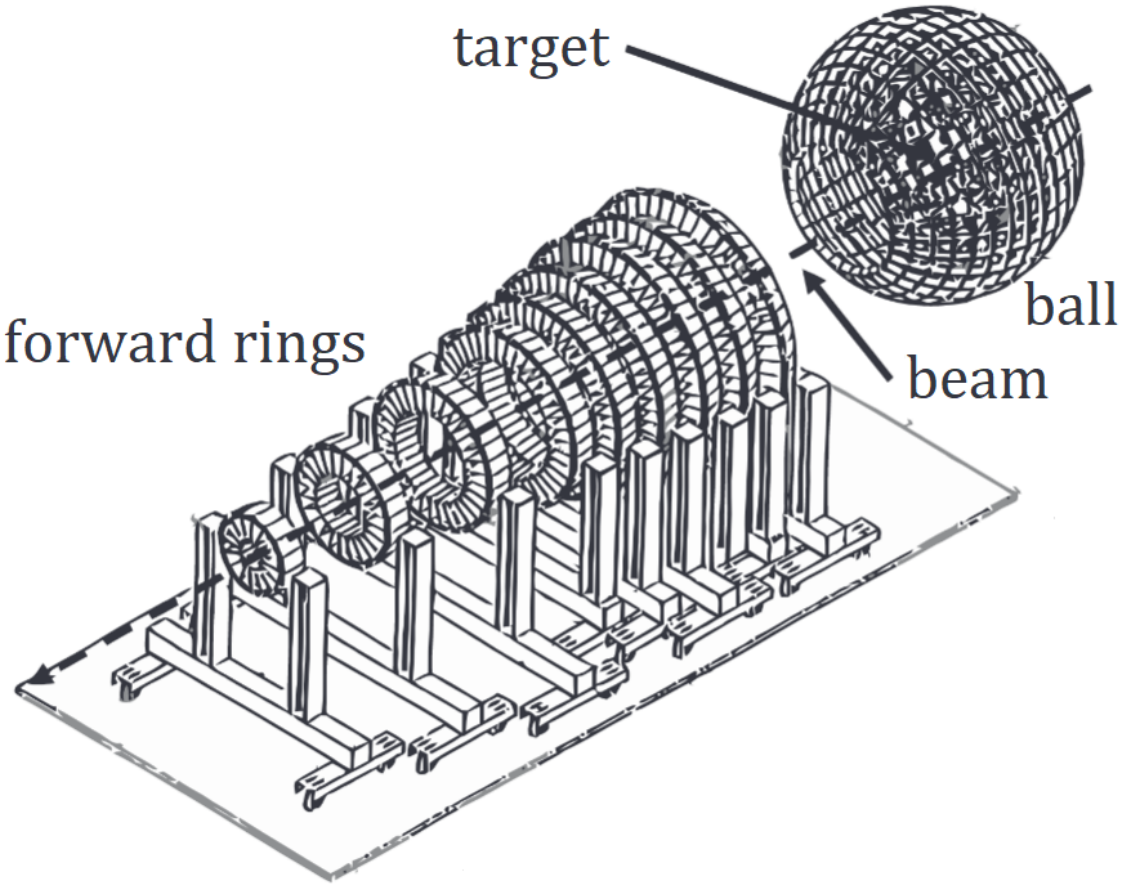

Figure 4.3: Schematic of the CHIMERA detector showing the placement of the rings. The rings at the smallest angles are furthest from the target at 350 cm and the forward rings cover up to 30° at 100 cm. Above the forward rings, the CHIMERA ball covers larger angles from 30° $\rightarrow$ 176° at a distance of 40 cm.

4.3.1 Individual telescope

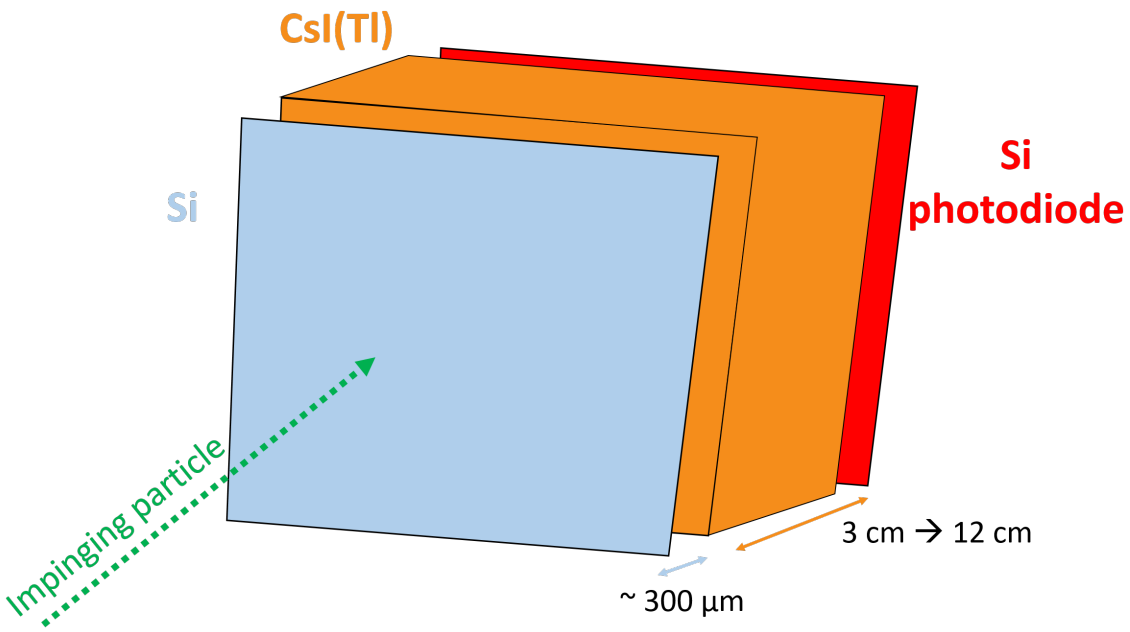

Figure 4.4: A single CHIMERA telescope showing the Si detector occluding the CsI(Tl) detector which is read out with a silicon photodiode

A single telescope (Figure 4.4) has two detection stages, the first is a 300 μm (nominal thickness) n-type planar silicon detector behind which is a CsI(Tl) scintillator. The scintillation light from the CsI(Tl) crystal is read out by photodiodes to allow for a compact detection system and passed through to a MICROTEL preamplifier which then feeds to a Silena 761F amplifier. To achieve the large-energy dynamic range, the charge output is handled along two different channels with differing ranges by the CAEN 9U QDC (Charge to Digital Converter). One of these chains has a low gain setting to allow for high energy events to avoid overflowing the QDC, the second of these chains has a high gain setting such that low energy events do not suffer from discretisation upon entering the QDC (for a range of 400 MeV a single ADC channel would therefore correspond to around 100 keV!). This point is particularly salient given the primary particles of interest in this experiment were α-particles where energy coverage down to around 2 MeV was desired. This would therefore correspond to a 5% error in energy, far in excess of that of the intrinsic resolution of the silicon stage.

In addition to the use of dual-gain channels, the CsI(Tl) signal is passed through a stretcher. The stretcher elongates the input signal by holding the output voltage at the

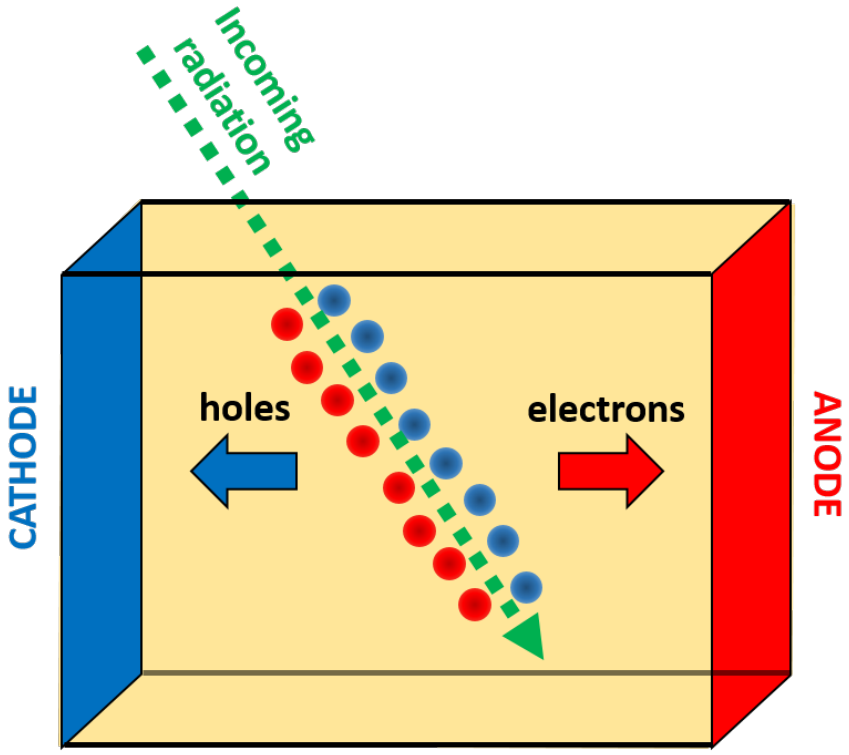

Figure 4.5: Diagram showing how incident radiation liberates electron-hole pairs which can be collected by the anode/cathode.

peak value for longer. This allows for information about the pulse-shape of the CsI(Tl) response to be inferred by the relation between the FAST-signal and the stretched SLOW-signal. This effect has been well studied for CHIMERA previously [108] and is due to the charge and mass dependence of the CsI(Tl) response. As discussed later, while this feature is useful for particle identification, it is a major disadvantage when the energy of the impinging particle is required.

4.3.2 Si detector

The first component to the telescope is a large capacitance (1nF) 25 cm^2 300μm (nominal) n-type planar silicon detector with a high silicon bulk resistivity (> 5 kΩ.cm) [109]. The silicon detector works as a semiconductor diode. By virtue of the high purity of the silicon in the detector, the electron levels are such that there are two energy bands separated by 1.1 eV. The lowest of these is called the valence band which is well occupied. The highest is the conduction band, which is unfilled except for thermal

excitations across the band gap. An interaction then takes place, whether by a gamma-ray/X-ray photoelectrically absorbing and producing a fast moving electron or a charged particle losing energy via the effects of the Coulomb interaction with the material. This energy is shared between many electrons and allows for liberation from the valence to the conduction band (see Figures 4.5 and 4.6). This also creates an unoccupied space known as a hole in the valence band. As the energy for each electron to be liberated is a constant, one can determine the energy deposited by counting the number of electron-hole pairs. The intrinsic resolution of the detector is therefore partly limited by the number of these electron-hole pairs n whose number's varying according to Poisson statistics and the standard deviation is therefore given by $\sqrt{n}$ which gives a measure of the resolution (and constant factor to take into account statistical correlations which is known as the Fano factor). In addition to the limitation by the number of electron-hole pairs, there is also a component from electronic noise which also contributes to the overall resolution of the detector.

To detect these electron-hole pairs, a (reverse) bias voltage is applied whose effect is two-fold. Firstly, the bias voltage creates an equilibrium across the silicon material creating a large intrinsic region devoid of charge carriers which can extend over the majority of the detector. This ensures that the electron-hole pairs are not reabsorbed by a majority carrier therefore a larger percentage of the electron-hole pairs are collected giving a larger signal and improved resolution. Secondly, the bias voltage means that the electrons and holes are drifted to the anode and cathode respectively where their charge can be detected. The current pulse this generates is then passed to a pre-amplifier which has a two-fold function. Firstly, to generate a shaped signal which is sizeable enough to be sent down the electronics chain and modify the output from a charge pulse to a voltage based signal. Secondly, the pre-amplifier also matches the impedance which increases the signal transition along the electronics chain.

The thickness of each detector has been measured previously by the CHIMERA experimental group (with each detector having a value which can deviate drastically from 240 $\rightarrow$ 310 μm) and is known to $\sim \pm 5\mu$m. The measured value was always used rather than the nominal 300 μm thickness for the analysis. The signal from the Si stage was passed into the QDC via a preamplifier-amplifier chain which dealt both with high gain and low gain events as demonstrated in Figure 4.7. The off-line resolution of the detector, as determined by the triple-alpha source (an example is shown later in Figure 4.19), was 2.3% at 5.5 MeV whereas the on-line resolution as calculated from the gold scattering data was 0.2 % at 160 MeV. An issue with these detectors, caused

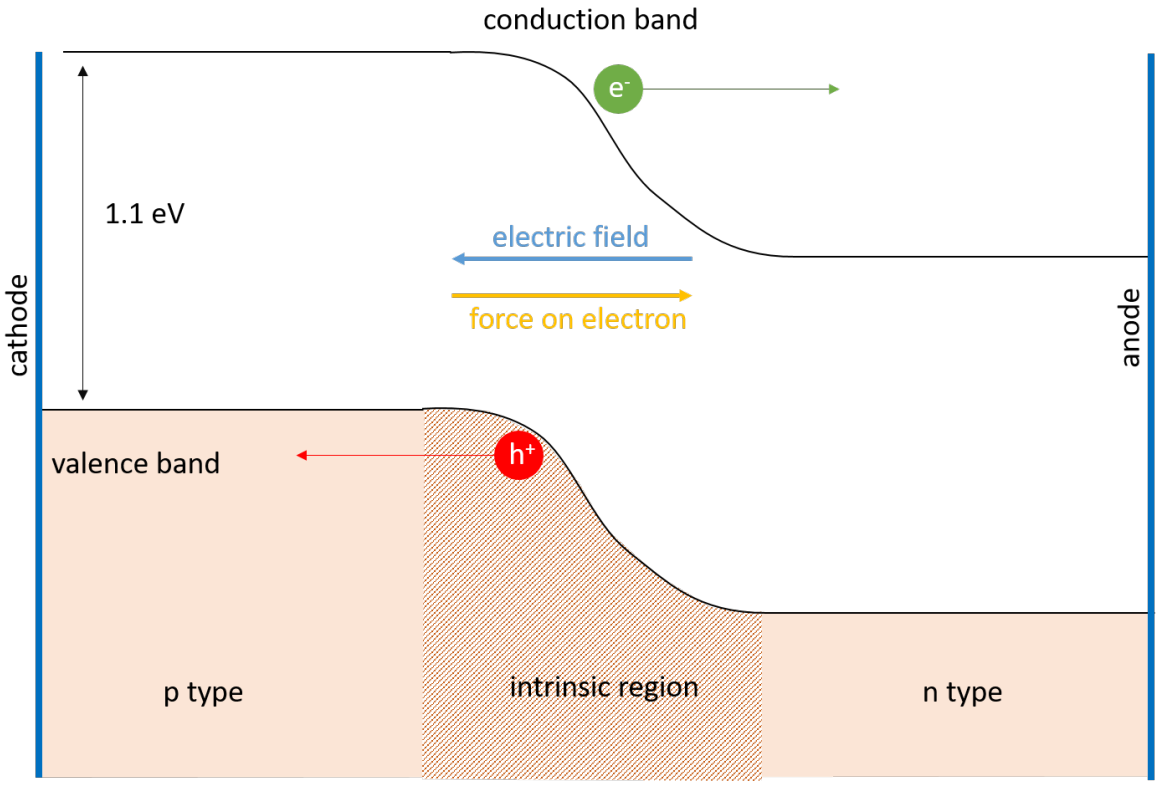

Figure 4.6: Schematic representation of a silicon diode while biased. The electric field across the intrinsic region means any electron-hole pairs which are created here are drifted and can be collected at the anode and cathode.

by the large dynamic range required for the type of experiment, is the effect of the pedestal for low energy events. The pedestal is a direct current offset [110] on top of which the signals sit as demonstrated in Figure 4.8a. This offset can be so severe that it pushes the noise above the threshold for a particular channel therefore requiring special care to remove these spurious trigger events.

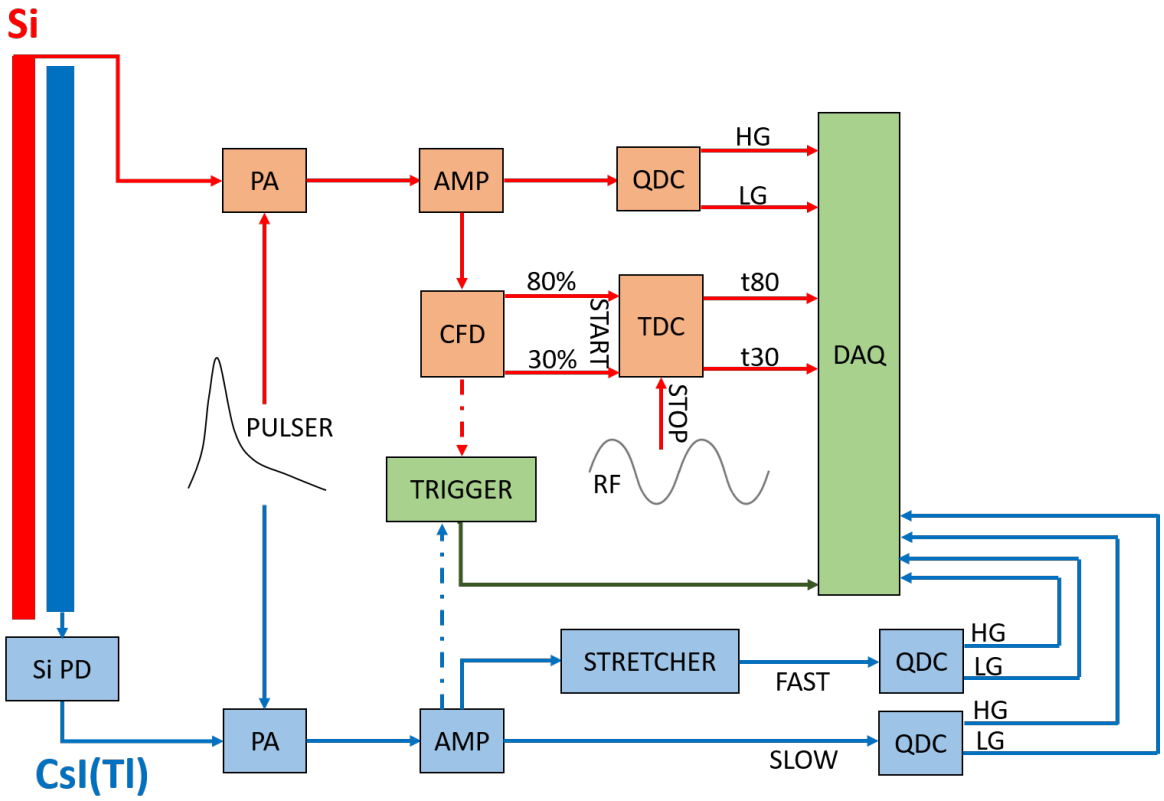

Figure 4.7: Electronics chain for a single CHIMERA telescope. Figure adapted from [111].

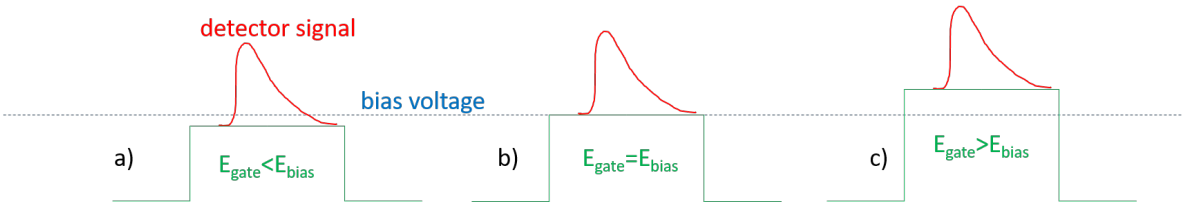

(a) Diagrammatic explanation of the pedestal. To correctly set the gate, one must ensure that the gate voltage is set equal to the bias voltage. If the gate voltage is set to less than the bias voltage as seen in a) then the amplitude of the detector pulse is reduced and low energy real events are lost. In b) the gate and bias voltage are equal and any real events sit above the threshold. The situation seen in c) is avoided, where the gate voltage exceeds the bias voltage and noise sits on the pedestal introducing a noise source into the system.

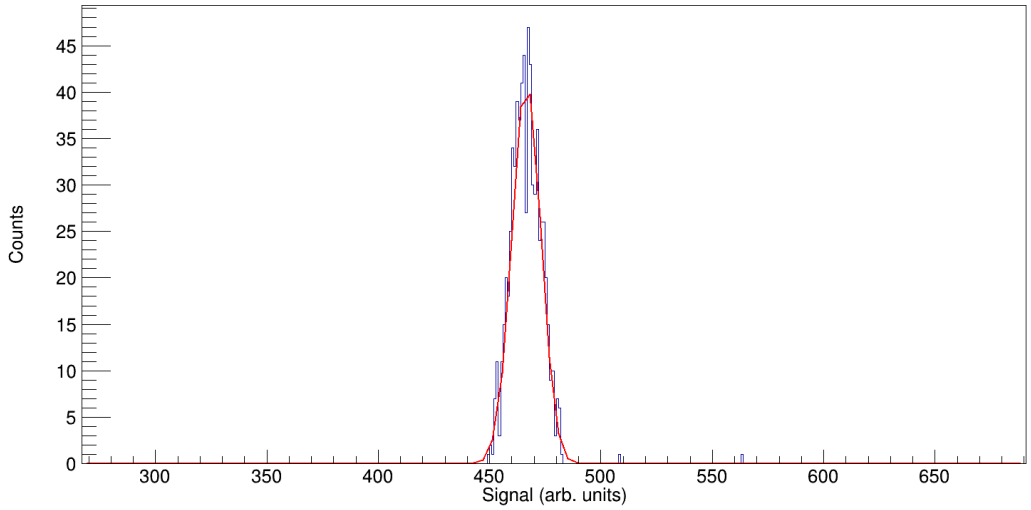

(b) An example from the 5 Hz pedestal trigger (with no physical signal) showing the Gaussian distribution caused by the gate voltage being set too high. The Gaussian fit is also shown in red which is used to set the lower threshold.

Figure 4.8: Pedestal effects caused by an incorrect setting of the gate voltage.

To deal with this effect, a 5 Hz trigger operated in addition to the main trigger which took all the QDC values (even if they are below the discriminator threshold) and had a flag to separate these events in the data file. Only these events were chosen to examine the effect of the pedestal on raising the noise. The program *NEWPED* [112] was used which automatically looped over each telescope and fitted a Gaussian to the pedestal data signal, an example of which can be seen in Figure 4.8b. An output was then generated with Gaussian fit parameters and a threshold which was then read in for further analysis. The threshold was chosen to be the centroid plus 2.5 times the width of the Gaussian. This automated process was not infallible and any detectors which had a

significant pedestal contribution after this threshold were then manually modified until a reasonable noise level was reached (no channel was a factor of 2 above the top 5-10% noisiest channels which was performed by eye). The effect of this pedestal DC offset was reasonably large which also meant a large number of detectors were left with a very high threshold. This meant the small silicon signal left in the detectors at high incident α-particle energies was unregistered and therefore contributed to an overall decrease in the detector coverage. The majority of the detected particles however sit in the energy region where the signal in the silicon stage is sufficiently above threshold so the sensitivity across the detector is reasonably uniform.

The OR signal from the silicon stage CFD (Constant Fraction Discriminators) was taken into the trigger unit which allowed for a global multiplicity to be set. Additionally, rings of detectors could be omitted from the trigger easily, a technique which was employed to remove the low angle CHIMERA rings from the trigger which were prone to high noise levels during the experiment and were therefore excluded. The trigger was operated with a multiplicity 3 condition with a scale-down of 200 used for multiplicity 1 events. For calibration runs, the overall multiplicity was set to 1. Due to the large number of channels where the pedestal is large enough to cause significant amounts of noise, the trigger operation was effectively limited to singles mode.

4.3.3 CsI stage

The second part of the telescope is a CsI crystal which functions as a scintillation detector. The presence of a dopant modifies the energy levels in the crystals band gap such that activator states can now exist within this region. For the CsI crystals used in CHIMERA, this activator constitutes a 0.1% thallium dopant. The physical mechanism for radiation detection is the liberation of electrons from the valence band (100% occupied) to a state in the conduction band ($\sim$ 0% occupied) which generates electron-hole pairs that travels through the crystal lattice which can be seen in Figure 4.9. These electron-hole pairs (excitons) must then interact with a dopant/impurity site before it is reabsorbed. The interaction of this exciton with the dopant/impurity then causes a rapid de-excitation via scintillation light. This has the effect of not only reducing the band gap energy and therefore improving the resolution by virtue of releasing more photons, but it also makes the material transparent to its own scintillation light (as the scintillation light is characteristic of the dopant/impurity - $\sim$ 565 nm for CsI(Tl) in comparison to an intrinsic scintillation wavelength of $\sim$ 305 nm). This is in addi-

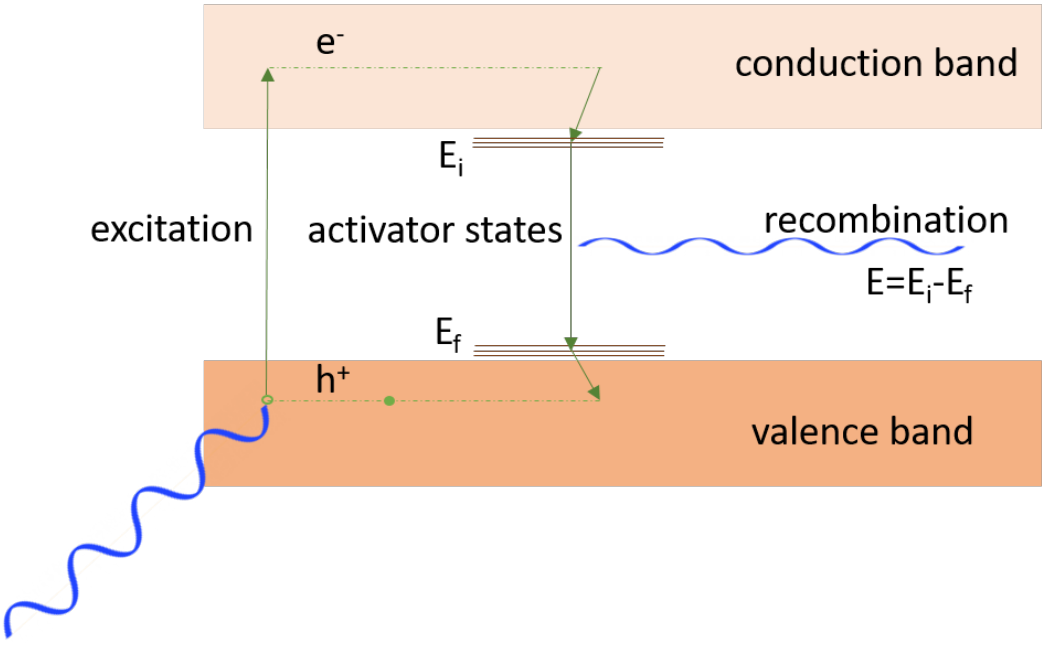

Figure 4.9: Electron energy levels in a doped inorganic scintillation crystal. The incoming radiation liberates an electron from the valence to the conduction band. This electron-hole excitation can then proceed via an interaction with an activator whereby the electron cascades through the activator energy levels emitting a photon with an wavelength determined by the energy difference of the activator states.

tion to the effect of the Stokes shift between emission and absorption which shifts the frequency of light due to the effect of momentum conservation. This light then passes through the material and can be detected, normally by a photomultiplier tube (PMT). In this detector array however, the scintillation light is read out by a Hamamatsu silicon photodiode which allows for a more compact telescope unit. The replacement of a photodiode has several advantages [113], primarily that a higher quantum efficiency can give a better energy resolution by virtue of the increased number of detected photons. This is due to the fact that the scintillation light emitted from a CsI(Tl) crystal has a poor transmission coefficient through the window of a PMT.

The CsI(Tl) crystals used had depths varying from 3 cm for the large scattering angles (covering the ball) to 12 cm at small scattering angles where the larger incident energy requires a thicker detector to avoid punch through of the CsI(Tl) (for the maximum beam energy used the punchthrough effect isn't a primary concern as the proton energy required to punch through 12 cm of CsI is $\sim$ 220 MeV). A particular feature of a CsI(Tl) crystal is the scintillation light given off via the de-excitation of

the exciton on the activator has two different time components, a fast and slow component with decay times of 0.68 and 3.34 μs respectively [114]. As with the Si signal, the CsI(Tl) signal has a high gain and a low gain channel giving a large dynamic range. In addition to this, the CsI(Tl) signals are split and one path passes through a stretcher which elongates the signal. This is the FAST signal which gives information on the fast component of the pulse shape. When this FAST signal is passed through the further electronics chain, only the first part of the pulse is processed. The non-stretched signal is the SLOW signal which gives information about the slow component of the pulse shape. The reason for this stretching is that by separately processing the SLOW and FAST signals, one can get a preliminary particle identification purely from the CsI(Tl) signal which is useful where the particle is light and the energy is high enough that the energy deposited in the Si stage is below threshold (i.e. protons with E $>$ 40 MeV and alpha-particles with E $>$ 100 MeV). The reason for this ability to differentiate by measuring the contributions from the fast and slow decay components in the crystal is that different particles have different energy deposition dependencies. The Bethe-Bloch equation shows the energy-loss per unit distance is proportional to mZ^2 therefore more massive (and more charged) particles lose their energy more rapidly thereby creating more ionisations per unit volume. Along the incident particle path, one is left with a number of lattice damage sites which act to quench the excitons in favour of the energy needed to dislocate these atoms from their lattice sites.

By plotting the FAST and SLOW signals against one another, one can see the differently charged nuclei occupy different loci as seen in Figure 4.10. Here, one can also see a contribution from gamma-rays which may prove useful in further studies involving particle-gamma coincidences, a current area of research at the CHIMERA detector [115]. While the silicon detector stage has a good linearity with energy and a very weak dependence on the incident particle, the CsI(Tl) (by virtue of it being a scintillator) has a strong signal dependence on the incident particle species and also displays energy alinearity. This makes the use of the CsI(Tl) to take an absolute energy very difficult unless one has performed a very good systematic calibration with a variety of beam energies and species. The behaviour has been well studied and the energy (E) of the incident particle of mass A and charge Z is described by Birks [116] semi-empirically in comparison to the light output (L) as:

$$E(L, Z, A) = aAZ^2L + b(1 + cAZ^2)L^{1-d\sqrt{AZ^2}} \tag{4.1}$$

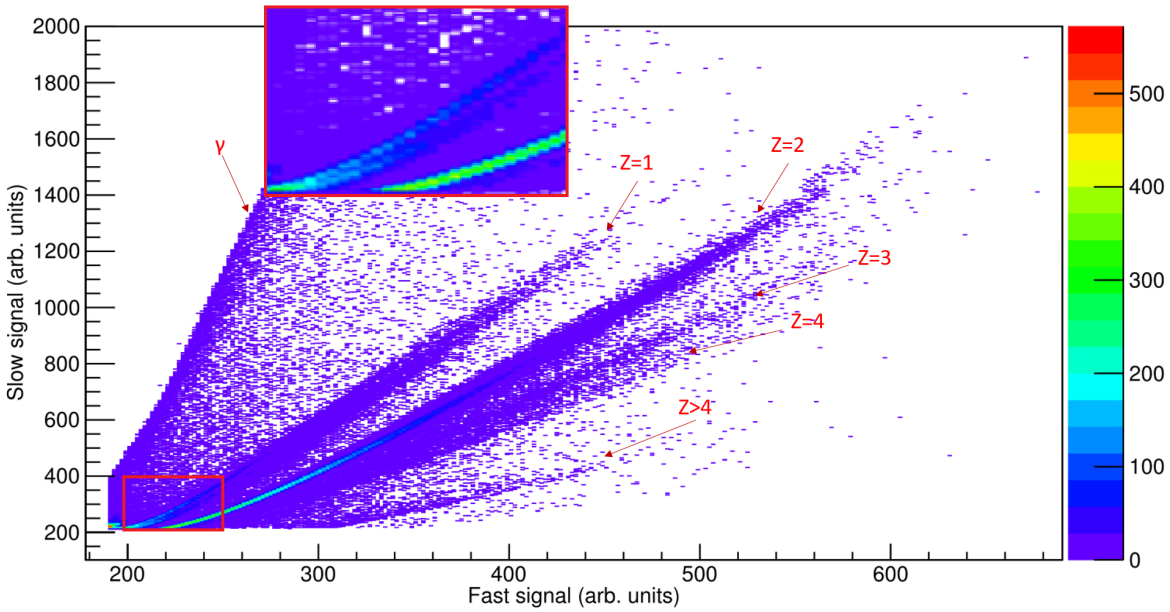

Figure 4.10: FAST signal against the SLOW signal for a single telescope in CHIMERA showing how different incident nuclei occupy different loci depending on their charge number. An additional splitting for Z=1 can also be seen at low signal amplitudes corresponding to a different mass number (inset in red).

with a, b, c and d being positive fit parameters depending on the properties of the crystal. Unfortunately, due to the lack of calibration data for different energies and beam species, the value of these parameters as required for determination of the energy from the light response was not possible.

4.3.4 Timing

Calibration

In order to provide more information on low energy events, where the energy of the particle is insufficient to penetrate the silicon stage of the telescope, a timing signal is taken from the silicon detectors in reference to the radio-frequency signal from the cyclotron. As demonstrated in Figure 4.7, the timing signal from the silicon chain CFD is taken as the stop signal. There are two parallel channels used with different CFD settings corresponding to a fraction of 30% and 80%. These timing signals have a typical time resolution of around 1 ns, however the overall accuracy of the timing signal was limited by the omission of a chopper being incorporated into the setup. The particle

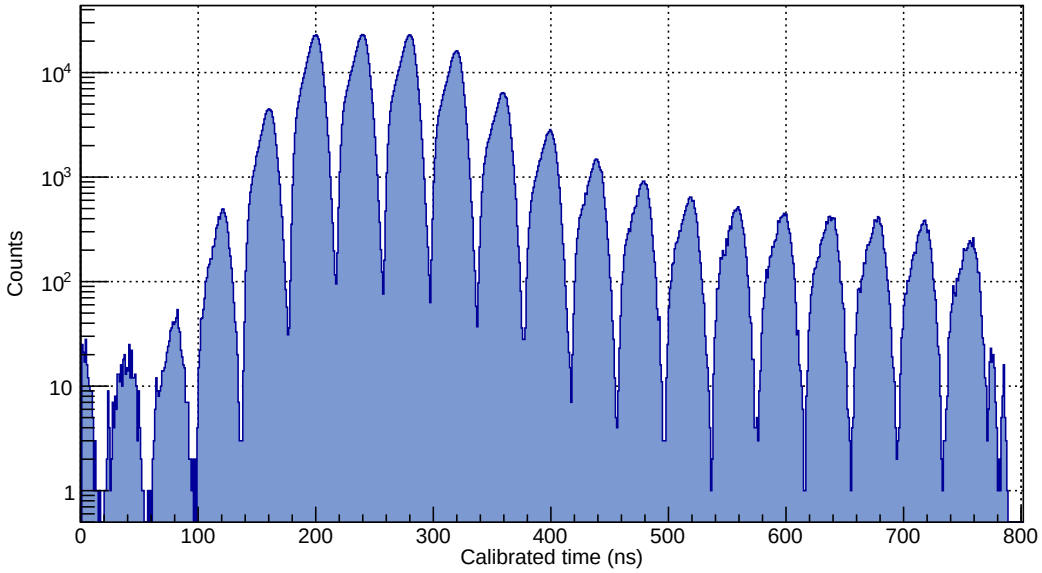

Figure 4.11: Aligned and calibrated time signal for CHIMERA ring 6E showing multiple pulses for $E_b = 400$ MeV.

identification from the timing signals was performed as follows:
Firstly, the timing signals from the data were taken and aligned with those in the same detector ring. The aligned signals for an example ring (6E) can be seen in Figure 4.11. Then, the elastic scattering data from the gold targets was used to calibrate the timing signals as these events had a well defined energy and mass. To do this, firstly the channels between subsequent peaks was used to determine the time gain against the cyclotron time period. The offset was determined by calculating the expected time-of-flight for a ^{16}O nucleus with the beam energy used.

Timing Particle Identification

Now one had a fully calibrated time signal detailing the time of flight (t) for a particle from the target to detection in a telescope at distance (d), one could then use this along with the energy information (E) to determine the mass of the particle (m). This is called TOF PID (Time of Flight Particle Identification)

$$t = \frac{d}{v} = d\sqrt{m/2E} \rightarrow m = \frac{2t^2E}{d^2} \tag{4.2}$$

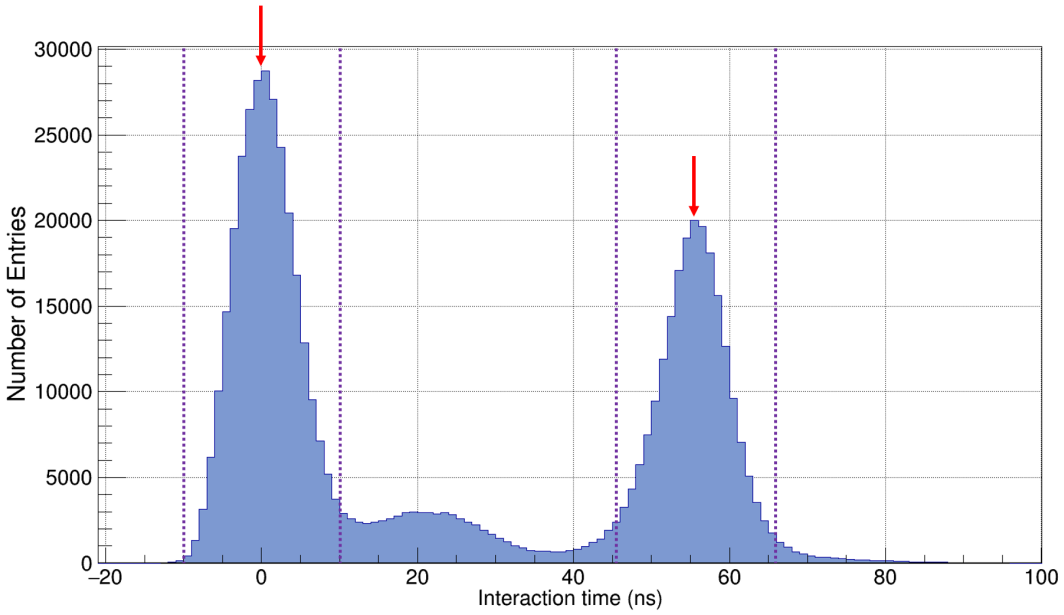

Figure 4.12: TOF PID for a complete ring (9I) showing the primary and secondary peaks marked with a red arrow corresponding to correct identification of α-particles. The secondary peak corresponds to where a low energy particle takes sufficiently long to hit the detector and is incorrectly attributed to the next beam pulse. This can easily be rectified by the second gate in conjunction with the primary gate. The combined peaks have a time uncertainty value of $\sigma_t = 4.8$ ns. Events inside the purple dotted lines within ± 10 ns of the centroid are selected as α-particles. The peak around 20 ns corresponds to a combination of mass 12 and 16 nuclei which are excluded from the current α-particle gate.

For very low energy particles where the time of flight is comparable to cyclotron beam temporal separation (where a pulse of particles appears every ~ 50 ns) there becomes an uncertainty about which bunch the particle belongs to meaning there exists an ambiguity about what the mass of the particle is. To reduce this effect, the interaction time in the target was calculated by first assuming that the silicon hit was an α-particle with mass 4. The time taken for a particle of mass m and energy E was then calculated and the interaction time was given as the difference between this time and the measured TOF. Appropriate gates were placed around the primary peak and the secondary peak where the particle was from the previous bunch as seen in Figure 4.12. Using this method allowed for particle identification for α-particles from ~ 4 MeV (average silicon energy threshold) to 24 MeV (minimum energy needed to punchthrough to the CsI(Tl) detector). As one goes to lower energy measured particles, the cleanliness of the PID

becomes less pure. This is due to the effect of previous interactions where a particle can have sufficiently low energy to take multiple cyclotron time periods to impact the detector. This therefore causes confusion about which cycle the interaction occurred in, effectively modifying the time of flight t to $t + t_{cycl}$ where t_{cycl} is the cyclotron time period. This is demonstrated in Figure 4.13, where 7 cycles are included and the energy and time signal are shown for different mass nuclei. As one tends towards lower energies, it can be seen that protons from many different interactions can very easily be incorrectly attributed to the interaction of interest. Any time two of these loci cross, there is a potential ambiguity (additionally one also has contributions from other mass stable nuclei e.g. Li, Be, B, N etc.) which aren't shown in the figure.

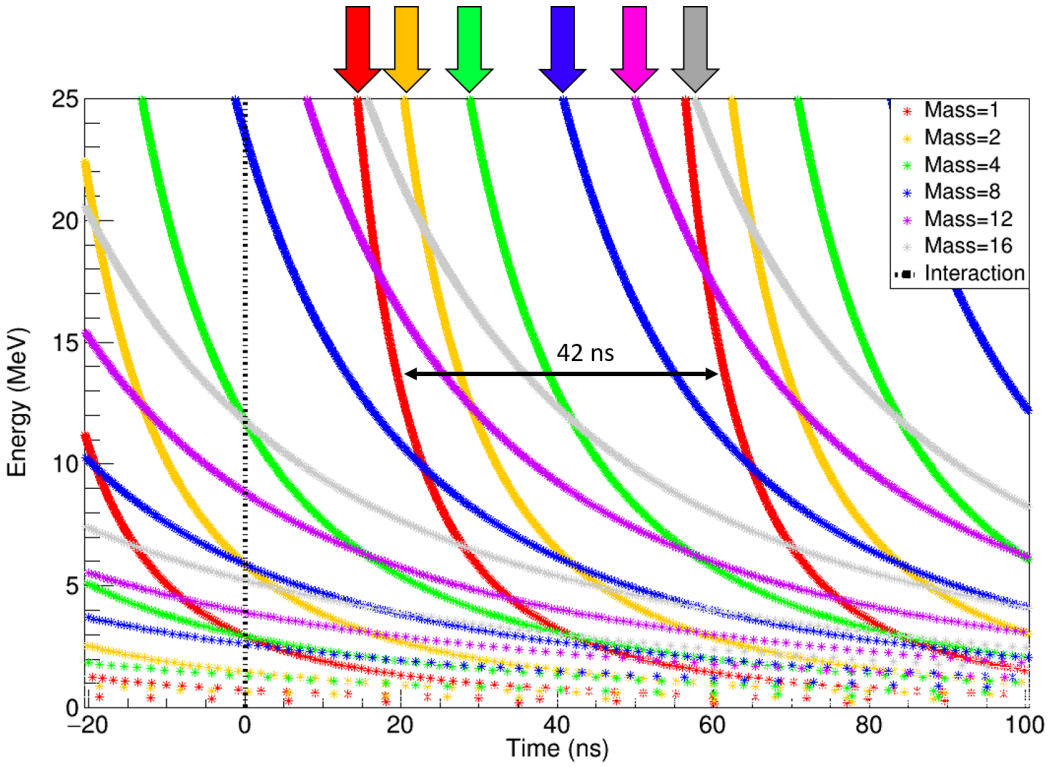

Figure 4.13: Calculation of 7 interaction cycles for different mass nuclei showing how low energy events can become contaminated by protons from previous events. The time between cyclotron pulses is 42 ns and the distance to the detector is 100 cm. The loci corresponding to the event at t=0 (marked by a dotted line) are shown by arrows.

This process can be repeated for m=6,7,9... etc. and when the correct mass is inserted, the interaction time will fall within the gates corresponding to a TOF identification. Additionally, one can use the information about the energy to remove certain

ambiguities. If, for example, a particle was measured at 45 MeV but was classified as an α-particle by TOF, this eventuality can be removed as this would be sufficientto be detected in the CsI(Tl) detector. Instead, heavier mass particles were tested where the energy is insufficient to be detected in the CsI(Tl).

4.3.5 dE-E particle identification

As previously mentioned, the CsI(Tl) has a charge and mass dependent light response meaning that in order to provide particle identification via dE-E, the experimental data require fitting of a form known to reproduce the seen relation. This has been previously studied by the CHIMERA group [108] which demonstrates the relationship between the signal from the CsI(Tl), E, and the signal in the silicon stage, ΔE. This relationship can be described as follows:

$$\Delta E = ((gE)^{\mu+\nu+1} + (\lambda Z^{\alpha} A^{\beta})^{\mu+\nu+1} + \xi Z^2 A^{\mu} (gE)^{\nu})^{1/(\nu+\mu+1)} - gE \tag{4.3}$$

with the parameters g, μ, ν, α, β, λ and ξ being free parameters (albeit with a large degree of correlation). These parameters were extracted using the program *DEEFIT* [117] where for each telescope, the user must draw along the loci for different species and mark their charge and mass. A screenshot of this process can be seen in Figure 4.14.

Once all the known/seen species are marked, a fitting for the free parameters was performed for the current experimental data. To initialise the fit, a Monte Carlo sampling of the search space is first generated as the fit has many local minima. These fit parameters are then stored for each telescope and later used in the particle identification to provide the charge and mass values which best fit the measured values in the Si and CsI(Tl) stages. These values are non-integer allowing for a characterisation of how good the particle identification process is by being able to see the mass separation at a given charge number. An example is shown in Figure 4.15 which shows the mass separation of the lithium isotopes with only a small overlap region where the mass becomes ambiguous. Also seen in Figure 4.16 which shows the separation of the helium isotopes demonstrating that the ^{3}He and ^{4}He can be separated with around 99.4% purity from fitting two Gaussians to the peaks. One can then also take into account the relative abundances between the two and the overall ^{4}He purity is much higher than this ($\sim$ 99.99 %).

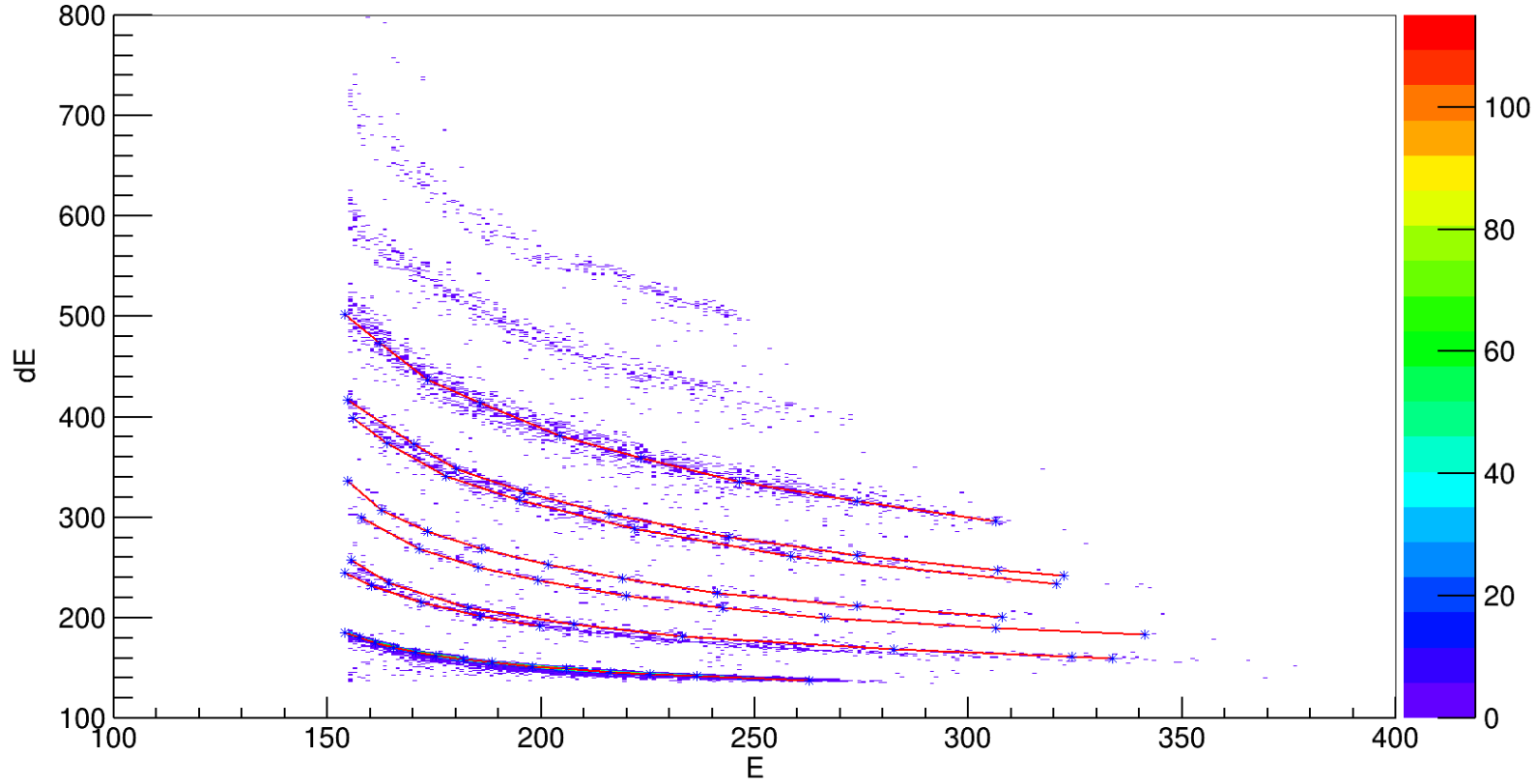

Figure 4.14: *DEEFIT* fitting program. The red loci drawn are user inputs drawn along the different isotope lines along with an assignment of their charge and mass. The program then describes the general form in terms of 9 parameters allowing for an extrapolation to higher charge and masses where statistics may be limited.

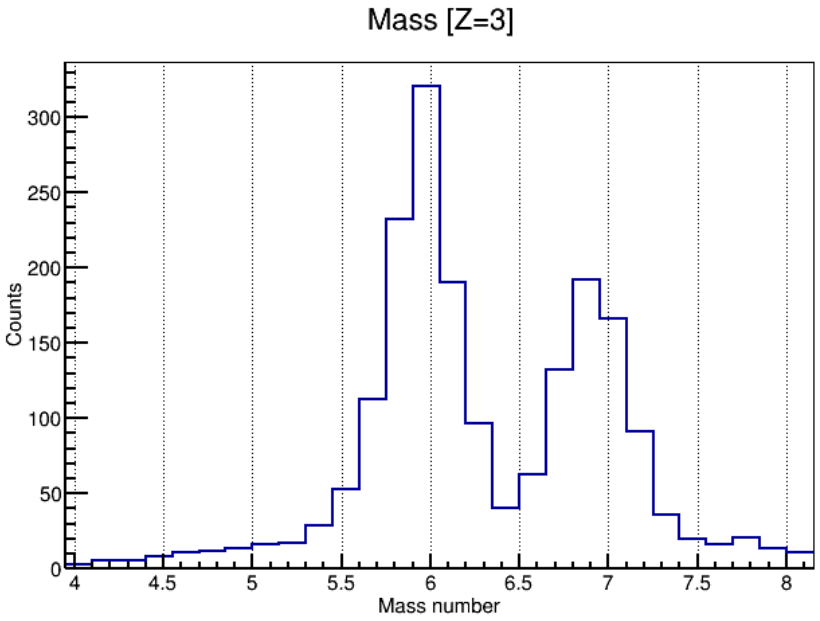

Figure 4.15: Mass separation of Z=3 lithium isotopes. The ^{6}Li and ^{7}Li can be well differentiated despite their comparative abundances.

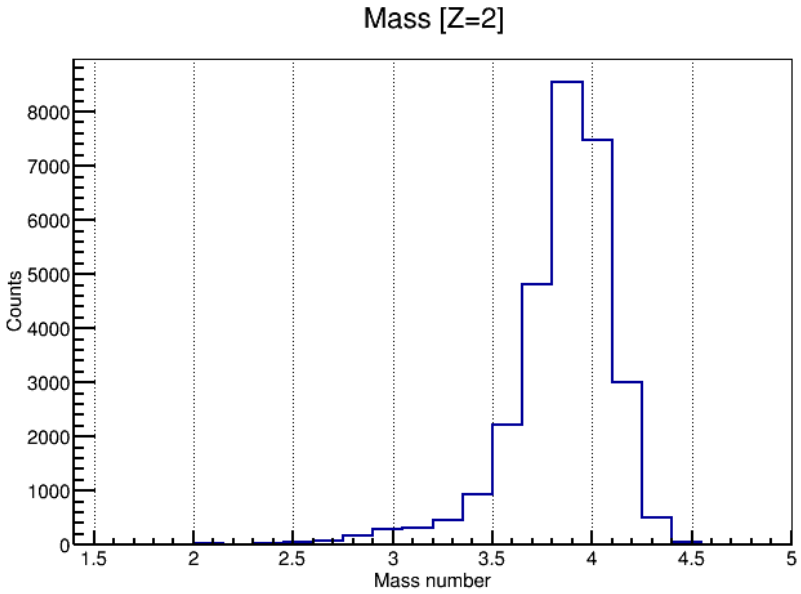

Figure 4.16: Mass separation of Z=2 helium isotopes showing the dominance of the ^{4}He. The measured width of $\sigma = 0.17$ shows the good separability between A=3 and A=4.

Nucleus	$E_{punchthrough}$ (MeV)
^{4}He	24.5
^{6}Li	46.3
^{7}Li	49.3
^{7}Be	68.3
^{9}Be	75.5
^{12}C	134.2

Table 4.2: Minimum energy for different nuclei to pass through the 300 μm silicon stage of CHIMERA.

The possibility of using these parameters for the dE-E particle identification to simultaneously calibrate both the Si and CsI(Tl) stage of the telescopes was also investigated as this information should be encoded. An examination of the best fit parameters however demonstrates than while these values describe the data well, they are not unique and the values vary drastically between detectors both in terms of magnitude and sign. This is by virtue of many local minima which, despite describing the system well demonstrate a certain degree of degeneracy of solutions. For traditional CHIMERA experiments which are performed with a higher mass system, one has more loci to fit therefore this fitting routine has not been well tested using a smaller sample of nuclei.

Table 4.2 shows the minimum energy required for various nuclei to be detected after passing through nominal 300 μm of silicon. The true value one can use is slightly higher than that listed, as the CsI(Tl) has a non-zero threshold and any remaining energy deposited here must exceed the limit set to eliminate pedestal effects.

The possibility of multiple hits on a single detector was also investigated (from a single event). For the purposes of this experiment, a particular interaction of interest is where one has a highly coherent emission of α-particles. As such, these α-particles may interact in the same detector via the decay of ^{8}Be(g.s) and ^{12}C(0_2^+) where the α-particles all have an extremely similar energy. Figure 4.17 shows how these multiple interactions look in the telescope dE-E PID plots. A double hit from ^{8}Be is extremely hard to distinguish from ^{7}Li whereas a triple hit from a decay of ^{12}C(0_2^+) is easily distinguishable as it occupies the loci normally populated by the direct measurement of ^{8}Be however due to its incredibly short lifetime, it cannot be detected directly in the detector without first decaying.

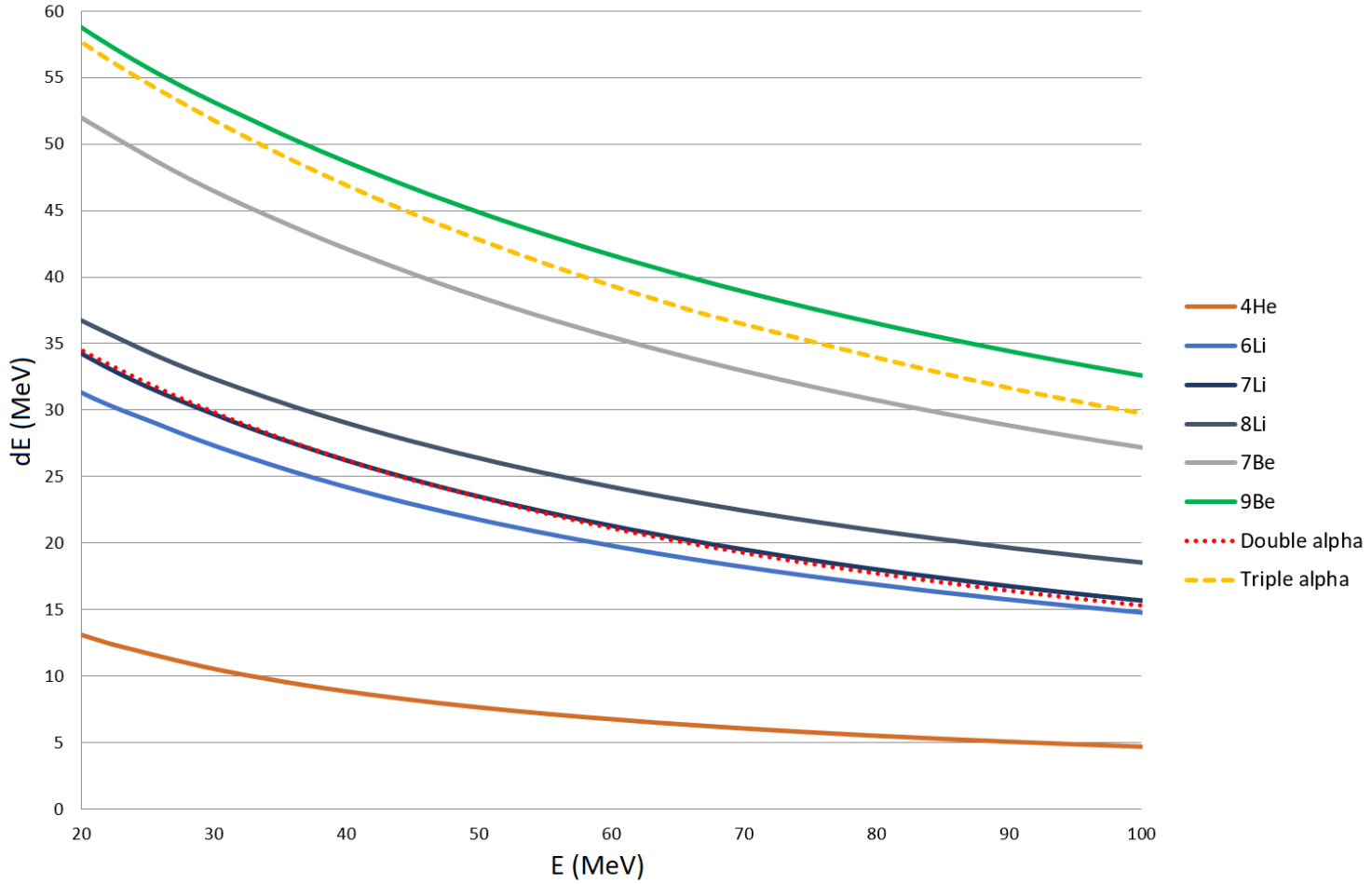

Figure 4.17: Schematic of the different loci for the CHIMERA dE-E PID plot for various light nuclei. The multiple hits from ^{8}Be and ^{12}C(0_2^+) decays corresponding to double and triple hits can also be seen.

4.3.6 Gain matching

In order to relate the high gain and low gain channels, the pulser data were used which provided a series of pulses of increasing voltage. These pulser signals are passed into the pre-amplifier and allow a conversion between the output signal voltage and the detector channel. By observing these pulses on both the high and low gain channels, the conversion factor between the two could be achieved. The program *Pillbug* [118] allowed for this gain matching by loading the spectra telescope by telescope. One can then fit the series of peaks and allocate each to a specific applied voltage, these being: 5, 10, 15, 20, 40, 60, 80, 100, 200, 400, 600, 800, 1000, 1500, 2000, 3000, 4000, 5000 mV. The pulses corresponding to 100 and 1000 mV occur twice as frequently to help identify these voltages. An example of this can be seen in Figure 4.18. These two channels had a nominal gain difference of 8.2 which was rarely exceeded by a factor of $> 10\%$.

In addition, this gain matching with pulser data also provided a vital calibration point as one could extrapolate this channel-voltage fit to 0 mV which also corresponds to an energy of 0 MeV. In tandem with either the triple-alpha data or one of the gold scattering energies, this provided the required minimum two calibration points for a detector as discussed below in Section 4.3.7.

4.3.7 Energy calibration

As previously mentioned, CHIMERA allows for a large dynamic-energy range in both detectors of the telescope, however the CsI(Tl) sees a different response to various incident nuclei. As such, this makes the use of this signal unhelpful for extraction of the total energy of the incident particle. Therefore, the CsI(Tl) was solely used for particle identification, once this particle's charge and mass had been identified then the total energy was extracted by the energy deposited in the silicon part of the detector.

In order to extract this energy, one first needed to calibrate the silicon detector. As discussed above, the pulser data extrapolated to 0 mV provided a calibration point for 0 MeV. The second calibration was then achieved either using a triple-alpha source ($\sim$ 12 hours of data) or from the elastically scattered beam on a gold target ($\sim$ 1 hour per beam energy).

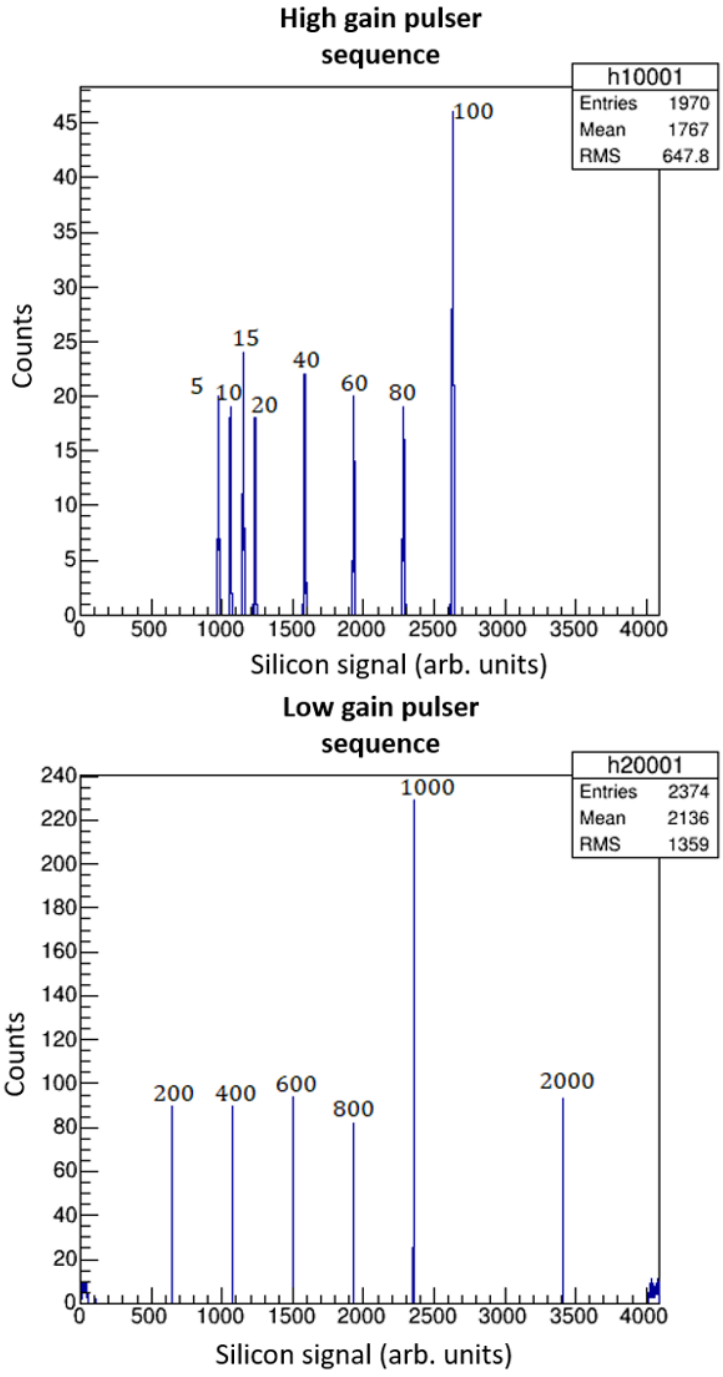

Figure 4.18: Example of pulser sequence for high gain and low gain matching. The individual pulses are labelled according to their voltage (in mV). As seen, the 100 and 1000 mV signals appear twice as often so they can be differentiated from the other pulses.

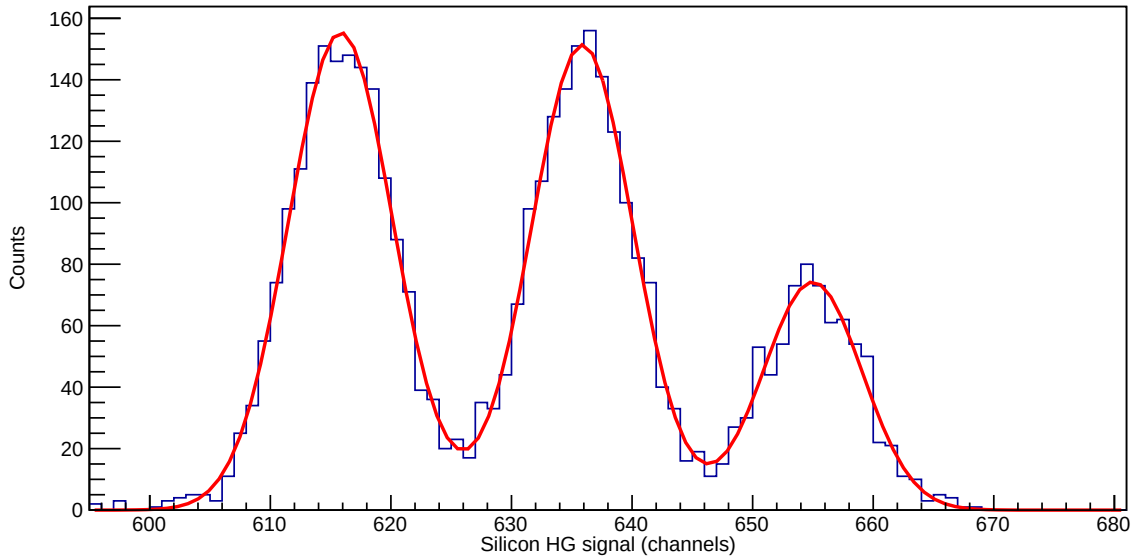

Figure 4.19: Example of a triple-alpha source spectrum from detector 530 - ring 8I. The resolution for this detector is ∼160 keV.

Triple-alpha source

The triple-alpha source contains a source with a mix of isotopes: ^{239}Pu, ^{241}Am and ^{244}Cm which have characteristic energies with the most prominent peaks having values of 5.155, 5.486 and 5.805 MeV. The triple-alpha source was placed at the target position and as such, provided good calibration data to those telescopes near to the detector (i.e. the ball). An example of the spectrum obtained can be seen in Figure 4.19. The nearest detectors were 40 cm away, whereas the lowest ring used (4E) was 210 cm away which yielded a $\sim$ 35 times decrease in the statistics due to the difference in solid angles. Therefore, the low angle detectors had very poor triple-alpha calibration data and these data were not used below 18 degrees.

Elastic scattering

Data from the elastic scattering of the beam were taken for all three beam energies (160, 280 and 400 MeV) using a 174 μg/cm^2 gold target. For the 160 MeV data, the scattered beam had insufficient energy to punch through the silicon and therefore all the energy was deposited in the first detector therefore providing the highest energy calibration point. The 280 MeV and 400 MeV beam energies had sufficient energy to

punch through the silicon detector and left 116 and 82 MeV respectively (for a nominal 300μm silicon thickness). Due to the sharp drop off with angle of the elastic scattering cross section, the data only covered up to 30, 19 and 12.25 degrees for the 160, 280 and 400 MeV beam energies respectively.

For each telescope, the energy of the elastically scattered beam is calculated for the central angle of the detector and then the energy loss determined for the measured thickness using a *Python* code taking energy-loss values from *LISE++* [119]. Given the energies in the silicon stage range from 2 $\rightarrow$ 24 MeV, these elastic scattering events provided a calibration point which may be prone to large extrapolation errors. Additionally, these calibrations also depend on the energy loss code used and any systematic errors in the measurement of the thickness of the detector as well as errors incurred from the gain-matching described in Chapter 4.3.6. This calibration point is therefore given a larger error of $\pm$ 1 MeV when used in tandem with the triple-alpha source calibration and the pulser zero-energy calibration point. These data were then fed into a least-square fit program which extracted the linear fit parameters giving the best calibration; an example fit can be seen in Figure 4.20.

Additional calibration points

A large number of detectors were left with either insufficient calibration points or the poor quality of the fit generated required additional information to produce a good calibration. This is a combination of the poor coverage at low angles for the triple-alpha source and the poor coverage at large angles for the elastic scattering data. In future, more beam time is required to allocated to calibration to improve the overall detector coverage and therefore efficiency. As the time calibration had been well established, the timing signal allowed their expected energy to be extracted (assuming they are α-particles). An example for a single telescope (238) can be seen in Figure 4.21.

This is a useful technique as there are many telescopes which have good timing data, one can perform a calibration by assuming the detection of an α-particle with $E_\alpha < 24$ MeV and calculating the energy from the TOF. The limitation of this method is given by the time resolution which is 3.4 ns as measured from the gold elastic scattering. The uncertainty in energy is then given by:

$$\sigma E = \frac{dE}{dT}\sigma T = \frac{md^2}{T^3}\sigma T = \frac{2\sqrt{2}E^{\frac{3}{2}}}{\sqrt{m}d}\sigma T \rightarrow \sigma E = \frac{2\sqrt{2}E^{\frac{3}{2}}}{\sqrt{m}d}\sigma T \tag{4.4}$$

For a 1 MeV α-particle this corresponds to an uncertainty of 27 keV but this rapidly rises to 880 keV for a 10 MeV α-particle. This technique must therefore be restricted to low energy particles otherwise this uncertainty becomes unmanageable. For calibration purposes however, only the centroid of this distribution is important rather than the width. Fitting the energy as calculated from the time against the silicon signal allows for a calibration from the timing signal. To verify this, the reconstructed ^{8}Be peak between two detectors (discussed later in Chapter 5.5.2) was used to verify the ground-state energy of 92 keV as well as a width consistent with other well-calibrated telescopes was achieved. The consistency between the offset attained using this method and that given from the pulser were also compared. This constitutes a laborious and less precise calibration method, however it was mandatory due to the insufficient calibration data obtained during the experiment.

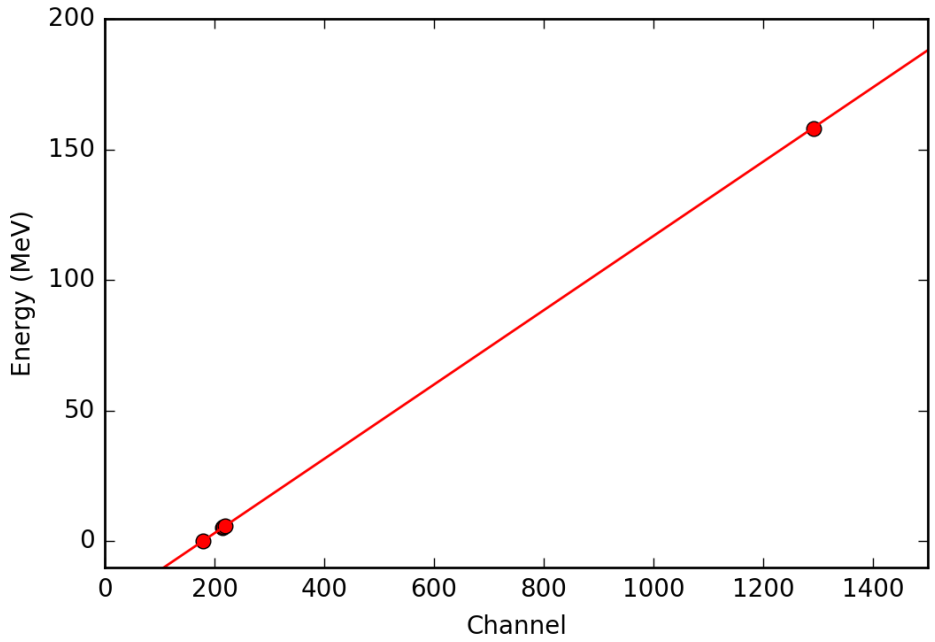

Figure 4.20: Least-squared fit result for a detector showing good linearity between the pulser, triple-alpha and gold scattering calibration points.

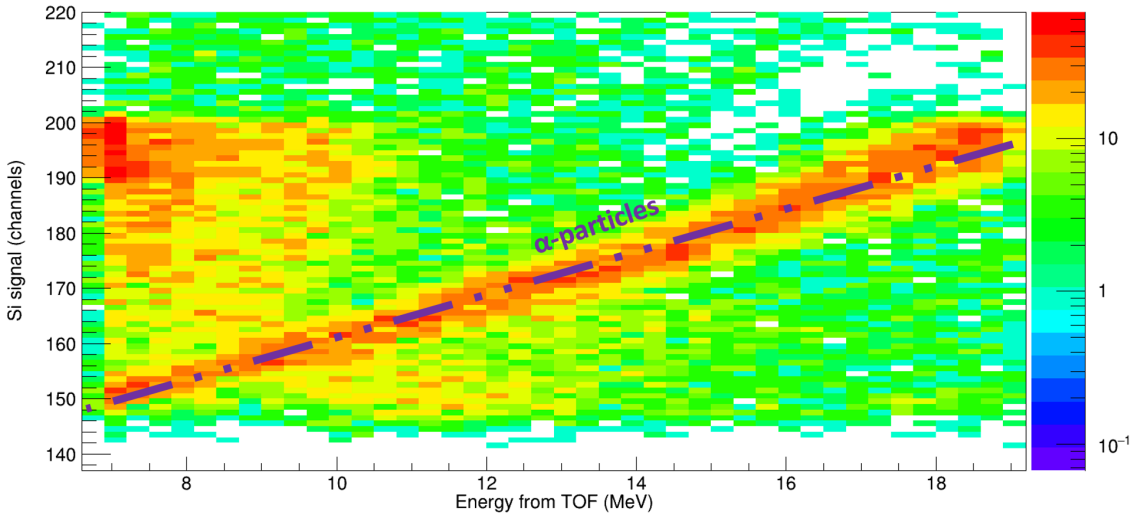

Figure 4.21: Energy of a hit calculated from the time-of-flight against the silicon signal. This allowed for a calibration of those detectors where insufficient calibration points were available. The α-particles are well defined by virtue of being the most populated line. Projections of this 2D spectrum at set energies and fitting the profile with a Gaussian allows for a series of calibration points to be obtained. The effect of leaking into the next time pulse can be seen where for the α-particle lines wraps around on the x-axis to appear at a lower energy (for an energy of $\sim$ 7 MeV and a silicon signal of $\sim$ 195).

4.3.8 Energy measurement

Given the energy deposited in the silicon stage, the energy of the incident particle (using the knowledge of its charge and mass via dE-E PID) can be determined. This was achieved using the energy-range-energy method (Figure 4.22) whereby for different species of incident particle, one knows the relation between their range and energy. A specific energy incident particle leaves a different amount in the silicon stage therefore one merely reverses this mapping to deduce the incident energy. Using this technique, the disadvantages afforded to using the CsI(Tl) signal are removed, this also allows for an estimate of the uncertainty in energy using this method. The CsI(Tl) used had a measured energy resolution of 1.1% for the 82 MeV deposited in the CsI(Tl) for the 400 MeV gold scattering calibration. There is a slight uncertainty ($\sim$ 100 keV) in this value as different energy-loss codes give different values for the range depending on the parameterisation used. This difference is illustrated in Figure 4.23 where the values from *LISE++* [119] and *DEDX* [120] are compared showing the deviations becoming

larger at smaller energies. As previously mentioned, for the 5.5 MeV α-source the silicon resolution was 2.3%. When scaling the CsI(Tl) resolution down to this energy using the $\sigma E \propto E^{\frac{1}{2}}$ method (where the noise contribution is expected to be negiligible at large energies) this gives a CsI(Tl) resolution of 4.5% for the α-source energies.

Figure 4.24 compares measuring the energy via directly determining the sum of the two stages to calculating it solely via the silicon stage signal to examine the energy resolution. This relation between the incident energy and the energy loss in the silicon was given by a power relation with the parameters fitting those from *LISE++* for a α-particle passing through a nominal 300 μm detector - dE = $528.77\text{E}^{-1.029}$ (MeV). The energy resolution was also evaluated for all thickness of detectors.

It can be seen that using the CsI(Tl) signal is advantageous over a broader energy range. This is particularly true at higher energies where the energy deposited in the silicon stage reaches a roughly constant value from a dE-E plot. This calculation omits any systematic uncertainty from the calibration for the CsI(Tl) which will deteriorate the resolution for this method. Over the principal energy range of interest < 50 MeV the two methods are extremely similar demonstrating the choice is suitable. As discussed later, this system is limited by angular resolution rather than energy resolution so this energy uncertainty isn't of primary concern.

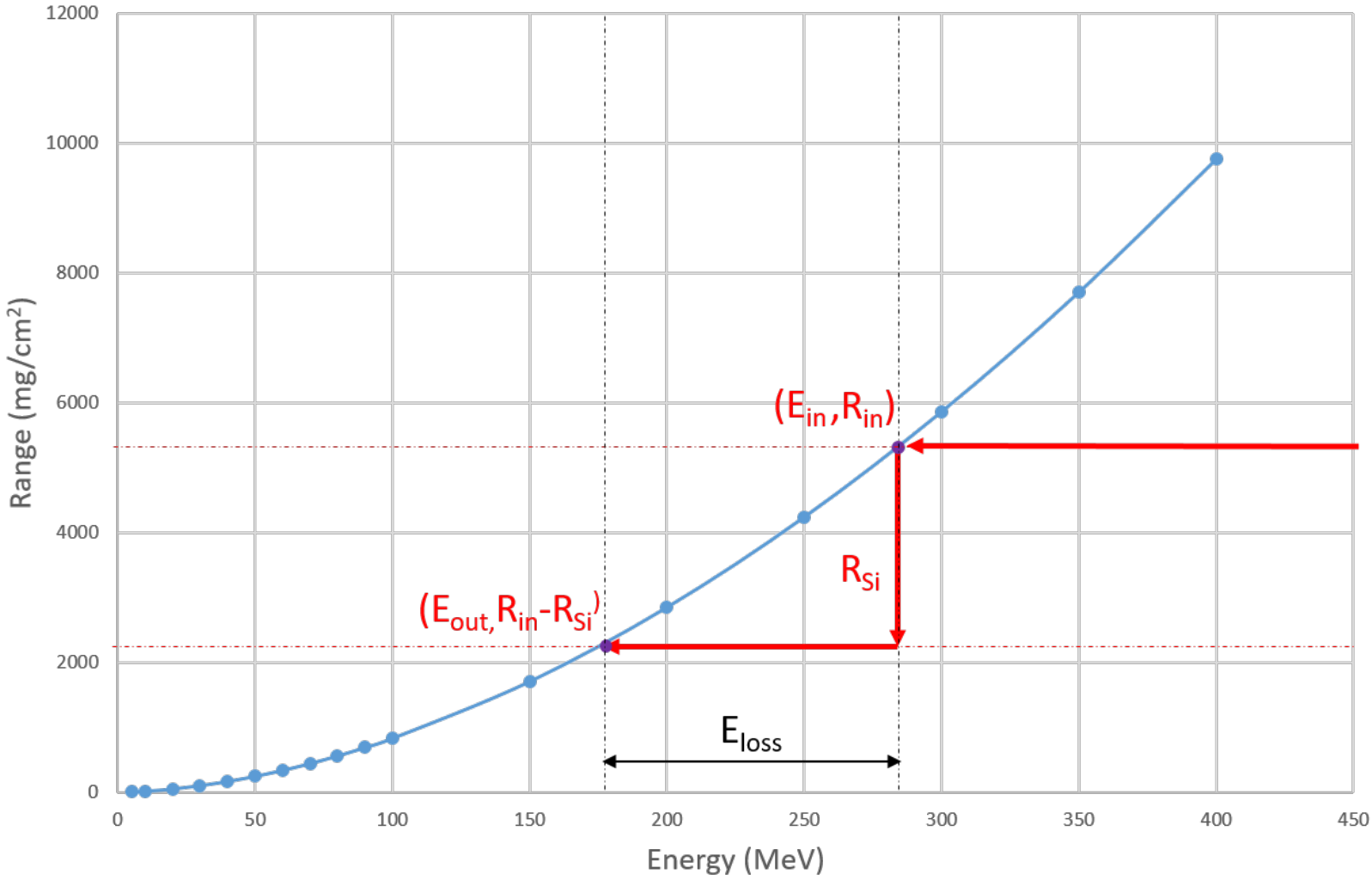

Figure 4.22: Demonstration of the energy-range method for calculating the energy after passing through a silicon dE detector of thickness R_{Si}. This relies on a good knowledge of the relation between energy and range. Firstly, the range at the input energy is calculated then a new range is determined after passing through the detector which is $R' = R_{in} - R_{Si}$. The energy that this corresponds to is then calculated from the energy-range relation which gives the energy after passing through detector. This method can also be employed in reverse to get the intial energy from that measured after the silicon detector.

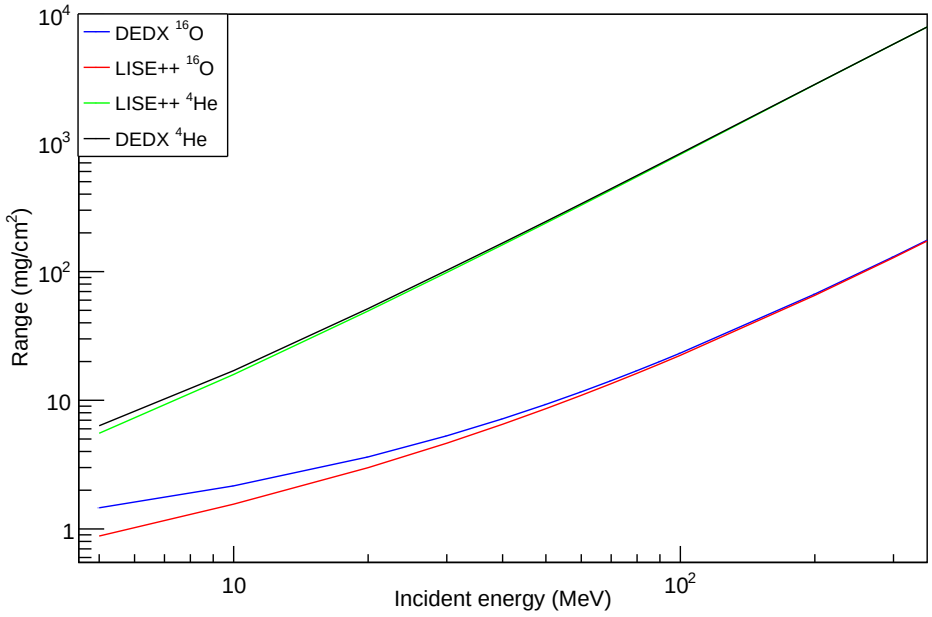

Figure 4.23: Comparison of the range values between *LISE++* and *DEDX* codes. The ranges shown are for ^{4}He and ^{16}O in silicon.

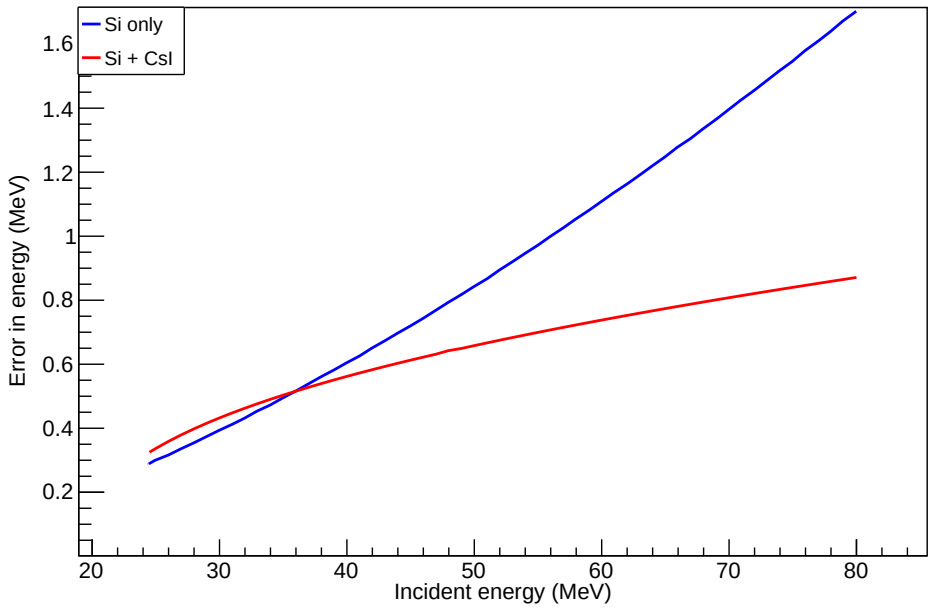

Figure 4.24: Comparison between using only the silicon and the silicon + caesium-iodide detectors to determine the incident energy for α-particles.

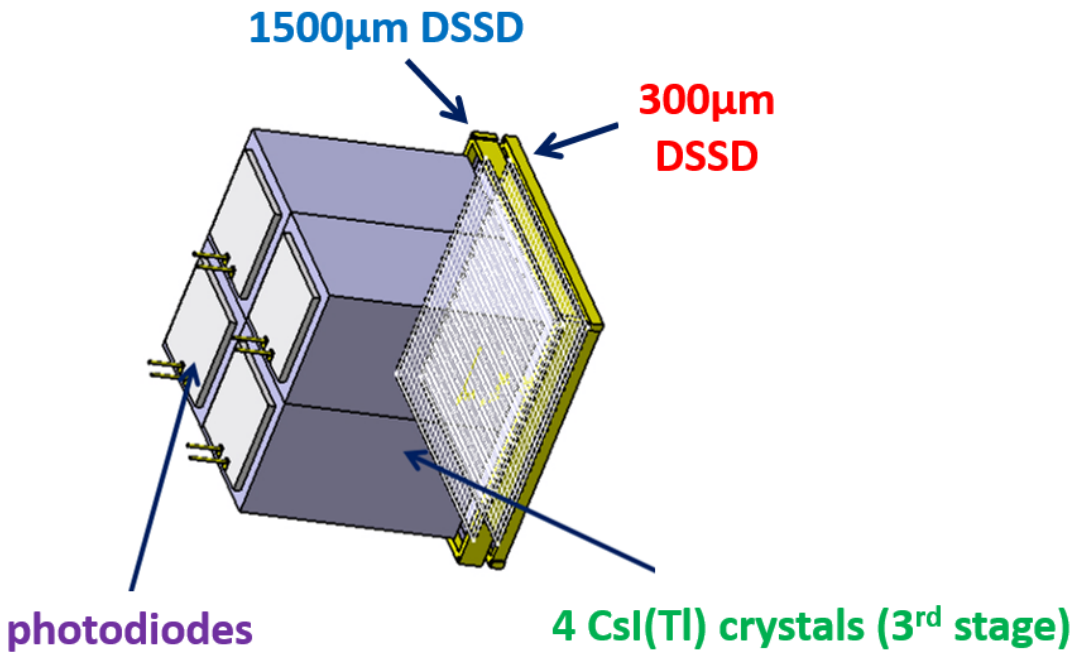

Figure 4.25: Schematic of the three stages of the FARCOS detector. Image adapted from [122].

4.4 FARCOS

The FARCOS (Femtoscope Array for COrrelation and Spectroscopy) detector [121] [106] is a high granularity, high resolution detector system mainly designed for heavy-ion collisions and studies of light-clustering. FARCOS comprises of three detector stages, the first being a nominal 300 μm DSSD (double-sided silicon strip detector) with 32 strips in both the vertical and horizontal direction. The second stage is a thicker nominal 1500 μm DSSD of the same strip number. Behind this is a set of four 6 cm thick CsI(Tl) crystals with a PIN diode read-out arranged in a 2 x 2 grid. The overall system is 64 x 64 mm in extent giving an angular resolution of around 0.1° for a single strip at a distance of 1 m. The setup has a form that can be seen in Figure 4.25.

At the phase of development of FARCOS during the experiment, the detector array had four such systems arranged to surround the beam in a rectangular fashion. The read-out electronics use an ASAD (ASIC-ADC (Application Specific Integrated Circuit

- Analogue Digital Converter)) mounted on a CoBo (COncentration BOard) which is then integrated into the CHIMERA analogue stream. As the system was still in development however, the 1500 μm DSSD only had one face utilised in the electronics setup due to insufficient ASAD channels. Recent upgrades have increased the channels available and all strips are now read out.

4.4.1 Calibration of the FARCOS array

For the FARCOS detector, another series of useful calibration points in addition to the triple-alpha and gold scattering data points (which both had excellent statistics for the FARCOS detectors by virtue of its proximity to the target/source ($\sim$ 70 cm) and low scattering angle) were available. These correspond to the punchthrough points for different nuclei. The punchthrough corresponds to the energy at which the particle has sufficient energy to completely traverse the detector and emerge from the other side. As such, the energy deposited in this detector reaches a maximum and any further increase in the energy of the impinging particle results in a decrease in the energy deposited. These punchthrough points are listed in Table 4.3.

Nucleus	$\mathbf{E_{punchthrough}}$ **(MeV)**
^{4}He	68.8
^{6}Li	129.6
^{7}Li	138.6
^{7}Be	190.8
^{9}Be	213.0
^{12}C	378.4

Table 4.3: Punchthrough energies for the FARCOS telescope for different nuclei. This is the energy required to pass through 1800 μm of silicon.

4.4.2 FARCOS particle tracks

In order to identify the momentum vector of the incoming particles, one must first process the individual strip values. Firstly, the pedestal events must be removed which is done channel by channel.

The front strip hits from the dE stage (f_1) were matched with the front strip hits from the E stage (f_2). These strip numbers must match to within 1 to demonstrate the hit arose from the same particle as shown in Figure 4.26. The multiplicity of these hit

pairings was then compared to the multiplicity of the hits from the dE back strips. The E stage back strips are missing as previously mentioned so cannot be treated in the same way as the front strips.

The energies for the strips are then calculated using the calibration. To verify a track, the energy of the front and back strips in the dE stage are then compared. For a set of n tracks, each of the n back energies is matched to the closest n front energies. If the energy difference is above a given value, the track is removed as the hit matchings are incorrect. In practice, the main multiple hit events correspond to the break-up of ^{8}Be, where the two α-particles have roughly the same energy and the break-up of the Hoyle state, where three α-particles have similar energies.

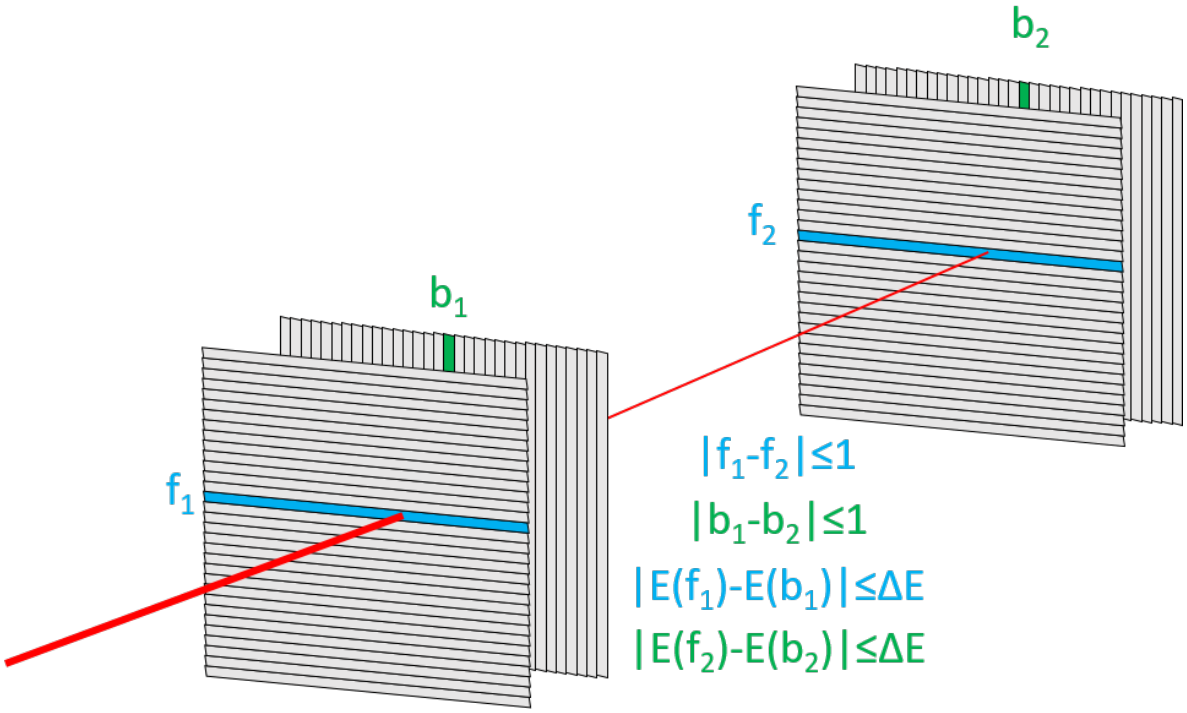

Figure 4.26: FARCOS particle tracks showing the criteria needed for a multiplicity 1 event. In the current experiment b_2 information was absent so some additional criteria could not be applied.

Finally, the particle identification is performed using the dE-E method. As the system is well calibrated and is a Si-Si telescope rather than a Si-CsI(Tl) telescope, the particle identification is instead given by finding the best minimum distance to the known dE-E curves for different nuclei.

Chapter 5

Experimental results and comparison of data with theoretical models

5.1 Work performed

This chapter details calculations performed as part of this thesis and the comparison of these models with the experimental data obtained. Chapter 5.2 discusses how one can attempt to understand the reaction mechanisms present at this high energy by using the statistical decay model to calculate the expected products (Chapter 5.2.1) which were performed for this thesis. Another insight into understanding high multiplicity reactions can also be obtained using the Fermi break-up model to study the phase space of n-body break-up reactions (Chapter 5.2.2). Finally, calculations were also performed using a Monte Carlo simulation to study the effect of the experimental setup on the results obtained (Chapter 5.2.3). These three results are then compared and contrasted to the experimental results which were extracted from the data (Chapters 5.3-5.7). This helps to understand the role of direct versus compound nucleus reactions as well as whether the system is better described by statistical decay or a break-up of the compound nucleus.

5.2 Simulations

5.2.1 Extended Hauser-Feshbach calculations

A theoretical understanding of the reaction mechanism can be gained by performing an extended Hauser-Feshbach calculation [123]. This relies on modelling the resonances inside nuclei as a sum of Breit-Wigner levels. One can formulate the cross section for a transition from state α to α' [19] as:

$$\sigma_{\alpha'\alpha}(J^{\pi}_{tot};E) = \frac{\pi}{k^2} g J_{tot} \sum_{p} \frac{\Gamma_{\alpha p}\Gamma_{\alpha' p}}{(E-E_p)^2 + \Gamma_p^2/4} \tag{5.1}$$

through the intermediate resonance p. The Hauser-Feshbach model relies on a link between this cross section and that determined by the so-called "optical model". This is a potential with a real and imaginary component (both parameterised with a Woods-Saxon form). The imaginary component gives information about the probability to exit the channel. To link to this optical potential, one averages over a large number of the resonances p over an energy range I ensuring this averaging region is much larger than the mean level spacing between resonances D, demonstrated in Figure 5.1. One can also model the density of states using the Fermi-gas model [124] [125]. This allows for a reformulation of Eq. 5.1 to give:

$$\langle \sigma_{\alpha'\alpha}(J^{\pi}_{tot};E) \rangle = \frac{\pi}{k^2} g J_{tot} \frac{2\pi \langle \Gamma_{\alpha} \rangle}{D} \tag{5.2}$$

$$\sigma_{\alpha'\alpha}(J^{\pi}_{tot};E) = \frac{\pi}{k^2} g J_{tot} (1 - |\mathbf{S}^{J_{tot}\pi,opt}_{\alpha'\alpha}|^2) \tag{5.3}$$

with the term $\mathbf{S}^{J_{tot}\pi,opt}_{\alpha'\alpha}$ coming from the optical potential. These are typically global optical potentials which have been studied for a range of nuclei and energy regions for proton, deuteron and α-particles [126][127]. This connection can then allow for a reformulation of Eq. 5.1:

$$T_{\alpha} = 1 - |\mathbf{S}^{J_{tot}\pi,opt}_{\alpha'\alpha}|^2 \tag{5.4}$$

$$\langle \sigma_{\alpha'\alpha}(J^{\pi}_{tot};E) \rangle = \frac{\pi}{k^2} g J_{tot} \frac{T_{\alpha} T_{\alpha'}}{\sum_{\alpha''} T_{\alpha''}} \tag{5.5}$$

where the introduction of the transmission coefficient T_{α} removes the need to know the average width in the channel α, denoted by $\langle \Gamma_{\alpha} \rangle$. The branching ratio to a decay

channel α' is then simply given by:

$$B_{\alpha'} = \frac{T_{\alpha'}}{\sum_{\alpha''} T_{\alpha''}} \tag{5.6}$$

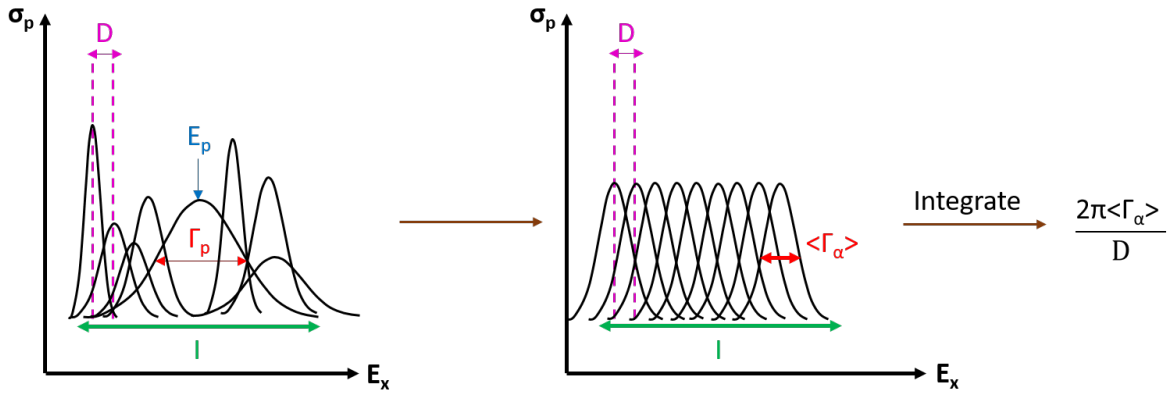

Figure 5.1: Schematic showing the reformulation of varying resonances to describing the system in terms of many overlapping resonances with a modified width $< \Gamma_\alpha >$. The averaging distance I is shown which is the range over which $< \Gamma_\alpha >$ is calculated. As one changes excitation energy in the system this value is prone to change.

The program used in this work was an *Extended Hauser-Feshbach* (EHF) code [128] that introduces the effect of clustering to the calculation with the addition of known discrete energy levels. The code first calculates the fusion cross section for the compound nucleus, then calculates the scission modes for the three beam energies. Scission is a more accurate description of fission in a reaction whereby the compound nucleus state is well in excess of the Coulomb barrier. As such, the shape evolution of the compound nucleus state can easily proceed via a necking reaction. This is shown in Figure 5.2, as the two nuclei quasi-fuse together, there is an overlapping region whereby the two maintain a connection. As this evolution continues, this necking region can then yield a different exit channel. To calculate the probability of this scission mode for all available decay paths, the phase space is compared at the scission point which gives the fission yields.

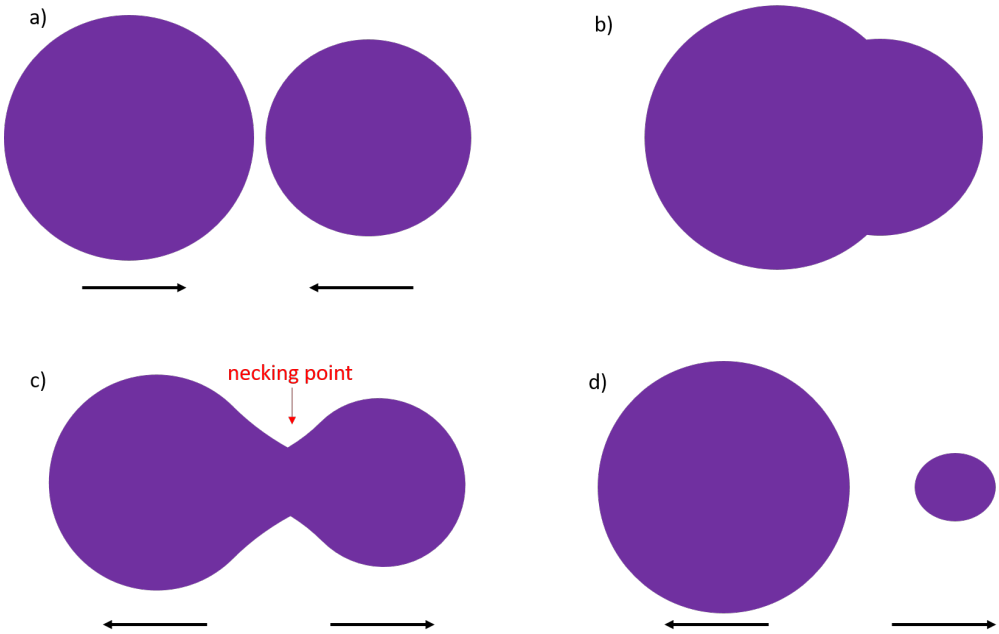

Figure 5.2: The various stages of the fusion-scission mechanism are shown here. In a) the beam and target coalesce to form the deformed compound system in b). The high energy in this process means the compound nucleus is unstable and the evolution of the system forms a necking point which is annotated in c). The severing of this necking point yields a rearrangement of the nucleons in the scission products which are shown in d).

These fractional populations can be used to inform the individual weights of the developed Monte Carlo codes discussed later in Chapter 5.2.3. It is also apparent that the lower beam energy tends towards more α-conjugate pathways (as a result of the reduced Q-value and therefore increased phase space for these decay modes).

Following the scission, the code then simulates the statistical emission of neutrons, protons and α-particles via the process shown in Figure 5.3. Each nucleus is divided into a set of energy bins with a given angular momentum. The initial compound nucleus reaction followed by scission populates these energy bins according to the phase space allocation mentioned above. To model the statistical decay, one then proceeds through the nuclei one by one. In this work, starting with ^{28}Si, the gamma decay followed by particle decay to ^{27}Al, ^{27}Si and ^{24}Mg and their corresponding energy levels was modelled. The decay of ^{27}Si is then modelled in the same way (see Figure 5.4). Once all the neutron decay channels are exhausted then the aluminium nuclei decays (i.e. one proton fewer) are modelled in the same way. This then allows for an investigation into the excitation energies populated in the intermediate states.

Nucleus	160 MeV	280 MeV	400 MeV
^{4}He	14.5	2.4	1.4
^{8}Be	0.0	0.1	0.4
^{12}C	7.4	13.5	8.6
^{16}O	7.4	13.5	8.6
^{20}Ne	6.2	6.9	4.8
^{24}Mg	14.5	2.4	1.4
Non α-conjugate	50.0	61.2	74.8

Table 5.1: Percentage population of various scission modes from the compound nucleus.

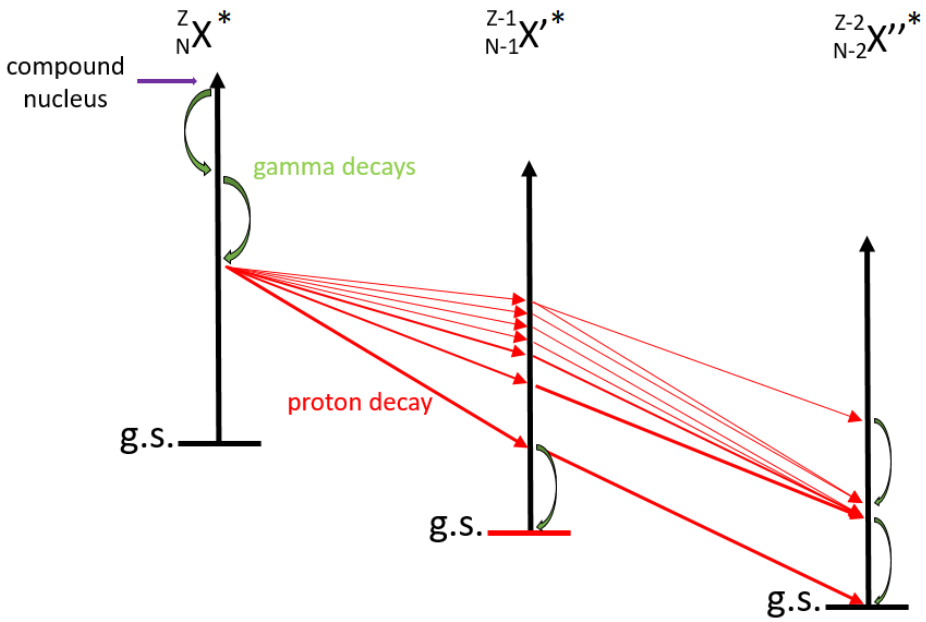

Figure 5.3: Hauser-Feshbach decay process showing how sequential proton decays can change the population of energy bins across different nuclei.

160 MeV

As seen in Table 5.1, at the lowest beam energy of 160 MeV, a larger population of α-conjugate states was seen by virtue of their decreased Q-values. The comparison between the scission and final yields are seen in Figure 5.5. For the heavier mass isotopes, one can see that while a large number are populated by the initial scission reaction, the number that decay to the ground state is very small as the probability for light particle evaporation is prohibitively large. Once a mass lower than 20 is reached, the final yield

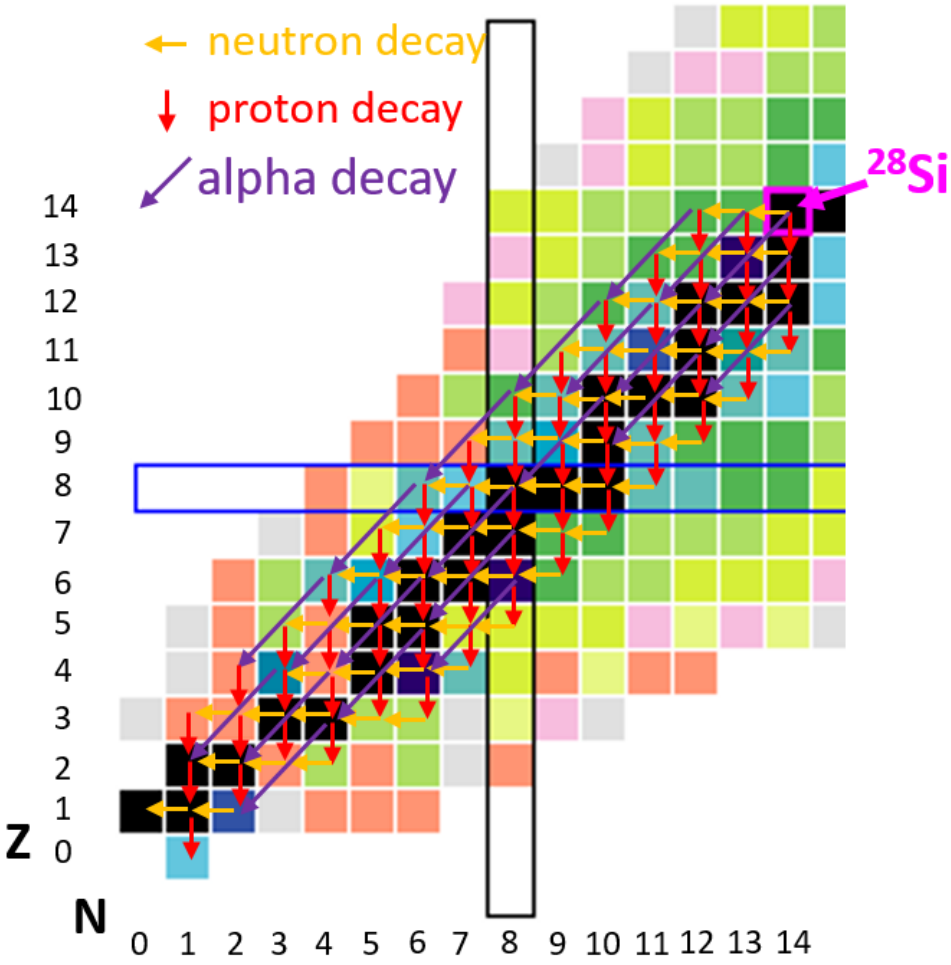

Figure 5.4: Hauser-Feshbach decay process whereby the system continues decaying via proton decay until the ground-state of the decay product is reached. Only the proton decay chain is shown here demonstrating the statistical decay process through various isotopes.

starts to exceed the initial scission yields for the majority of nuclei. In particular, one notes a large increase ($\sim$ a factor of 10) for the final yield compared to the scission yield for ^{1}H, ^{4}He and ^{8}Be.

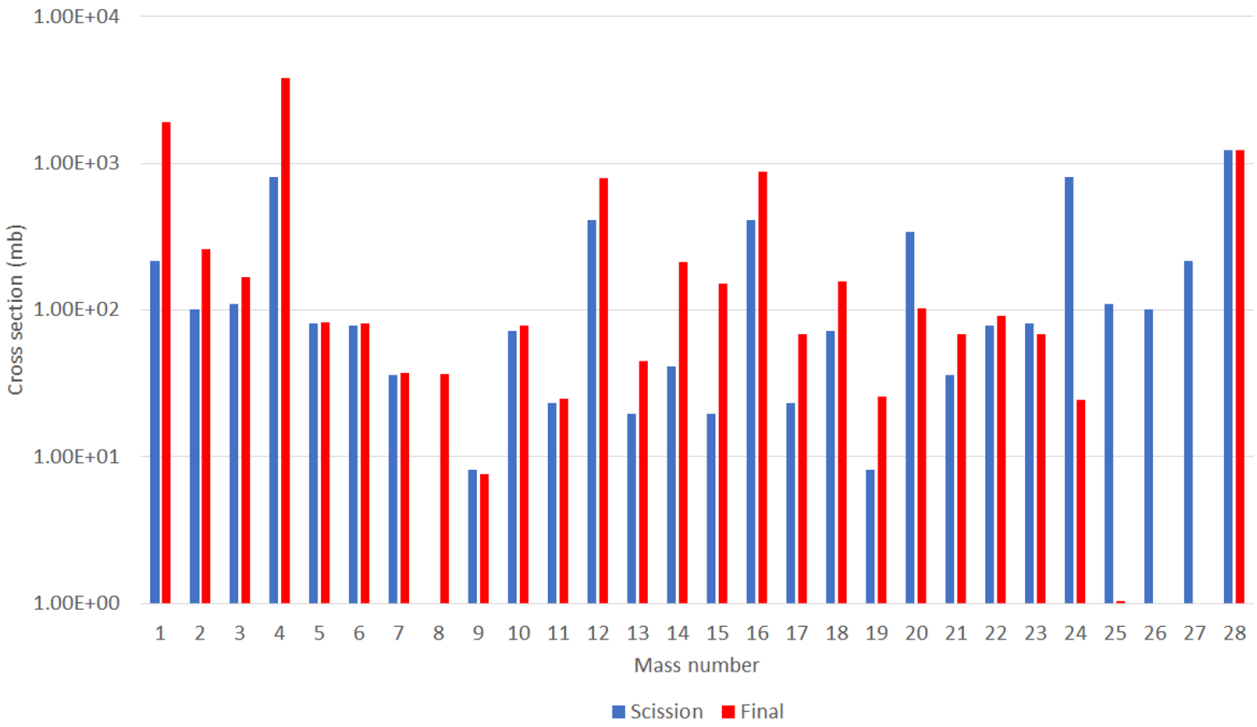

Figure 5.5: Results from the EHF calculations for the 160 MeV beam energy.

To determine an approximate cross section for the 7-α decay, the sequential decay probabilities for α-decay (i.e. ^{28}Si $\rightarrow$ ^{24}Mg $\rightarrow$ ^{20}Ne $\rightarrow$ ^{16}O $\rightarrow$ ^{12}C $\rightarrow^{8}$ Be $\rightarrow$ α) were analysed. This can also be compared to additional decay paths such as ^{28}Si $\rightarrow$ ^{20}Ne $\rightarrow$ ^{16}O $\rightarrow$ ^{12}C $\rightarrow$ ^{8}Be $\rightarrow$ α to give a comparison for the 7-α decay channels. To calculate the total expected α-multiplicity, one can analyse the prevalence of n sequential α-decays following the population of any nucleus via scission. The results from this can be seen in Figures 5.6 and 5.7. One sees a sensible decline in the cross section as the multiplicity of α-particles is increased. After a rapid decline, one sees a value of 0 mb for 6 α-particles as the predicted calculation for 6 sequential α-decays falls below the cross section threshold. A cross section of 12 mb is predicted for 7 sequential decays as the first step of scissioning to ^{24}Mg is well populated whereas to end with 6 α-particles rather than 7, one must initially populate a non α-conjugate nucleus so after 6 sequential decays, the nucleus you are left with is not ^{4}He. E.g. ^{28}Si $\rightarrow$ ^{27}Si $\rightarrow$ ^{23}Mg $\rightarrow$ ^{19}Ne $\rightarrow$

$^{15}\mathrm{O} \rightarrow {}^{11}\mathrm{C} \rightarrow {}^{7}\mathrm{Be} \rightarrow {}^{3}\mathrm{He} + \alpha$. From an energetics point of view, this decay mode is suppressed as this means effectively breaking apart a ^{4}He nucleus which requires roughly 20 MeV.

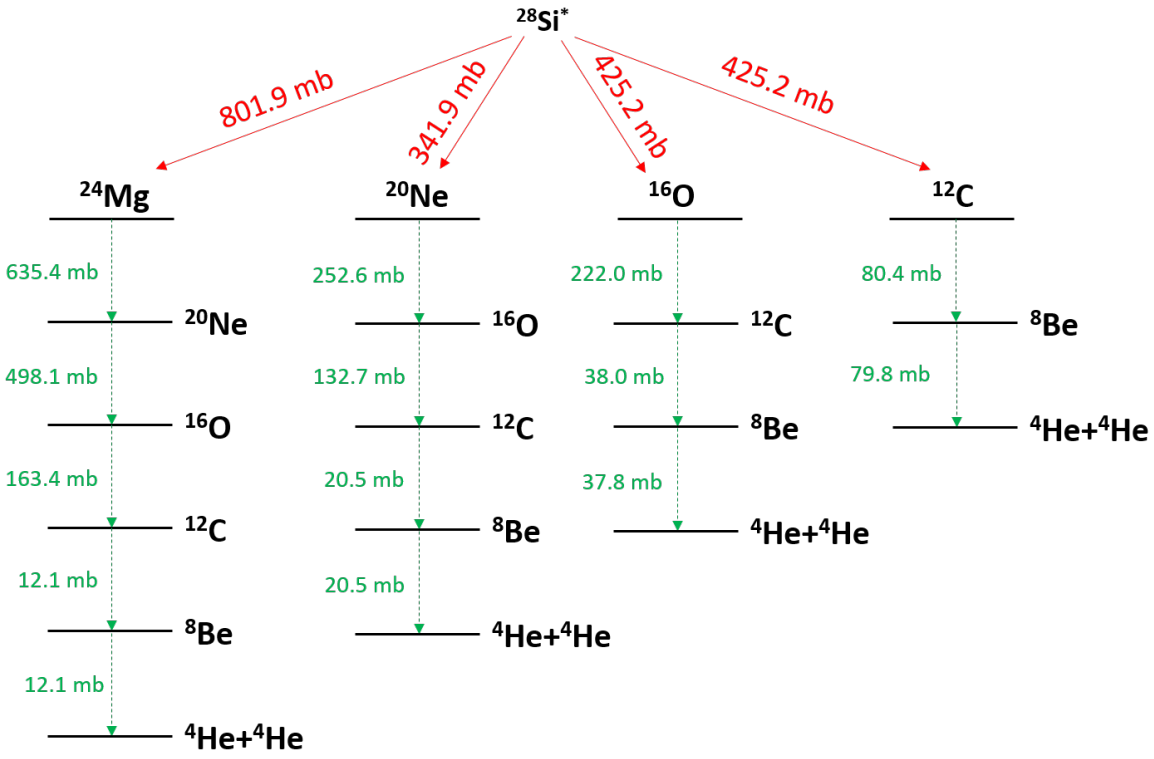

Figure 5.6: EHF predictions for $E_b = 160$ MeV through the different α-conjugate nuclei. The initial scission cross section is shown in red for the different decay paths with the sequential strengths shown in green. σ_{fus}=3562 mb.

It is also possible to have a decay whereby a few α-particles are emitted followed by a proton or neutron emission before continuing with sequential α-particle emission. To examine the strength of this contribution (the number of channels for which a calculation is needed is prohibitively large), a few cases were tested (e.g. ^{3}He,n,α,α,α) was compared with the solely sequential α-decay mode and these **non-α paths were shown to have a cross section suppressed by roughly an order of magnitude**. This suppression is by virtue of the need for an additional decay step in comparison to the α-only decay.

To understand the mechanisms involved in the statistical decay, the excitation energy before the particle decay can be examined. This includes contributions from all different decay paths i.e. when looking at ^{12}C, one sees population from $^{13}\mathrm{C} \rightarrow {}^{12}\mathrm{C} + \mathrm{n}$,

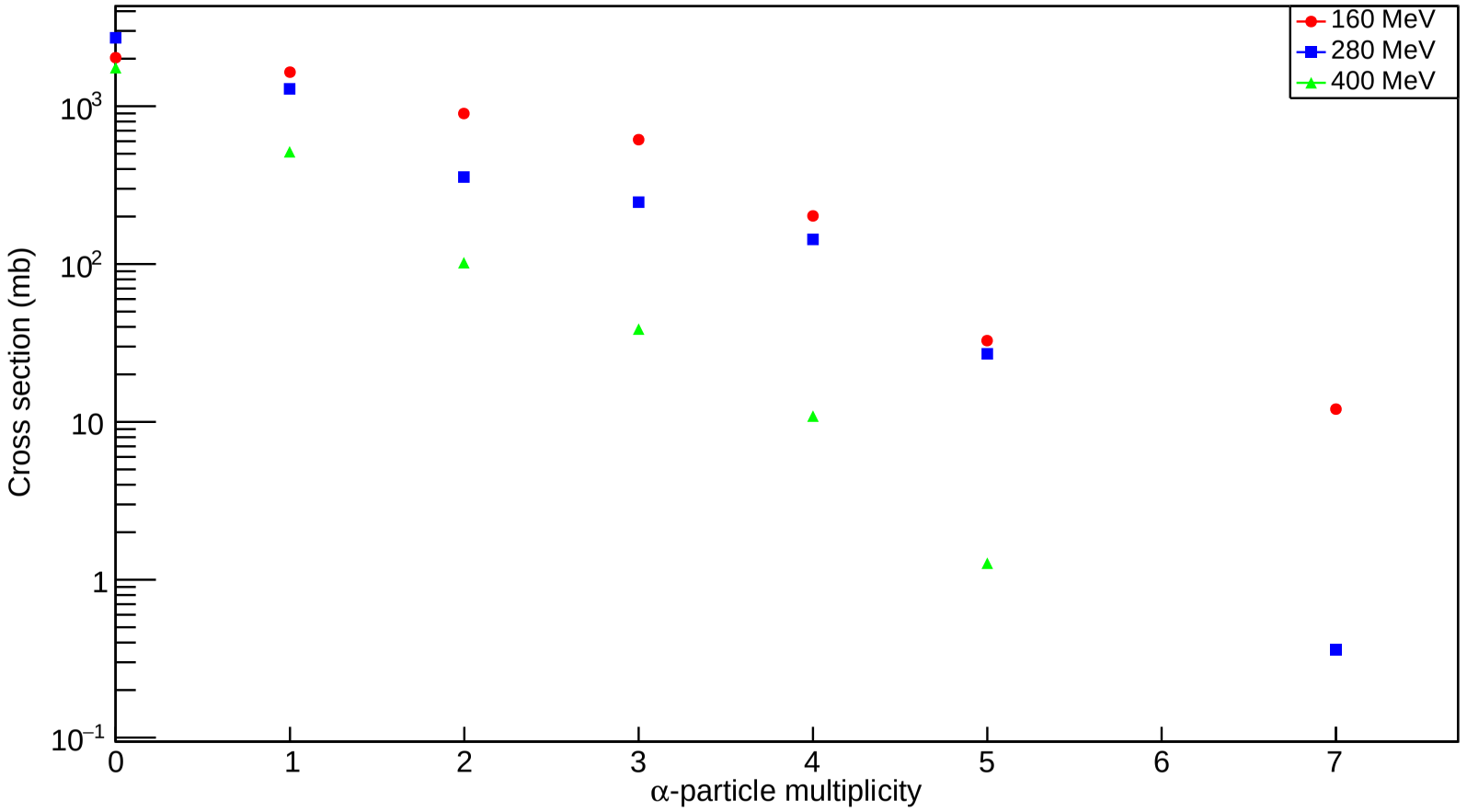

Figure 5.7: α-particle multiplicity predictions from the EHF for the three beam energies. One sees a steady decrease in the expected multiplicity. Note the multiplicity 6 value is 0 as all predictions for this multiplicity fell below the tolerance of the program.

direct scission, $^{16}\mathrm{O} \rightarrow {}^{12}\mathrm{C} + \alpha$ etc. Figures 5.8-5.11 show the results of the sum of these decay paths for the different nuclei compared to the different beam energies. The 160 MeV calculations show a population which is highly centred towards low excitation energies, particularly in ^{12}C and ^{16}O where discrete energy levels (i.e. the 2_1^+ in ^{12}C) can be seen to have a reasonable cross section. In addition there is also a high energy tail with a rapidly decreasing cross section with increasing energy. For the heavier systems ^{20}Ne and ^{24}Mg, these smooth contributions peak at 20 and 40 MeV respectively suggesting any potential α-gas states in this area can be well populated. It can also be seen that a reasonable amount of the compound nucleus ^{28}Si decays via γ-emission to the ground-state however this decay mode is undetectable with the given set-up as the reaction products will only slightly deviate from the beam-line where there is no detector coverage.

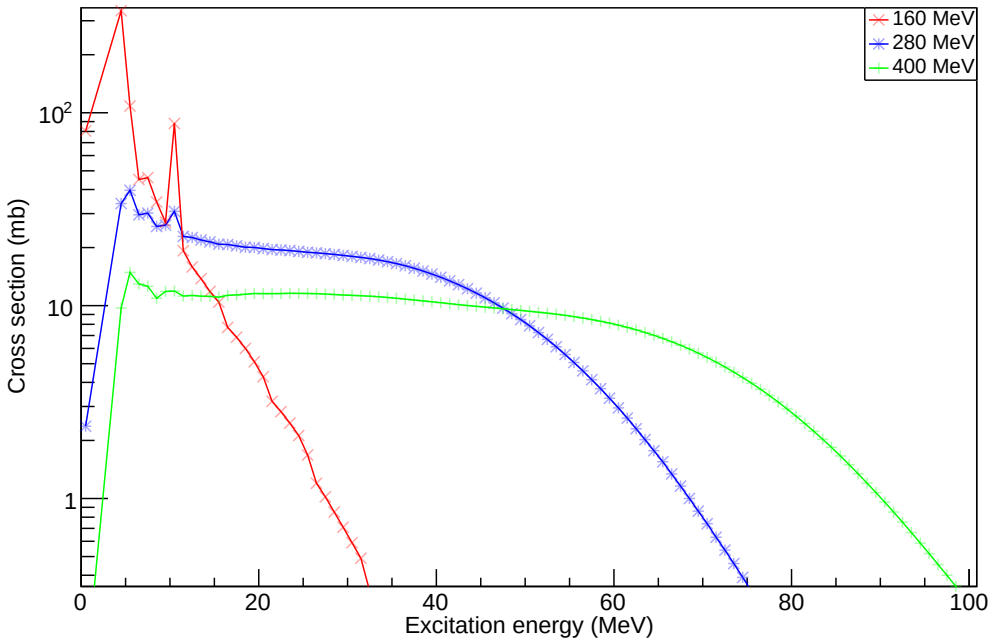

Figure 5.8: Population of ^{12}C from the EHF.

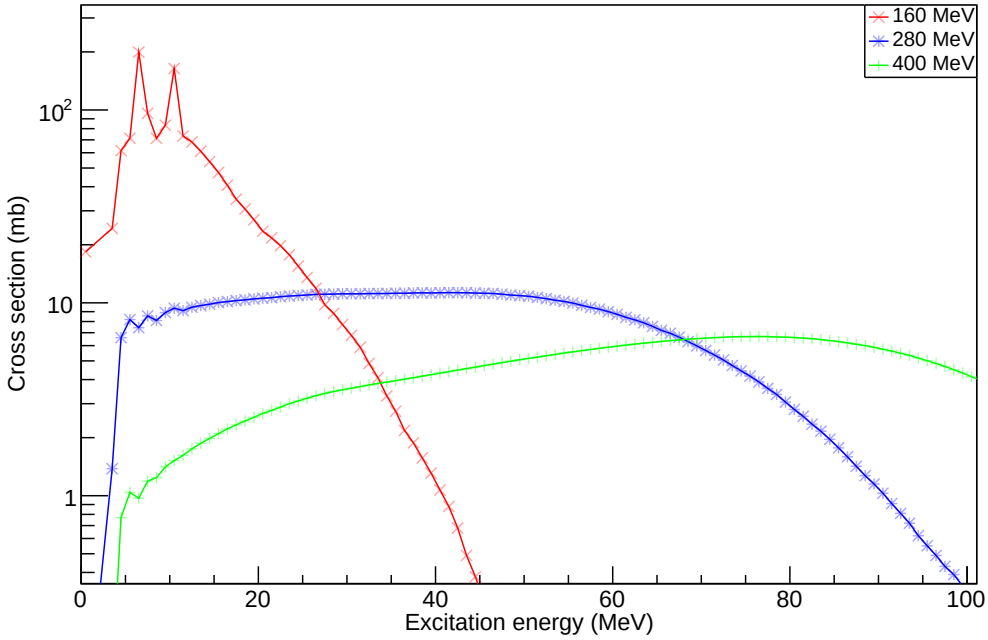

Figure 5.9: Population of ^{16}O from the EHF.

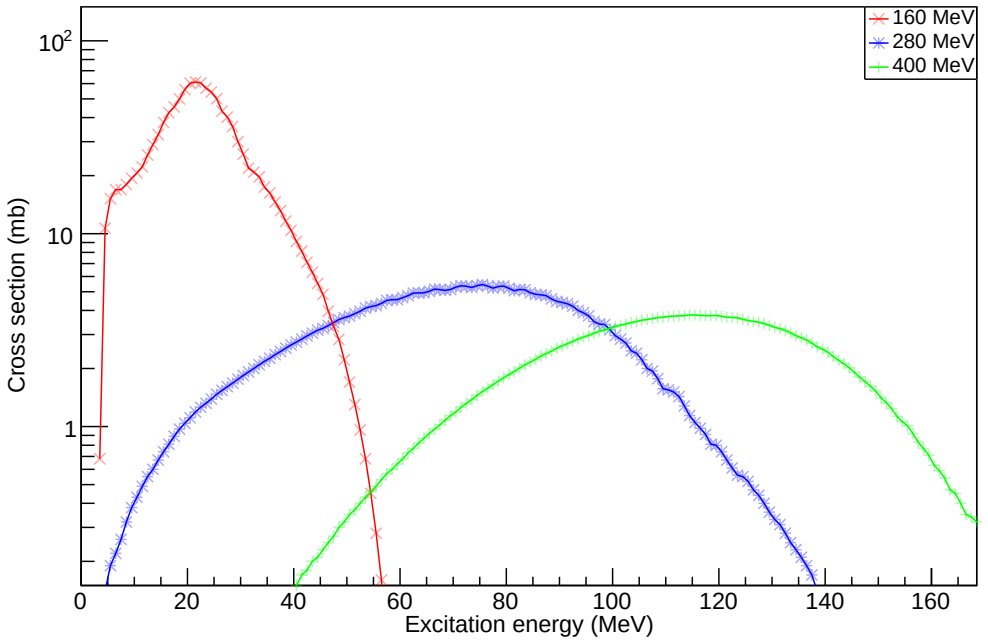

Figure 5.10: Population of ^{20}Ne from the EHF.

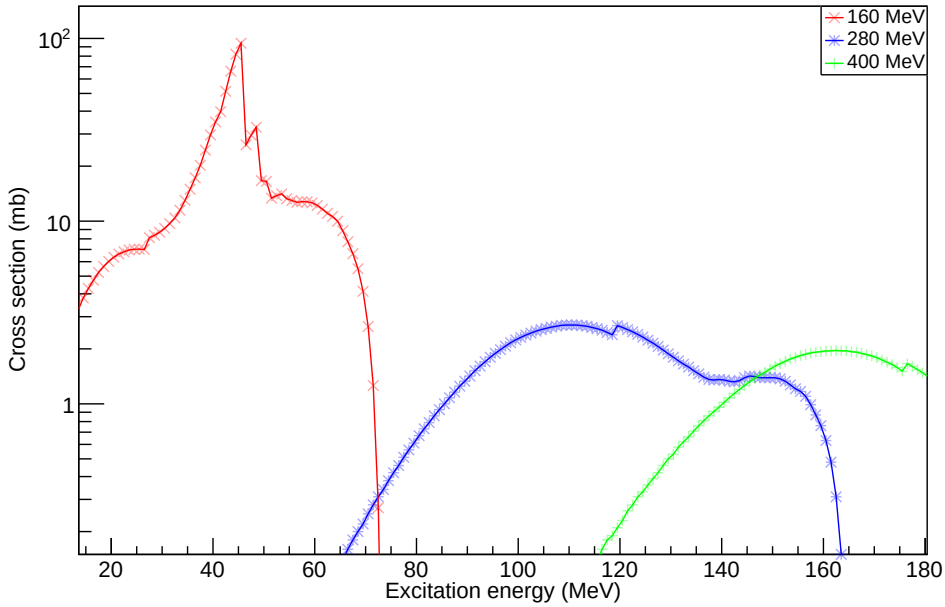

Figure 5.11: Population of ^{24}Mg from the EHF.

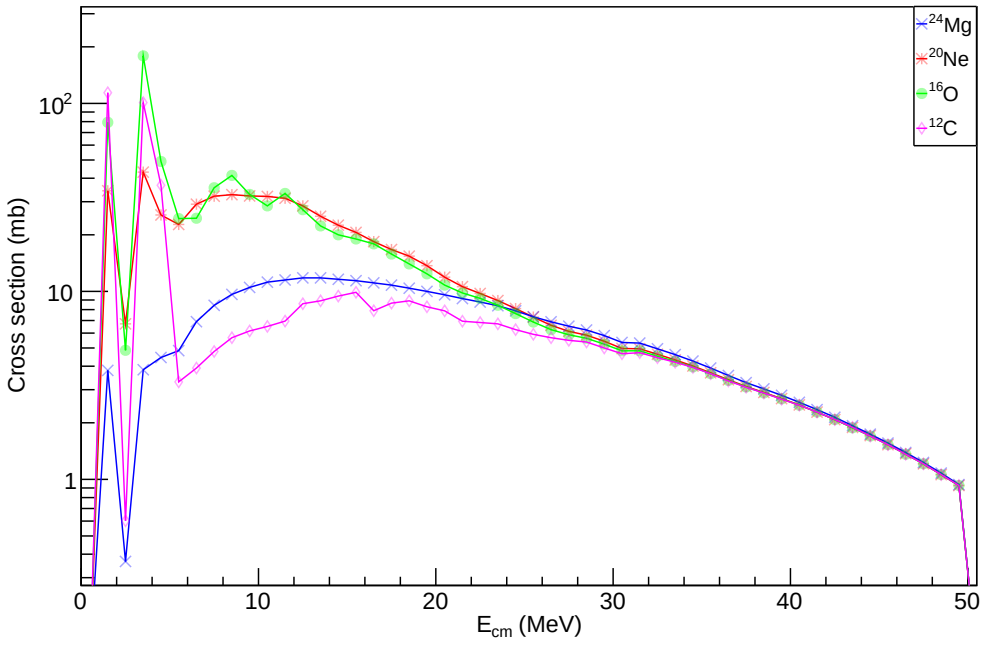

Figure 5.12: α-particle energies in the centre-of-mass as predicted from the EHF following the population of different α-conjugate nuclei for $E_b = 160$ MeV.

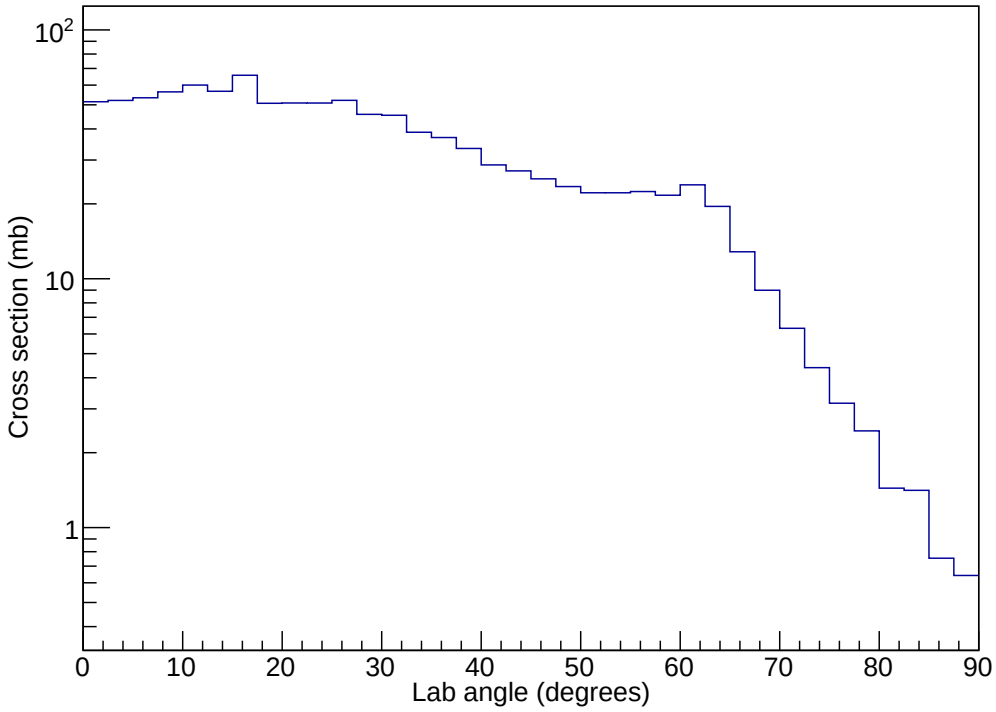

Figure 5.13: Predicted distribution of α-particles in the lab frame from the EHF for E_b = 160 MeV.

In conclusion, for this beam energy one sees that the dominant contribution is to excited states in ^{24}Mg with a large contribution from ^{12}C and ^{16}O. These decay paths have a large chance to decay solely via α-decay. The contribution from non α-conjugate states to the α-particle multiplicity is seen to comprise around 20% for $m_\alpha = 1$ with an ever decreasing contribution as the multiplicity is increased.

Looking at the excitation energies, ^{12}C and ^{16}O can be seen to populate levels around the particle decay threshold where single states can sit above the continuum. The energy in ^{24}Mg is sufficiently high that subsequent α-decays are very likely and single α-clustered states would be unlikely to be populated at a level that could be distinguished above the contribution from the continuum.

To demonstrate the earlier assertion about the distribution of particles, the centre of mass (COM) energy from sequential α-decay from the α-conjugate nuclei was taken as an output from the EHF code, the results of which are shown in Figure 5.12. Taking an isotropic decay angle, the lab scattering angle was then calculated and the yield

plotted for α-particles. The results from this calculation are seen in Figure 5.13. This output clearly shows for the areas of interest studied in CHIMERA ($\theta_{\text{lab}} > 6°$), one sees a continuous distribution.

280 MeV

The scission modes for the 280 MeV beam energy (Figure 5.14) are predicted to be similar to those for the 160 MeV beam energy. The higher energy available increases the homogeneity of the reaction products as the effect of the Q-value becomes less important. The increased excitation energy in the system however does mean the probability for γ-decay to the ground-state in ^{28}Si becomes negligible. An additional effect of this increased energy however is that scission products are created with a higher internal energy therefore can undergo further decay stages. This is evident by the increase in the final yields for p, d, t, ^{3}He and ^{4}He (m=1, 2, 3, 4) corresponding to evaporation of light reaction products.

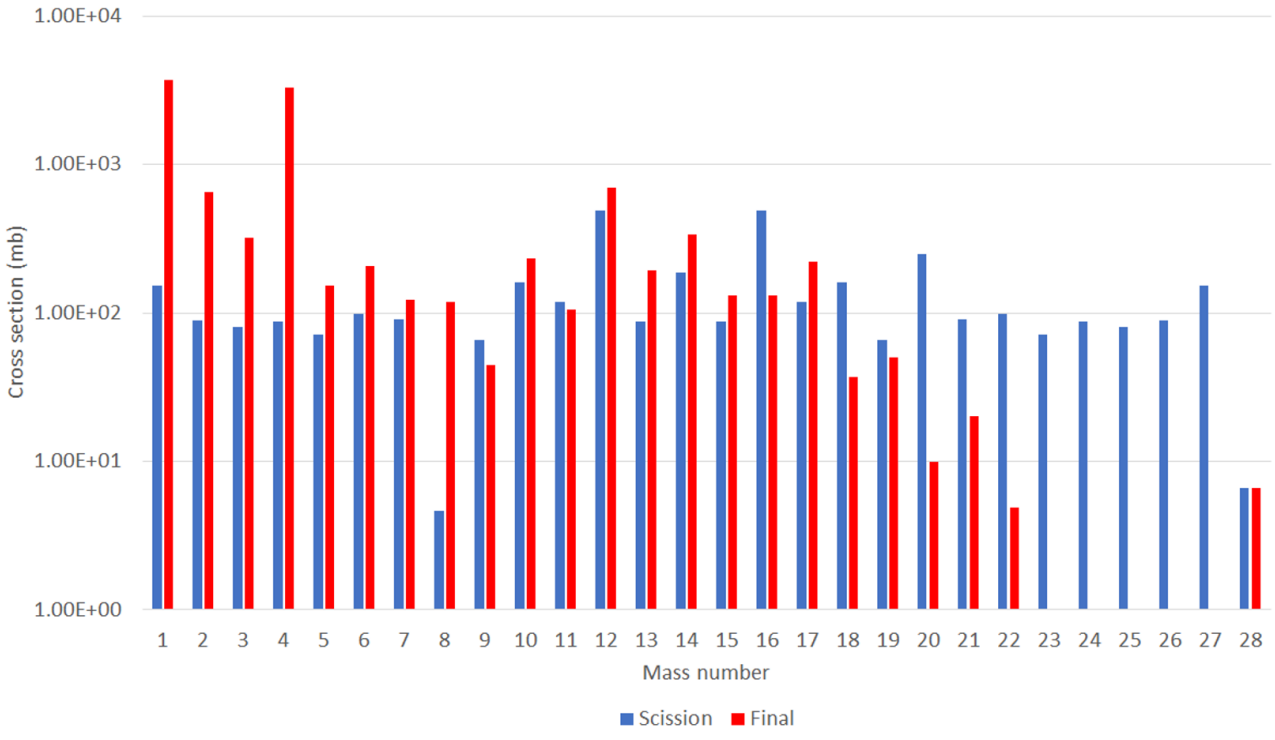

Figure 5.14: Results from the EHF calculations for the 280 MeV beam energy.

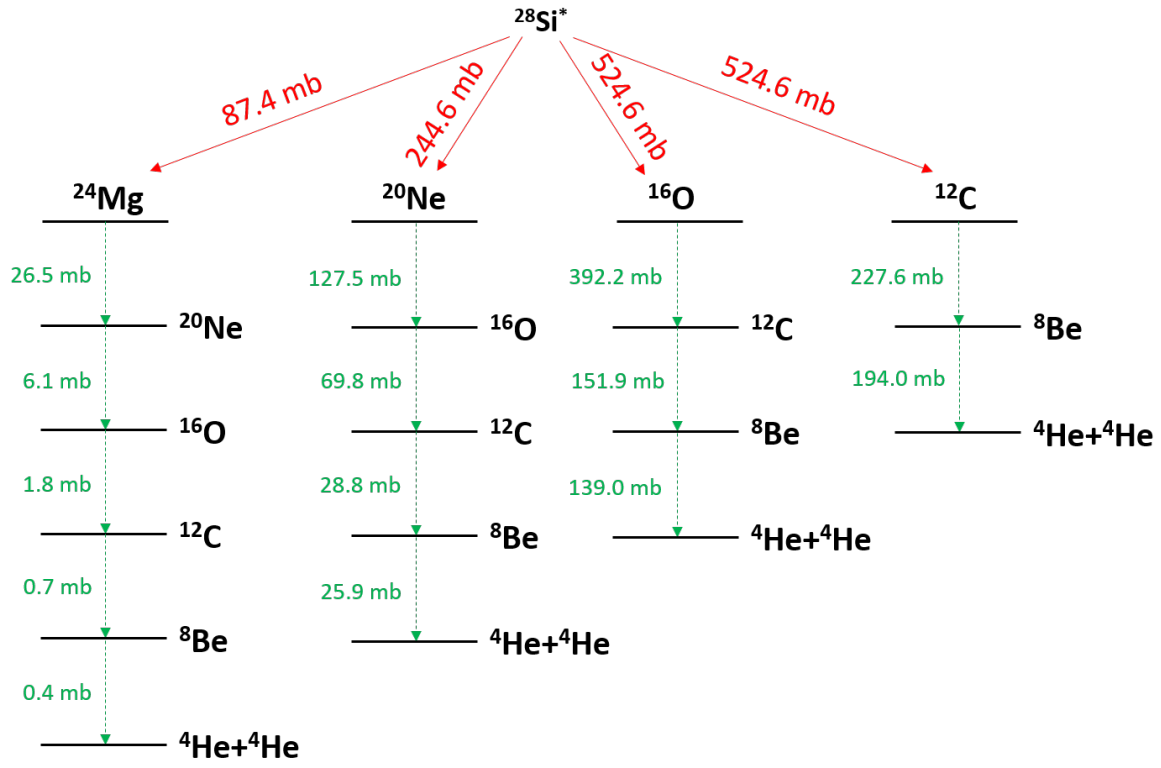

Figure 5.15: EHF predictions for E_b = 280 MeV through the different α-conjugate nuclei. The initial scission cross section is shown in red for the different decay paths with the sequential strengths shown in green. σ_{fus}=1526 mb.

As with the 160 MeV data, one can analyse the sequential decay paths (Figure 5.15) to generate an expected α-particle multiplicity. This is shown in Figure 5.7 where it can be seen that the expected multiplicities are lower than those expected for the 160 MeV data for $m_\alpha = 2$ and 3 while being very similar for $m_\alpha = 4$ and 5. For 7 sequential α-decays, one sees an order of magnitude decrease in the cross section. This is due to the increase in excitation energy whereby the α-decay path is no longer the most energetically favourable and must compete with additional light decay modes. Subsequently, the overall sequential emission rate is reduced. The assumption made previously regarding the unimportance of α-decays interspersed with proton and neutron decays being unimportant is re-examined here. In the same way as the 160 MeV data, the contributions to the α-decay multiplicity are an order of magnitude lower than the α-only decay paths.

Investigation of the excitation energies populated in the α-conjugate nuclei shows a different situation from the 160 MeV simulations. The effect of the low excitation energy

region is reduced for ^{12}C and ^{16}O and the population of discrete states is reduced with the increased energy in the system. These simulations suggest that discrete energy levels should be entirely swamped by the emission of statistical α-particles. The energy distribution of α-particles emitted from the population of the different α-conjugate nuclei are shown in Figure 5.16 where the smooth contribution can be seen to dominate the discrete peaks seen.

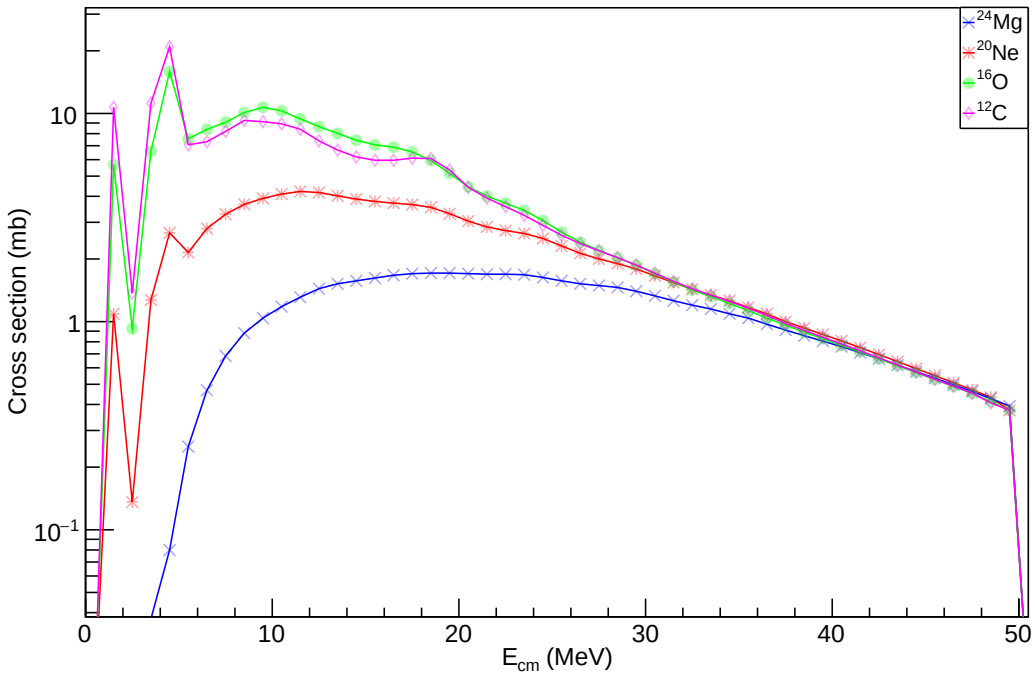

Figure 5.16: α-particle energies in the centre-of-mass as predicted from the EHF following the population of different α-conjugate nuclei for $E_b = 280$ MeV.

400 MeV

The results for the 400 MeV (Figure 5.17) are extremely similar as those for 280 MeV calculations. The scission modes follow a similar pattern and only differ by a factor of ~ 2. The final decay products are similarly heavily focused towards p, d, t, ^{3}He and ^{4}He. Nuclei heavier than ^{16}O do not manage to decay to their ground-state at an appreciable rate demonstrating the excitation energies populated in ^{16}O are well above the particle-decay threshold where the γ-decay branching ratio is small.

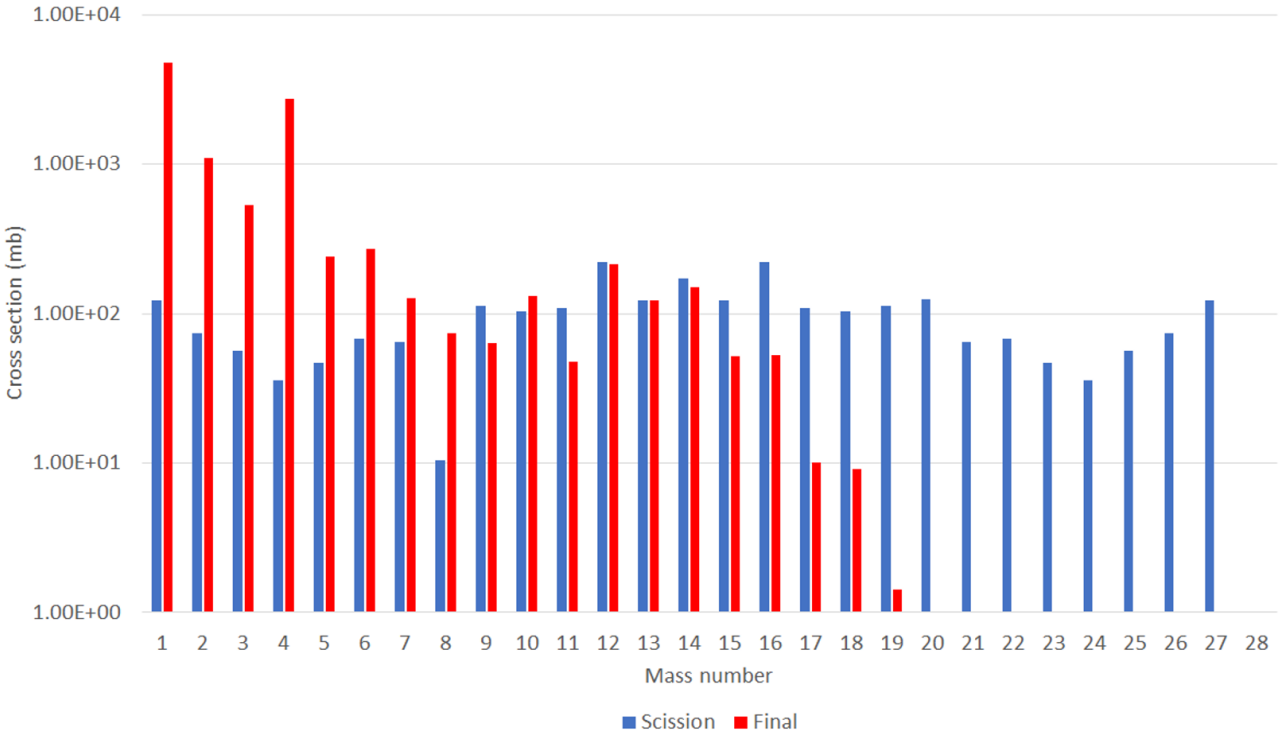

Figure 5.17: Results from the EHF calculations for the 400 MeV beam energy.

As with the 280 MeV data, the equivalence of the different decay paths means that sequential α-particle emission (Figure 5.18) should no longer be preferred. This effect means that the multiplicity drops off extremely rapidly where the $m_\alpha = 7$ cross section is $< 10^{-3}$ mb and the 7-α decay path is predicted to be extremely unlikely.

The populated energy levels at this beam energy are largely dominated by the continuum. As such, discrete energy levels should be difficult to observe in the experimental data. The energy distribution of α-particles is shown in Figure 5.19 where the dominance of the smooth contribution can clearly be seen.

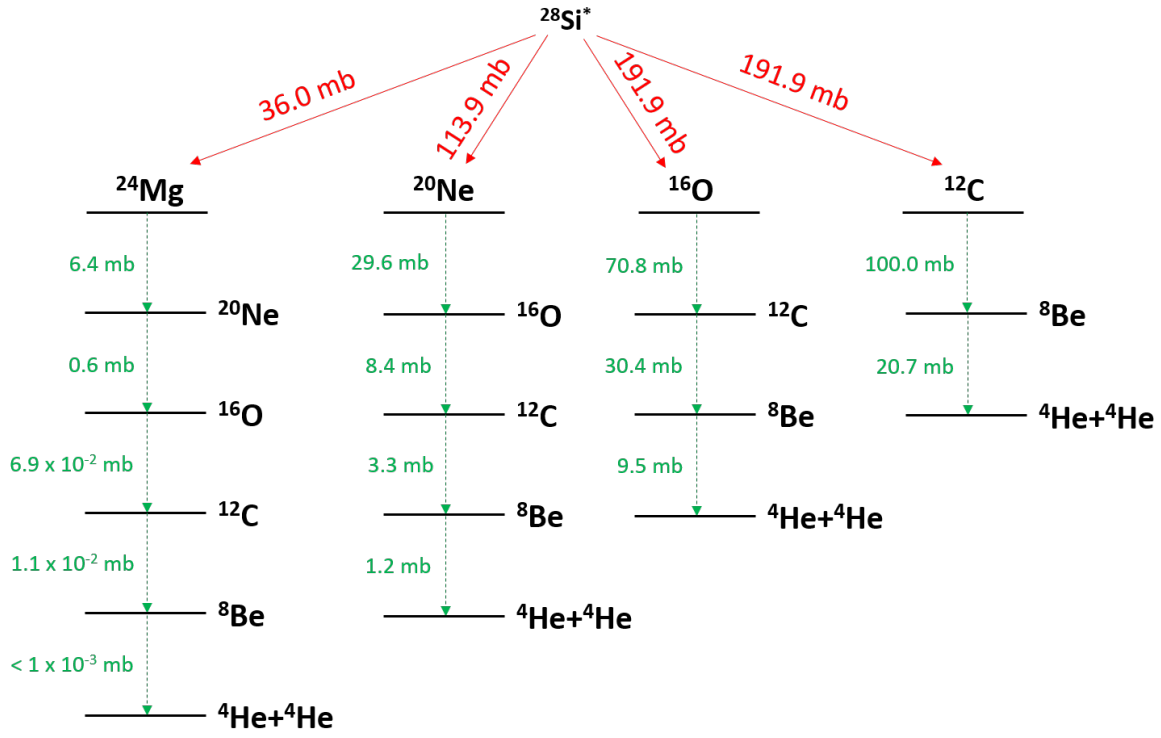

Figure 5.18: EHF predictions for $E_b = 400$ MeV through the different α-conjugate nuclei. The initial scission cross section is shown in red for the different decay paths with the sequential strengths shown in green. σ_{fus}=1425 mb.

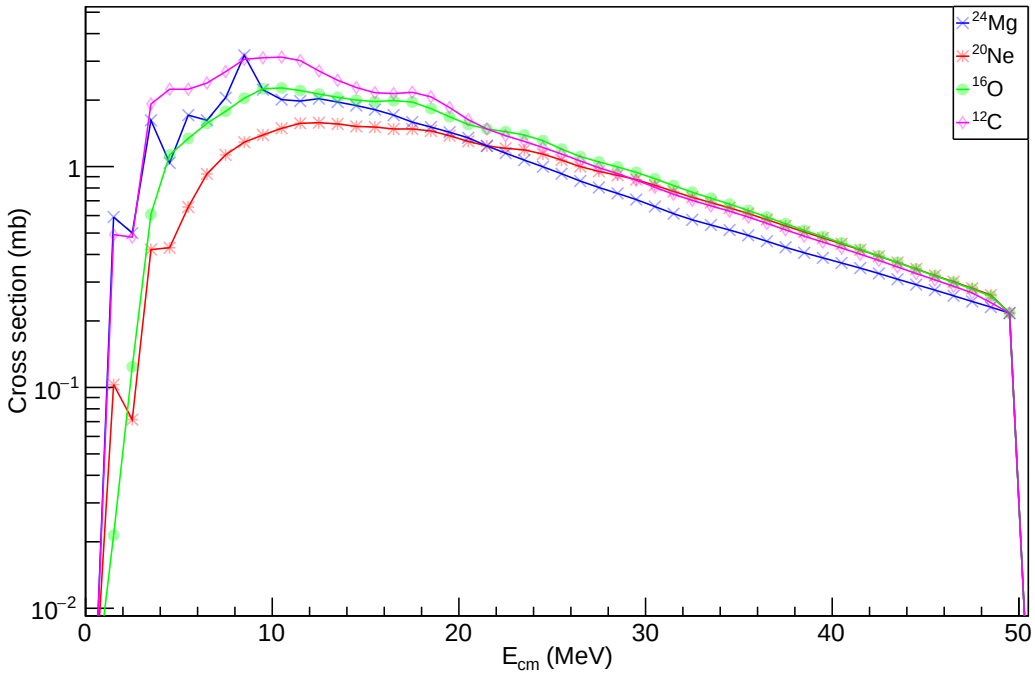

Figure 5.19: α-particle energies in the centre-of-mass as predicted from the EHF following the population of different α-conjugate nuclei for $E_b = 400$ MeV.

5.2.2 Fermi break-up model calculations

In addition to the EHF calculations, Fermi break-up model calculations were performed to investigate the splitting of the compound nucleus into a system of α-conjugate nuclei. This calculation is driven by modeling the decay according to Fermi's golden rule [129]:

$$R_{if} = \frac{2\pi}{\hbar}|A|^2\omega_f, \tag{5.7}$$

with $|A|^2$ corresponding to the transition matrix between the initial state i and the final state f. The important factor in the Fermi break-up calculations originates from the ω_f term which describes the density of states. One can then describe the phase space available for a decay of the system of mass number A into n fragments by:

$$\omega_{if} = \prod_{b=1}^{n}(2s_b+1)\prod_{j=1}^{k}\frac{1}{n_j!}\left(\frac{r_0^3 A}{6\pi^2\hbar^3}\right)^{n-1}\left(\frac{1}{\sum_{b=1}^{n}m_b}\prod_{b=1}^{n}m_b\right)^{\frac{3}{2}}\frac{(2\pi)^{3(n-1)/2}}{\Gamma(3(n-1)/2)}E_{\text{kin}}^{3n/2-5/2}, \tag{5.8}$$

with s_b being the spin of particle b and n_j is the number of particles of type j. There is a very strong dependence therefore on n, particularly in the term $\left(\frac{r_0^3 A}{6\pi^2\hbar^3}\right)^{n-1}$ which describes the partition of the phase space of the decay. Additionally, the energy available in the decay also provides a very large density of states for large n decays. For a break-up of a system into 7-α, one generates an 8^{th} power dependence on the kinematically available energy. This is usually offset by a correspondingly smaller energy available for higher multiplicity decays. For a decay to provide 1 α-particle, 10.0 MeV is needed to break-up the system whereas for 7-α particles one requires 38.5 MeV. Therefore, for a state decaying with an excitation energy of $\sim$ 40 MeV, the small available energy is therefore prohibitive to the 7-α break-up and preferential towards a smaller n break-up.

Decay path	**Break-up particles**	**α-particles**
^{24}Mg + α	2	1
^{20}Ne + ^{8}Be	2	2
^{16}O + ^{12}C	2	0
^{16}O + ^{12}C(0_2^+)	2	3
^{20}Ne + α + α	3	2
^{16}O + ^{8}Be + α	3	3
^{12}C + ^{12}C + α	3	1
^{12}C(0_2^+) + ^{12}C(0_2^+) + α	3	7
^{12}C + ^{8}Be + ^{8}Be	3	4
^{12}C(0_2^+) + ^{8}Be + ^{8}Be	3	7
^{12}C + ^{8}Be + α + α	4	4
^{12}C(0_2^+) + ^{8}Be + α + α	4	7
^{8}Be + ^{8}Be + ^{8}Be + α	4	7
^{16}O + α + α + α	4	3
^{12}C + α + α + α + α	5	3
^{12}C(0_2^+) + α + α + α + α	5	3
^{8}Be + α + α + α + α + α	6	7
α + α + α + α + α + α + α	7	7

Table 5.2: α-conjugate Fermi break-up modes.

An additionally important factor is the permutation factor - $\prod_{j=1}^{k} \frac{1}{n_j!}$ which avoids multiple counting of possible final states. If one has a system of n identical particles, one must therefore divide the total phase space by $n!$ as allocating a state ϕ_1 to particle 1, ϕ_2 to particle 2, ϕ_n to particle n etc. is identical to allocating state ϕ_1 to particle n, ϕ_2 to particle $n-1$ etc.

Using this Fermi break-up formulation, the available phase space for different 2, 3, 4, 5, 6 and 7 body decays was examined using a code provided by M. Freer [130]. Initial investigations were limited to α-conjugate nuclei which are expected to dominate the phase space by virtue of their favourable Q-values, however many other n body partitions are also available. By investigating partitions that can be constructed from α-condensed states, one can use the idea that the transition matrix to all these states is identical allowing a direct comparison [84]. This means, taking Eq. 5.7, a direct comparison can be made between the phase space calculated and the rate R_{if} which gives the yield by taking $|M_{if}|^2$ to be equal for all channels.

One can also demonstrate in the Fermi break-up model that the 2-body phase space is considerably smaller than $n > 2$ body phase space. Taking the ratio of all binary fissions from the compound nucleus and dividing by the phase space from all the α-conjugate decay break-up paths gives a value of $\mathbf{0.02}\%$ for the 400 MeV data. This conclusion is in agreement with that seen experimentally (to be discussed in Chapter 5.3.1) where the binary scission is shown to be of extremely limited importance given that the measured nuclei did not reproduce the correct Q-value when the missing particle was reconstructed (apart from a small contribution from ^{18}F). Figure 5.20 shows the phase space for the different decay paths shown in Table 5.2 against the number of break-up particles. The preference towards a higher multiplicity break-up at higher energies can clearly be seen. Similarly, one can also see that the high α-particle multiplicity reactions have a much larger phase space than the paths to several ground state nuclei. The 7-α final states comprise of 40 %, 76 % and 89 % of the total phase spaces calculated in Table 5.2 for E_b = 160, 280 and 400 MeV respectively.

To allow for a prediction of the observed 7-α decay paths, one can use these Fermi break-up calculations in tandem with the Monte Carlo simulation (to be discussed in Chapter 5.2.3) which demonstrate the efficiency for each of these different paths. Some of the Monte Carlo paths correspond to a similar final state partition of particles in Table 5.2 therefore the path with the highest efficiency was chosen. This is to avoid the shortcoming of the Monte Carlo simulations in this situation where the process modelled is sequential decay rather than a non-sequential n-body break-up. These two processes however both generate an isotropic spray of particles in the COM therefore they should be comparable. One decay path, $^8\mathrm{Be} + \alpha + \alpha + \alpha + \alpha + \alpha$ which does not correspond to a modelled decay path was nonetheless given the same efficiency as the $^{12}\mathrm{C}(0_2^+) + \alpha + \alpha + \alpha + \alpha$ as these processes are extremely similar. For a prediction of the partitions for the different final states particles, the phase space for each ω_f was

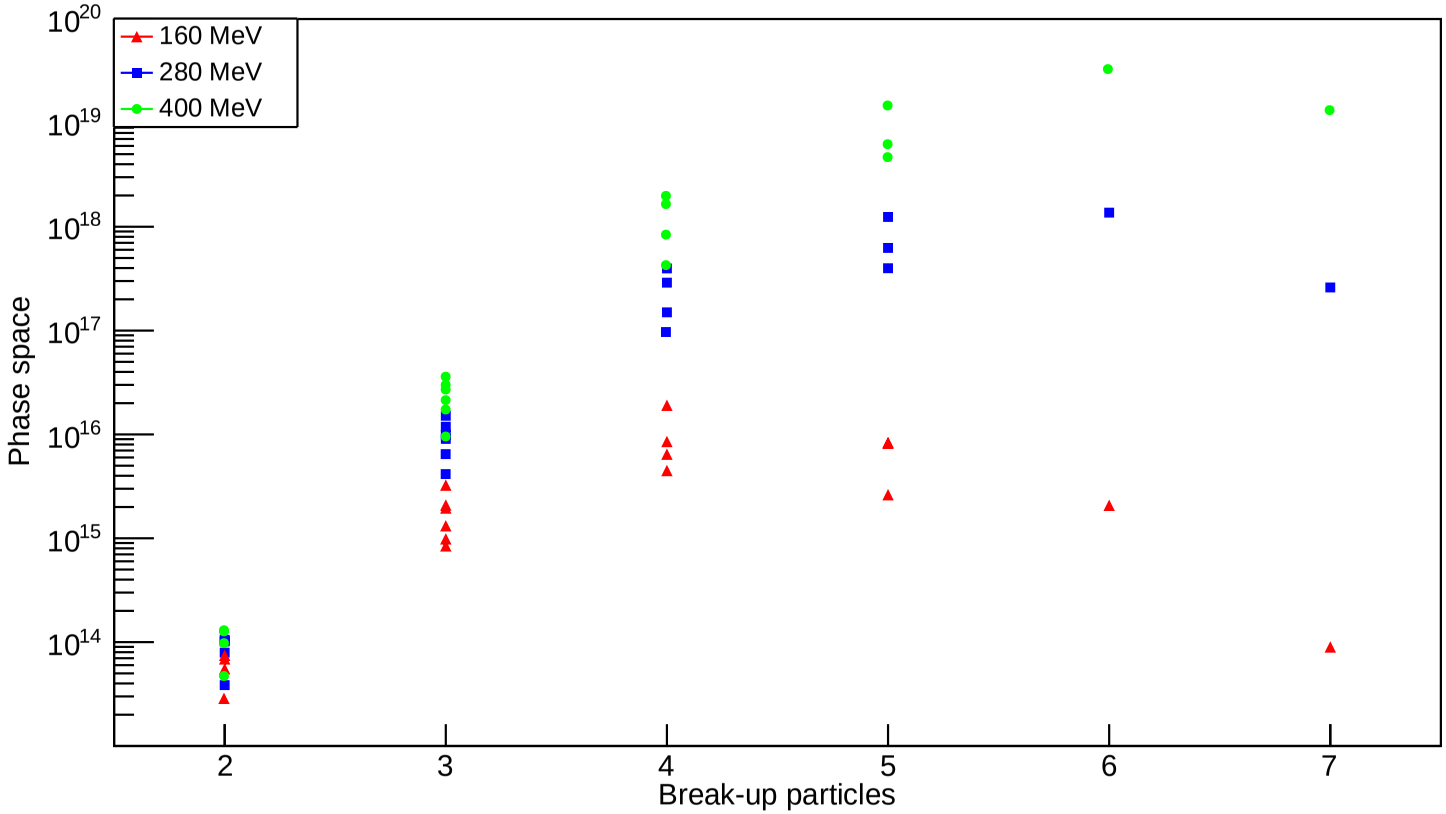

Figure 5.20: Phase space for the different α-conjugate decay paths at the three beam energies plotted against the number of break-up particles. These predictions calculate a larger multiplicity of particles emitted than those the from the statistical decay model (Figure 5.7).

multiplied by the efficiency for that decay path, ϵ_f including all detector effects to be discussed in Chapter 5.2.3. The percentage predicted for the final state f is then given by:

$$\Gamma_f = \frac{\omega_f \epsilon_f}{\sum_i \omega_i \epsilon_i} \tag{5.9}$$

which ensures the sum of the decay paths then sums to 100 %. The results for the three beam energies can be seen in Table 5.10 and are discussed in Chapter 5.7.

5.2.3 Monte Carlo Simulations

To validate the code used to analyse the data, as well as to properly model the detector response (efficiency and resolution), a Monte Carlo (MC) simulation was performed. A Monte Carlo is a widely used algorithm to randomly sample a large number of "what if" scenarios. In this instance, the Monte Carlo simulation modelled the break-up of the compound nucleus into the chosen excitation ranges/energy levels. Additionally, detector effects such as energy resolution, angular resolution and energy thresholds were introduced.

The package *RESOLUTION8.1* was used for this purpose as developed by N. Curtis [131][132]. The Monte Carlo allows for the generation of multi-stage break-up reactions to be simulated. It is possible to simulate all detector effects within the code however to properly simulate the unique nature of the CHIMERA detector array (by virtue of its large number of detectors and unusual shape which is not currently available in the *RESOLUTION8.1* package) this option was not utilised and the truth level momentum vectors for all particles were read in to the code. A modification to the code was made to accomodate the needs of the current analysis and apply the detector effects specific to the CHIMERA detector array. The momentum vector was then smeared according to the CHIMERA ring's angular and energy resolution given by the form seen in Figure 4.24. These hits were then further analysed if the telescope that was hit was working and the signal is above the threshold for the specific telescope. From setting the pedestal and from the energy calibration, the threshold was known for each telescope and therefore whether the hit would register (either in both the Si and CsI(Tl) or just in the Si for the case of $E_\alpha < 24$ MeV) was known for each particle. This threshold was extremely stable throughout the experiment and differed by less than 1%. This threshold is fairly constant with angle therefore removing a possible source of systematic effects.

Label	Path
1	$^{24}\mathrm{Mg}^{\star} + \alpha \rightarrow ^{20}\mathrm{Ne}^{\star} + \alpha \rightarrow ^{16}\mathrm{O}^{\star} + \alpha \rightarrow ^{12}\mathrm{C}^{\star} + \alpha \rightarrow ^{8}\mathrm{Be} + \alpha$
2	$^{24}\mathrm{Mg}^{\star} + \alpha \rightarrow ^{20}\mathrm{Ne}^{\star} + \alpha \rightarrow ^{16}\mathrm{O}^{\star} + \alpha \rightarrow ^{8}\mathrm{Be} + ^{8}\mathrm{Be}$
3	$^{24}\mathrm{Mg}^{\star} + \alpha \rightarrow ^{20}\mathrm{Ne}^{\star} + \alpha \rightarrow ^{12}\mathrm{C}^{\star} + ^{8}\mathrm{Be} \rightarrow ^{8}\mathrm{Be} + \alpha$
4	$^{24}\mathrm{Mg}^{\star} + \alpha \rightarrow ^{16}\mathrm{O}^{\star} + ^{8}\mathrm{Be} \rightarrow ^{12}\mathrm{C}^{\star} + \alpha \rightarrow ^{8}\mathrm{Be} + \alpha$
5	$^{24}\mathrm{Mg}^{\star} + \alpha \rightarrow ^{16}\mathrm{O}^{\star} + ^{8}\mathrm{Be} \rightarrow ^{8}\mathrm{Be} + ^{8}\mathrm{Be}$
6	$^{24}\mathrm{Mg}^{\star} + \alpha \rightarrow ^{12}\mathrm{C}^{\star} + ^{12}\mathrm{C}^{\star} \rightarrow ^{8}\mathrm{Be} + ^{8}\mathrm{Be}$
7	$^{20}\mathrm{Ne}^{\star} + ^{8}\mathrm{Be} \rightarrow ^{16}\mathrm{O}^{\star} + \alpha \rightarrow ^{12}\mathrm{C}^{\star} + \alpha \rightarrow ^{8}\mathrm{Be} + \alpha$
8	$^{20}\mathrm{Ne}^{\star} + ^{8}\mathrm{Be} \rightarrow ^{16}\mathrm{O}^{\star} + \alpha \rightarrow ^{8}\mathrm{Be} + ^{8}\mathrm{Be}$
9	$^{20}\mathrm{Ne}^{\star} + ^{8}\mathrm{Be} \rightarrow ^{12}\mathrm{C}^{\star} + ^{8}\mathrm{Be} \rightarrow ^{8}\mathrm{Be} + \alpha$
10	$^{16}\mathrm{O}^{\star} + ^{12}\mathrm{C}^{\star} \rightarrow (^{12}\mathrm{C}^{\star} + \alpha) + (^{8}\mathrm{Be} + \alpha) \rightarrow ^{8}\mathrm{Be} + \alpha$
11	$^{16}\mathrm{O}^{\star} + ^{12}\mathrm{C}^{\star} \rightarrow (^{8}\mathrm{Be} + ^{8}\mathrm{Be}) + (^{8}\mathrm{Be} + \alpha)$

Table 5.3: Different decay paths through α-gas type states until the system has decayed to ^{8}Be or an α-particle.

Pileup particles in a single detector can also be treated accordingly, in particular looking at 2 α-particles hitting a single detector although these were shown to constitute a small fraction of the total events. These events correspond to high-energy ^{8}Be break-up events which are of importance in the current analysis. As 7-α events are those that are of interest, 11 different decay paths through the α-conjugate nuclei can be simulated. These are listed in Table 5.3. As the states of interest are near-threshold states, the excitation energies populated are taken as the expected N-α gas states. These energies are tabulated in Table 5.4 and where experimental or theoretical calculations have not predicted an energy, a linear increase in energy above threshold with the number of α-particles in the system ($E_x(\mathrm{N}\alpha) = E_{\mathrm{thr}} + 0.284\mathrm{N} - 0.475$ MeV) was used. The value for ^{24}Mg is increased by 300 keV from this formula to 30.0 MeV to accommodate the decay to $^{12}\mathrm{C}(0_2^+)+^{12}\mathrm{C}(0_2^+)$. In addition, break-up in the continuum was also modelled. Here nuclei were allowed to occupy any kinematically allowed excitation energy rather than the near α-threshold states with an even weighting. These simulations will be compared and contrasted to the experimental results throughout this chapter.

5.3 Data analysis

In order to better understand the reaction mechanisms involved in the $^{12}\mathrm{C}(^{16}\mathrm{O},^{28}\mathrm{Si}^{\star})$ reaction, one can first look at the particle yields in the low-angle FARCOS detectors. Its

Nucleus	E_x (MeV)
^{8}Be	0.0
^{12}C	7.65
^{16}O	15.1
^{20}Ne	20.1
^{24}Mg	30.0

Table 5.4: Excitation energies used in the Monte Carlo for α-condensates in the first α-conjugate nuclei.

superior energy and position resolution allows for an investigation into whether these particles originate from a direct reaction or from sequential decay.

5.3.1 FARCOS particle yields

The three beam energies show different particle yields (shown in Figures 5.21, 5.23 and 5.24), mainly as a result of the lower excitation energy of the compound nucleus due to the change in beam energy. Two-body decays from a higher initial excitation energy are much more likely to produce daughter nuclei with an excitation energy above their particle decay thresholds therefore undergoing secondary decay processes. Additionally, as the energy of the system increases, the phase space for 3 body decays becomes significantly larger. To examine this, one can firstly examine the data taken with a beam energy (E_b) of 400 MeV.

^{12}C(^{16}O,^{28}Si*), $\mathbf{E_b = 400}$ MeV

At these low angles ($\theta_{\text{lab}} < 8^{\circ}$), a vast array of nuclei can be seen using the dE-E PID (see Figure 5.21). In particular, ^{4}He, ^{12}C and ^{16}O are all seen to be strong. By virtue of their strong binding-energies, it may be energetically favourable to emit these nuclei in favour of other (heavier) products.

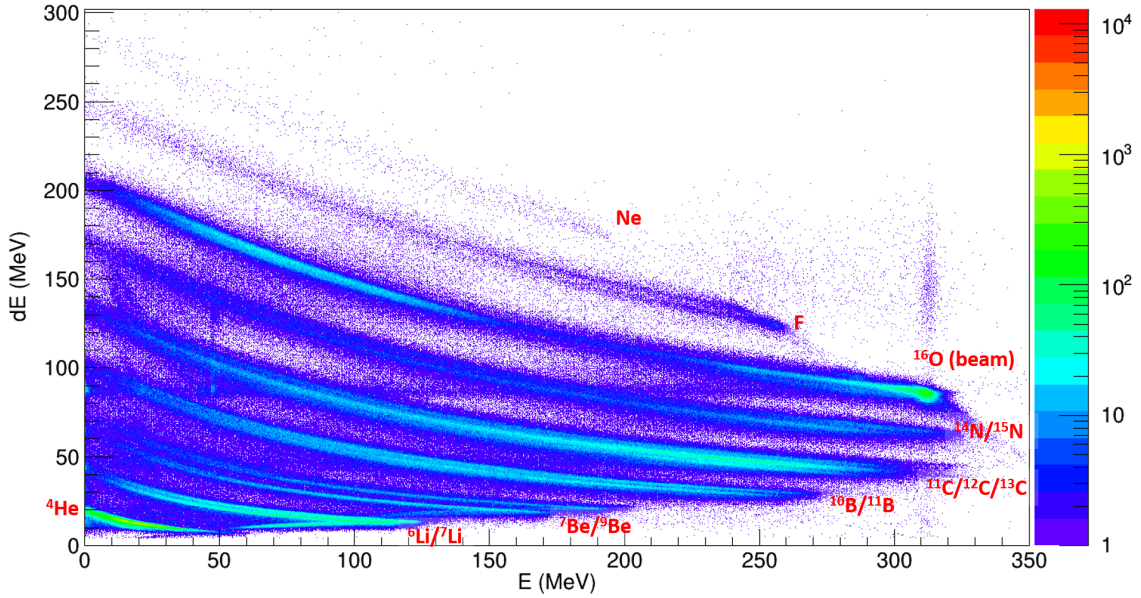

Figure 5.21: Yields in the FARCOS detector for a beam energy of 400 MeV

Yields are also seen from nuclei heavier than the beam. These demonstrate that the physics observed is not solely from a break-up of the beam. By observing fluorine-18 and reconstructing the missing momentum corresponding to ^{10}B, one can see that the ^{18}F arises from a direct reaction as the Q-value of -17.7 MeV is reproduced corresponding to around 1/3 of the total measured particles.

This Q-value is calculated by:

$$\vec{P}_{\text{missing}} = \vec{P}_{\text{beam}} - \vec{P}_{\text{detected}} \tag{5.10}$$

$$Q = \frac{\vec{P}_{\text{missing}}.\vec{P}_{\text{missing}}}{2m_{\text{missing}}} + E_{\text{detected}} - E_{\text{beam}} \tag{5.11}$$

Being potentially populated via an $\ell = 2$ deuteron transfer with a large Q-value, the maximum cross section for this reaction is pushed out to larger angles [133] hence can be observed in the FARCOS detectors over other contributions. Apart from the ^{12}C and ^{16}O measured, the other reaction products do not originate from a direct reaction as their Q-values vastly differ from those expected from a simple break-up.

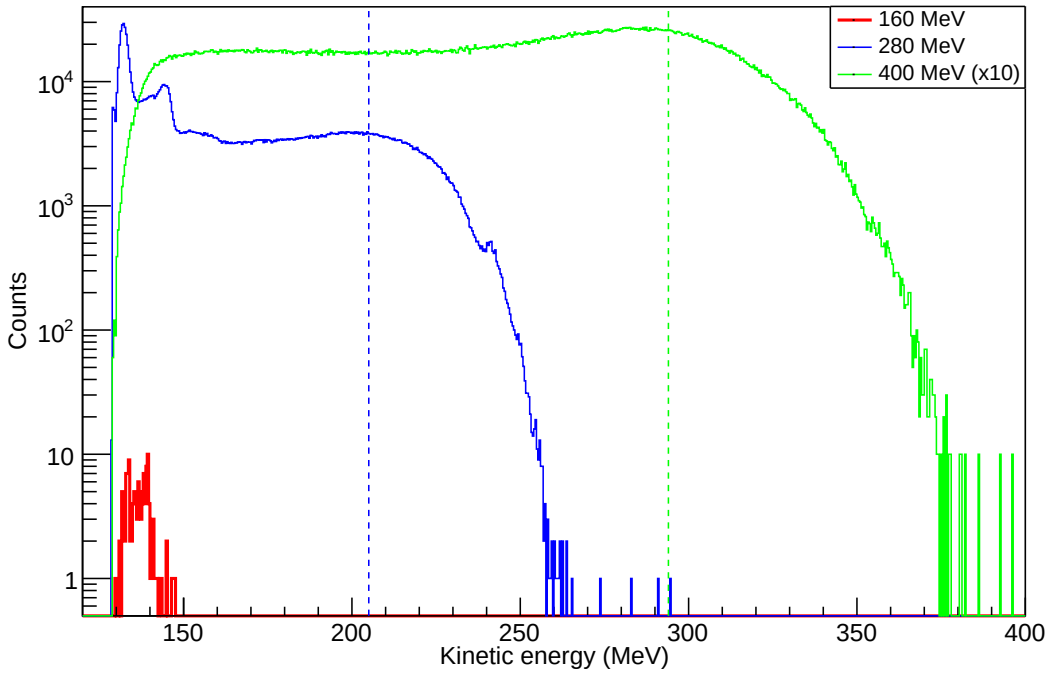

Figure 5.22: Comparison of the ^{12}C kinetic energy for the three beam energies. Also shown by a dashed line is the energy one would expect from a break-up of the beam into $^{12}\mathrm{C} + \alpha$ - given by $E_b \frac{m_C}{m_O}$. The line for 160 MeV is omitted as this is below the threshold for ^{12}C dE-E PID.

An additional reaction which may occur is the break-up of the beam. One can analyse this possibility by looking at the kinetic energy of the ^{12}C which may arises from a break-up of ^{16}O. A larger yield would be expected at $E_b \frac{m_C}{m_O}$ as the ^{12}C and α share the beam energy while conserving momentum. The results for the kinetic energy of ^{12}C can be seen in Figure 5.22. While this value coincides with a maximum in the kinetic energy plot, the distribution is very broad and is not the expected signature for the beam breaking up.

^{12}C(^{16}O,^{28}Si*), $\mathbf{E_b = 280}$ MeV

The results for the 280 MeV data collected also show a large swathe of particles produced (see Figure 5.23). In particular, the ^{12}C and ^{16}O loci can be seen to be strong as well as an extremely strong ^{4}He contribution. Examining the sources of these products demonstrates that as with the 400 MeV data, the ^{10}B has a small component ($< 5 \times 10^{-3}\%$) which shows the correct Q-value of -17.7 MeV suggesting a direct

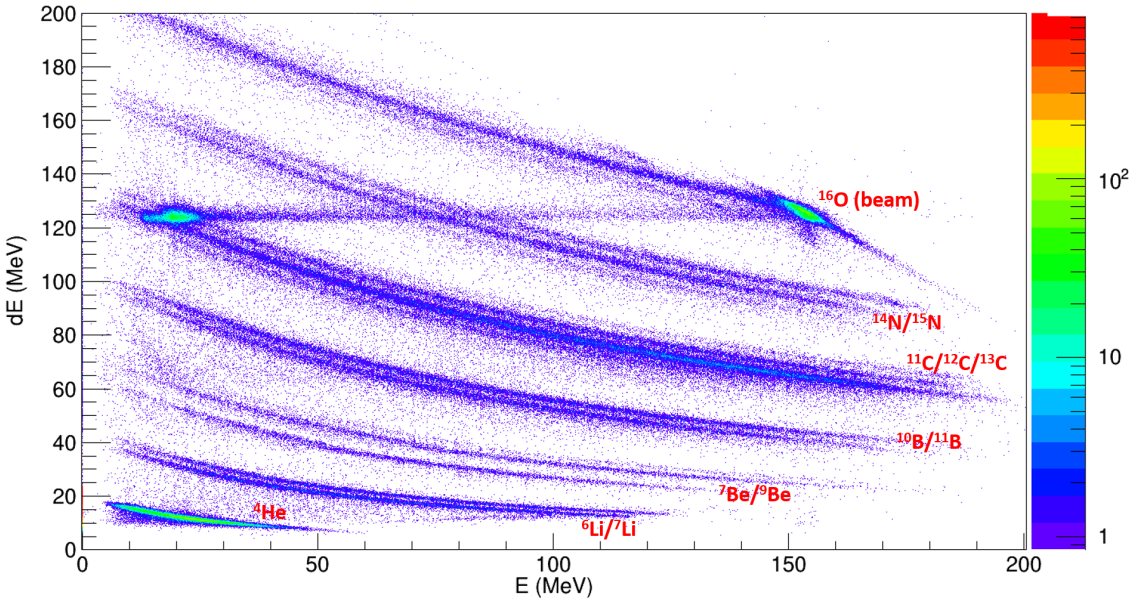

Figure 5.23: Yields in the FARCOS detector for a beam energy of 280 MeV. The horizontal band arises from pileup of the elastically scattered beam and another particle.

component for ^{10}B+^{18}F reaction at this beam energy. In the 280 MeV data however, the ^{10}B is the detected particle compared to the ^{18}F being measured in the 400 MeV data. The ^{12}C and ^{16}O are the only other nuclei measured in FARCOS that correspond to a direct decay.

For possible beam break-up, one would expect an increase in the ^{12}C energy around 205 MeV. The ^{12}C kinetic energy plot can be seen in Figure 5.22 where no increased yield can be seen here suggesting no direct beam break-up. The peak at 145 MeV is due to the effect of the elastically scattered beam pileup with events corresponding to an α-particle which is clearly visible in Figure 5.23.

^{12}C(^{16}O,^{28}Si*), $\mathbf{E_b = 160}$ MeV

As the 160 MeV data are at a lower energy, the results are harder to compare as strong contributions are seen only for He and Li isotopes (see Figure 5.24). Despite nuclei up to ^{10}B being detectable at this beam energy with sufficient energy to provide dE-E PID, only very weak contributions are seen here. The majority of the yield is associated at this small angle with ^{4}He with a small contribution ($\sim$ 3%) from $^{6/7}$Li. The $^{7/9}$Be lines are also visible but this constitutes a negligible contribution ($<$ 0.05%)

at this beam energy.

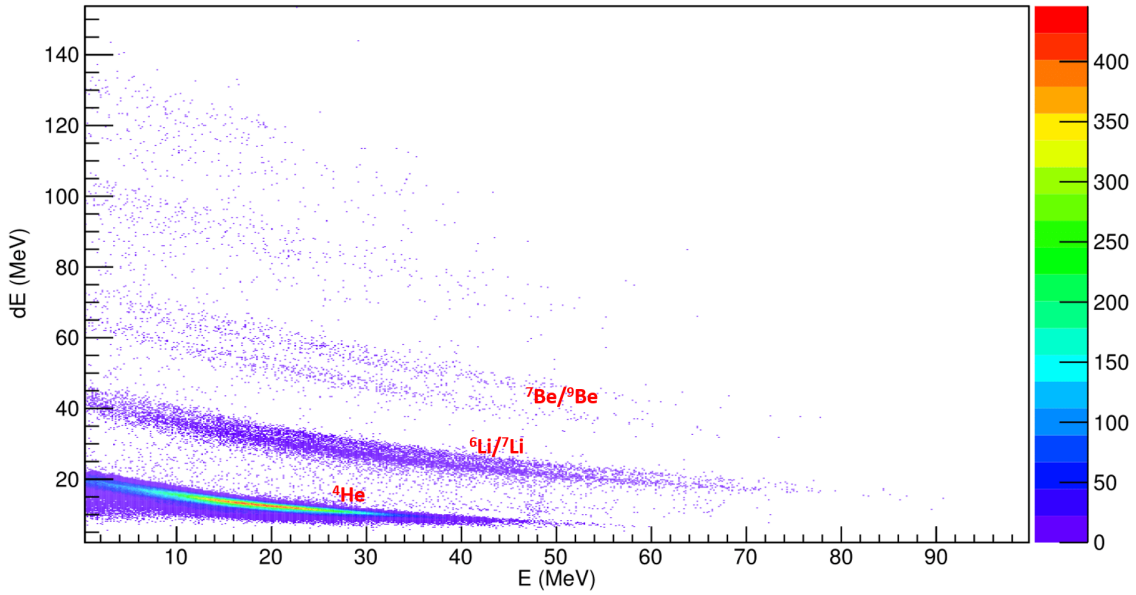

Figure 5.24: Yields in the FARCOS detector for a beam energy of 160 MeV

There is also an extremely small contribution ($< 0.03\%$) from the ^{12}C locus. A large angle elastic scattering event ($< 130°$) is needed to transfer sufficient energy to the ^{12}C for it to have the 134 MeV needed to punchthrough the 300 μm silicon stage. This heavily suggests the contribution seen here is due to the decay of the compound nucleus whereby the beam axis is no longer the preferred direction for decay. Examining the Q-value spectrum from reconstructing these measured particles demonstrates no direct decay component to two ground-state nuclei. Reconstruction of the ^{12}C shows the reconstructed ^{16}O energy lies between 9 and 22 MeV. Examination of the origins of the different α-conjugate nuclei is discussed later in Chapter 5.5.

Beam break-up

Additional investigations of the Q-value spectra of these particles as originating from the break-up of the beam projectile were carried out. This is performed by assuming the projectile continues along the original beam axis and reconstructing the unmeasured particle i.e. measuring ^{12}C and reconstructing the missing α. This demonstrates the measured nuclei do not originate from the beam break-up, as the correct Q-value is not

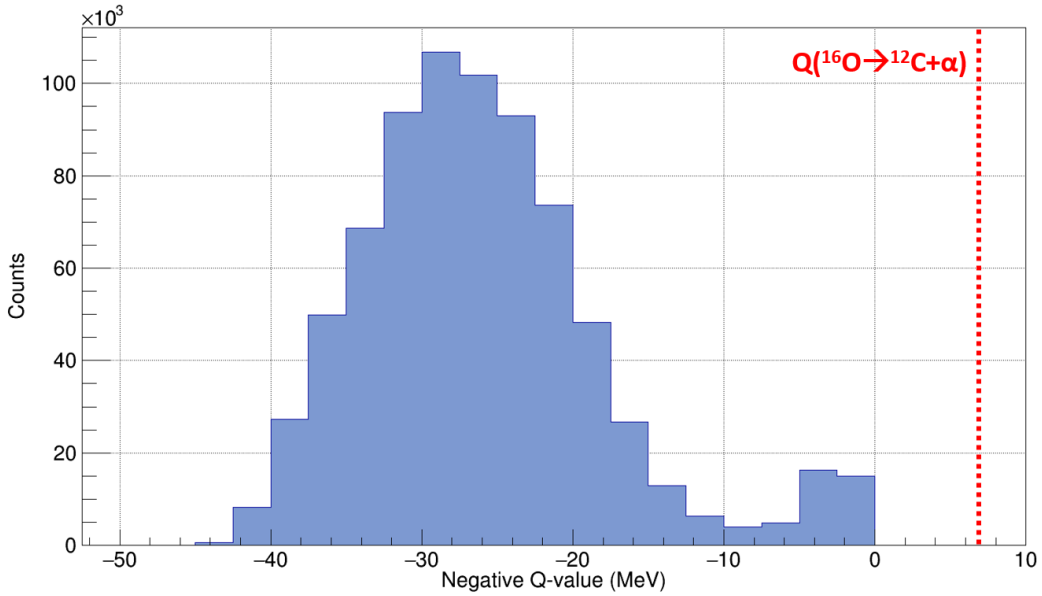

Figure 5.25: Negative Q-value spectrum for the $^{16}\mathrm{O} \rightarrow {}^{12}\mathrm{C} + \alpha$ reaction from the measurement of a $^{4}\mathrm{He}$ in FARCOS. The expected negative Q-value at 7.162 MeV is shown in red.

obtained. An example Q-value spectrum is shown in Figure 5.25 for $^{4}\mathrm{He}$ to test the $^{16}\mathrm{O} \rightarrow {}^{12}\mathrm{C} + \alpha$ beam break-up reaction.

5.3.2 CHIMERA Particle yields

As mentioned above, the experiment was performed at a high incident energy and as such, the probability of compound nucleus formation decreases and the likelihood of direct contributions (transfer, break-up, inelastic scattering) becomes larger. Additionally, the compound nucleus formation is at such high incident energy and angular momentum that a fusion-fission reaction can occur whereby shortly after fusion, the compound nucleus fissions to daughter products. It was shown by examining the yields in the FARCOS detector that direct contributions (break-up and inelastic scattering) were not dominant at these small angles ($\theta_{\mathrm{lab}} < 8°$). In these direct contributions, the decay products are much more forward focused in the centre of mass. One can also demonstrate the non-dominance of these contributions, via an examination of the yield of different products measured in CHIMERA. In a situation whereby the decay products result from the statistical decay of nuclei, the expected distribution is almost

isotropic in the COM. Figures 5.26, 5.28 and 5.30 show the yields of the α-conjugate nuclei against the lab angle after an efficiency correction for broken/missing telescopes for $E_b = 160$, 280 and 400 MeV respectively. The values for this correction are given by the ratio between the total number of telescopes and the number of working telescopes in a given ring in Table 4.1 as well as taking into account the different solid angle as the lab angle changes. The same angular behaviour can be seen for all nuclei suggesting their common source despite the unsmooth corrective factor across different lab angles which differed up to a factor of ~ 3. This factor is only dependent on the yield in a given ring being azimuthally constant and the errors shown are solely statistical errors based on the counting statistics in a ring. This same angular behaviour is also true for the lithium, beryllium and boron isotopes as seen in Figures 5.27, 5.29 and 5.31 in comparison with the ^{4}He nuclei (again for 160, 280 and 400 MeV respectively). The overall yield for the Li, Be and B isotopes is drastically lower than for ^{4}He. There is also a slight bias with angles as some nuclei will be produced below the threshold for silicon punch through, an effect which is enhanced for the lower beam energies (particularly at 160 MeV). For α-particles, ^{12}C(g.s) and ^{16}O(g.s) this is not an issue as TOF particle identification works well for these isotopes but for other nuclei this separation is not possible (due to the indistinguishability of e.g. ^{9}Be, ^{10}B and ^{11}B where the time resolution is insufficient to separate these very similar masses while they are also much more weakly populated than other nuclei). The important feature is only to show rough uniformity in the yields rather than a largely forward focused spray of nuclei or different angular behaviour for different isotopes. This comparison was done using the *PACE4* fusion-evaporation code [134] which allows a prediction of the angular distribution of the different isotopes. As can be seen from Figure 5.32 for $E_b = 400$ MeV, they have very similar behaviour. While this calculation doesn't capture the full reaction mechanisms experienced due to the high initial excitation energy (the initial fission step is omitted), it demonstrates the same approximate angular dependence as seen experimentally.

To elucidate the reaction mechanism, one can also look at the Q-values for different fission modes against the yield. The results in Table 5.5 show a reasonable relation between the Q-value and yield where the reaction products with a lower negative Q-value (^{4}He, ^{8}Be and ^{12}C) are favoured (with the exception of ^{16}O whose yield is consistent with those reaction products with a more negative Q-value). The preference towards well-bound systems (i.e. ^{4}He, ^{12}C and ^{16}O) suggests these particles come from statistical decay processes.

From these yields, one can also see by comparison of the ^{6}Li and ^{7}Li that events

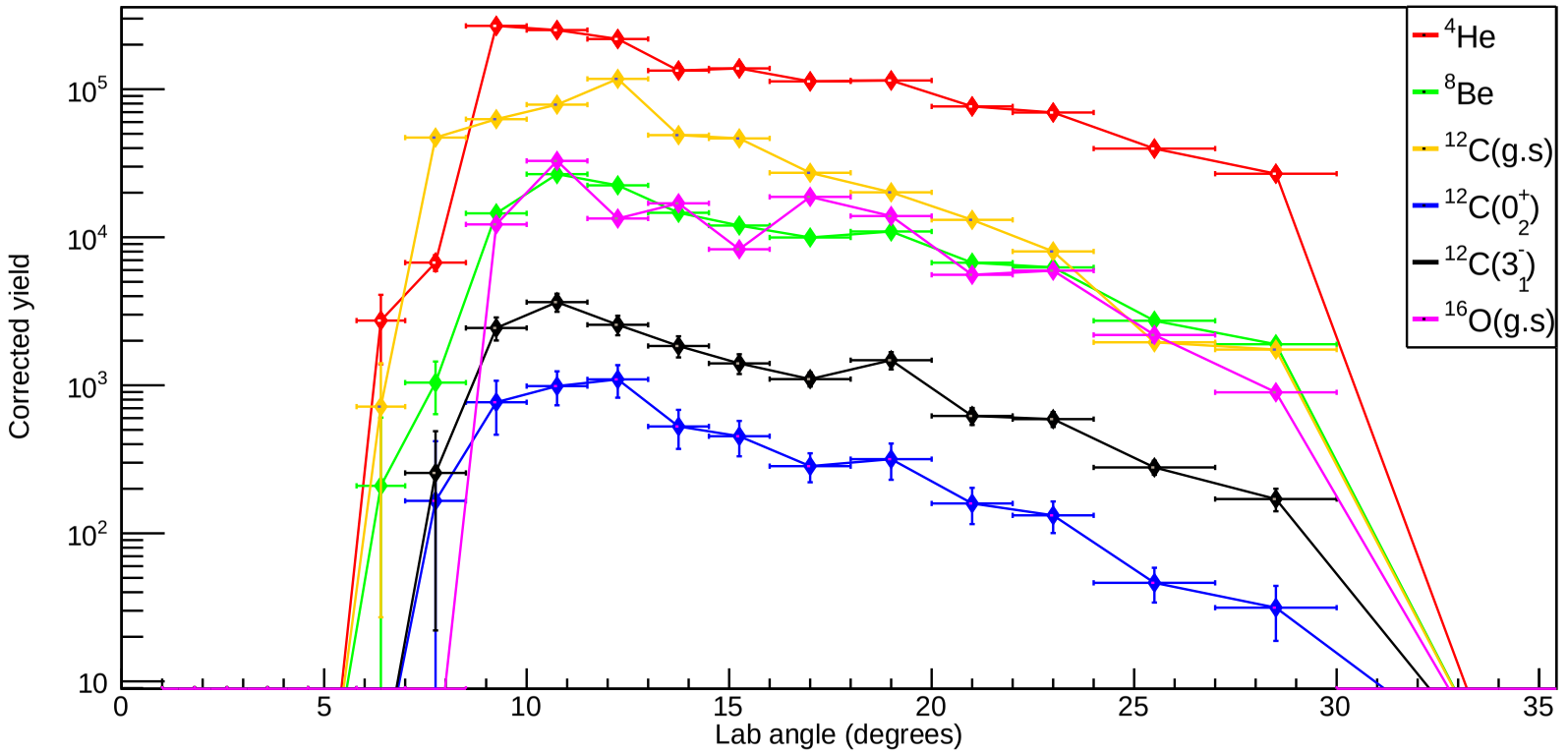

Figure 5.26: Angular dependence of yields of α-conjugate nuclei in the CHIMERA forward rings for $E_b = 160$ MeV.

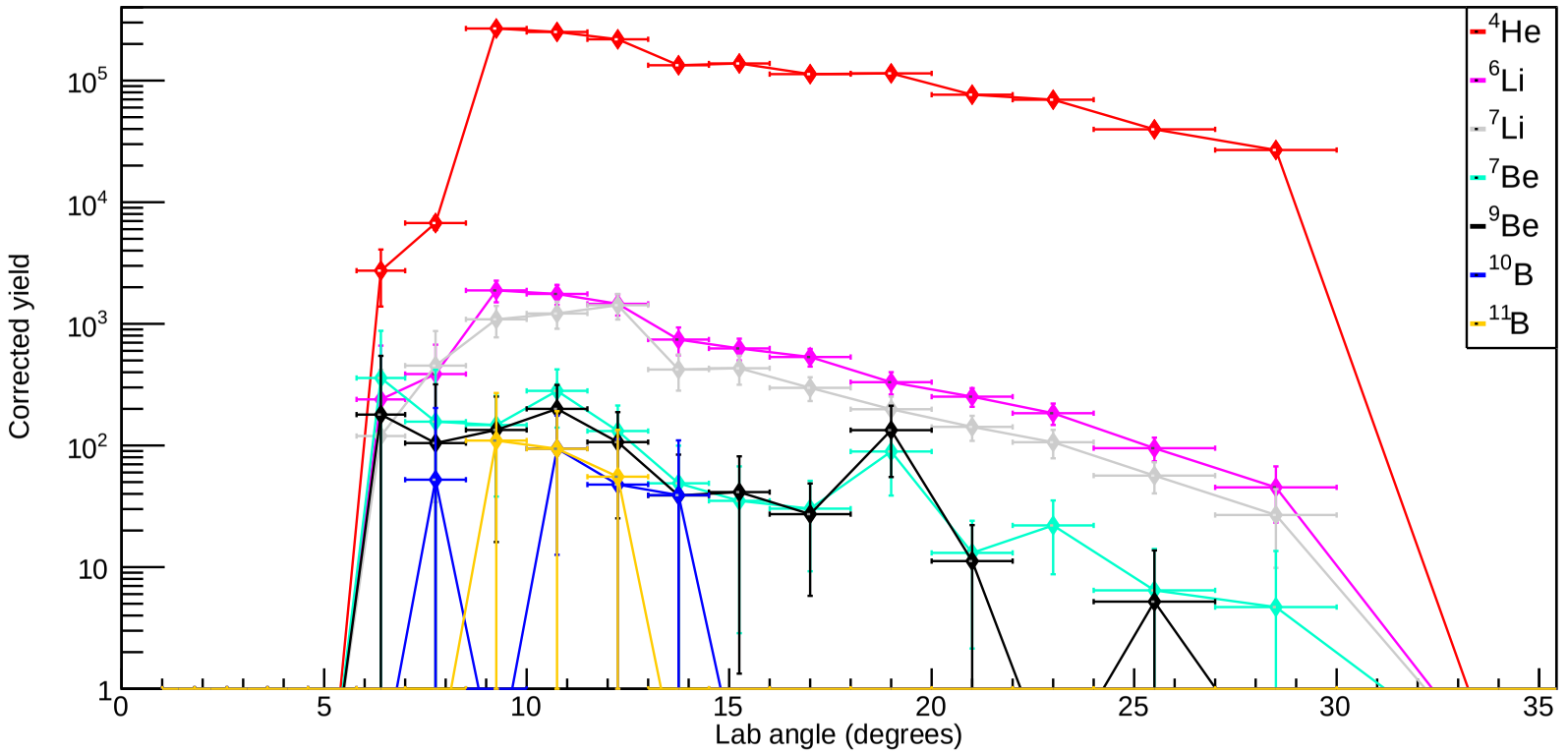

Figure 5.27: Angular dependence of Li, Be, B nuclei in the CHIMERA forward rings compared to ^{4}He for $E_b = 160$ MeV.

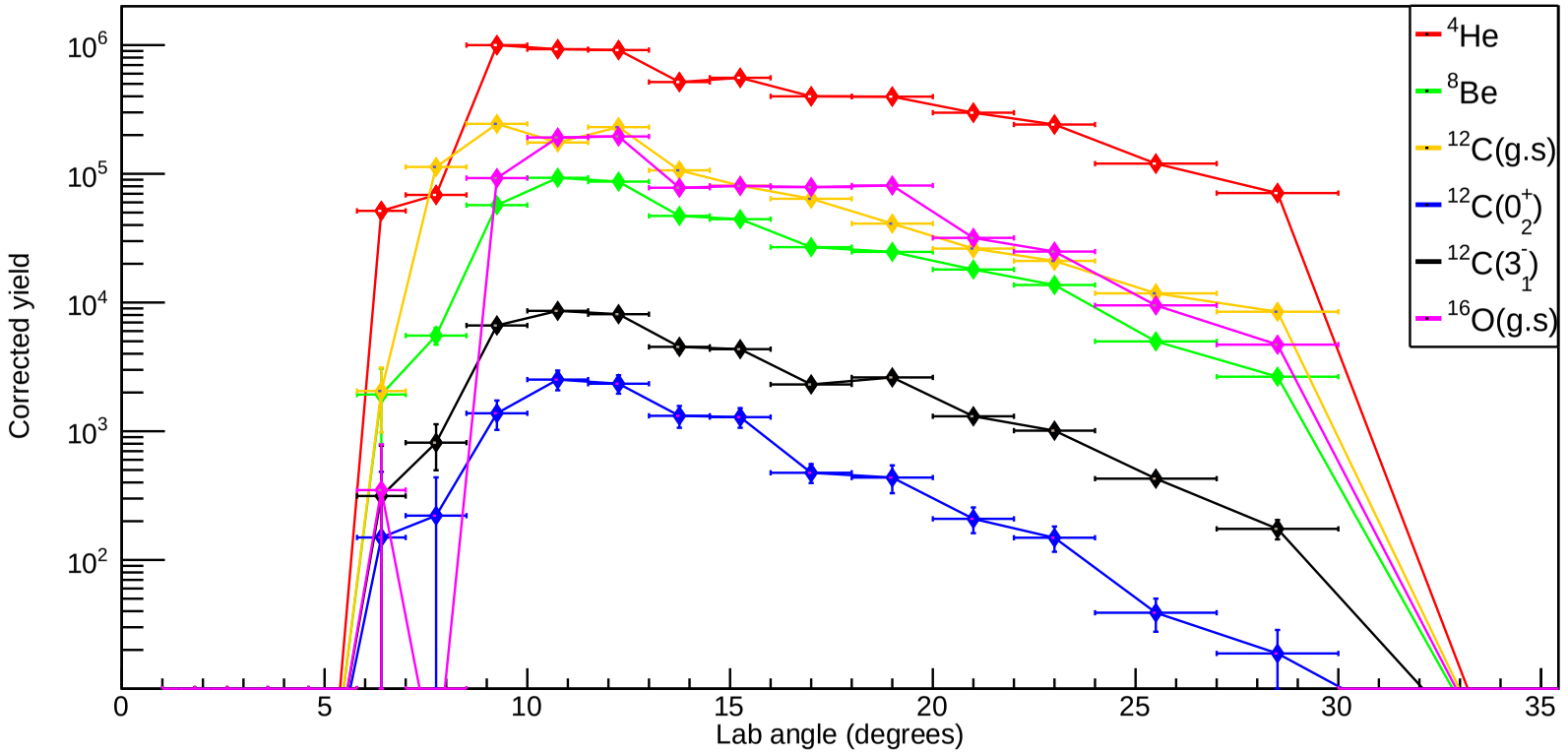

Figure 5.28: Angular dependence of yields of α-conjugate nuclei in the CHIMERA forward rings for $E_b = 280$ MeV.

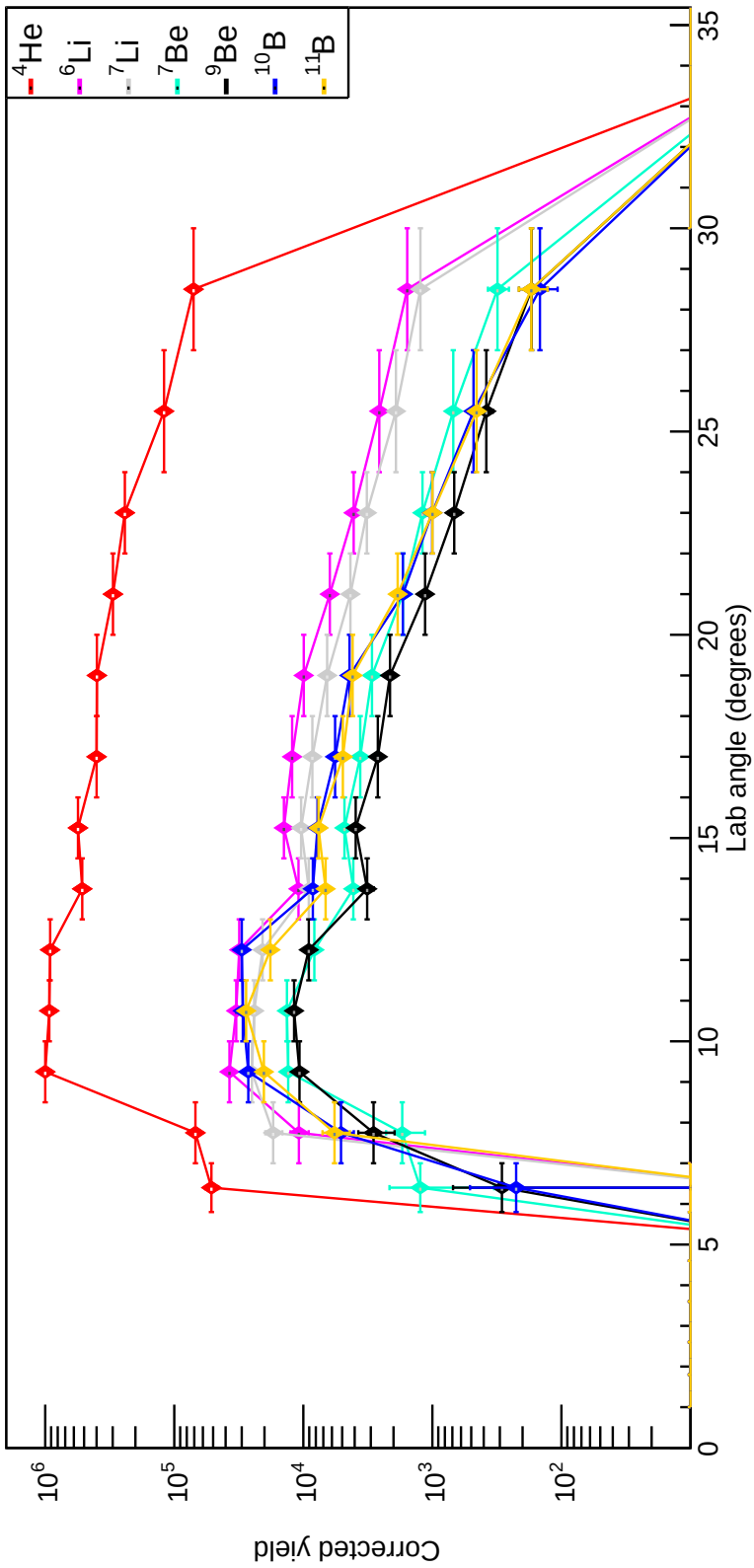

Figure 5.29: Angular dependence of Li, Be, B nuclei in the CHIMERA forward rings compared to ^{4}He for $E_b = 280$ MeV.

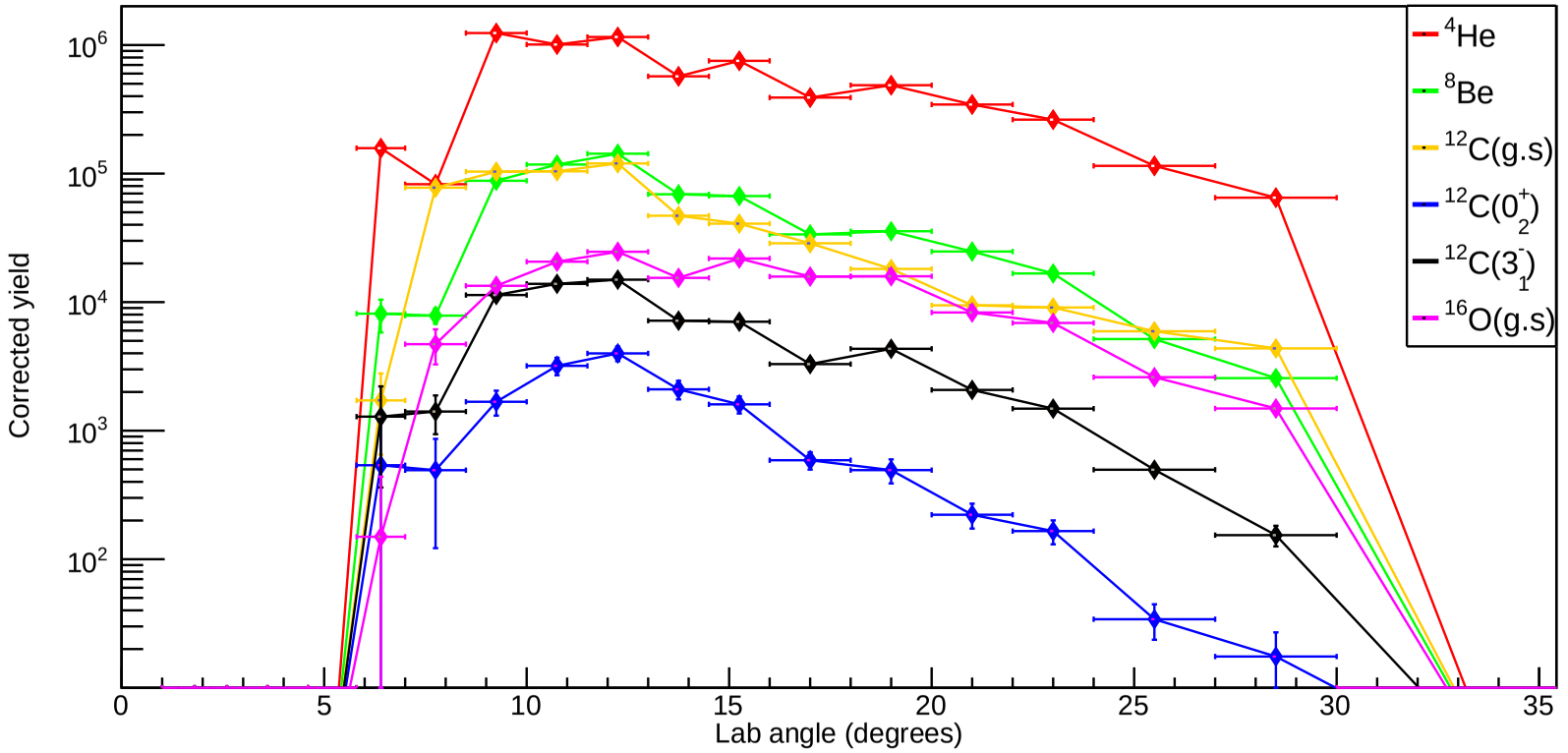

Figure 5.30: Angular dependence of yields of α-conjugate nuclei in the CHIMERA forward rings for $E_b = 400$ MeV.

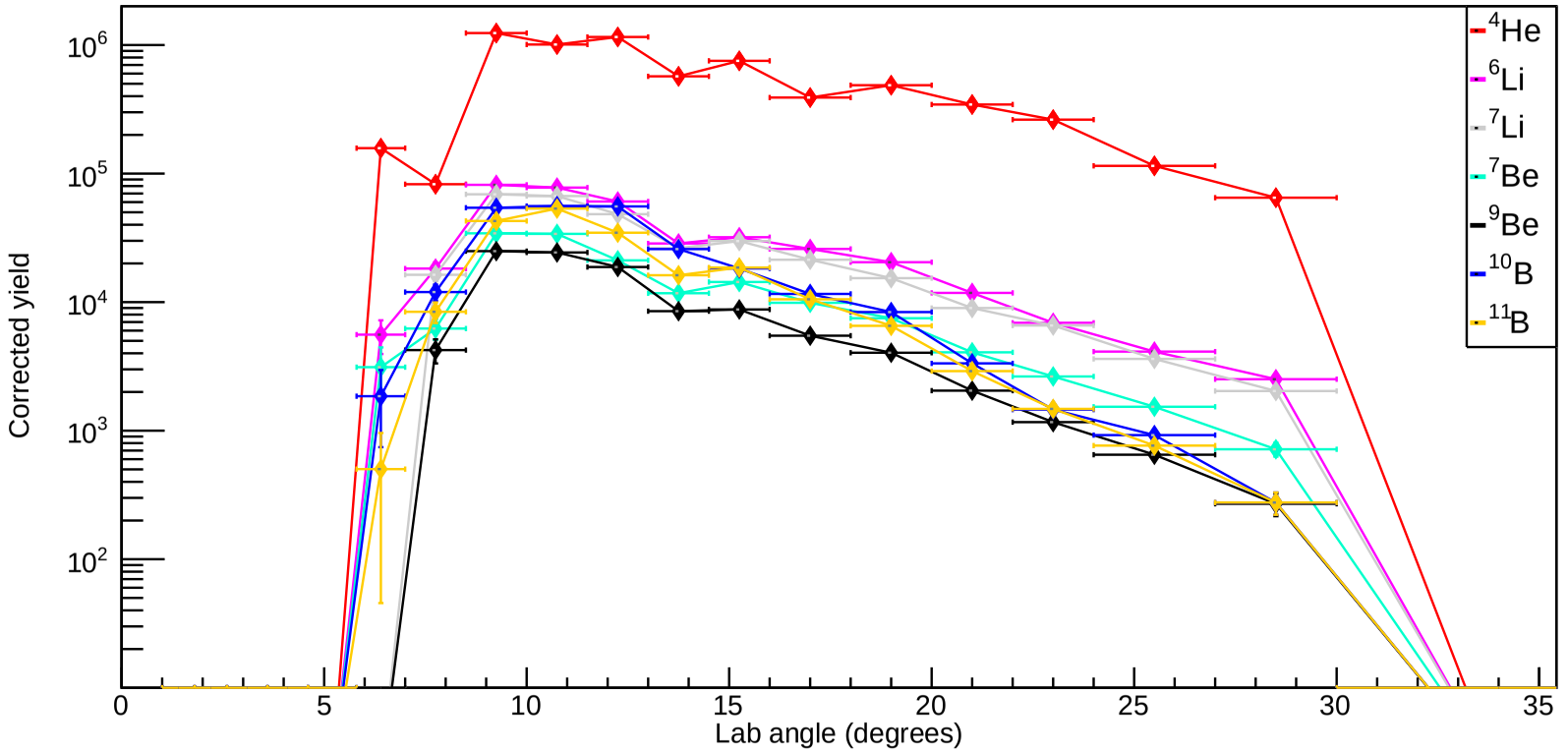

Figure 5.31: Angular dependence of Li, Be, B nuclei in the CHIMERA forward rings compared to ^{4}He for $E_b = 400$ MeV.

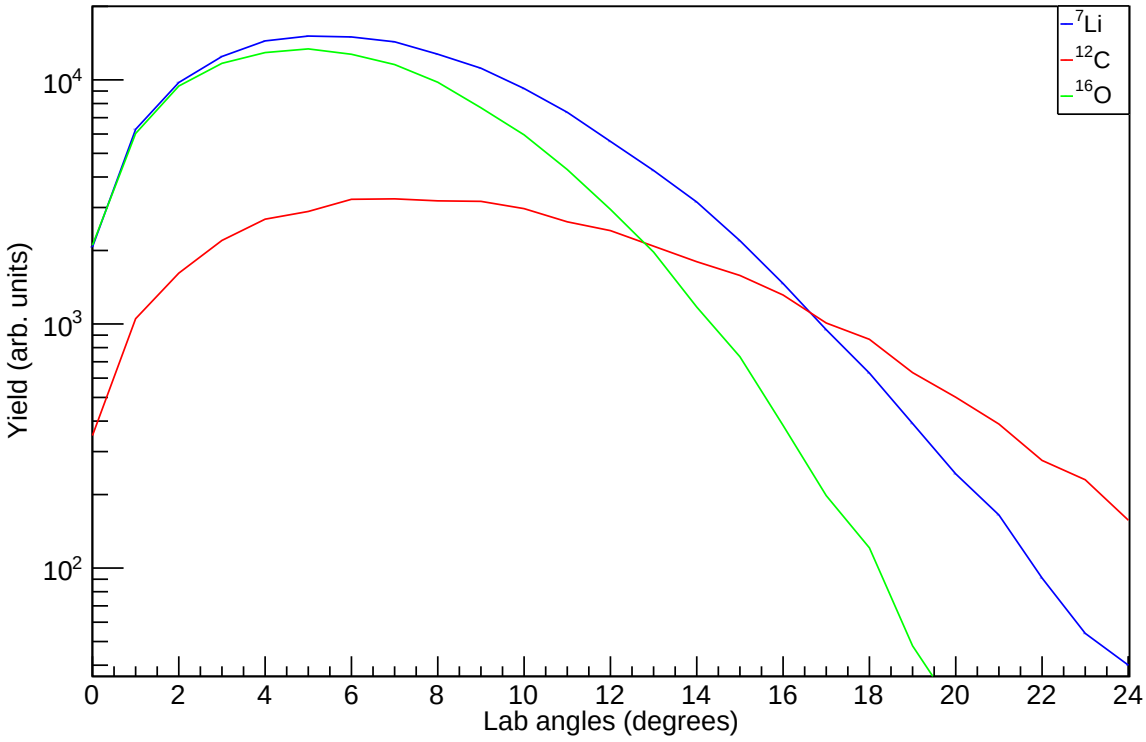

Figure 5.32: Predicted distribution of three different nuclei from a fusion-evaporation code as calculated using *PACE4* for $E_b = 400$ MeV.

Nucleus	Q-value (MeV)	Corrected yield
^{4}He	**-9.984**	**1.3 $\times 10^{6}$**
^{6}Li	-30.398	9.4 $\times 10^{4}$
^{7}Li	-34.215	7.6 $\times 10^{4}$
^{7}Be	-31.530	3.6 $\times 10^{4}$
^{8}Be	**-19.393**	**1.6 $\times 10^{5}$**
^{9}Be	-34.593	2.6 $\times 10^{4}$
^{10}B	-34.417	6.0 $\times 10^{4}$
^{11}B	-32.112	5.3 $\times 10^{4}$
^{12}C	**-16.756**	**1.2 $\times 10^{5}$**
^{16}O	**-16.756**	**2.7 $\times 10^{4}$**

Table 5.5: Experimental population of various scission modes from the compound nucleus against their Q-value for E_b = 400 MeV.

where 2 α-particles hit the same detector do not comprise a large fraction of the data. These 2 α-particles are indistuinguishable from ^{7}Li solely from dE-E PID and the m=7 Li yield is lower that from m=6. The total ^{8}Be yield was seen to be strong therefore suggesting any high energy incident ^{8}Be, where both products would hit a single telescope are very weak in the data.

Comparison of EHF predictions with CHIMERA yields

In order to examine the applicability of the sequential decay model to the data, one can compare the yields from CHIMERA to the predictions from the EHF calculations. The results from this can be seen in Figures 5.33-5.35 where the experimental yields are normalised to the ^{4}He cross section without a correction for missing detectors as discussed above as this correction is identical for all nuclei and is taken into consideration during the normalisation. The errors shown are counting statistics for the different mass nuclei measured, the majority of which are too small to be seen. Any systematic errors are omitted.

For the 160 MeV data, one sees a drastically reduced yield for the non α-conjugate nuclei. In particular, the ^{8}Be yield is far in excess of that predicted from the statistical decay model. Additionally, one expects a large amount of mass 10 and 11 nuclei (^{10}B and ^{11}B) however the data show an extremely small contribution. As discussed in Chapter 5.3.2, this can attributed partially to the effect of the punch through energy required for the boron isotopes and the difficulties associated with TOF PID which

constitute the largest systematic effect. The EHF output does not generate the energy and angle for the decaying particles therefore a correction for this systematic effect was not possible.

Increasing the beam energy to 280 MeV, one sees a much better agreement with the expected yields although once again, the ^{8}Be exceeds the cross section from the EHF model. This is indicative that the data contain additional α-clustering effects compared to the EHF calculations which also explains the reduced yields for the non α-conjugate nuclei as the data are normalised to the α-particle yield.

For the 400 MeV beam energy, the situation is slightly reversed. The observed yields for some non α-conjugate nuclei (m=7 and m=11) exceed those predicted from the EHF code. This discrepancy is reasonably small and suggests a reasonable agreement with the EHF predictions. Once again, the seen ^{8}Be contributions far exceed those expected from the sequential decay model.

Conclusion

It can be seen from these results that the limiting factor for high α-particle emission is not the energy available in the system but as one increases the energy, other decay modes start to be equally preferential. One must therefore ask whether the EHF calculations fall short by not modeling 3-body or above decays as well as heavier particle emissions such as ^{8}Be. As was seen in Chapter 5.2.2, modeling of ^{8}Be is made difficult by the requirement for a global optical potential for ^{8}Be. These models are generated from experimental data usually involving the scattering of the nucleus of interest which, for ^{8}Be given its extremely short half-life, is impossible to achieve experimentally.

Additionally, the EHF code treats the continuum in such a way that ignores the fact that once a nucleus α-decays, continuum states which are α-clustered are more likely to be populated than shell-model like states and therefore a subsequent α-decay is more likely while proton and neutron decays will be impeded. This is treated correctly by a width correction term in some Hauser-Feshbach calculations however drastically increases the computational time necessary for the calculations [135].

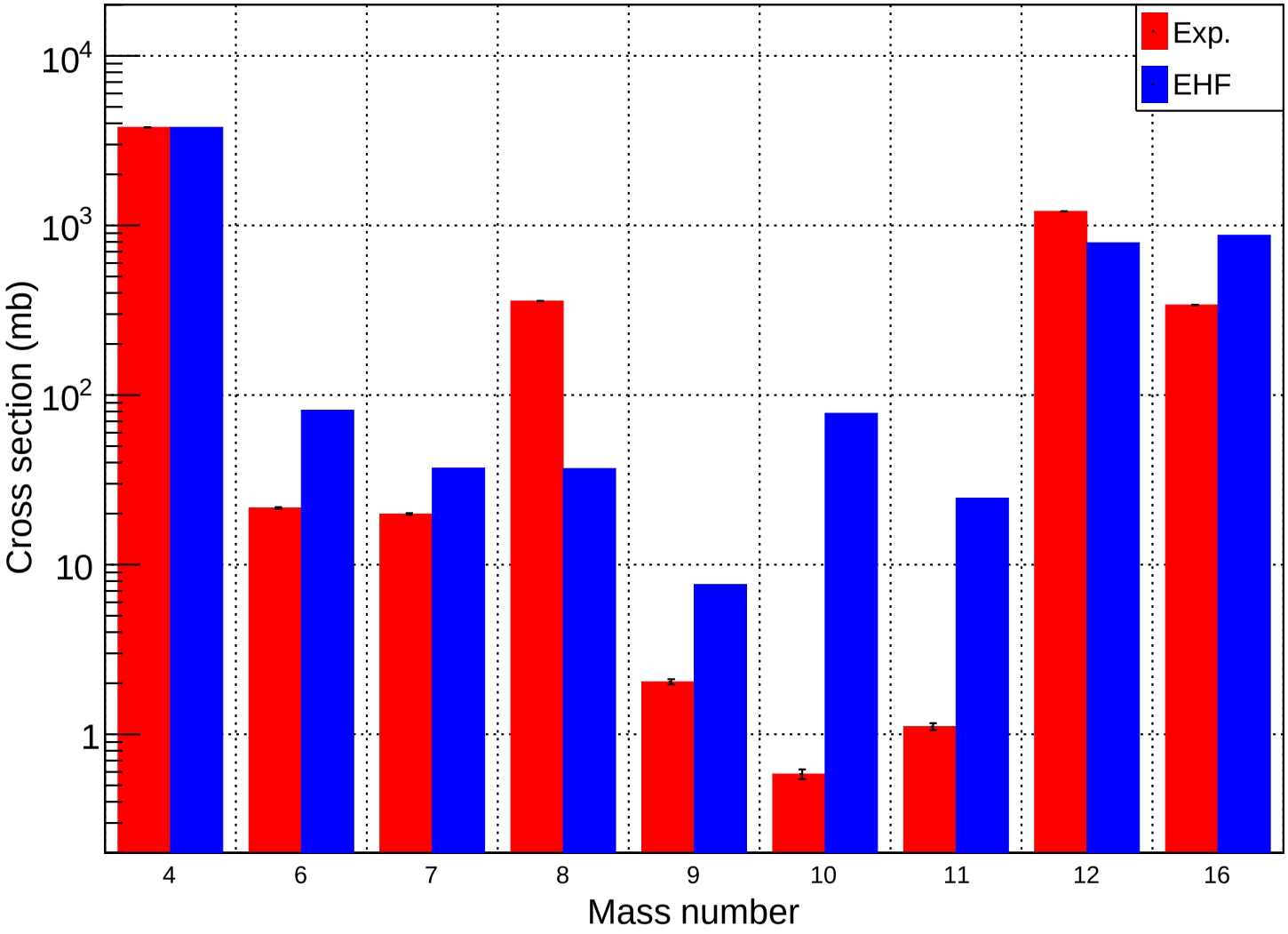

Figure 5.33: Comparison between the EHF predictions to the yields from the CHIMERA detector (normalised to the m=4 (α-particle) yield) for $E_b = 160$ MeV.

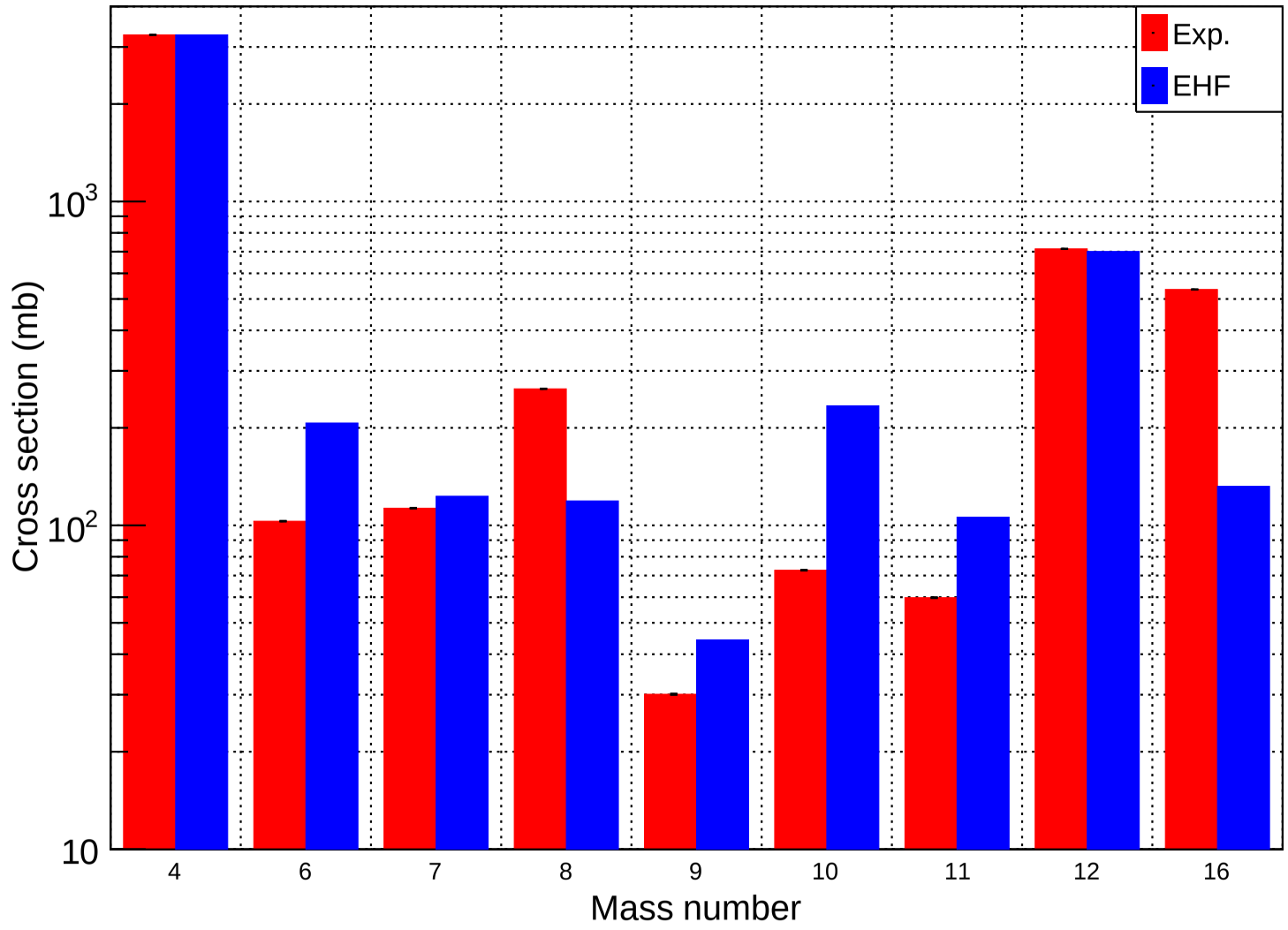

Figure 5.34: Comparison between the EHF predictions to the yields from the CHIMERA detector (normalised to the m=4 (α-particle) yield) for $E_b = 280$ MeV.

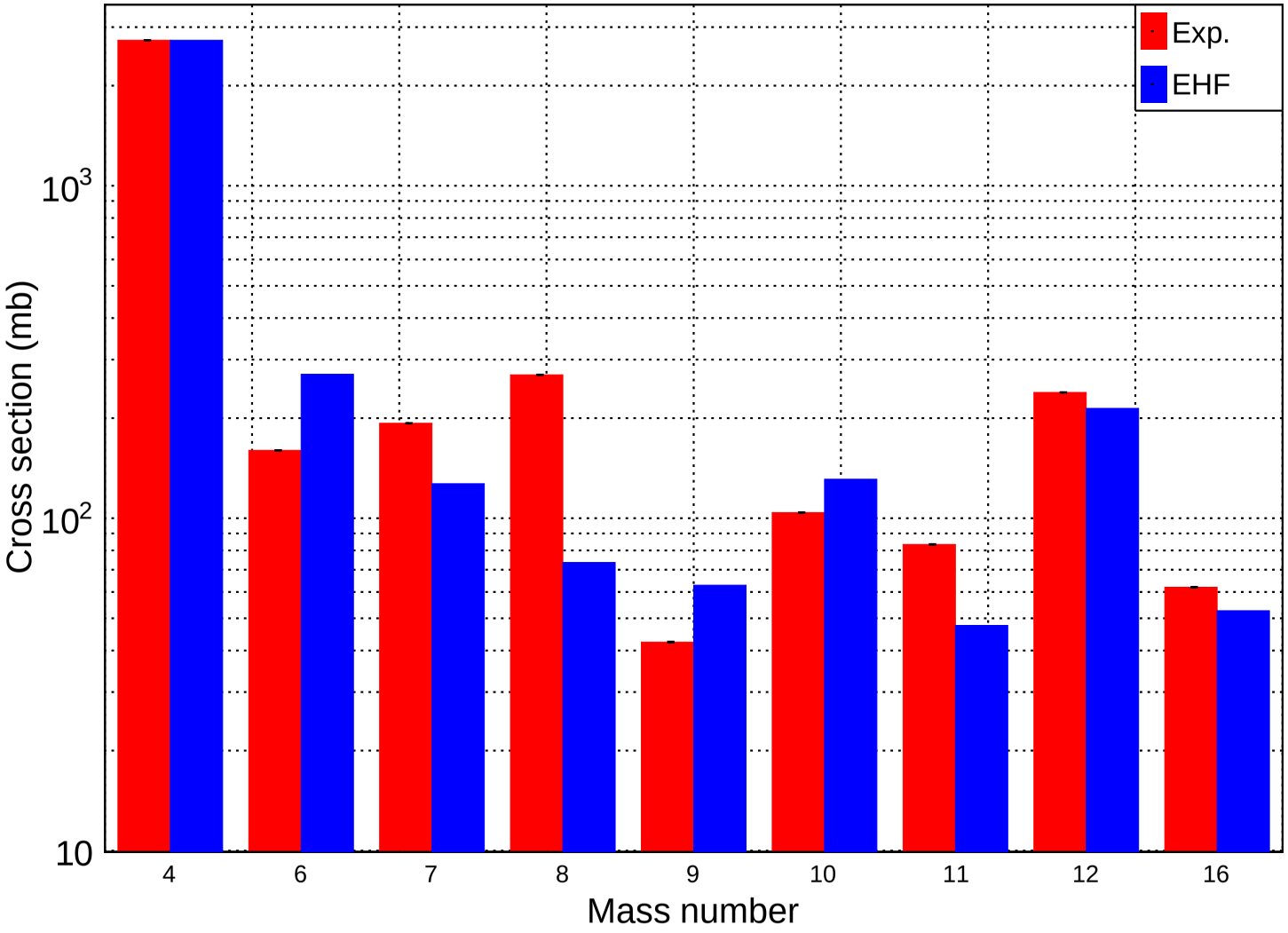

Figure 5.35: Comparison between the EHF predictions to the yields from the CHIMERA detector (normalised to the m=4 (α-particle) yield) for $E_b = 400$ MeV.

5.4 Further investigations into the reaction mechanisms

5.4.1 Inelastic scattering

As mentioned in Chapter 5.3.2, there is also expected to be a contribution to the data from inelastic scattering. One can clearly see the scattered beam in the FARCOS detectors and by virtue of measuring its energy and momentum components, one can infer the excitation imparted to the target ^{12}C.

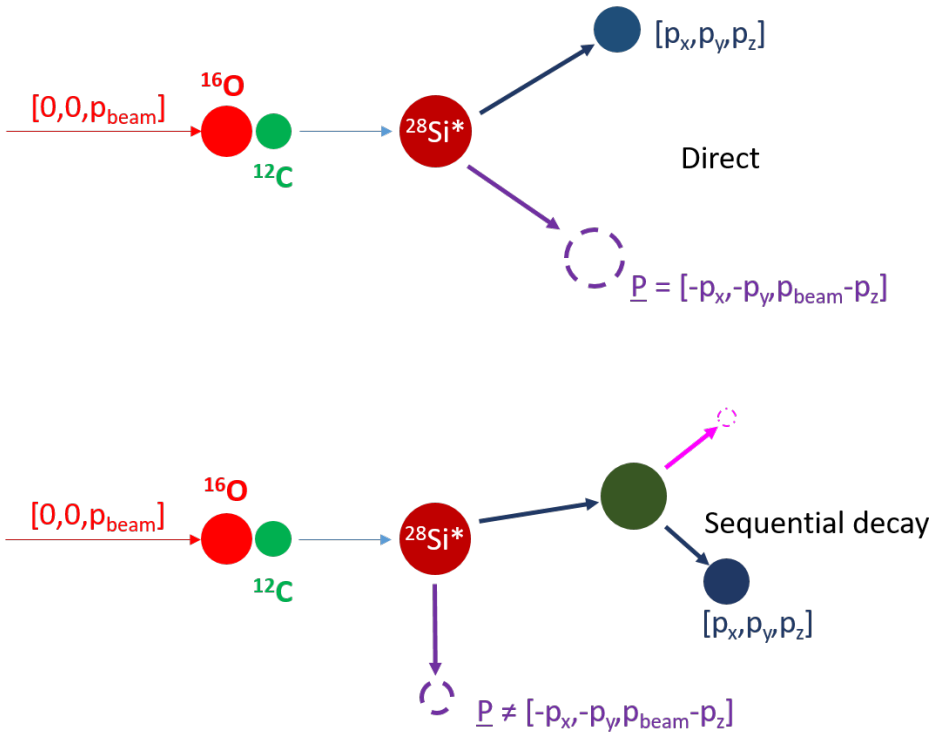

Figure 5.36: Reconstruction of missing momentum to differentiate direct and sequential decay products. The sequential decay reconstruction will yield the incorrect Q-value.

To conserve momentum, as in Figure 5.36, one clearly requires:

$$p_x^O = -p_x^C \tag{5.12}$$

$$p_y^O = -p_y^C \tag{5.13}$$

$$p_z^O = -p_x^C + p_z^{beam} \tag{5.14}$$

$$\tag{5.15}$$

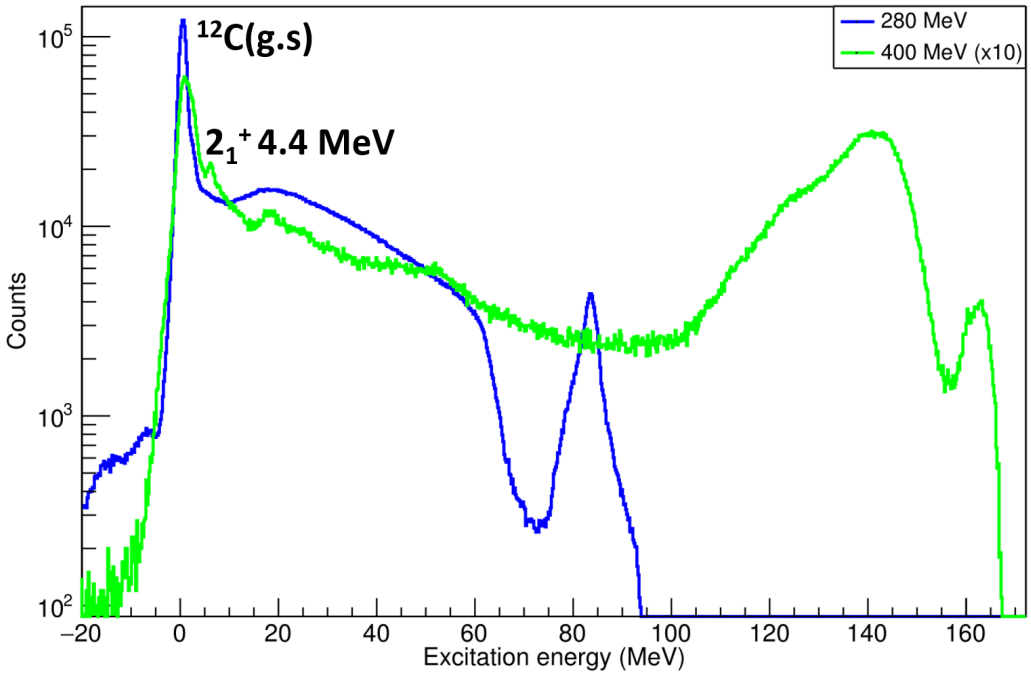

Figure 5.37: Inelastic scattering excitation function for ^{12}C from the detection of ^{16}O(g.s) in the FARCOS detector for $E_b = 280$ MeV (blue) and $E_b = 400$ MeV (green). The $E_b = 160$ MeV data are omitted as the scattered beam has insufficient energy to punch through the 300 μm of the FARCOS dE and therefore cannot be uniquely identified. The ground-state can clearly be seen in addition to several broad continua.

Therefore by conservation of energy for the elastic channel:

$$E_{before} = E_{after} \tag{5.16}$$

$$E^O + E^C + E_x = E_{beam} \tag{5.17}$$

$$\tag{5.18}$$

The results for the 280 and 400 MeV beam data can be seen in Figure 5.37 whereas the 160 MeV beam data are omitted due to the insufficient energy in the reaction for the ^{16}O nucleus to punch through the silicon stage of the telescope. One can see the primary component here is elastic scattering with the ^{12}C nucleus left in its ground state and a potential contribution from the continuum. There is also a very high excitation energy tail which may correspond to non-inelastic events (i.e. compound nucleus reactions).

Beam energy (MeV)	**σ (barns)**	**I_{beam} (enA)**	**Target thickness ($\mu g/cm^2$)**	**n (Hz)**	**τ (ns)**	**Pileup probability**
160	3.6	0.5	92	6200	49	4.0×10^{-4}
280	1.5	0.5	58	4700	17	8.0×10^{-5}
400	1.4	2.5	58	4000	62	3.2×10^{-4}

Table 5.6: Parameters for pileup consideration for the three beam energies

For the 280 MeV beam data, the spectrum rapidly drops off around 95 MeV. This is where the ^{16}O has insufficient energy to punch through the 300 μm silicon and therefore any higher energy components cannot be observed (as TOF PID was not available for FARCOS). One identifiable peak exists at $\sim$ 15 MeV in the 400 MeV data which will be discussed later. There is also a small peak corresponding to the 2_1^+ at 4.4 MeV although this state is not of interest in this investigation. The lack of significant features in the inelastic scattering suggest than any low-lying states in ^{12}C (where the density of states is sufficiently low to pick out individual resonances using the scattered beam) do not originate from inelastic scattering.

5.4.2 Multiplicities

A good probe of the physics processes is to examine the multiplicity of particles emitted. In particular, the multiplicity of α-particles is useful as the probe of our α-gas state as discussed in Chapter 3. The multiplicity of α-particles determined by both TOF and dE-E PID are then calculated, the results of which are seen in Figure 5.38 for the three beam energies. For all three energies, a similar fall off with increasing multiplicity can be seen. The termination at multiplicity 7 (as expected) for the 160 and 280 MeV data can be seen whereas the 400 MeV data show a small number of multiplicity 8 events. These can be attributed to a small number of pileup events as well as a small impurity in the TOF PID. The effect of the event pileup was removed as follows.

Firstly, the compound nucleus formation cross section was calculated with the EHF code. With this cross section, the beam intensity and target thickness, the probability of pileup can be calculated. The key values for the three energies can be seen in Table 5.6. One must first calculate the total reaction rate. This is given from the beam flux in particles/s/cm^2 (Φ), multiplied by the cross section per nucleus (σ), multiplied by the

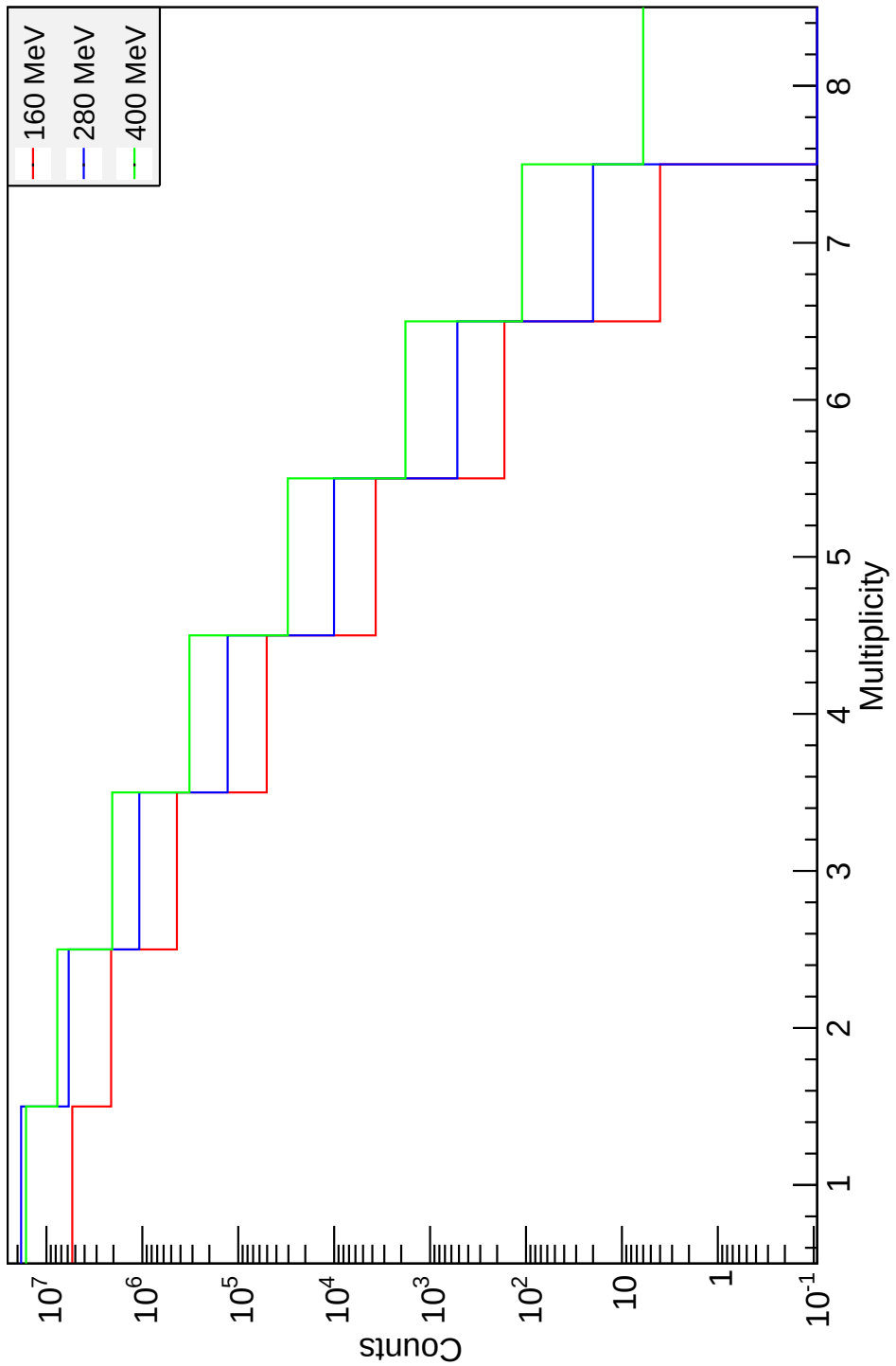

Figure 5.38: Multiplicity of α-particles for the 3 beam energies.

number of nuclei the beam passes through (N).

$$n = \Phi \times \sigma \times N \tag{5.19}$$

If we have a pulse every τ ns then we have $N_{pulses} = 1/\tau$ beam pulses per second. One can then calculate the probability a given beam pulse produces an event which is n/N_{pulses}. If the primary event occurs in a given beam pulse, this same value is then the pileup probability.

$$P_{pileup} = n\tau \tag{5.20}$$

This pileup probability is around 10^{-4}, showing our beam current is sufficiently low to avoid considerable pileup. The effect of this pileup on the measured multiplicity was considered. The measured multiplicity vector $\mathbf{N}$ (which is normalised to sum to 1) is given by the following equation [136]:

$$\mathbf{N} = \mathbf{N}_{\text{nopileup}} + \mathbf{N}_{\text{pileup}} = (1 - \gamma_{pileup})\mathbf{M} + \gamma_{pileup} \sum_{ij}^{7} \delta_{i+j,k} \left(\mathbf{M}_i \mathbf{M}_j\right), \tag{5.21}$$

where $\mathbf{M}$ is the actual single event multiplicity vector, γ_{pileup} is the probability of pileup and δ is the traditional Kronecker delta function. The Kronecker delta selects combinations of the two pileup events that match the corresponding multiplicity being measured, i.e. multiplicity 3 events (k=3) can be made up of measuring 2 α-particles from the primary event (i=2) and 1 (j=1) from the secondary event or 3 (i=3) and 0 (j=0) etc. To obtain $\mathbf{M}$ from $\mathbf{N}$, a fit was performed with $\mathbf{N}$ as a free parameter using *MINUIT* [137] as part of the *ROOT* package [138] that effectively inverts Eq. 5.21. The results from this inversion can be seen in Figures 5.39-5.41.

The effect of the pileup is therefore shown to be small. This is attributed mainly to the small pileup probability but also that for a considerable multiplicity pileup event to occur, one needs to multiply the two individual M_i and M_j together which are both small fractions therefore their product is even smaller. For $E_b = 160$ MeV the multiplicity 8 prediction can be seen to be comensurate with the value used from the experimental data corresponding to a count of 0.1 events. The choice for this is taken pseudo-arbitrarily as for these data, no m=8 events were measured. The fit showed little sensitivity to this choice provided the chosen value was less than 1.

The 280 MeV data also show a similarly small effect from the pileup probability.

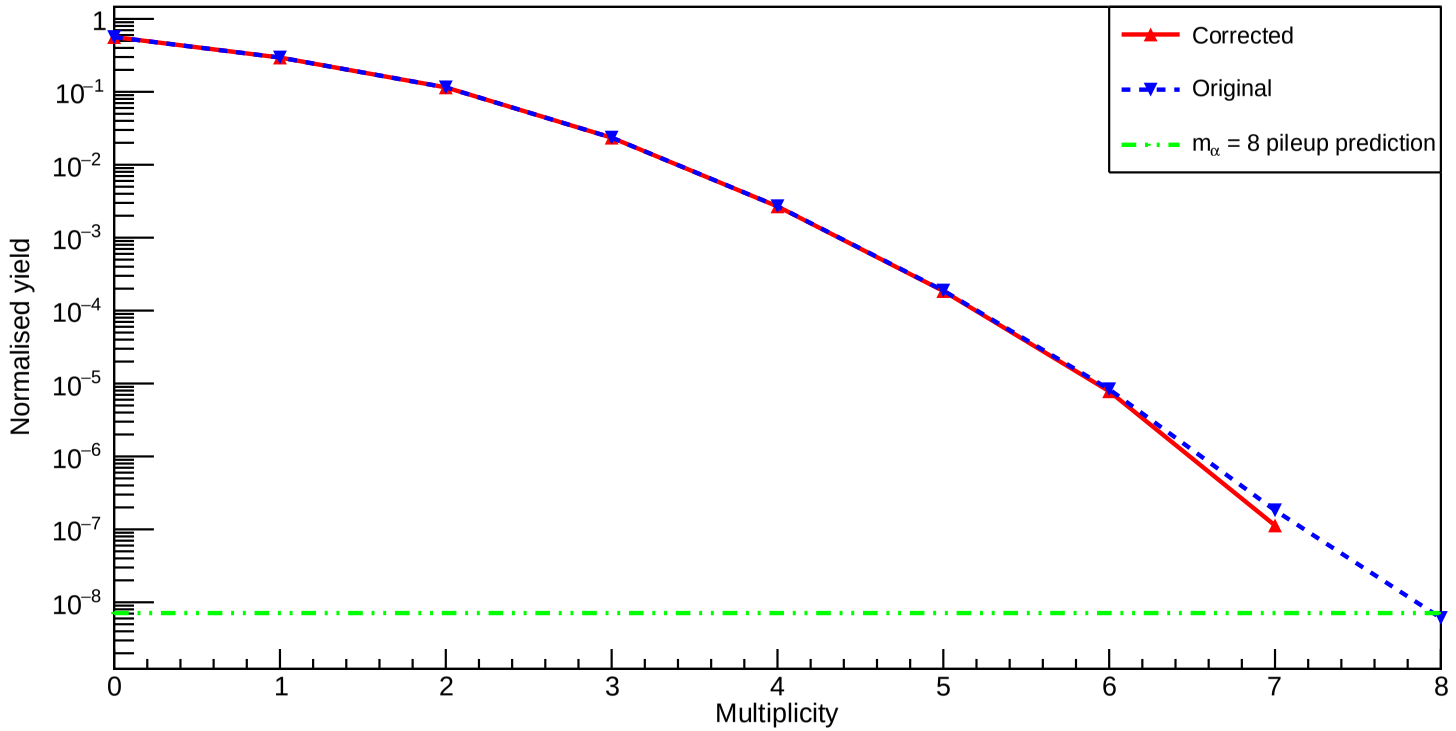

Figure 5.39: Corrected multiplicities (red) for the 160 MeV beam energy using the pileup values calculated in Table 5.6 against the measured multiplicity (blue). The corrected multiplicities can be seen to have a very small effect with only the m=7 events being noticeably modified. A value of 0.1 was used for the m=8 event. The multiplicities are normalised to sum to 1.

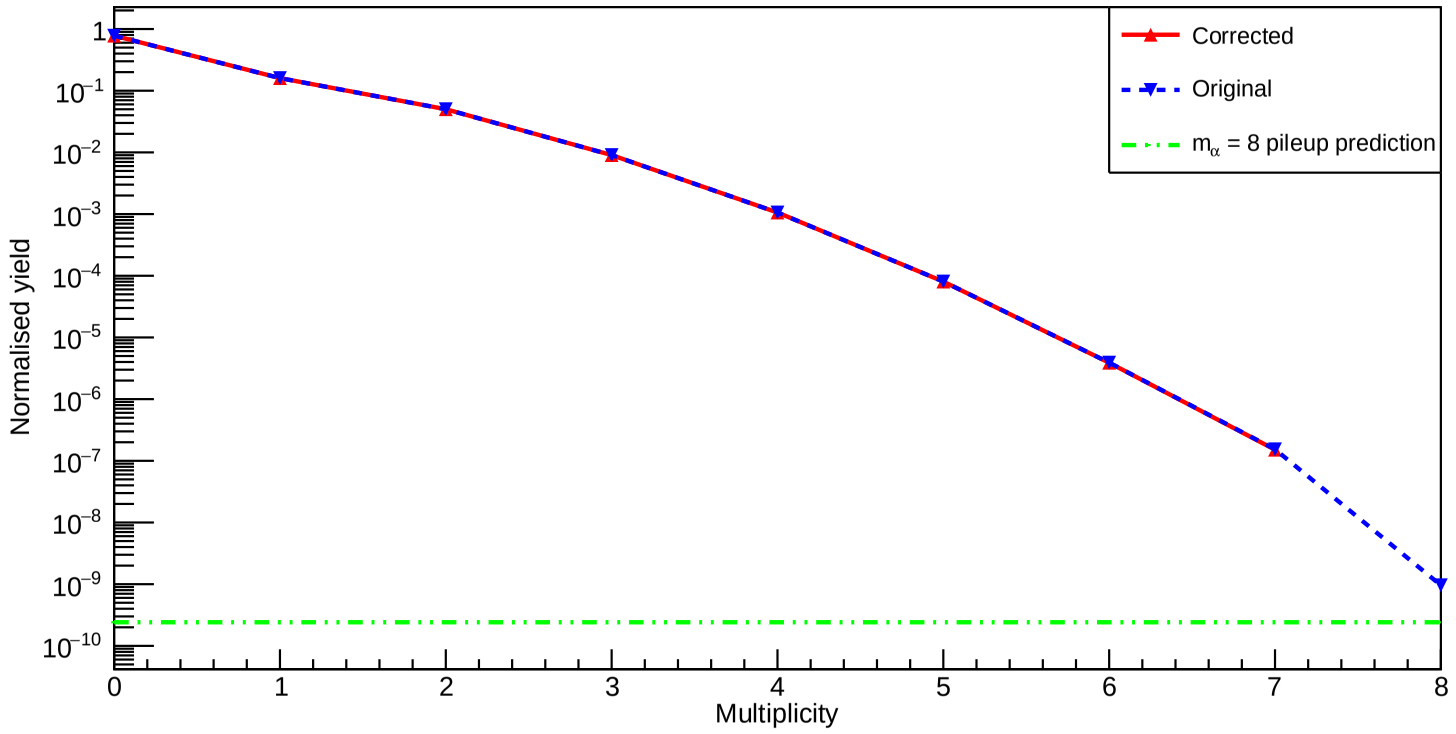

Figure 5.40: Corrected multiplicities (red) for the 280 MeV beam energy using the pileup values calculated in Table 5.6 against the measured multiplicity (blue). The corrected multiplicities can be seen to have an almost negligible modification. A value of 0.1 was used for the m=8 event. The multiplicities are normalised to sum to 1.

Multiplicity of event	160 MeV	280 MeV	400 MeV
0	1.3×10^{-8}	3.1×10^{-10}	2.1×10^{-8}
1	2.4×10^{-8}	1.5×10^{-9}	6.2×10^{-8}
2	6.2×10^{-8}	4.8×10^{-9}	1.3×10^{-7}
3	3.0×10^{-7}	2.7×10^{-8}	5.1×10^{-7}
4	2.7×10^{-5}	2.3×10^{-7}	3.3×10^{-6}
5	3.8×10^{-5}	3.0×10^{-6}	3.6×10^{-5}
6	9.1×10^{-4}	6.2×10^{-5}	6.3×10^{-4}
7	5.9×10^{-2}	1.6×10^{-3}	1.1×10^{-2}

Table 5.7: Impurity of events as calculated from pileup corrections.

For these data, the m = 8 pileup prediction is slightly lower than the 0.1 value used here, mainly due to the smaller pileup probability for this beam energy.

For the 400 MeV data, there were 4 events measured with m = 8 which agrees well with the results from the pileup correction.

Using the correct multiplicities, one can also calculate the purity P_k of the different events i.e. what fraction of the $m_\alpha = i$ correspond to single events rather than a mixing of events. This is given by:

$$P_k = \frac{(1-\gamma_{pileup})\mathbf{M_k}}{(1-\gamma_{pileup})\mathbf{M_k} + \gamma_{pileup}\sum_{ij}\delta_{i+j,k}\left(\mathbf{M}_i\mathbf{M}_j\right)} \tag{5.22}$$

As these values are extremely close to unity, their impurity (equal to 1 - purity) is instead shown in Table 5.7. The multiplicity 7 states of interest can still be seen to maintain a good level of purity which is of prime importance for later analysis.

Once the effect of the pileup has been taken into account, the single-event measured multiplicity is obtained. This does not represent the true multiplicity of the event however, as the efficiency of the different reaction channels must be taken into consideration. As previously mentioned, in compound nucleus statistical decay (and the Fermi break-up model) the products are emitted isotropically. The efficiency of detecting a given multiplicity event should then be (to first order) related to the detector coverage. If each particle is randomly emitted across the detector which has a coverage of p, the efficiency for detecting i α-particles when j α-particles were emitted is then given by

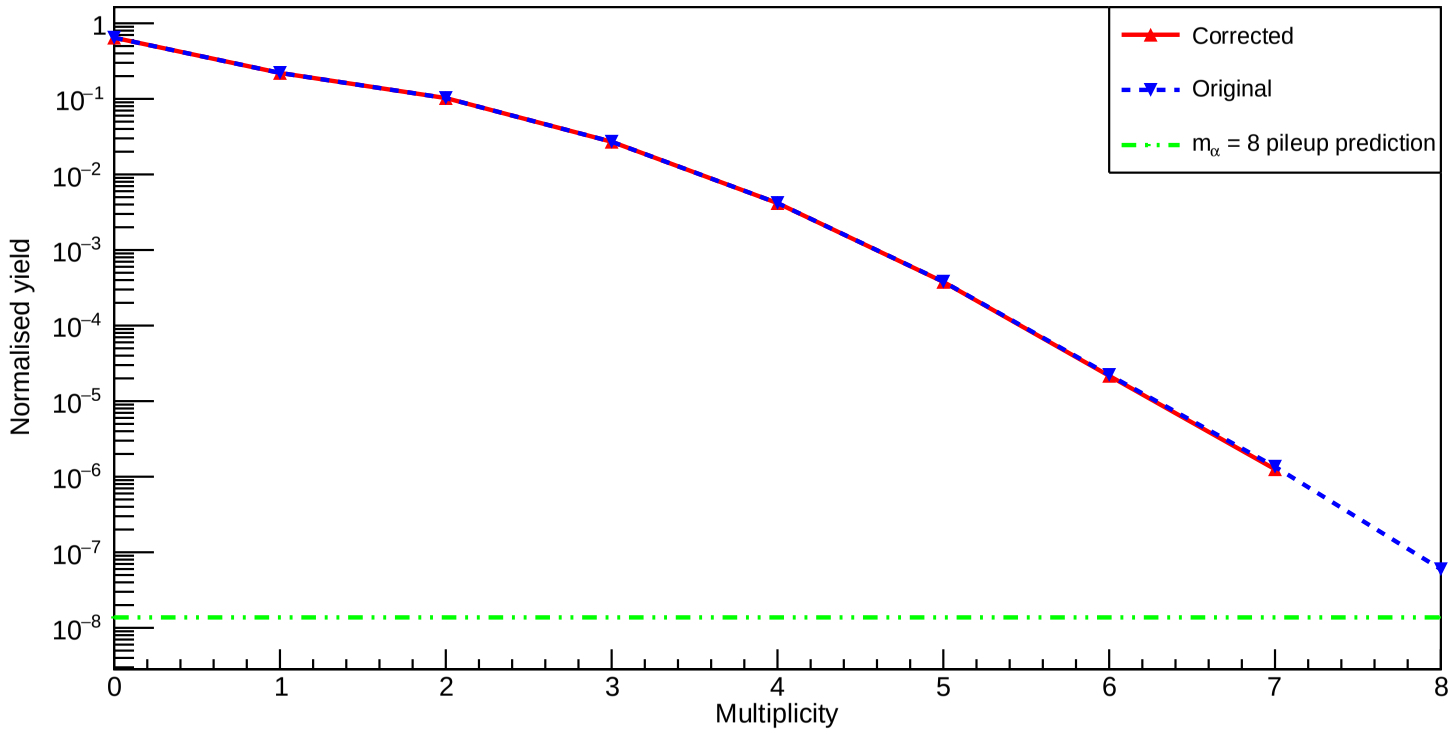

Figure 5.41: Corrected multiplicities (red) for the 400 MeV beam energy using the pileup values calculated in Table 5.6 against the measured multiplicity (blue). The corrected multiplicities can be seen to have an almost negligible modification. The multiplicities are normalised to sum to 1.

the binomial probability:

$$\epsilon_{i,j} = \binom{j}{i} p^i (1-p)^{j-i} \tag{5.23}$$

The detector coverage p was taken as 0.28 by fitting the multiplicity of the Monte Carlo break-up channel data with the binomial probability and gave a good result for all three beam energies. This constitutes a very simple model however any more complicated model relies on a good understanding of the exact reaction mechanism. As this was not available, relying on an isotropic spray of particles from the Monte Carlo data was used which included the detector response in terms of working detectors and threshold effects. The single event multiplicity $\mathbf{M}$ is then given by:

$$\mathbf{M} = \epsilon \mathbf{M}', \tag{5.24}$$

where $\mathbf{M}'$ is the true multiplicity and $\boldsymbol{\epsilon}$ is the efficiency matrix whose elements are defined as in Eq. 5.23.
To extract the true multiplicity $\mathbf{M}'$ one must then invert the matrix and calculate:

$$\mathbf{M}' = \boldsymbol{\epsilon}^{-1} \mathbf{M} \tag{5.25}$$

The effect of this inversion can be seen in Figure 5.42. This can easily yield unphysical results as there is no restriction that the elements of the matrix $\mathbf{M}'$ must be positive. This unphysicality is only seen for the 400 MeV data where the m_α=6 is given a modest negative value (-2.6×10^{-3}). This negative value is removed when slightly increasing p to 0.29 although the yield for m_α=6 is still small, suggesting that while the result is unphysical, it is indicative of a small yield for 6-α events. These results were compared to theoretical predictions in Chapters 5.2.1 and 5.2.2 and will be discussed further in Chapter 6.

For m_α=6 events, the missing momentum was used to reconstruct the energy of a final undetected α-particle. By placing a gate on the total reaction Q-value, the events (which lay within the gate) were then selected and the undetected α-particle was passed through for further analysis, therefore improving the overall statistics. This can be seen in Figure 5.43. The majority of the counts can be seen to be well contained around the expected Q-value demonstrating that the majority of the multiplicity 6 events corresponding to a single event rather than a pileup as demonstrated in Figures 5.39-5.41.

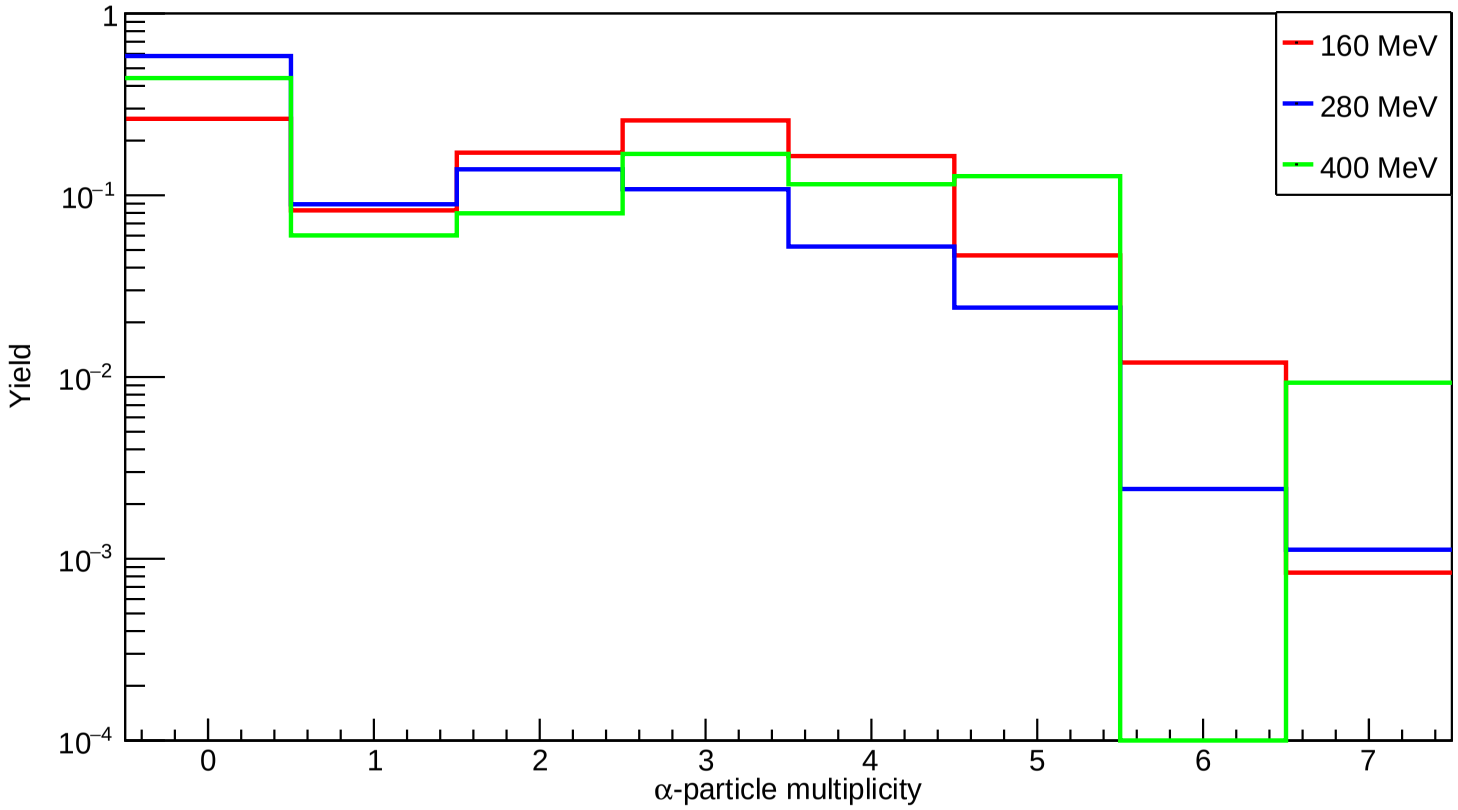

Figure 5.42: True α-particle multiplicities after efficiency correcting from the measured values from Equation 5.25.

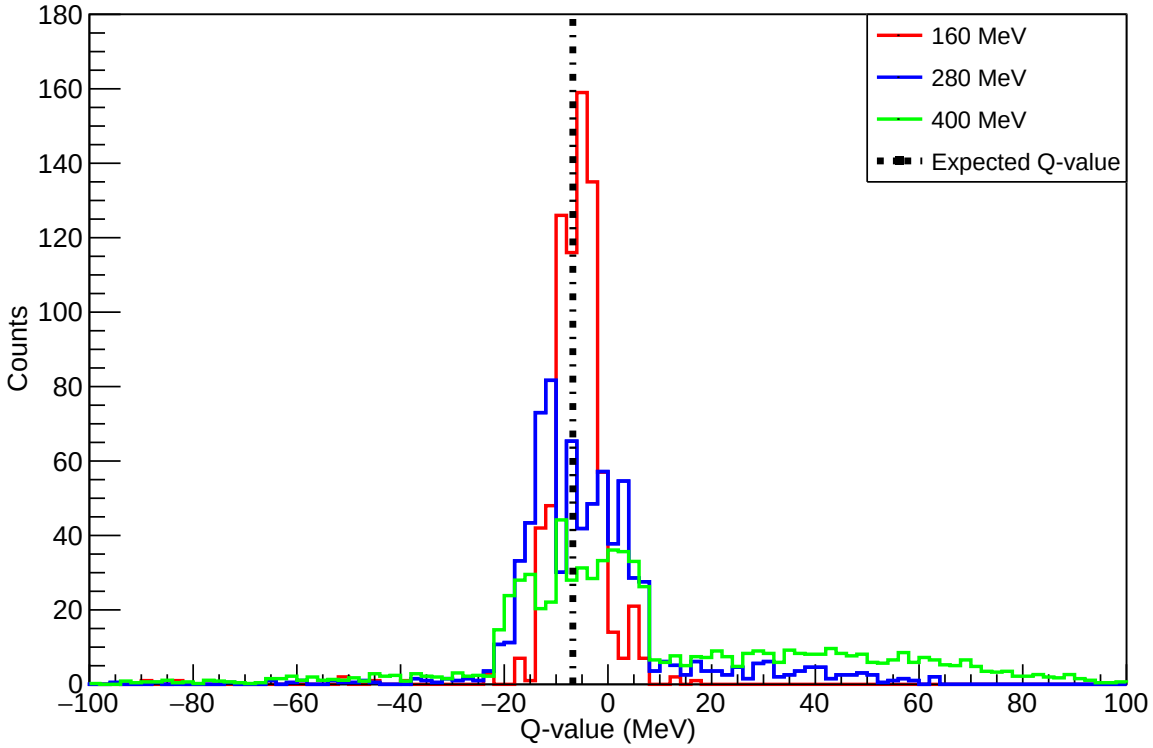

Figure 5.43: (Negative) Q-value for reconstructing a missing α-particle from an m_α=6 event.

5.4.3 Energetics of alpha particles

Examination of the energies of the α-particles emitted from the system is also indicative of the reaction mechanisms. At lower energies, one expects a continuous contribution from the decay of the compound nucleus by virtue of the smooth continuum of energies. At higher energies where the compound nucleus contribution is negligible, one may also see a more slowly varying contribution from pre-equilibrium reactions. Finally, this spectrum is also superimposed with discrete peaks from the direct reaction contributions. The general form of such a spectrum can be seen in Figure 5.44.

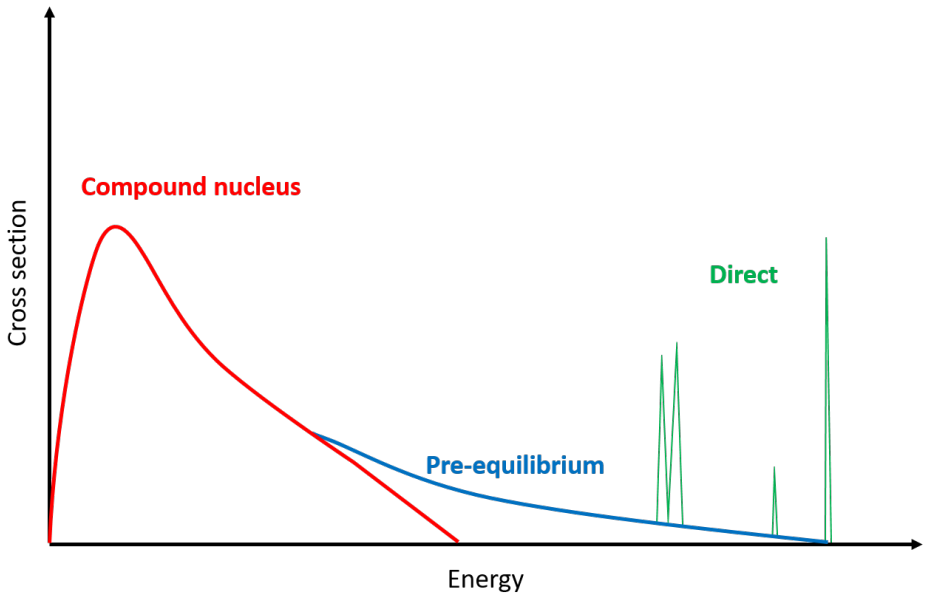

Figure 5.44: Diagram showing the energy spectrum from a high energy reaction with features corresponding to different reaction mechanisms. Compound nucleus reactions give a broad energy spectrum with a high energy tail associated with pre-equilibrium reactions. Discrete energy peaks correspond to direct reactions.

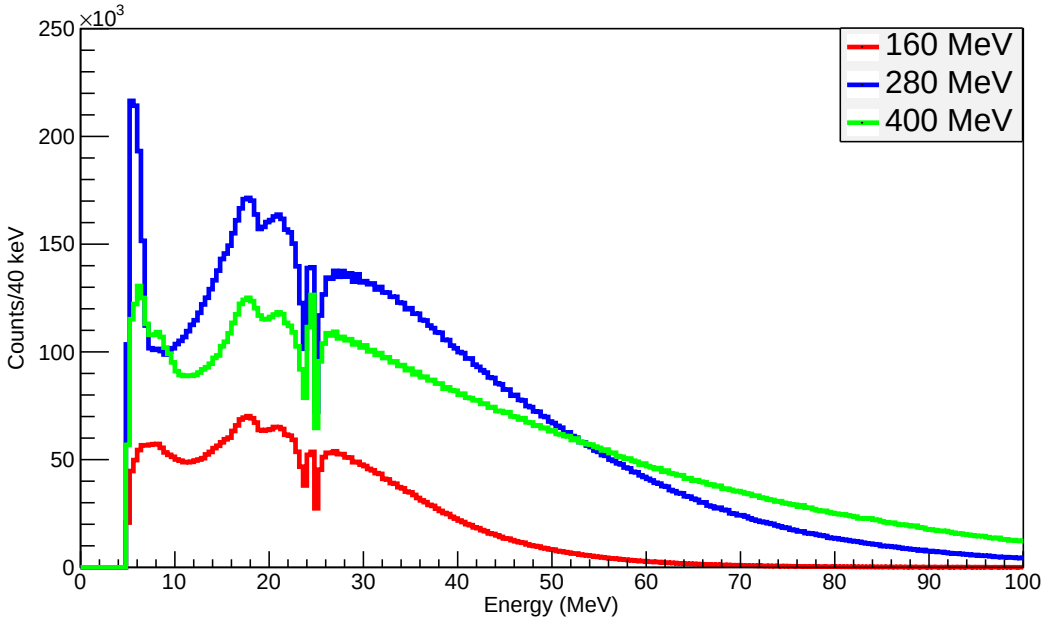

Figure 5.45: Energy of the measured α-particles showing the dominant source of α-particles from compound nucleus formation giving the smooth contribution. The decrease in counts around 25 MeV can be seen where there is a small gap between the dE-E and TOF PID.

One can then examine the α-particle energy spectrum to elucidate the reaction mechanisms taking place. This can be seen in Figure 5.45. It is evident from the spectrum that the structure seen corresponds to compound nucleus decay. There is a small gap between 23 and 25 MeV which, as previously mentioned, is due to the gap in dE-E and TOF particle identification. This cannot be fully corrected for by the Monte Carlo as the exact energy and angle behaviour needs to be fully understood. By virtue of the complicated reaction mechanism, this was possible with the Monte Carlo simulation and only the break-up and α-gas sequential decay paths could be included. Additionally, one also sees a secondary bump below 10 MeV (particularly in the 280 MeV data). This is attributed to a combination of near-threshold events and a decreasing purity of the TOF PID at low energies where bleed-through from previous pulses means hydrogen and other light nuclei are incorrectly assigned as α-particles as shown previously in Figure 4.13.

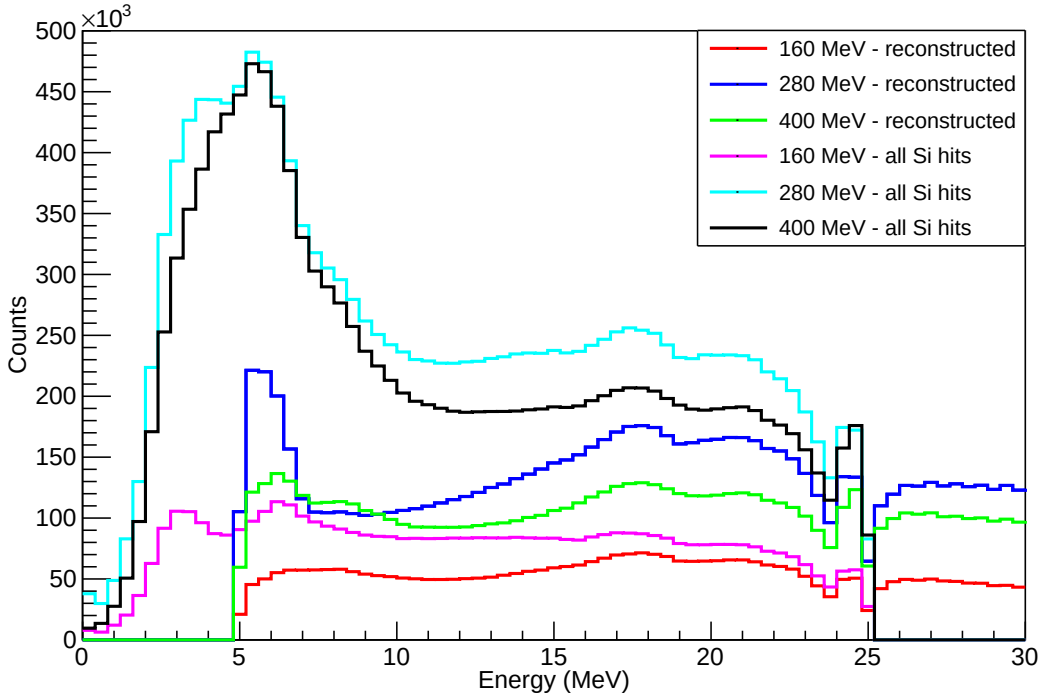

Figure 5.46: Energy of the measured silicon hits against those identified as α-particles showing the dominance source of α-particles from compound nucleus formation except for low energies.

To examine the effect of TOF impurities on this α-particle energy spectrum, one can look at the energy spectrum of **all** particles that hit the silicon stage. This is shown in Figure 5.46 and shows the majority of the silicon hits are classified as α-particles and the anomalous bumps seen are reasonably enhanced by taking all the silicon hits. Around half of these low energy hits are identified as α-particles suggesting a reasonable amount of these are genuine low-energy α events. This fact is demonstrated by the absence of increased yield for the Hoyle state as discussed later in Chapter 5.5.3 when taking all silicon hits. Additionally, one sees a large number of Hoyle state decays with α-particles at this low energy. The kinematics of the α-particles will be examined throughout this current Chapter.

5.5 Reconstruction of α-conjugate nuclei and event mixing

Taking events with an α-particle multiplicity greater than one, it is possible to reconstruct the momentum vectors of these α-particles in an effort to elucidate their origin. Events where a non α-conjugate nucleus was detected were rejected to clean the data. The results were also checked without cleaning these events and the contribution was seen to be extremely negligible. The comparison for the multiplicity solely with α-particles and those with additional nuclei are shown in Figure 5.47 where this difference is noticeably small (particularly for the higher multiplicities). By combining two α-particles, the $\alpha - \alpha$ correlation function corresponding to states in ^{8}Be can be formed. The excitation for an N-α system (an α-conjugate nucleus made of N α-particles) is given by:

$$E_x = \sum_i E_i - \frac{(\sum_i \vec{p_i})^2}{2\sum_i m_i} - Q \tag{5.26}$$

The results for ^{8}Be are shown in Figures 5.48 and 5.49 in red where the Q-value is omitted for ease of visualisation. The ground-state peak can clearly be seen at 92 keV. The small break-up energy of ^{8}Be(g.s) means that the signature of a ^{8}Be break-up is two α-particles hitting adjacent or the same detector. The first excited state of ^{8}Be sits at 3.03 ± 0.01 MeV with a large width of 1.5 MeV. The bump around this energy can easily be attributed to this state however, this peak can also be described by event mixing of uncorrelated α-particles as well as a contribution from ^{9}Be excited states with decay to $\alpha + \alpha + n$ which will now be discussed.

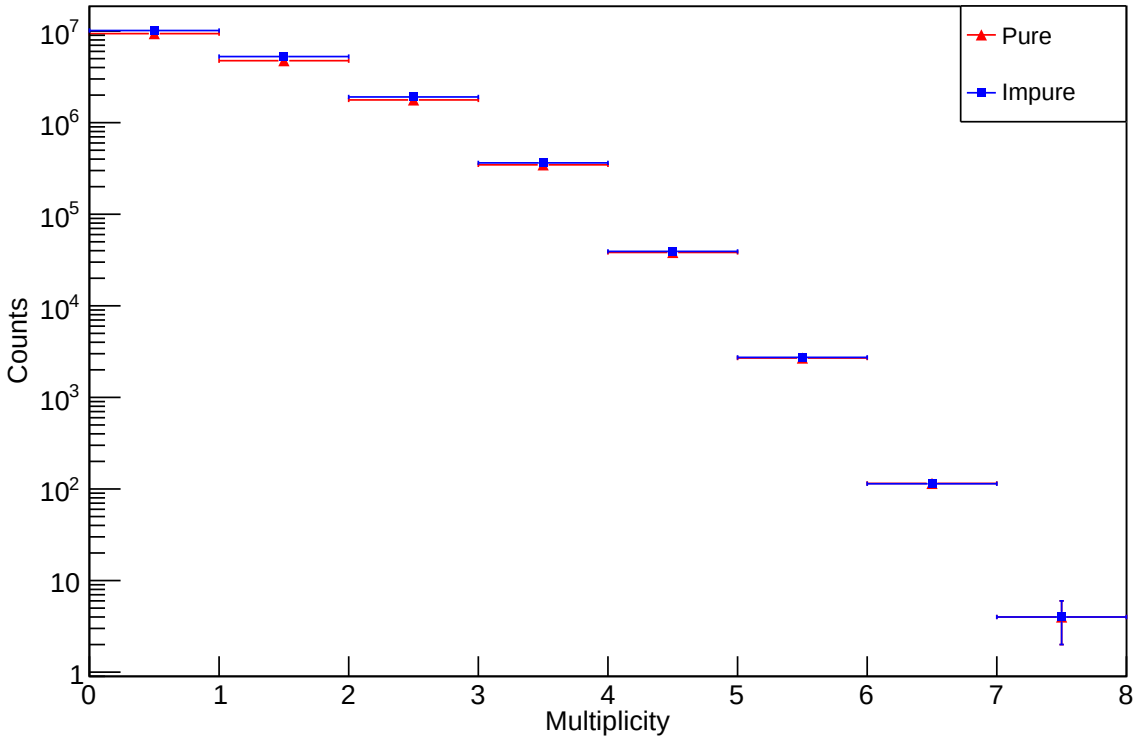

Figure 5.47: Multiplicity comparison for those events comprised solely of α-particles against those with additional nuclei for $E_b = 160$ MeV.

5.5.1 Event mixing

With large solid-angle coverage detectors, there is an implicitly higher geometric efficiency and as such, one must ensure the beam current is sufficiently low that pileup of events does not occur. As seen in the previous section, this pileup occurs in around 1 in 10^4 events. Additionally, with a high multiplicity event, one may start pairing particles that didn't originate from the same stage of the decay. Given the combinatorial nature of these pairings, a large background can appear in any correlation functions (as seen in the α-α excitation function with a contribution at $\sim$ 2 MeV in Figure 5.48). In order to identify the degree to which these two facts contribute to any excitation or correlation function, one may resort to event mixing [139]. Event mixing is widely used in heavy-ion physics and relies on taking particles from separate events (therefore ensuring they are uncorrelated) then passing these through the reconstruction process. By removing the significance of correlated events, one can therefore ascribe features in

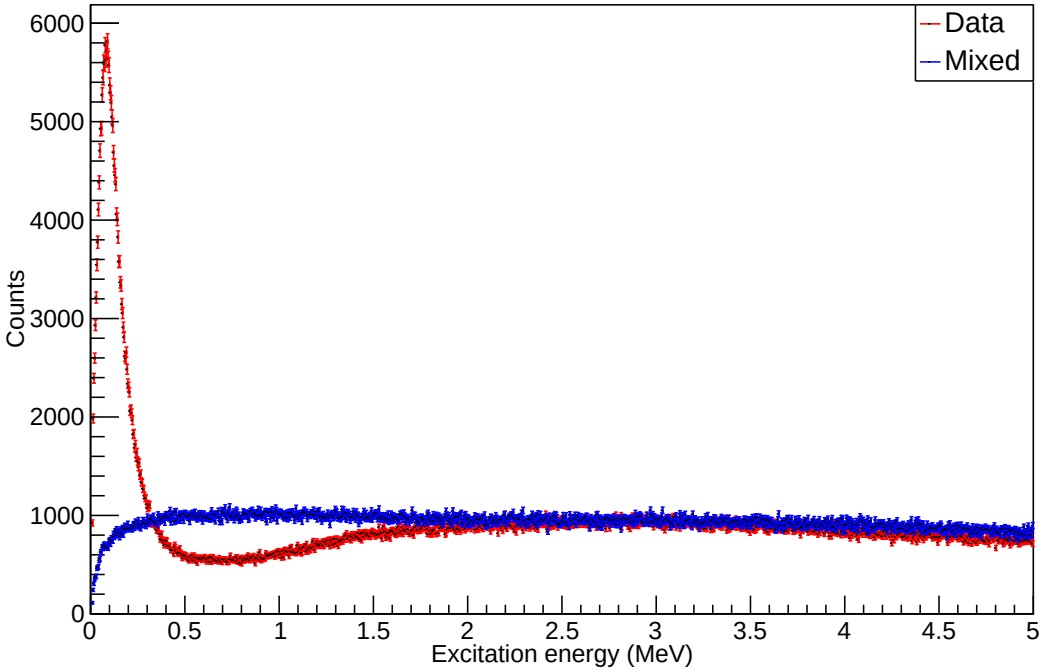

Figure 5.48: Event mixing of type δ_1 applied to the 2-α excitation function for ^{8}Be. The experimental data are shown in red in comparison with the mixed event results in blue.

the correlation function to the result of these uncorrelated events. One can then take a ratio of the mixed and unmixed events and any coherent effects will have a ratio larger than order unity while all other features should be removed. For each real event, the same multiplicity was generated by taking a random α-particle from a random event. In addition to mixing unique events - noted as δ_1, the effect of partially mixing two events was investigated - noted as δ_2 type mixing. Here, adjacent events were mixed with a pool of preceeding events which are assumed to still be independent. For a multiplicity event m, a random number of α-particles (from 1 to m-1) was taken and the missing α-particles replaced by a random selection from the previous 20 α-particles that were sorted. The preceeding 20 α-particles were chosen purely to simplify the analysis code and this method shows the effect of mixing partially correlated sub-events.

5.5.2 ^{8}Be

Figure 5.48 shows how the δ_1 event mixing contributes to the ^{8}Be excitation function as a smooth continuum. The effect of the δ_2 (Figure 5.49) mixing between two

events shows a small contribution from the ground-state at 92 keV still persists but the continuum seen in the δ_1 mixing between uncorrelated α-particles is also seen.

Both event mixing types largely exceed the seen data around $0.5 \rightarrow 1$ MeV showing a contribution of around half of the seen mixing strength is required here as the ratio of uncorrelated to correlated events must not exceed unity. Choosing this value leaves a reasonable yield around 3 MeV which can be seen in Figure 5.50 showing the difference between the data and the δ_1 mixing. The additional yield centered around 3 MeV could potentially be assigned as a contribution from the first excited state in ^{8}Be as the 2^+_1 which has an observed large width of 1.5 MeV. The seen width here however is well in excess of this ($\Gamma \sim 3$ MeV) suggesting this peak has an additional source which isn't from mismatching of uncorrelated α-particles.

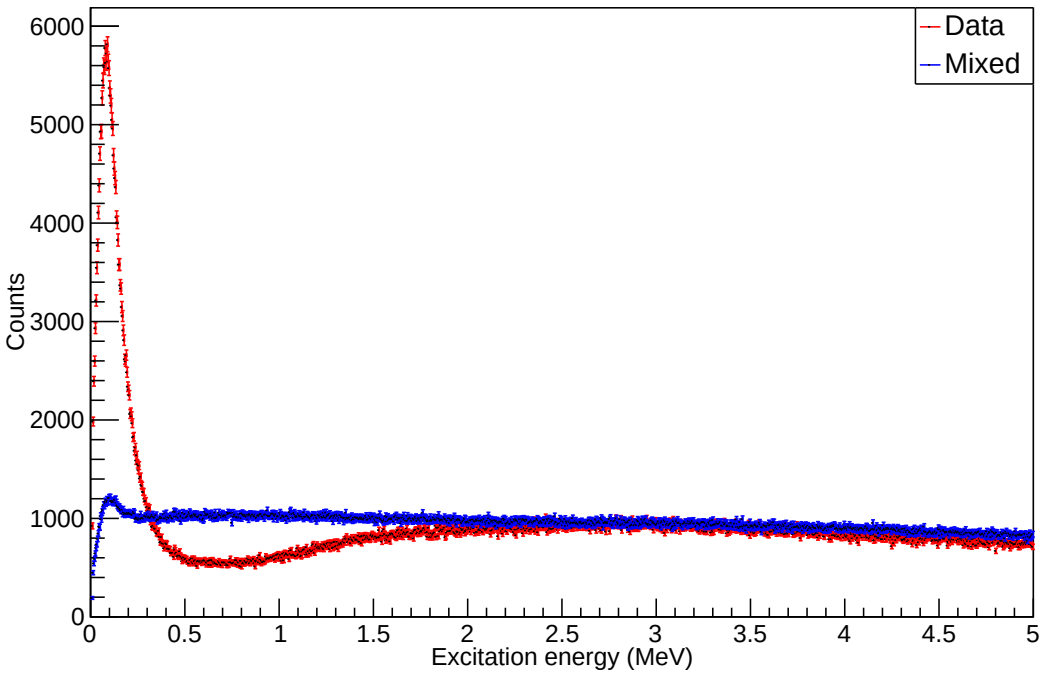

Figure 5.49: Event mixing of type δ_2 applied to the 2-α excitation function for ^{8}Be. The experimental data are shown in red in comparison with the mixed event results in blue.

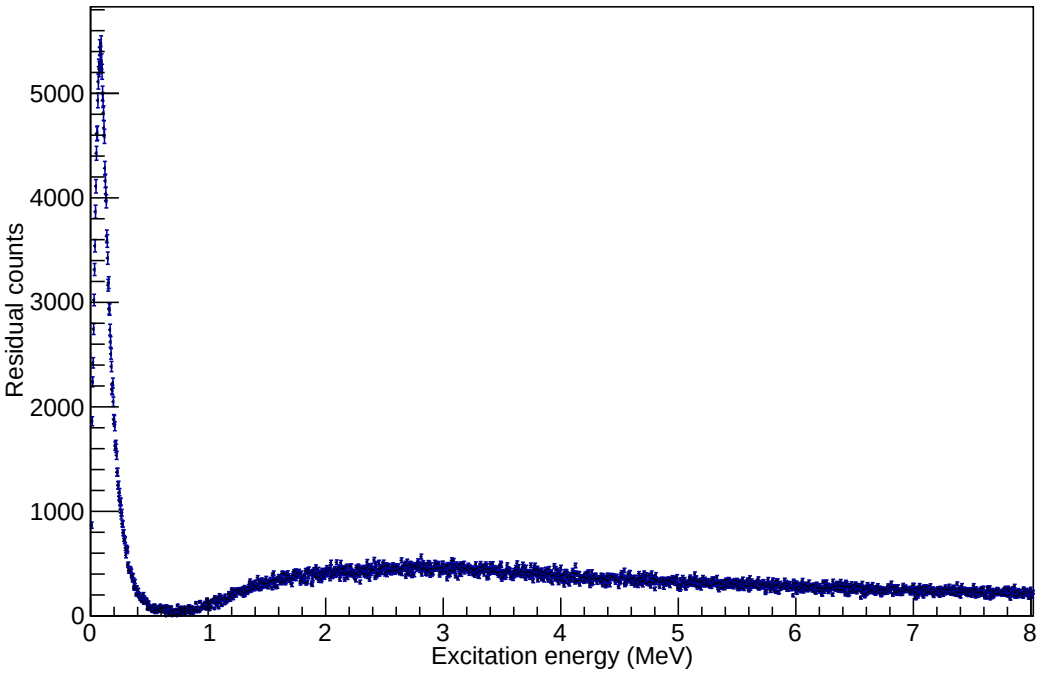

Figure 5.50: Difference between the δ_1 and data for the 2-α correlation function. The strong yield for the ground-state can be seen in addition to a residual yield around 3 MeV with an abnormally large width.

5.5.3 ^{12}C

Once α-particles have been reconstructed to find ^{8}Be(g.s), one can then use any further α-particles to reconstruct states in ^{12}C. As the primary state of interest is the Hoyle state which has a well understood 3-α structure and is the best candidate for a condensate state in ^{12}C, one can further clean the data by looking at the ^{8}Be+α path as the $^{12}\mathrm{C}(0_2^+) \rightarrow 3\alpha$ decay path is measured to be negligible [87] [88].

With a high multiplicity of events, one must ensure to be careful when reconstructing the ^{8}Be(g.s)+α path. The following steps are then taken:

- All combination of 3 α-particles are taken and 2 α-particles are combined in pairs.
- To ensure the pair of α-particles form the ^{8}Be ground state, the ^{8}Be excitation energy is calculated.
- A gate is placed around the ^{8}Be(g.s) to select events which lie in the ground state peak.

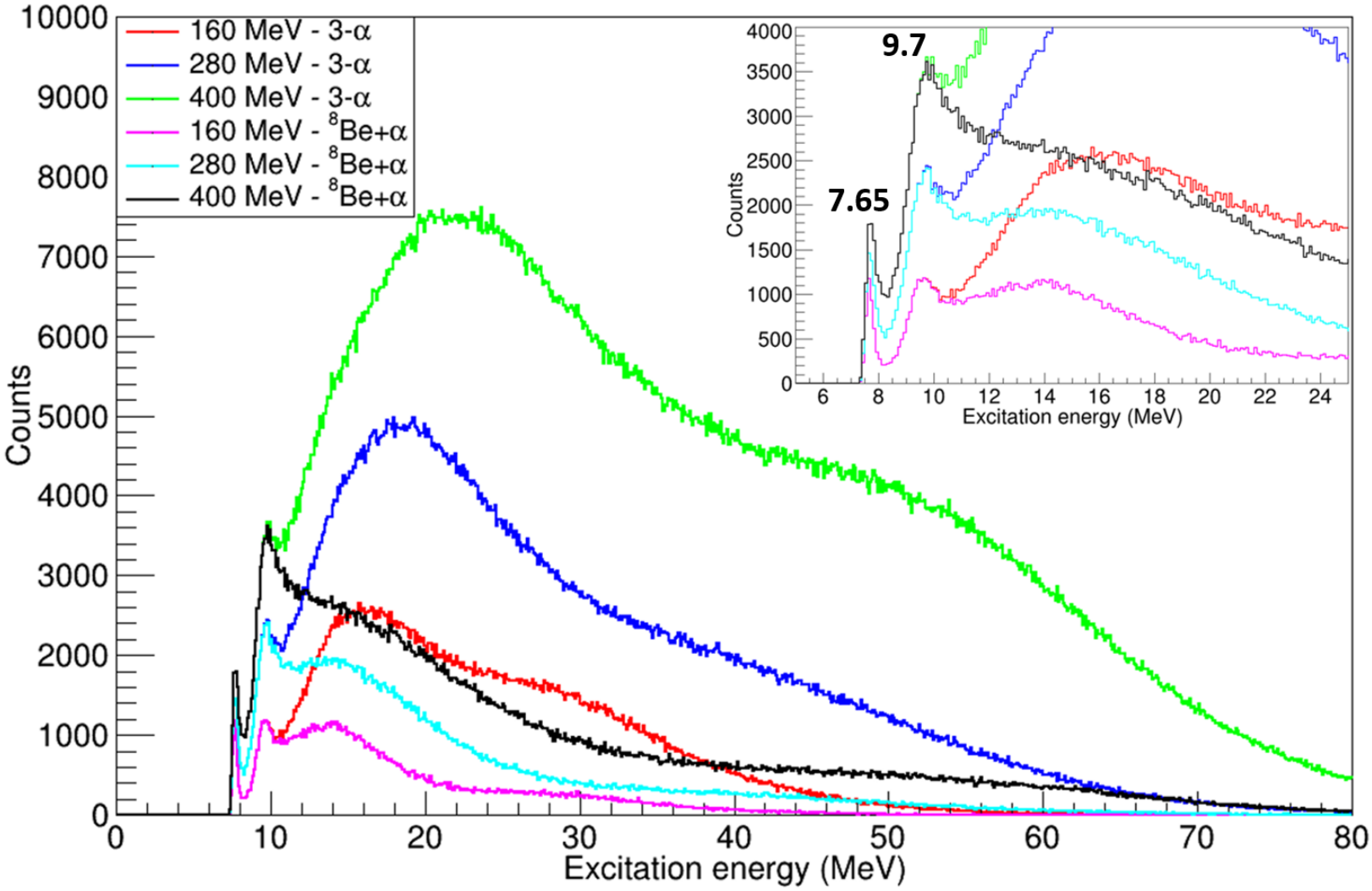

Figure 5.51: ^{12}C excitation function for all 3 beam energies: 160 MeV (red), 280 MeV (blue) and 400 MeV (green). The events whereby the decay proceeds via ^{8}Be(g.s) are also shown: 160 MeV (magenta), 280 MeV (cyan) and 400 MeV (black). An exploded view of the low excitation energy is also shown inset.

- These two α-particles are marked such that they should be treated as a ^{8}Be and not partially mixed with other α-particles.
- The remaining particle is added to and the $^{12}C^{\star}$ excitation spectrum is calculated using Equation 5.26.

The result of this reconstruction process can be seen in Figure 5.51 along with the 3-α path with no such gating on the ^{8}Be(g.s). Two significant contributions can be seen at 7.65 MeV and 9.6 MeV. The lowest excitation peak corresponds to the Hoyle state whereas the higher energy peak is probably a contribution from the usually well populated 9.64 MeV 3^{-}_{1}. The excitation function shows however that the measured width exceeds that expected from the 3^{-}_{1} peak with a natural width of 48 keV [140] and an experimental width given in Table 5.8 where these can be compared to those from the Hoyle state. This additional width can be described by a contribution from the 2^{+}_{2} rotational excitation of the Hoyle state discussed in Chapter 3.6 with an energy of 9.8 MeV. To understand this possible contribution, the Monte Carlo simulations performed allowed for a study of how the experimental width changes as a function of excitation energy. To model this, sequential α-decay to high excitations in ^{24}Mg, ^{20}Ne and ^{16}O was modelled followed by a decay to the Hoyle state, followed by ^{8}Be(g.s)+α break-up. This dependence is shown in Figure 5.52 for the three beam energies. These expected values can be seen to be smaller than those experienced experimentally.

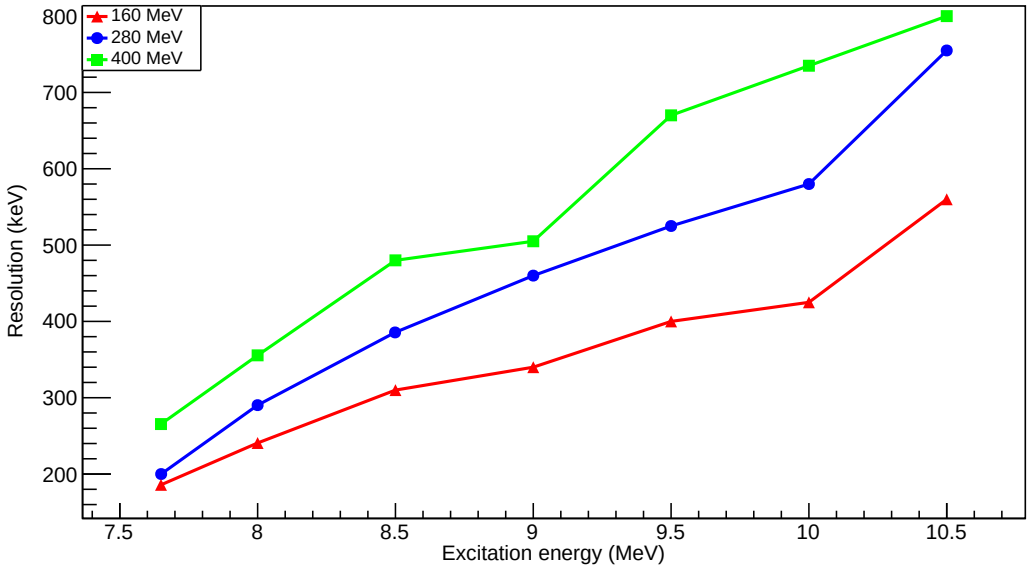

Figure 5.52: Experimental resolution as deduced from Monte Carlo simulations for a state in ^{12}C. The fitting errors are omitted as they are smaller than the data points.

The experimental resolution appears to have no strong dependence on the incident energy of the constituent α-particles. This increased width could therefore be partially attributed to the wide range of different reaction mechanisms which produce the seen $^{12}\mathrm{C}(0_2^+)$ which have slightly different artificial offsets to the excitation function which further smears the resolution of the peak. Alternatively, drifting of the electronics chain over the course of the experiment and uncertainties from the calibration may also contribute. To test this latter hypothesis, the Monte Carlo simulation was repeated while increasing the energy smearing across all detectors. For a 300 μm detector, this ΔE has a value of 200 keV. Figure 5.53 shows the effect of increasing this to dramatically large values of 2000 and 5000 keV. Changing the smearing to 2000 keV has a very small effect and only when increasing the smearing to 5000 keV does the effect of the energy resolution begin to dominate over the angular resolution. This suggests incorrect energies are not responsible for this increased smearing. Additional factor investigated included the effect of incorrect angle measurements. The Monte Carlo simulation was performed with the high and low angles for each telescope scaled by a factor of 1.1 to represent a large systematic error in the angles. The effect of this was to offset the peak of the Hoyle state by ~ 50 keV but with no corresponding increase in the width. Similarly, modelling a systematic energy error of 100 keV makes a negligible (< 25 keV)

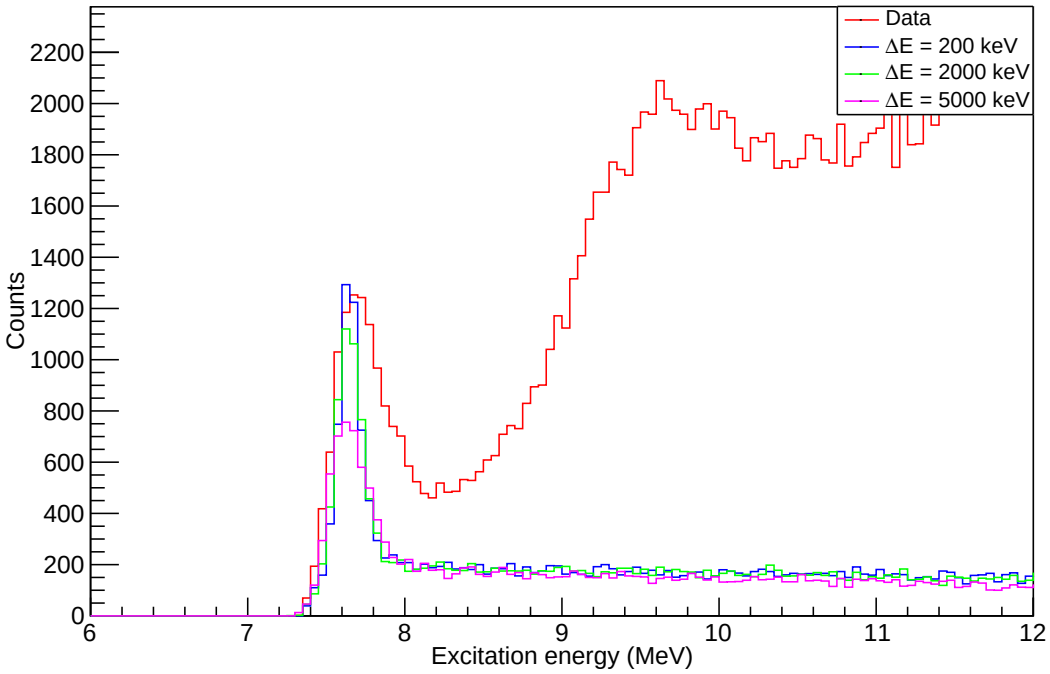

Figure 5.53: Demonstration of how changing the energy smearing ΔE on the Monte Carlo simulation affects the resolution of the Hoyle state. The experimental data are shown for reference.

shift in the energy centroid. This suggests that the cause of this increased resolution is an effect not modelled within the Monte Carlo such as the effect of δ-electrons hitting the detector causing issues with charge collection during the beam-time.

As the origin of this decreased resolution could not be identified, the results were then scaled to match those seen experimentally which gave a predicted width of 700, 890 and 1060 keV. This gives predictions of the seen $3^-/2^+$ width via $\Gamma = \sqrt{\Gamma^2_{\text{meas}} - \Gamma^2_{\text{exp}}}$ as 570, 555 and 665 keV. This is far in excess of that expected from a 3^-_1. Given the population method, it is therefore possible that this contribution can be partially attributed to the 2^+_2 rotational excitation of the Hoyle state previously measured [141][142][20].

Below $\sim$ 10 MeV, all decays proceed via the ^{8}Be(g.s) as expected due to the inhibiting of the 3-body phase space at this low excitation. The effect of event-mixing in ^{12}C can be seen in Figures 5.54 and 5.55 for the 160 MeV data. It can clearly be seen that both the δ_1 and δ_2 type event mixing describe the continuum seen at higher excitation energies and fit the background beneath the $^{12}\text{C}(0^+_2)$ and $3^-/2^+$ extremely well. The additional high energy yield can therefore be attributed to uncorrelated α-

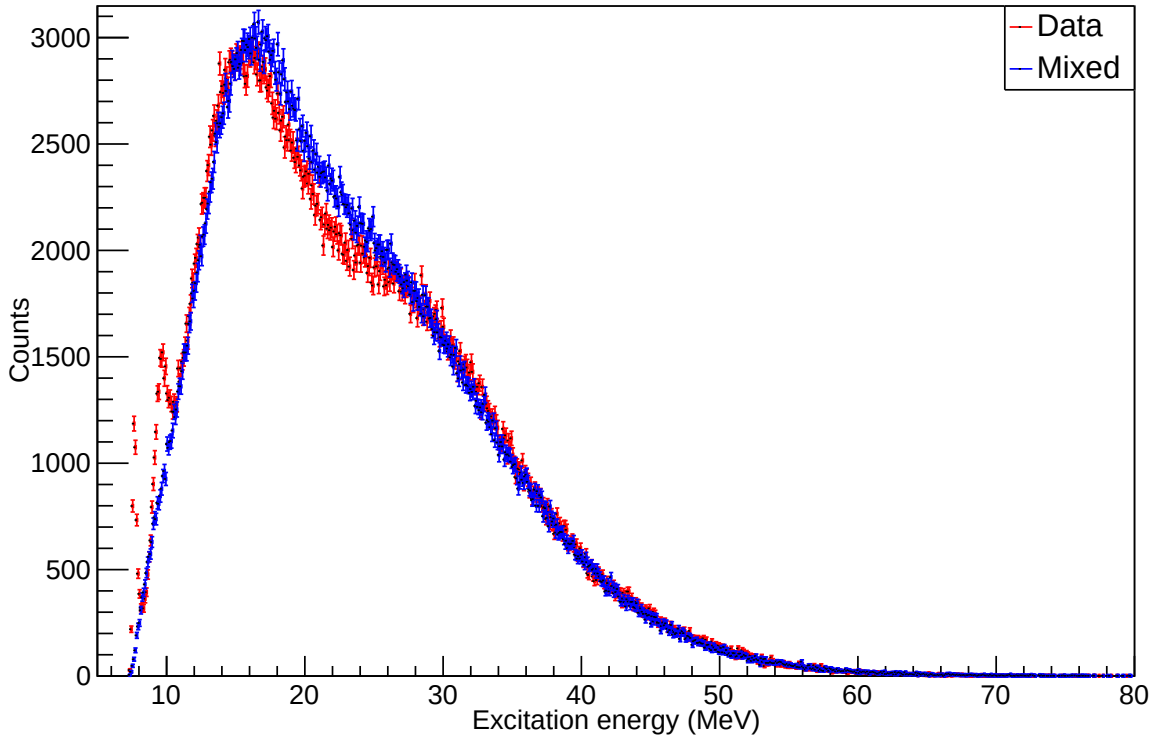

Figure 5.54: Event mixing of type δ_1 for the 3-α excitation function. The experimental data are shown in red in comparison with the mixed event results in blue.

Beam energy (MeV)	**^{12}C(0_2^+) exp. width (keV)**	**^{12}C(3_1^-) exp. width (keV)**	**^{12}C(0_2^+) MC width (keV)**	**^{12}C(3_1^-) MC width (keV)**	**^{12}C(3_1^-) scaled width (keV)**	**^{12}C(3_1^-) total width (keV)**
160	300	900	185	400	700	570
280	330	1050	200	525	890	555
400	420	1250	265	670	1060	665

Table 5.8: Resolution of different states in the ^{12}C excitation function given both by the experimental data and the MC simulations. The scaled widths are modified by a constant factor to match the experimental resolution of the Hoyle state to the resolution from the MC.

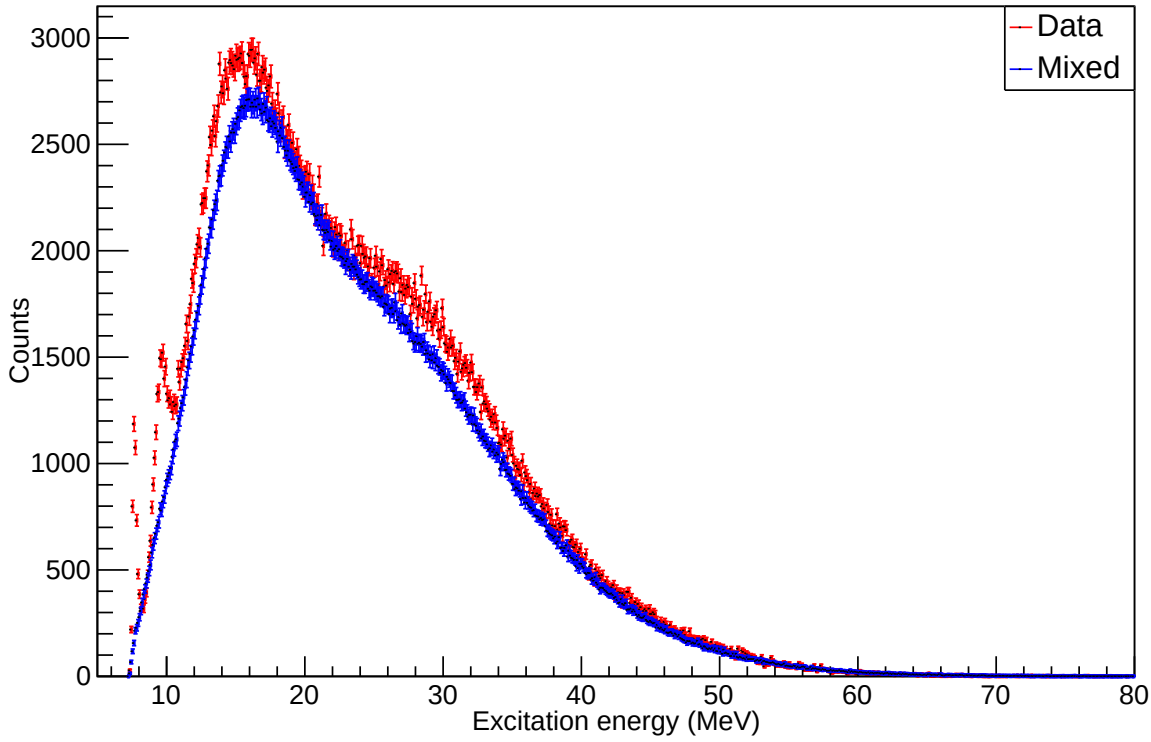

Figure 5.55: Event mixing of type δ_2 for the 3-α excitation function. The experimental data are shown in red in comparison with the mixed event results in blue.

particles rather than solely contributions from the continuum. Additional techniques were therefore employed to remove the contribution from uncorrelated α-particles.

Dalitz plots

To better understand the role that the background (via uncorrelated particles) makes to the excitation function, the dynamics of three-body break-up were investigated. To do so, one can use a formulation first described in particle physics [143]. This technique relies on calculating the energy of the three particles in the centre-of-mass system, denoted by ϵ_i. Comparing their energies then allows for discerning between different decay paths. To see this, one can examine the decay of the Hoyle state via two different decay mechanisms; sequential and direct decays. When the Hoyle state decays into a ^{8}Be(g.s) + α system, this two-body decay severely limits the energy available. To conserve momentum, the ^{8}Be and α must have equal and opposite momenta. As the ^{8}Be then breaks up, the energy is shared between the two α-particles with a small addition from the 92 keV gained from the break-up of this unstable nucleus. Denoting the two α-particles from the ^{8}Be as α_1 and α_2 with the initial α-particle denoted as α_3.

$$p_{\alpha_3} = p_{^8\mathrm{Be}} \tag{5.27}$$

$$E_{\alpha_3} = \frac{p_3^2}{2m_\alpha} \tag{5.28}$$

$$E_{\alpha_1} + E_{\alpha_2} = \frac{p_3^2}{4m_\alpha} + Q_{^8\mathrm{Be}} \tag{5.29}$$

$$E_{\alpha_1} + E_{\alpha_2} + E_{\alpha_3} = Q_{^8\mathrm{Be}} + Q_{^{12}\mathrm{C}(0_2^+)} = E_{tot} \tag{5.30}$$

$$E_{\alpha_1} + E_{\alpha_2} = \frac{E_{\alpha_3}}{2} + Q_{^8\mathrm{Be}} \tag{5.31}$$

$$\frac{3}{2}E_{\alpha_3} = Q_{^{12}\mathrm{C}(0_2^+)} \tag{5.32}$$

From the first decay stage, α_3 then takes away $\frac{2}{3}$ of the available energy. The two α-particles from the decay of ^{8}Be then share the remaining $\frac{1}{3}Q_{^{12}\mathrm{C}(0_2^+)} + Q_{^8\mathrm{Be}}$. As the second decay stage is no longer in the centre of mass, depending on the decay angle of the ^{8}Be relative to the direction of α_3, one α-particle can be "boosted" to increase their relative energy if it decays in the same direction as the recoiling ^{8}Be and its co-product is retarded as it decays back in the same direction it originally decayed in. This is shown by case a) in Figure 5.56.

As a consequence of this sequential method and taking into account the energy released by the break-up of ^{8}Be, α_3 ends up with roughly half of the total energy available in the decay with the remaining half shared between the other two α-particles.

In comparison, one can analyse the situation whereby a direct (non-sequential) decay occurs without the intermediate ^{8}Be(g.s) resonance. Here, there are no kinematic restrictions of the sharing of energies between the particles (apart from total conservation of momentum and energy). This limits the decay to the region within the circle shown in Figure 5.56. To compare the two, one can use the calculated energies in the centre-of-mass of the decay and normalise these values to unity. By taking linear combinations of these three energies ϵ_i, one can create a "Dalitz plot" which allows for a representation of the decay. The formulation for the Dalitz plot is as follows:

$$x = \frac{1}{\sqrt{3}}(\epsilon_2 - \epsilon_1) \tag{5.33}$$

$$y = \frac{1}{3}(2\epsilon_3 - \epsilon_2 - \epsilon_1) \tag{5.34}$$

By taking the linear combinations in this way, if the indices are re-arranged, this corresponds to a rotation of the Dalitz plot through 120° therefore maintaning the triangular symmetry. Sequential decays then occupy a triangular region on the Dalitz plot which is shown in Figure 5.56 in red which corresponds to one α-particle taking around half of the total energy (for the Hoyle state decay) and the remaining two sharing the energy.

The experimental data were analysed to see the cleanliness of the two resonances apparent in ^{12}C. These Dalitz plots can be seen in Figure 5.57 for the ^{12}C(0_2^+) and $3^-/2^+$. As the excitation energy in ^{12}C increases, the line corresponding to sequential decay increases in distance from the centre of the circle.

This Dalitz formulation was used as an additional constraint to remove any erroneous 3-α events. Random events, as demonstrated both from event-mixing of the real data and from Monte Carlo simulations of decays which do not proceed via the Hoyle state, demonstrate the background to this Dalitz plot is isotropic. This is particularly useful when analysing the 3^- Dalitz plot data. The true sequential decays populate a much smaller region of the triangle due to the increase in the excitation energy which makes the two α-particles from the decay of ^{8}Be have energies which are more similar. This means the sequential decay populates the region seen in Figure 5.57. By selecting only the data pertaining to the sequential decay, the background can be reduced. For

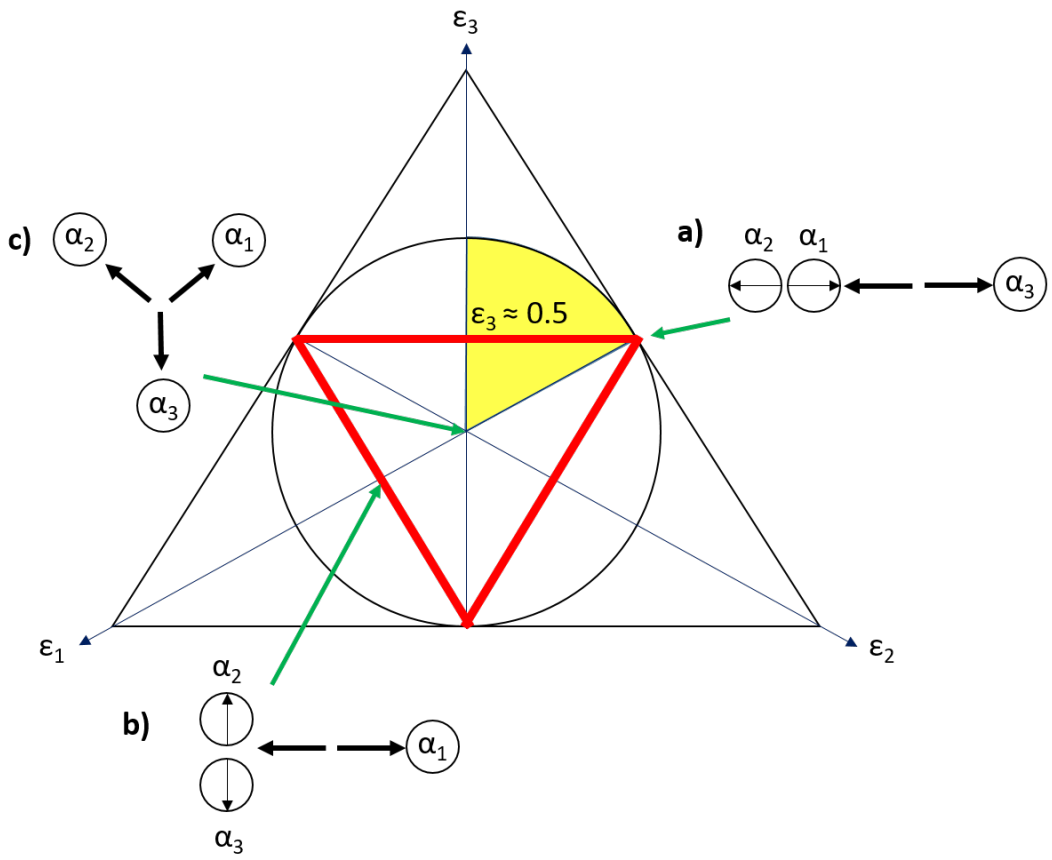

Figure 5.56: Dalitz plot with labelled regions corresponding to: a) a collinear decay where particles 2 and 3 share the total energy, b) an orthogonal decay where the decay products from ^{8}Be share the energy equally and c) a non-sequential direct decay where all three α-particles have a very similar energy. The region occupied by a sequential decay through the ^{8}Be(g.s) is marked by the red line whereas the sector where $\epsilon_3 > \epsilon_2 > \epsilon_1$ is filled in yellow.

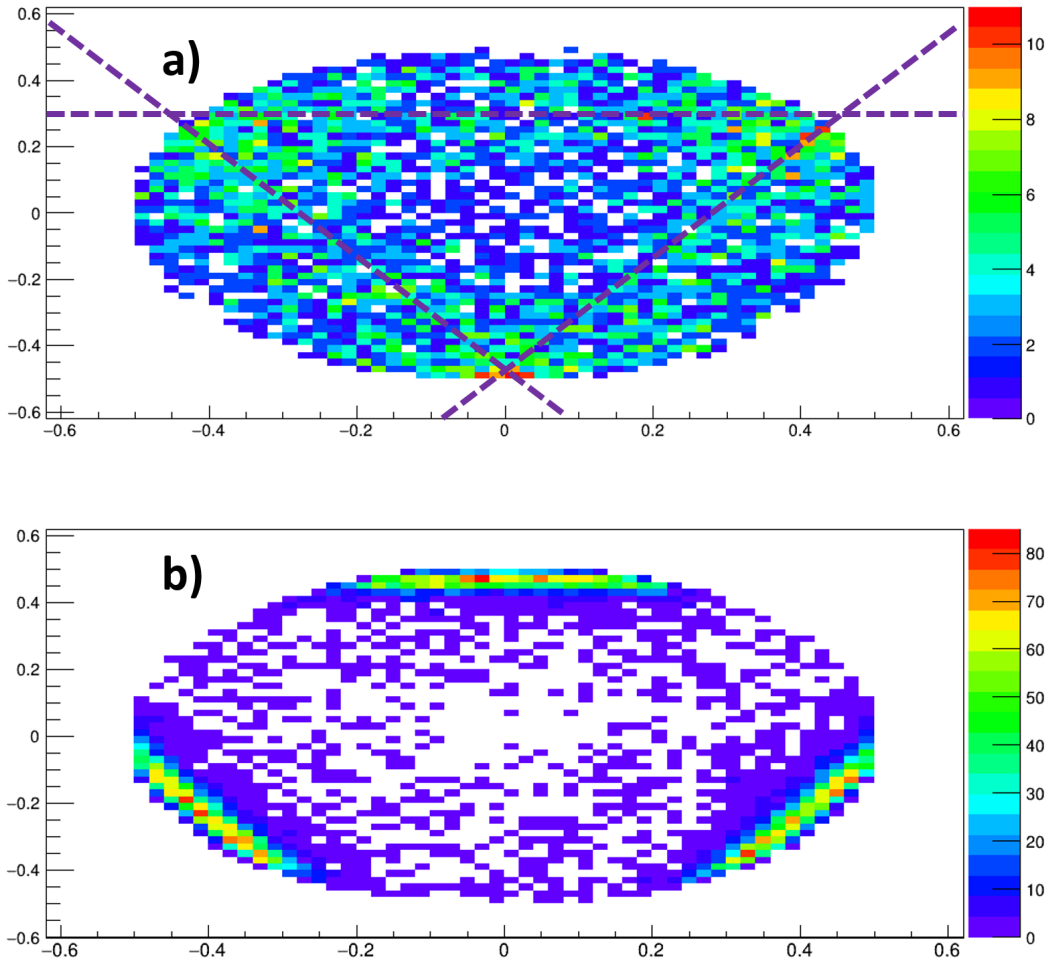

Figure 5.57: Dalitz plots for the observed energy levels in ^{12}C. Figure a) is gated on the Hoyle state with the region occupied by the sequential path overlaid with purple dashed lines. Figure b) shows the data gated on the broad 3^- state. The increased excitation energy limits the region of population for the sequential decay making it easier to distinguish true events.

the broad $3^-/2^+$ contribution, the background was reduced by $\sim 50\%$.

5.5.4 ^{16}O

In events with an α-particle multiplicity greater or equal to 4, one can search for states in ^{16}O. As with ^{12}C, one must be careful to ensure the correct decay path is reconstructed. Due to the poor angular resolution of the CHIMERA detectors, the width of the ^{8}Be(g.s) and ^{12}C(0_2^+) states is very broad so there can be ambiguities between the ^{8}Be+^{8}Be and ^{12}C(0_2^+)+α channels. The steps to produce these excitation spectra are as follows:

- Following the 3-α excitation function being created, a gate is placed around the Hoyle state. Any combination of 3 α-particles which fall within this gate are marked as originating from the decay of the Hoyle state.
- All combination of 4 α-particles are taken. Regardless of if these α-particles belong to a ^{8}Be(g.s) or Hoyle state decay, their excitation function is calculated using Equation 5.26.
- All combination of 2 α-particles which do not belong to a ^{8}Be(g.s) or to the Hoyle state are combined with all the previously "paired" ^{8}Be(g.s) that passed through the ground-state gate to produce the $^8\text{Be} + 2\alpha$ channel.
- All the possible pairings of ^{8}Be(g.s)+^{8}Be(g.s) are created to give the ^{8}Be+^{8}Be channel provided these ^{8}Be(g.s) did not originate from the Hoyle state.
- For the ^{12}C(0_2^+) channel, all α-particles (which do not belong to a ^{8}Be or ^{12}C(0_2^+)) are then combined with those α-particles which did arise from the Hoyle state to give the excitation spectrum for the $^{12}\text{C}(0_2^+) + \alpha$ channnel.

The results of the 4-α excitation functions will be presented for each beam energy.

Results for E_b = 160 MeV

The 4-α excitation function is shown in Figure 5.58 where a large double humped continuum can be seen. It is immediately apparent that, in comparison to ^{8}Be* and ^{12}C*, there is no near-threshold state apparent in the excitation function. The second peak in this excitation function seems to arise in roughly the same area (and with the same width) as the reconstructed ^{16}O from the measurement of a ^{12}C(0_2^+) which will

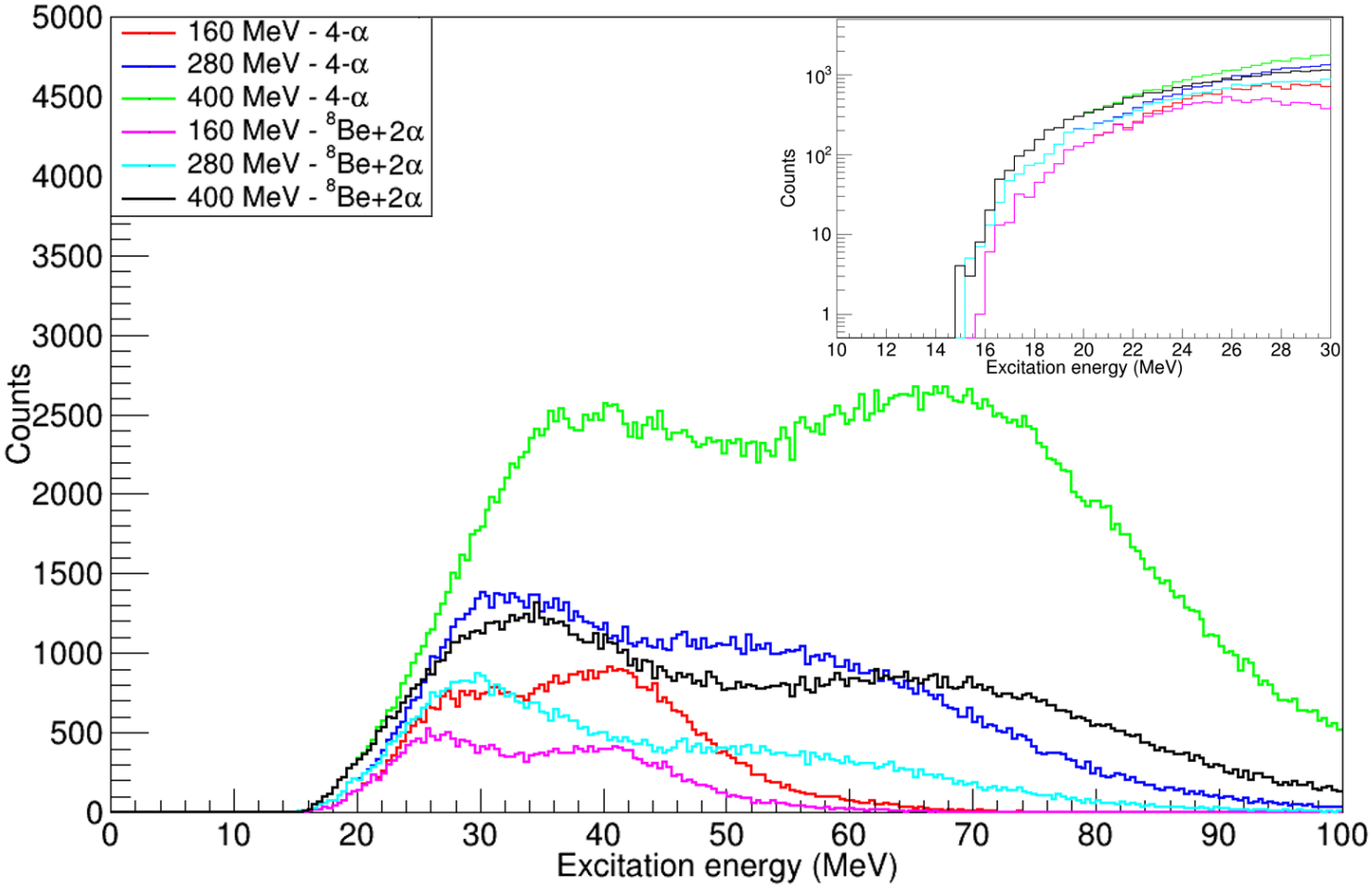

Figure 5.58: Excitation functions for ^{16}O for 4-α and those events where a ^{8}Be(g.s) is contained within the 4 α-particles. The inset shows an expanded view near the 4-α threshold (log-scale) where the yield rapidly tends to zero around the 4-α threshold at 14.44 MeV.

be discussed shortly. This decay mode is indicative of an immediate fissioning of the compound nucleus to excited states in both ^{12}C and ^{16}O. This decay mode was shown to have a large predicted contribution from the EHF calculations. An additional peak arises at a similar energy to those seen in the $4-\alpha$ and ^{8}Be paths albeit with a smaller intensity.

Examining the contribution of the $^{12}\mathrm{C}+\alpha$ channel (Figure 5.59) shows no obvious features in coincidence with the 4-α decay modes. One can observe that above the 4-α threshold the yield drops suggesting that events where the $^{16}\mathrm{O}^{\star}$ system is populated, the newly open channels reduce the branching ratio to the α_0 channel.

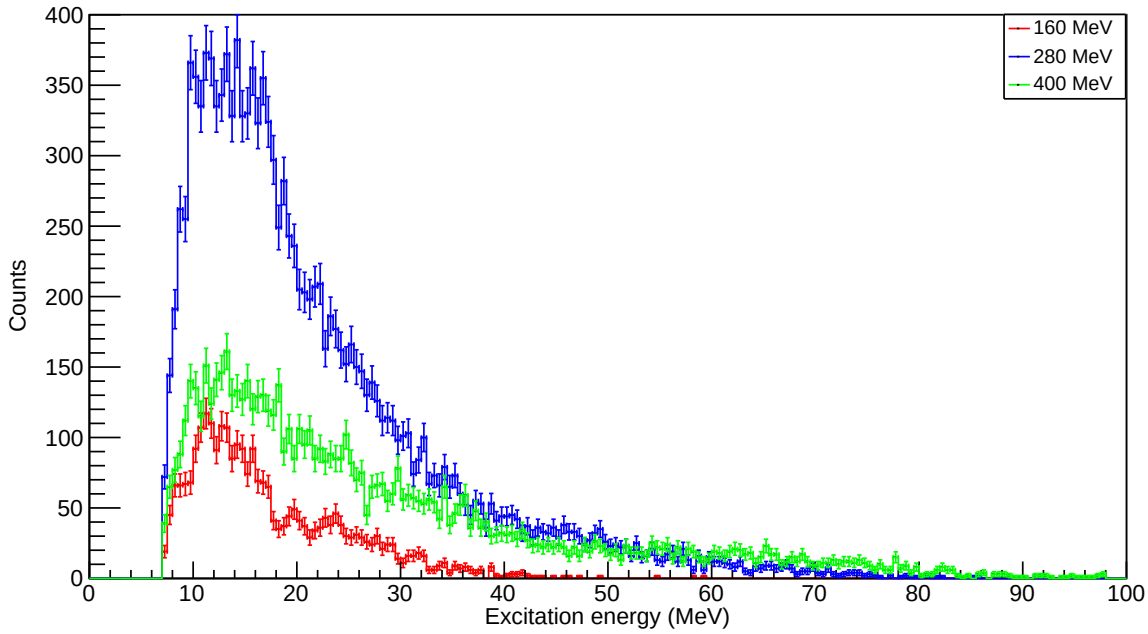

Figure 5.59: Excitation function in ^{16}O for the three beam energies in the ^{12}C(g.s) + α path.

As the excitation energy decreases towards the break-up threshold at 14.44 MeV, the 4-α yield rapidly decreases to zero. Examining the expected α-condensate decay channels, ^{8}Be + ^{8}Be and $^{12}\mathrm{C}(0_2^+)+\alpha$ as seen in Figure 5.60, the yield at higher excitation energies is reduced. This can be attributed to an increase of the 3 and 4-body phase space at higher excitation energies as well as removing the effect of incorrect combinatorial reconstructions for higher multiplicity events. At lower excitation energies, the ^{8}Be + ^{8}Be and $^{12}\mathrm{C}(0_2^+)+\alpha$ channels can be seen to constitute nearly 100% of the

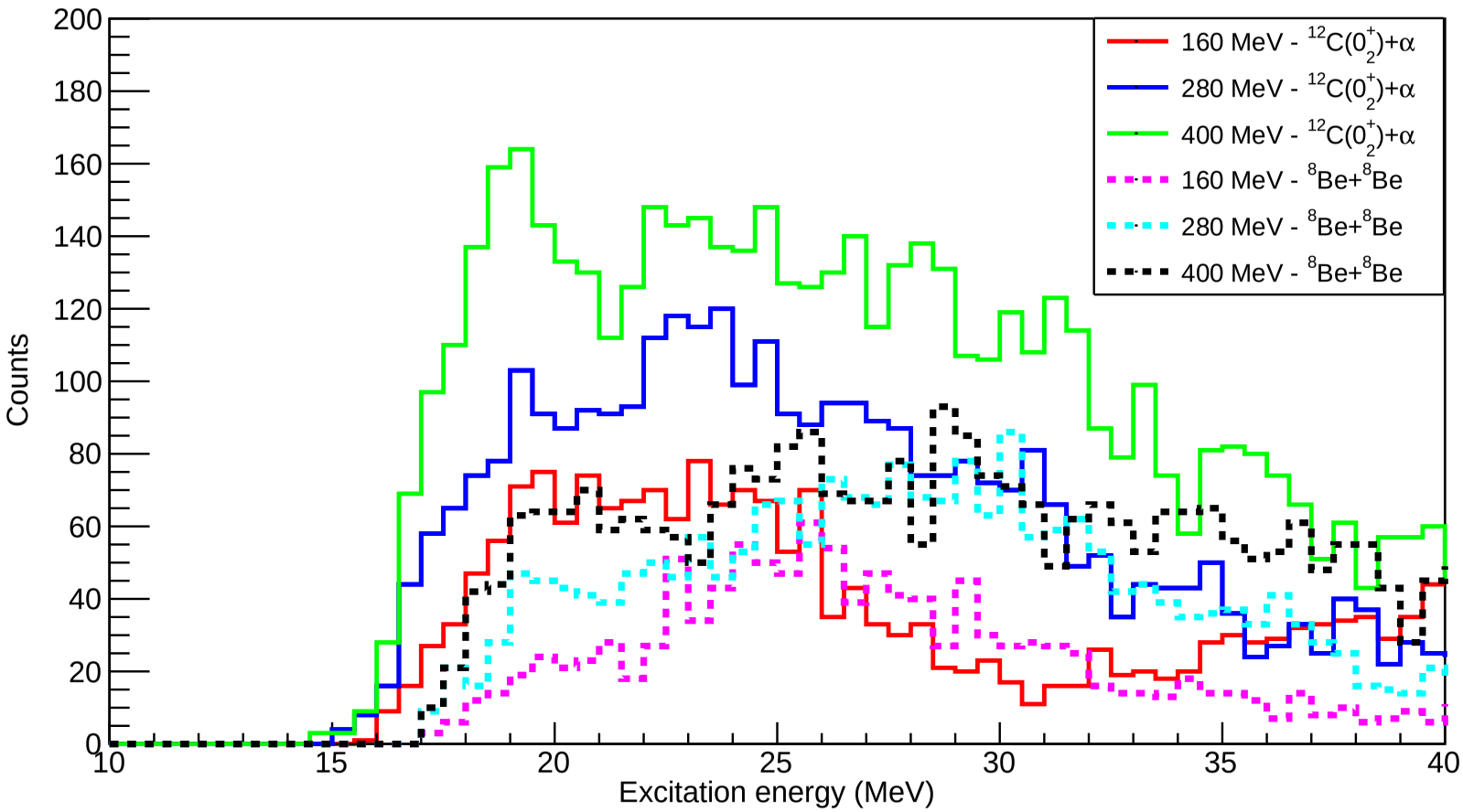

Figure 5.60: Excitation functions for ^{16}O for 4-α for those events which were from the ^{8}Be(g.s) + ^{8}Be(g.s) and $^{12}C(0^+_2)$ + α channels.

4-α decays suggesting the 4-α yield here is not the result of incorrect combinatorials.

To understand the features of these excitation functions, one can return to the event-mixing technique to generate the correlation function. Figure 5.61 shows the correlation function for type δ_1 (taking α-particles from separate events). This shows a good agreement overall with the shown data, especially at lower excitation energies where one sees a near one-to-one correspondence between the two. The event-mixing fails to describe the secondary bump in the data from 35 MeV $\rightarrow$ 45 MeV and at higher excitation energies, the mixing over-describes the random contribution here. The δ_2 mixing type (Figure 5.62) also describes the data well for low excitation energies and shares a very similar form to the δ_1 mixing although the contribution around 25 MeV is not described well by this mixing type. As with δ_1, the secondary hump is also not well described and the higher excitation energies are over-estimated by the mixing in comparison to the data. This is perhaps attributed by the fact that uncorrelated α-particles from a single event still include energy conservation so at high excitation energies (which correspond to larger differences in the α-particle energies) the data are more inhibited than the event-mixing where no such energy conservation is included.

This additional bump around 35 $\rightarrow$ 45 MeV is also evident in the reconstructed ^{16}O spectrum from measured $^{12}\mathrm{C}(0_2^+) + \alpha$ decays (Figure 5.63) as well as in the data from reconstructing the $^{12}\mathrm{C}(3_1^-) + \alpha$ path where a prominent secondary bump can be seen at the same energy (Figure 5.64). This, in combination with the absence of this feature from event-mixing suggests this contribution is a real feature of the 4-α break-up channel rather than from either mismatching between decay paths or uncorrelated events. The primary peak, which is not quite fully described by the δ_1 or δ_2 mixing is also evident in this decay mode. As suggested from the direct observation of the 4-α decay, this peak is weaker than that at a higher energy but also matches extremely well with the reconstructed spectrum from $^{12}\mathrm{C}(0_2^+)$ decays. Figure 5.63 shows the comparison between the measured $^{12}\mathrm{C}(0_2^+)+\alpha$ channel and the reconstructed ^{16}O spectrum which is calculated from the measurement of the Hoyle state with the ^{16}O generated from the missing momentum. For the 160 MeV data, there is a similarity between the two demonstrating the congruency of the $^{12}\mathrm{C}(0_2^+)+^{16}\mathrm{O}^\star$ as an important reaction mechanism at this excitation energy.

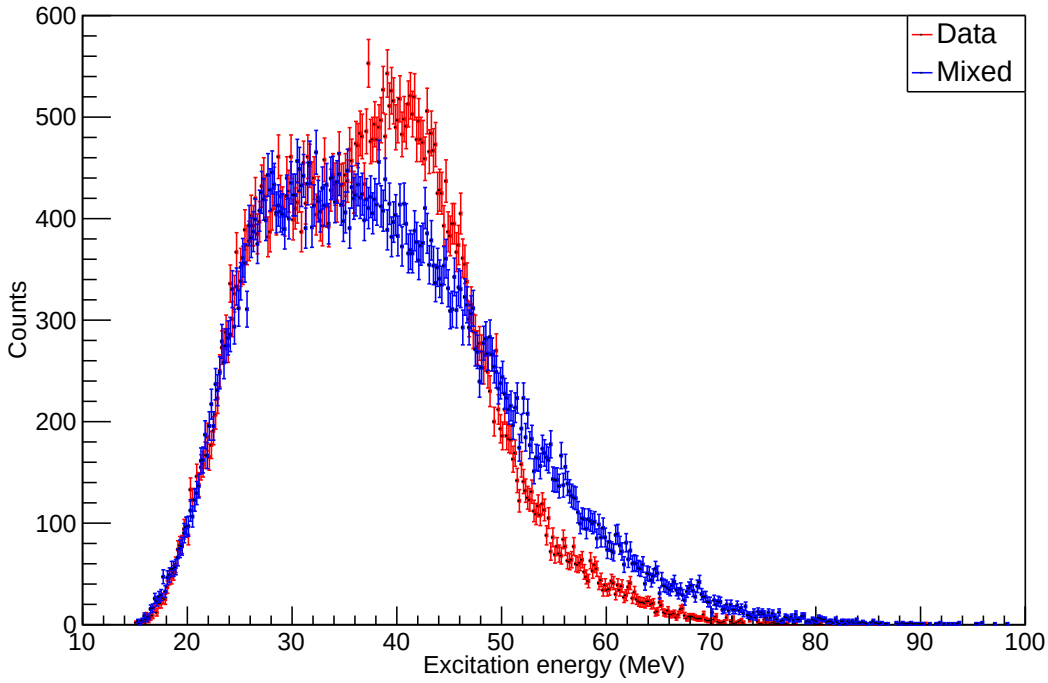

Figure 5.61: Event mixing - type δ_1 for the 4-α excitation function showing potential states in ^{16}O. The experimental data are shown in red in comparison to the event mixing results shown in blue for $E_b = 160$ MeV.

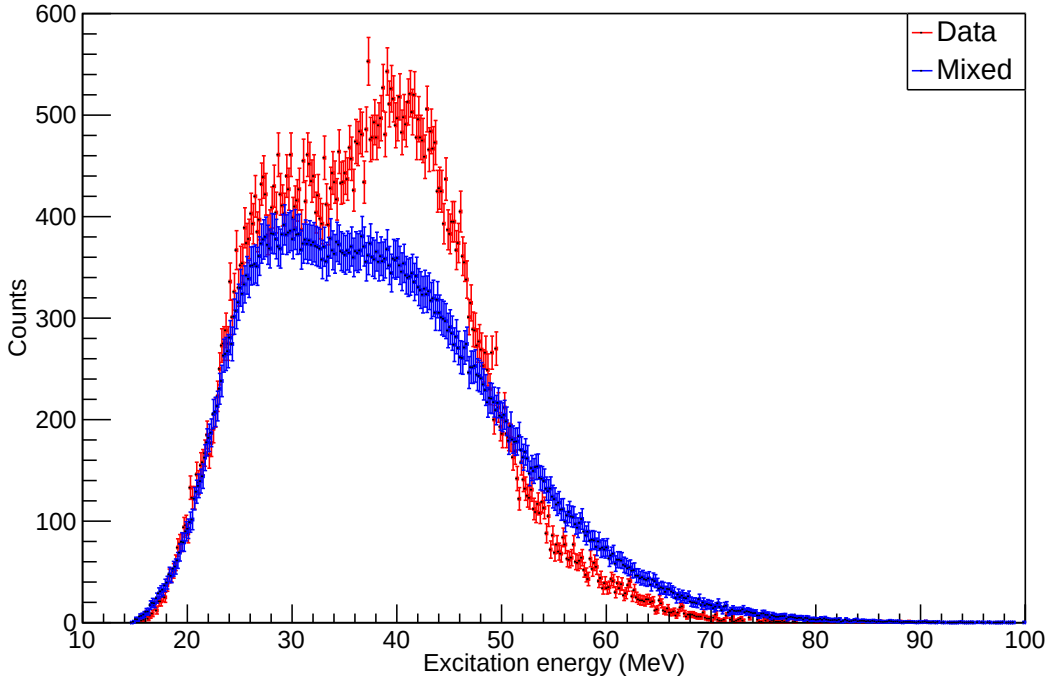

Figure 5.62: Event mixing - type δ_2 for the 4-α excitation function showing potential states in ^{16}O. The experimental data are shown in red in comparison to the event mixing results shown in blue for $E_b = 160$ MeV.

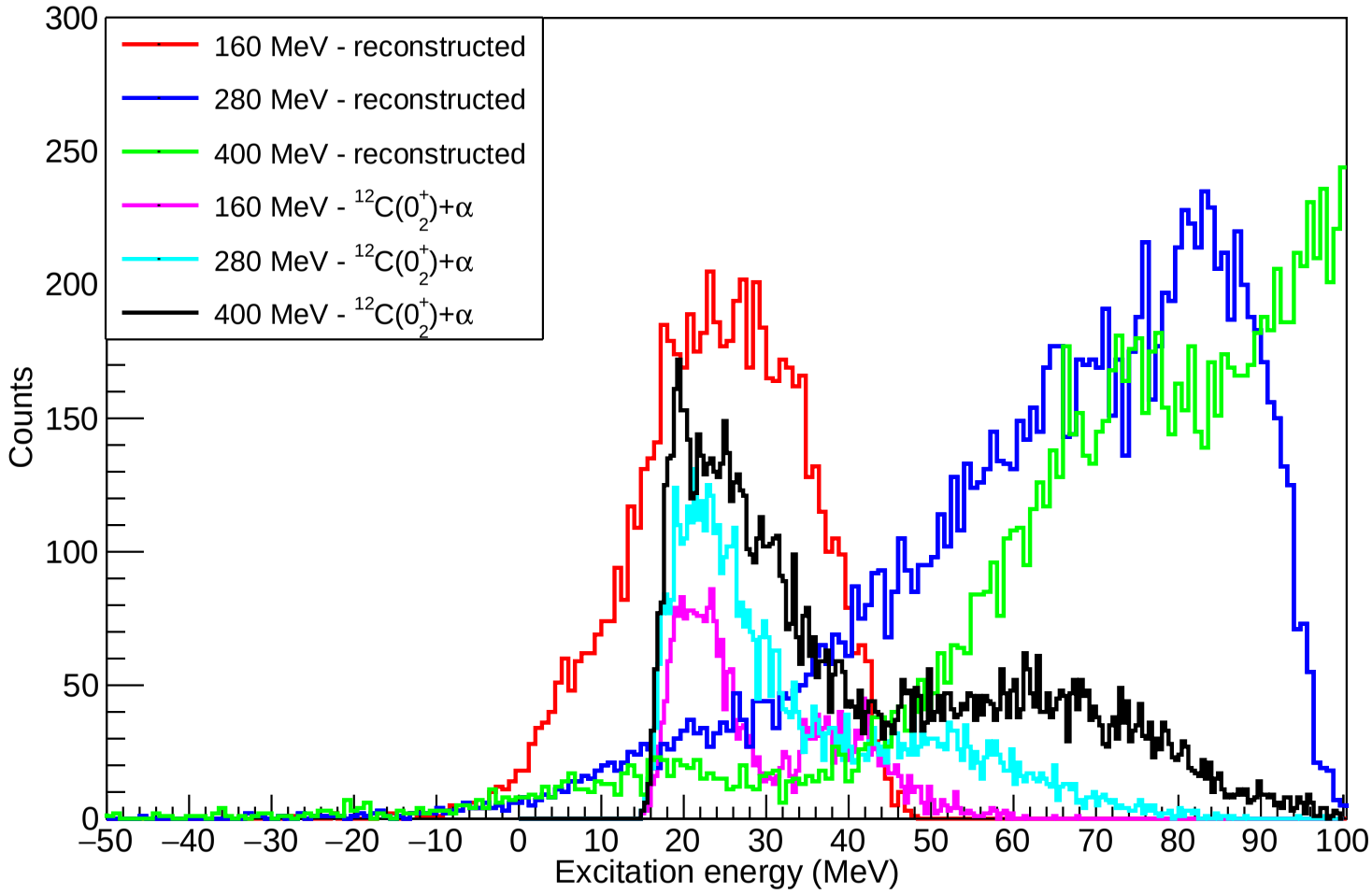

Figure 5.63: Comparison between the reconstructed ^{16}O excitation function (from measuring a $^{12}C(0_2^+)$ decay) versus the measured 4-α $^{12}C(0_2^+) + \alpha$ channel data.

Results for $E_b = 280$ MeV

One can follow the formulations used above in the 160 MeV data set and apply these to the 280 MeV beam data. The 4-α excitation function can be seen in Figure 5.58. The form, in both the 4-α and ^{8}Be channels, show a remarkably similar form to that seen in the 160 MeV data set albeit at a higher energy. Here however, the reconstructed spectrum from measuring the Hoyle state does not well describe the contribution seen and has a smaller yield in comparison to the measured 4-α excitation function. This is also visible in Figure 5.63 with the data from the other beam energies.

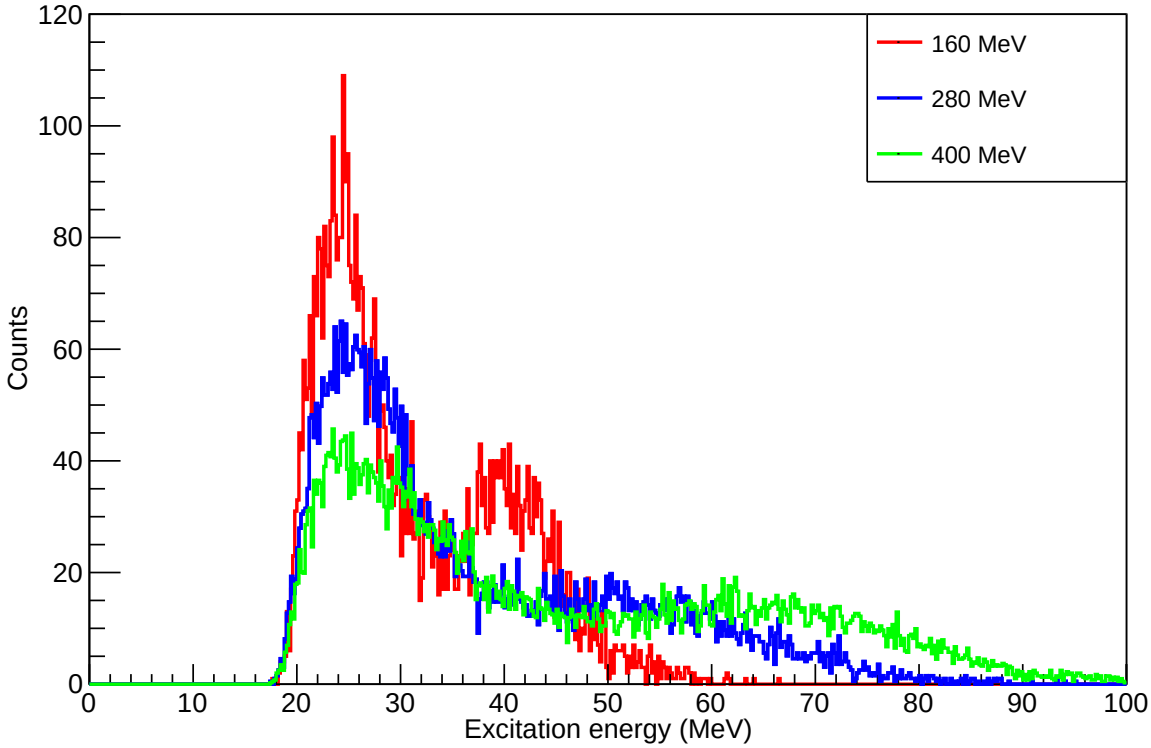

Figure 5.64: Excitation energy of ^{16}O in the $^{12}\mathrm{C}(3^-_1) + \alpha$ channel.

Examining the effect of event mixing to separate the uncorrelated and correlated α-particles, one sees that the δ_1 and δ_2 event mixing types both reasonably well describe the data seen (Figures 5.65 and 5.66). This is also consistent with these 4 α-particles belonging to uncorrelated (statistical decay) α-particles.

When one gates on 4-α events which can be comprised of $^{12}\mathrm{C}(0^+_2) + \alpha$ or ^{8}Be + ^{8}Be, a small amount of structure is apparent at this energy (Figure 5.60). At an energy of $\sim$

19 MeV, there is an increased yield which is particularly apparent in the $^{12}C(0_2^+) + \alpha$ channel as well as a smaller contribution in the $^8Be + ^8Be$ channel. Enhancements at this energy have been seen before in studies of ^{16}O with non-resonant population methods. An investigation into α-clustered states at this energy using the $^{13}C(\alpha, 4\alpha)n$ saw a state at around this energy with a strong cluster structure [144]. Previous investigations [100] have shown the existence of strongly populated states in this region with a high spin which may be preferentially populated due to the large angular momentum in the system at this higher energy.

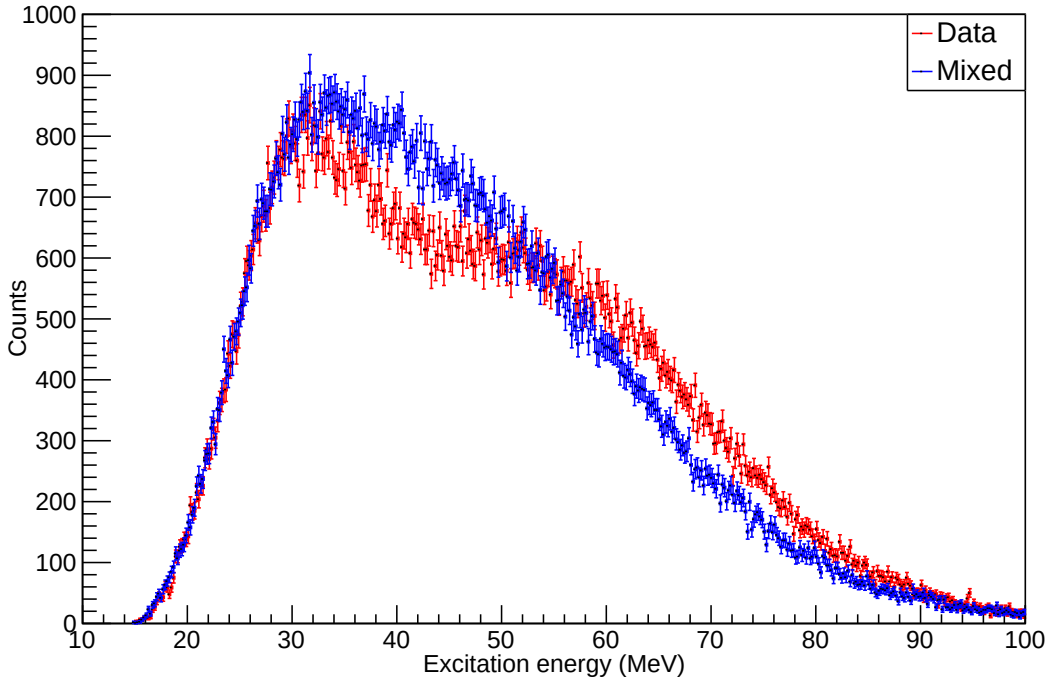

Figure 5.65: Event mixing - type δ_1 for the 4-α excitation function showing potential states in ^{16}O. The experimental data are shown in red in comparison to the event mixing results shown in blue for $E_b = 280$ MeV.

There is also an additional small enhancement at an energy of 23 MeV which is only visible in the $^{12}C(0_2^+) + \alpha$ channel. A large resonance has been seen in previous studies [99] albeit it most strongly in the $^8Be + ^8Be$ channel. The angular behaviour of the state at this region is consistent with a $J^\pi = 6^+$ therefore suggesting once again the large angular momentum of the state means it is preferentially populated.

Examination of the $^{12}C(3_1^-) + \alpha$ for the 280 MeV data shows very similar behaviour

to the $^{12}C(0_2^+) + \alpha$ channel (without the visible resonances) with a dominant peak from $\sim$ 20 MeV $\rightarrow$ 35 MeV with a broader tail. This suggests the two arise from the same source, an inference which will be revisited in Chapter 5.6.

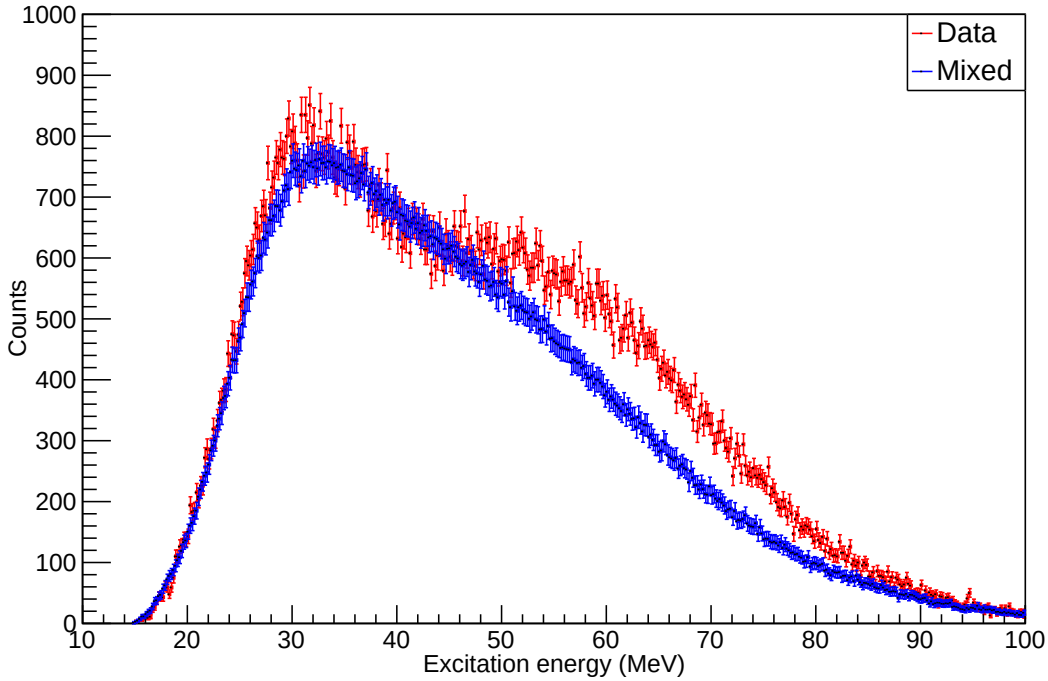

Figure 5.66: Event mixing - type δ_2 for the 4-α excitation function showing potential states in ^{16}O. The experimental data are shown in red in comparison to the event mixing results shown in blue for $E_b = 280$ MeV.

Results for $E_b = 400$ MeV

The 4-α excitation function can be seen in Figure 5.58. Here, one sees again very similar structure to the lower two beam energies albeit with a higher excitation.

When investigating the more clustered decay paths in Figure 5.63, the structures seen in the 280 MeV data at 19 MeV and 23 MeV are also apparent here with a seemingly stronger contribution, particularly in the $^{12}C(0_2^+) + \alpha$ channel at $E_x = 19$ MeV. The occurrence of these enhancements with two different beam energies and therefore different kinematic distributions strongly suggests these contributions to be real features. The extremely large width of the 19 MeV enhancement ($\sim$ 6 MeV) means that this is most likely a convolution of several states rather than a contribution from

a single strongly populated resonance whereas the 23 MeV state has been observed to have a large width of $\sim$ 1 MeV so these results are reasonably consistent.

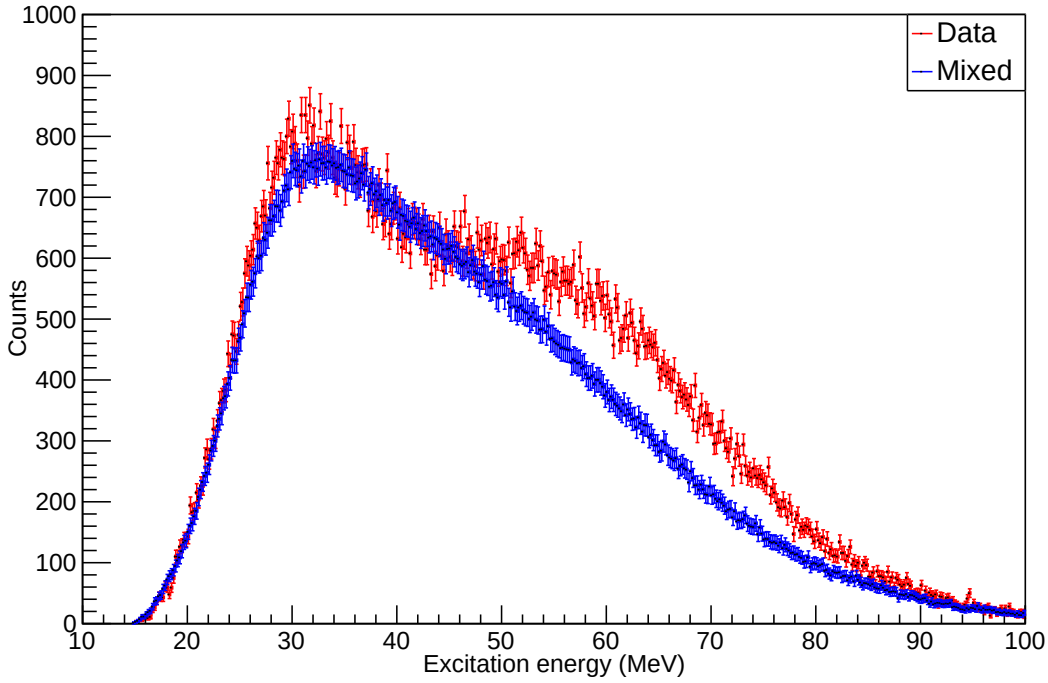

Figure 5.67: Event mixing - type δ_1 for the 4-α excitation function showing potential states in ^{16}O. The experimental data are shown in red in comparison to the event mixing results shown in blue for $E_b = 400$ MeV.

As with the previous beam energies, the $^{12}\mathrm{C}(3^-_1) + \alpha$ data show identical behaviour to the $^{12}\mathrm{C}(0^+_2) + \alpha$ channel without the evidence of the resonances seen at 19 and 23 MeV demonstrating for this beam energy, the $^{12}\mathrm{C}(0^+_2)$ and $^{12}\mathrm{C}(3^-_1)$ originate from the same source.

Conclusions

The only resonances seen are evident in the 280 and 400 MeV data at around 19 MeV and 23 MeV. One also sees structure at all three beam energies which cannot be described by event-mixing. This latter contribution can be attributed to the $^{12}\mathrm{C}^\star$ + $^{16}\mathrm{O}^\star$ decay mode as demonstrated from reconstruction of a ^{16}O from measuring the Hoyle state to give the missing energy.

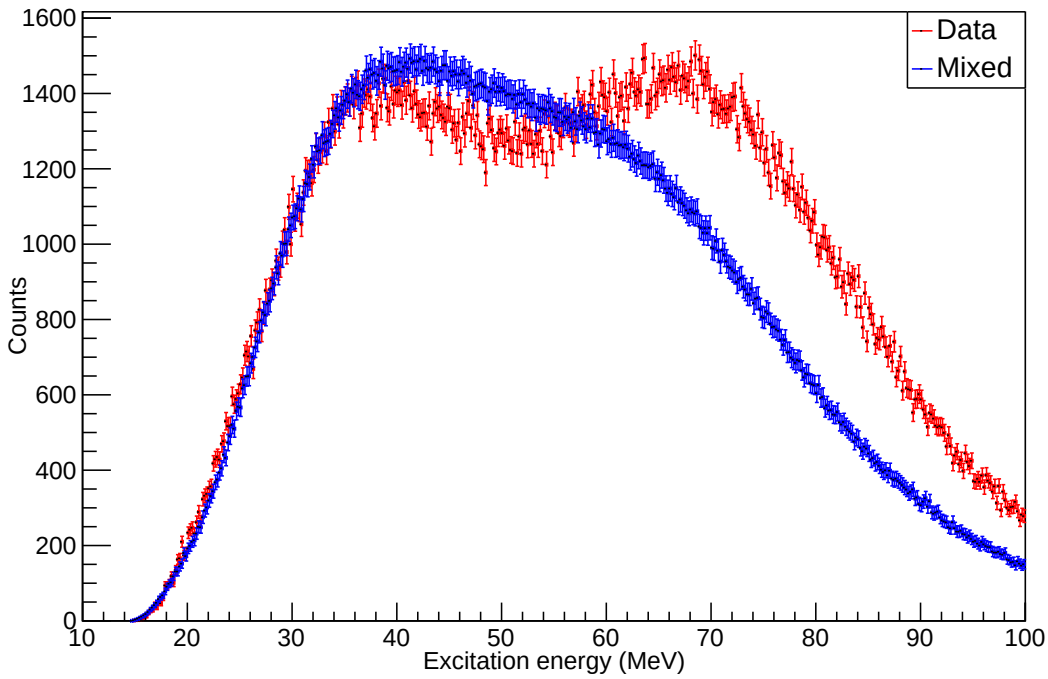

Figure 5.68: Event mixing - type δ_2 for the 4-α excitation function showing potential states in ^{16}O. The experimental data are shown in red in comparison to the event mixing results shown in blue for $E_b = 400$ MeV.

The additional features, including the yield extending down to the break-up threshold, can be described in terms of statistical α-particles which do not necessarily originate from the decay of ^{16}O. This result is at odds with the predictions from the EHF which showed that the population of ^{16}O for the 160 MeV should be focused to lower excitation energies therefore populating a larger number of discrete states. For the 280 and 400 MeV data, the majority of the cross section is expected in the continuum so any resonances should be dwarfed by uncorrelated α-particles. The situation seen however is the opposite with only the 280 and 400 MeV data showing any evidence of resonances. This suggests that the mechanisms explored by the EHF code (i.e. binary scission and statistical decay) do not explain the observed data well. This is backed up by the lack of agreement between the EHF multiplicity predictions and those from the data. A better description of the physics seen may therefore be placed in the Fermi break-up predictions where a larger cross section is predicted for 4-α break-up via no intermediate states.

5.5.5 ^{20}Ne

Following the chain of α-conjugate nuclei, one can investigate any possible discrete states populated in ^{20}Ne. This is first investigated for the 5-α path where all combinations of 5 α-particles are taken and reconstructed. The results for this can be seen in Figure 5.69. It is immediately apparent that, as with ^{16}O, there is no near threshold contribution evident in ^{20}Ne. For the three beam energies, one sees a single broad continuum. Examining the low excitation energy region, it is unusual that the counts here do not extend up to the 5-α threshold at $\sim$ 19.2 MeV. Instead, the three beam energies all extend no lower than $\sim$ 23 MeV. This can be attributed to the fact that the 5-α decay mode is energetically unfavourable over other paths such as the $^{16}\mathrm{O} + \alpha$ or ^{12}C+^{8}Be paths. To introduce a large degree of selectivity, events were selected where a $^{12}\mathrm{C}(0_2^+)$ and a ^{8}Be had previously been reconstructed. These two particles were then further investigated to examine their potential origin as from ^{20}Ne and the α-particles from the Hoyle state were combined with α-particles from ^{8}Be(g.s) (provided it did originate from the decay of the Hoyle state) and the excitation function calculated using Equation 5.26. The results for this mode are extremely limited but are presented in Figures 5.70 and 5.71. The 160 MeV data (Figure 5.70) show a contribution at an energy of $\sim$ 36 MeV with the 280 and 400 MeV data (Figure 5.71) showing a contribution at a slightly higher energy of $\sim$ 39 MeV. A similar contribution has been seen previously in a $^{12}\mathrm{C}(^{12}\mathrm{C},^{8}\mathrm{Be}+^{12}\mathrm{C}(0_2^+))^{4}$He reaction [145]. In this previous experiment, the 5-α contribution was also seen to be limited to $>$ 25 MeV. This apparent quenching of low energy strength is also apparent in compound nucleus experiments. The $^{16}\mathrm{O}(\alpha,^{20}\,\mathrm{Ne})$ reaction was previously examined to study states which decay into 5 α-particles via the ^{8}Be + ^{8}Be + α and $^{12}\mathrm{C}(0_2^+)$ + ^{8}Be paths [146]. The lowest energy state seen was at 24.5 MeV which is consistent with the current result. Examining the results from the EHF calculations earlier, a good population was expected (particularly for the 160 MeV predictions) above the 5-α threshold. Additionally, the predicted population for ^{20}Ne at 39 MeV was seen to be very small for the 400 MeV data suggesting mechanisms beyond the sequential decay model covered by this calculation.

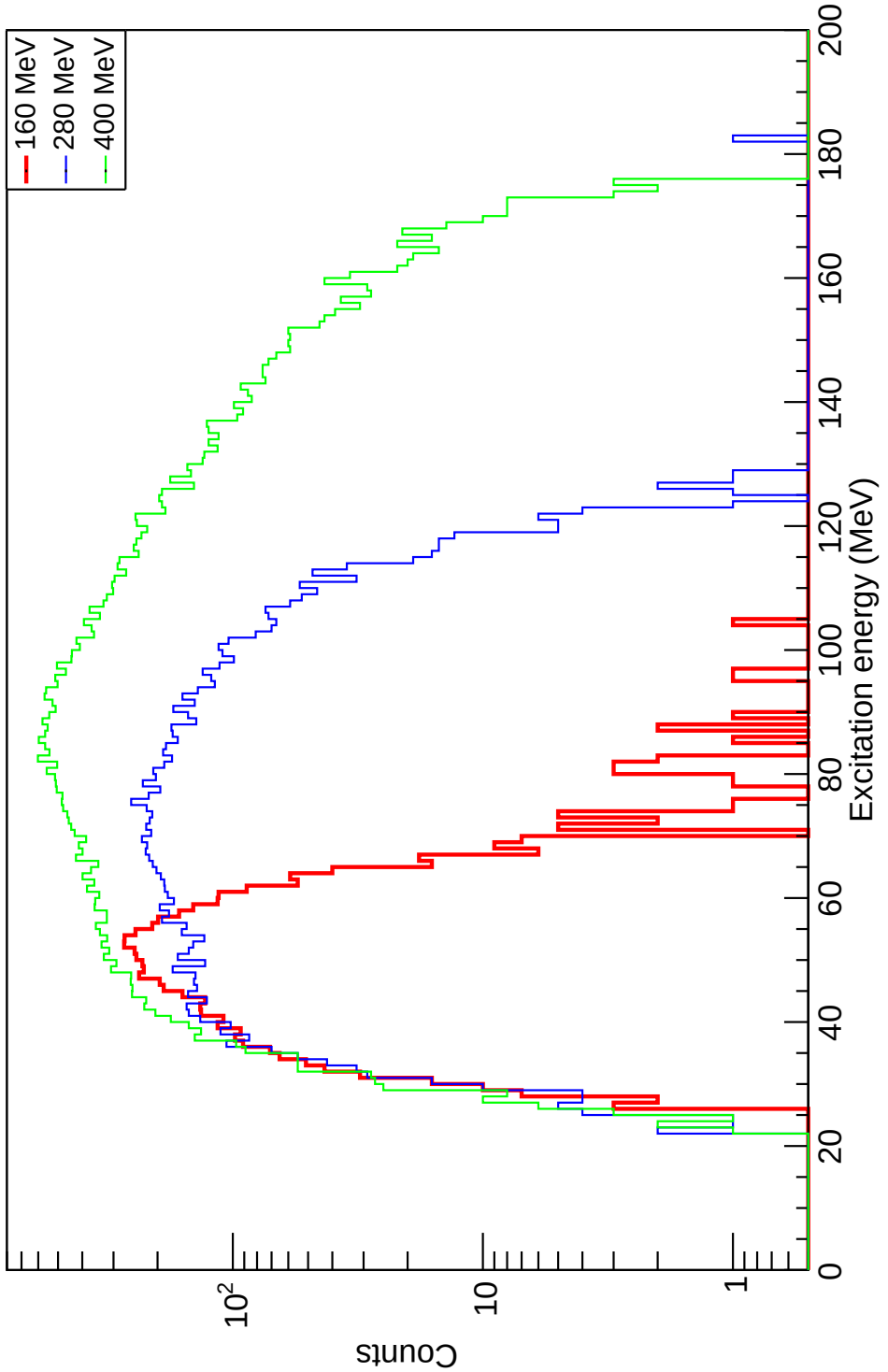

Figure 5.69: Excitation energy of ^{20}Ne via the 5-α correlation function (^{20}Ne,5α).

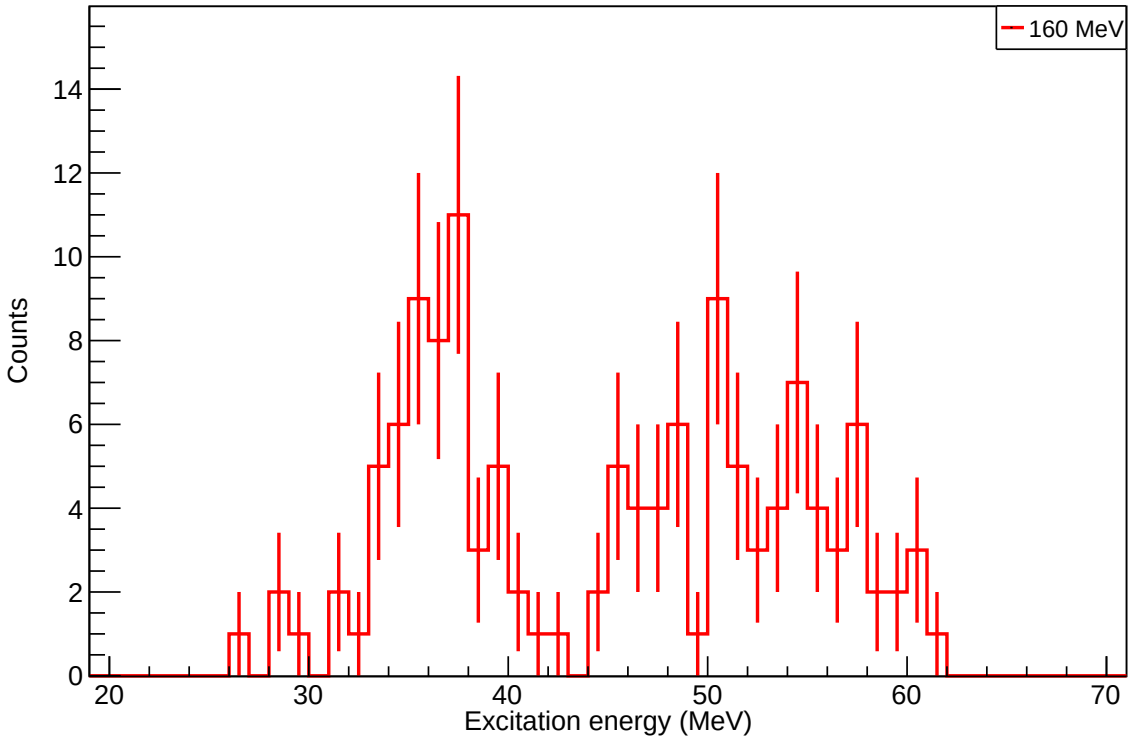

Figure 5.70: Excitation energy in ^{20}Ne reconstructed via ^{12}C(0_2^+) + ^{8}Be for E_b = 160 MeV showing a potential contribution from discrete resonances sticking above the continuum.

Analysis of the effect of event mixing for the 5-α system shows that the contribution of uncorrelated α-particles does a poor job (particularly for lower energies) at describing the excitation function seen. Figures 5.72-5.74 shows how the δ_1 type event mixing poorly describes the structure seen, in particular over-describing at small excitation energies close to the 5-α threshold. This suggests that the contributions seen for the 5-α structure at 160 MeV are perhaps indicative of genuine 5-α decays which are at least partially correlated. As the beam energy increased, the statistical α-particles better describe the seen structure as the uncorrelated particles start to dominate moving from a system best described by statistical decay to one which should be described in terms of the Fermi break-up model.

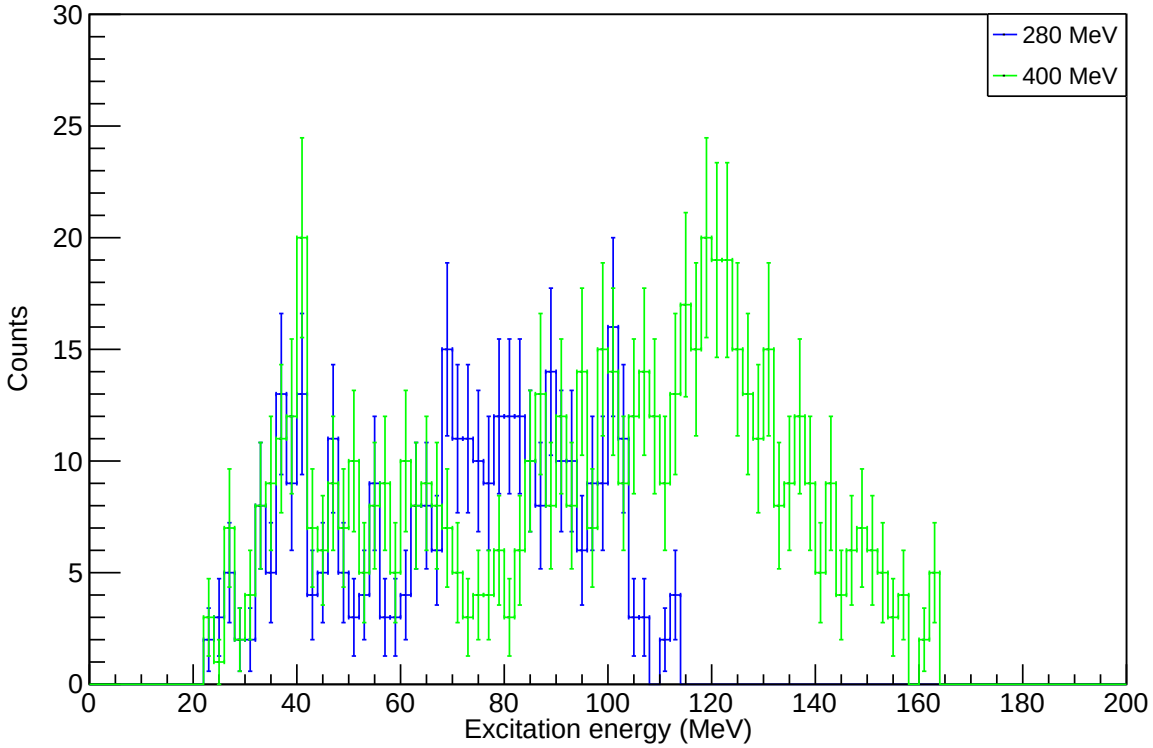

Figure 5.71: Excitation energy in ^{20}Ne reconstructed via ^{12}C(0_2^+) + ^{8}Be for E_b = 280 and 400 MeV. These data show an additional very broad distribution although any contributions may be limited by the statistics.

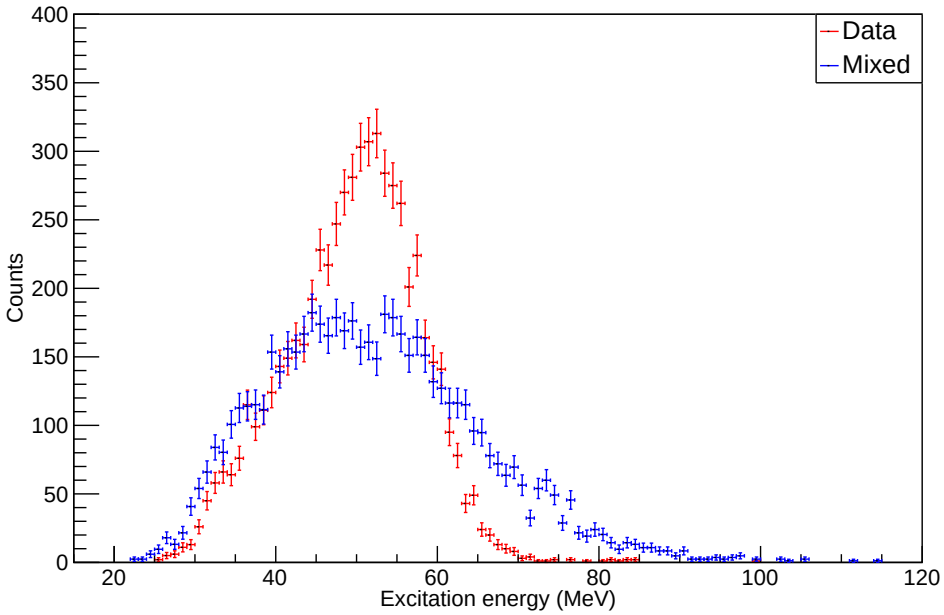

Figure 5.72: Comparison between the data and the event mixing of type δ_1 for E_b = 160 MeV for ^{20}Ne.

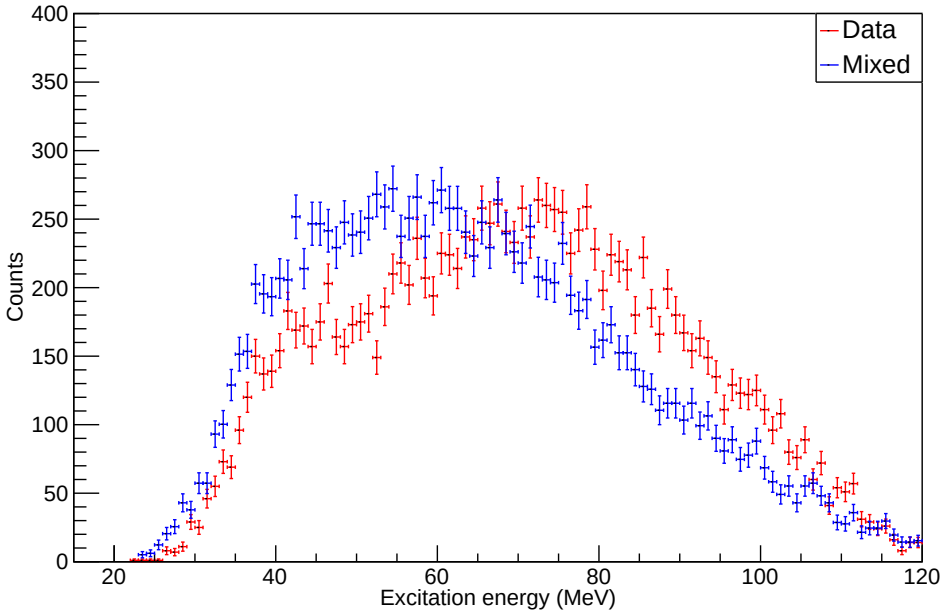

Figure 5.73: Comparison between the data and the event mixing of type δ_1 for E_b = 280 MeV for ^{20}Ne.

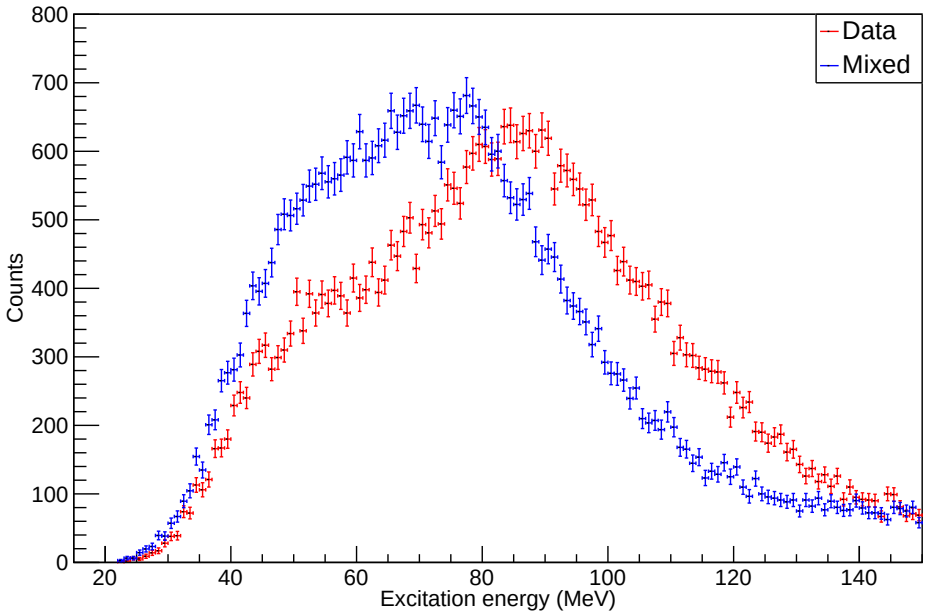

Figure 5.74: Comparison between the data and the event mixing of type δ_1 for E_b = 400 MeV for ^{20}Ne.

5.5.6 Conclusions

For all the α-conjugate nuclei seen, only near-threshold states were seen for ^{8}Be and ^{12}C, states already known to potentially be α-gas states. For ^{16}O and ^{20}Ne, one sees no such contribution. For the 160 MeV data, the EHF calculations showed that the N-α threshold region is expected to be well populated by the various modes (particularly fission). It is therefore unusual that no such states has been observed. The MC simulations was used here to demonstrate a good efficiency down to the barrier by virtue of the low energy coverage and granularity of the detector.

Figures 5.75 and 5.76 show the efficiency profiles for the three beam energies for ^{16}O and ^{20}Ne. These were calculated by the ^{16}O*+^{12}C(g.s) decay path to remove any incorrect combinatorials from mismatching of α-particles. These demonstrate the good efficiency down to the N-α thresholds for both ^{16}O and ^{20}Ne. The lack of counts here is therefore not indicative of the detector response but rather can be attributed to the inhibiting of the desired N-α decay channel by the small energy available in the system to overcome the Coulomb barrier. To directly detect the evidence of $N-\alpha$ gas states via their characteristic break-up channel into N α-particles, one must therefore move

to a system where this Coulomb barrier is no longer prohibitive. This is discussed in Chapter 8.

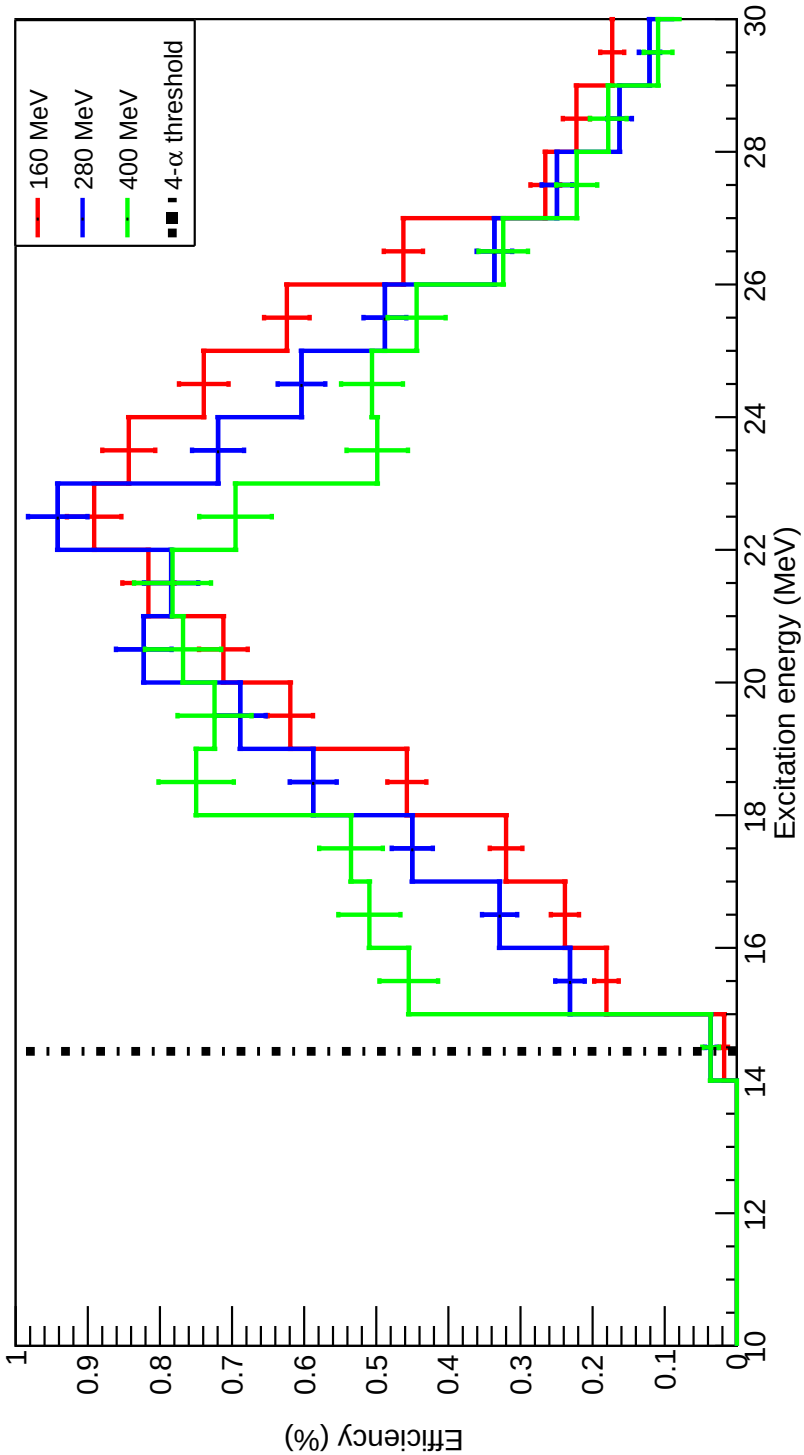

Figure 5.75: Efficiency profile for $^{16}\mathrm{O} \rightarrow 4\alpha$.

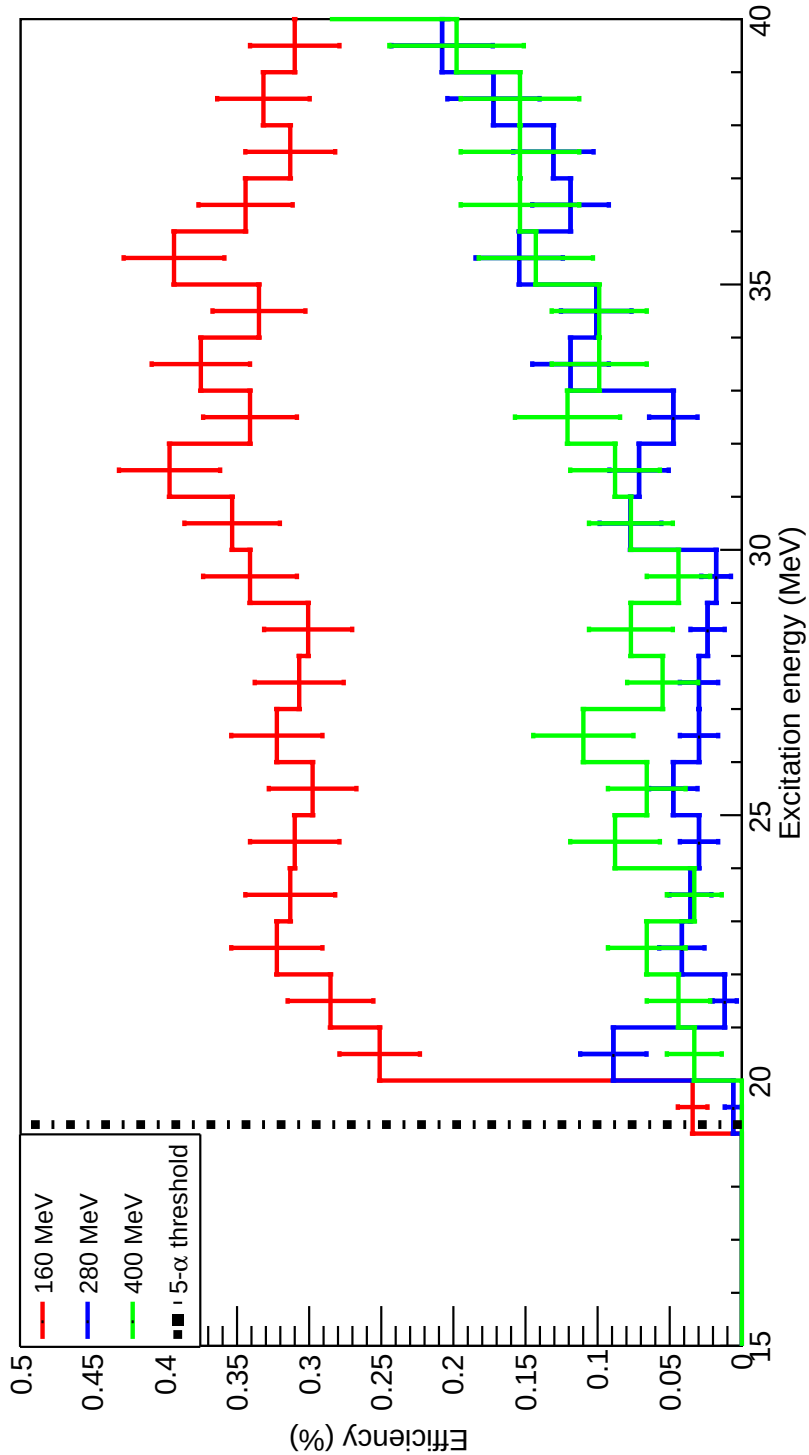

Figure 5.76: Efficiency profile for ^{20}Ne $\rightarrow 5\alpha$.

5.6 Origins of the reconstructed states in the nuclei of interest

Following the conclusions that the dominant reaction mechanism for high multiplicities isn't that of statistical decay but rather multi-particle break-up, it is important to discuss where this population of the seen states arises from. One must be careful to ensure they do not originate from inelastic scattering of the beam and target as this reaction mechanism will interfere with the signatures one requires from the compound nucleus formation. Previous investigations have shown the formation of ground-state nuclei detected do not primarily originate from direct reactions or two-body fission, however this must be proven for the excited states too.

To test the origin of these N-α systems, one can reconstruct the missing momentum to examine any possible missing particle. By looking at the total energy of the N-α system and the energy of the reconstructed particle one can calculate the reaction Q-value (as in Chapter 5.3.1 the negative Q-value is plotted such that one can clearly see the excitation energy inside the reconstructed particle). If this generates a peak corresponding to the expected break-up energy of the system then one knows this system arose from the two-body decay. If the missing particle is either a ^{12}C(g.s) or ^{16}O(g.s) then this can potentially be ascribed to inelastic scattering. If the yield is isotropic (or rather less forward focused) then this can be attributed instead to compound nucleus break-up rather than inelastic scattering.

These total reaction Q-value plots will be discussed for each N-α system.

5.6.1 ^{8}Be

To examine the source of the ^{8}Be nuclei, a gate was placed on the ^{8}Be(g.s) ($E_x < 1$ MeV) and the undetected ^{20}Ne was reconstructed from the missing momentum. The total reaction (negative) Q-value is then plotted, the results of which can be seen in Figure 5.77. The double-humped aspect to the plot originates from the efficiency profile for ^{8}Be as a function of lab angle. A region of poor coverage then corresponds to the dip in between the two features.

For the 160 MeV data, a small amount ($2 \times 10^{-3}\%$) of ^{8}Be measured correspond to the correct Q-value for ^{8}Be + ^{20}Ne(g.s) break-up (-2.6 MeV) however the vast majority suggest alternate decay pathways. One can compare the results to those obtained from Monte Carlo simulations which were performed for paths that procede via the

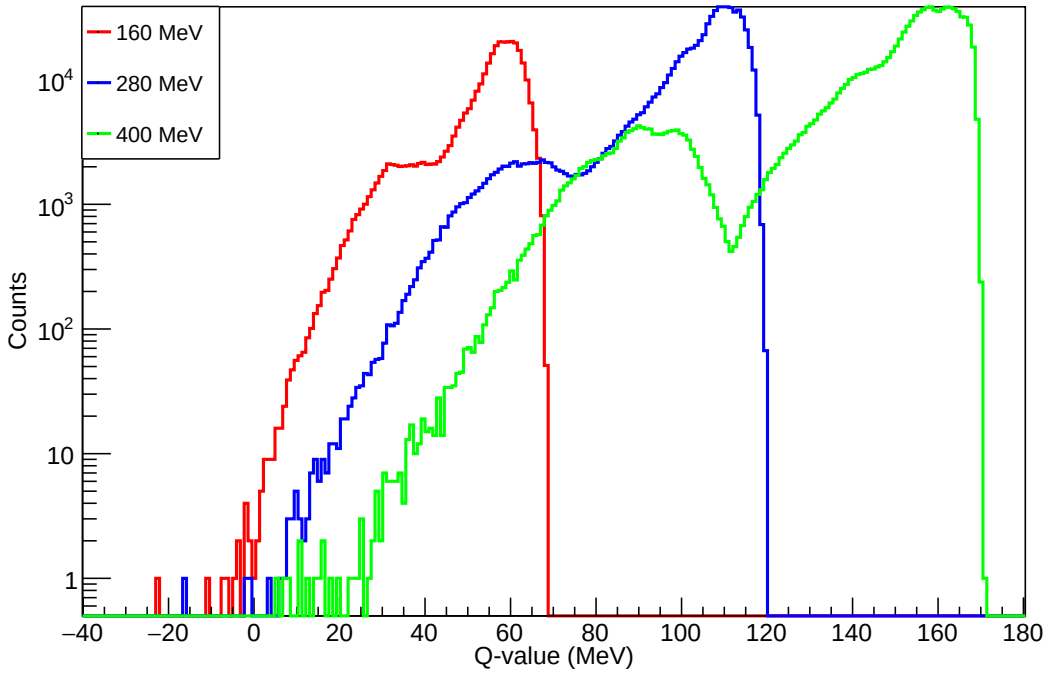

Figure 5.77: (Negative) Q-value spectrum when reconstructing an unmeasured ^{20}Ne from the missing momentum from a measured ^{8}Be(g.s).

^{8}Be+^{20}Ne* channel. These Monte Carlo simulations model a decay to a near-threshold state at $E_x = 20.1$ MeV. This is a great test of the efficiency of reconstructing a ^{20}Ne*. If there is an additional component above a constant background, this could be indicative of a ^{20}Ne condensed state. Such a resonance may be extremely close to the α + ^{16}O(0^+_6)-decay barrier and therefore favour other decay modes (i.e. ^{16}O(g.s)+α). This method can be used to measure the population of states in ^{20}Ne regardless of their subsequent decay modes. Additionally, states which have an α-cluster signature are more likely to be populated if they are a decay product along with ^{8}Be. The results from the Monte Carlo show the overall reconstruction of a narrow resonance from measuring the ^{8}Be as reasonably poor with resolution, $\Gamma_{\text{exp}} \sim 5.2$ MeV at $E_b = 160$ MeV. However, when one limits the results to ^{8}Be measured at low angles this value improves to $\Gamma_{\text{exp}} \sim 1.5$ MeV as the angular resolution is much better here. This behaviour can be seen in Figure 5.78a which shows the Q-value against the angle of the detected ^{8}Be. The results from the experimental data are shown below the Monte Carlo data in Figure 5.78b where similar features can be seen as in the simulated data. The constant band visible

across a range of lab-angles giving a constant Q-value however is absent suggesting the **absence of a strong non-sequential ^{8}Be+^{20}Ne* break-up**. This prediction follows the EHF calculation predictions which show the majority of the ^{8}Be one populates are via the sequential decay with only a negligible contribution arising from binary scission. The same conclusion arises from the Fermi break-up model.

5.6.2 ^{12}C(0_2^+)

As many of the measured ^{8}Be can also be attributed to the decay of ^{12}C(0_2^+), one may expect more interesting results from reconstructing the missing ^{16}O from a two-body ^{28}Si $\rightarrow$ ^{16}O +^{12} C(0_2^+) break-up. For a possible ^{12}C(0_2^+)+^{16}O(0_6^+) decay, the emitted ^{12}C(0_2^+) can be expected to have a reasonably large total kinetic energy as in the COM system, the ^{12}C* and ^{16}O* share the high excitation available in the compound nucleus. Figures 5.79-5.81 show the kinetic energy of any population of the Hoyle state for the different Monte Carlo decay modes. Decay paths 10 and 11 (from Table 5.3) correspond to ^{12}C*+^{16}O* products which can be seen to have the highest kinetic energy Hoyle decay products. The data also show a number of similarly high energy Hoyle decay products which cannot be explained by the other decay paths. Reconstruction of any ^{12}C(0_2^+) from 3 α-particles at a low total kinetic energy are more likely to correspond to more sequential α-decays (e.g. path 1) where the kinetic energy can be seen to peak at smaller values. At these lower energies, the remaining decay paths are hard to differentiate solely from the kinetic energy with the current energy thresholds for this experiment. For the 400 MeV data however, an increased count at low energies can be seen to agree well with decay paths 10 and 11 suggesting as previously seen a good contribution from the ^{12}C* +^{16} O* scission.

To follow the possibility of Hoyle decays from the ^{12}C*+^{16}O* decay paths, one can see the Q-value spectrum from reconstructing the missing ^{16}O from the decay of ^{12}C(0_2^+). Figures 5.82, 5.83 and 5.84 show this Q-value spectrum for the three beam energies in comparison to the Monte Carlo simulations for the different decay paths.

Examination of the data for all three beam energies can be seen to have two components, one peak centered $\sim \frac{3}{8}E_b$ corresponding to a ^{12}C(0_2^+) generated from a source other than ^{12}C* + ^{16}O* (which is reproduced well by the MC). The second peak is centered around 0 MeV and corresponds to a two-body break-up of the compound nucleus into ^{12}C(0_2^+) + ^{16}O(g.s). This peak is broader than expected from the MC. Examination of the simulated data shows reconstruction of paths 10 and 11 for ^{16}O at 15.1 MeV has

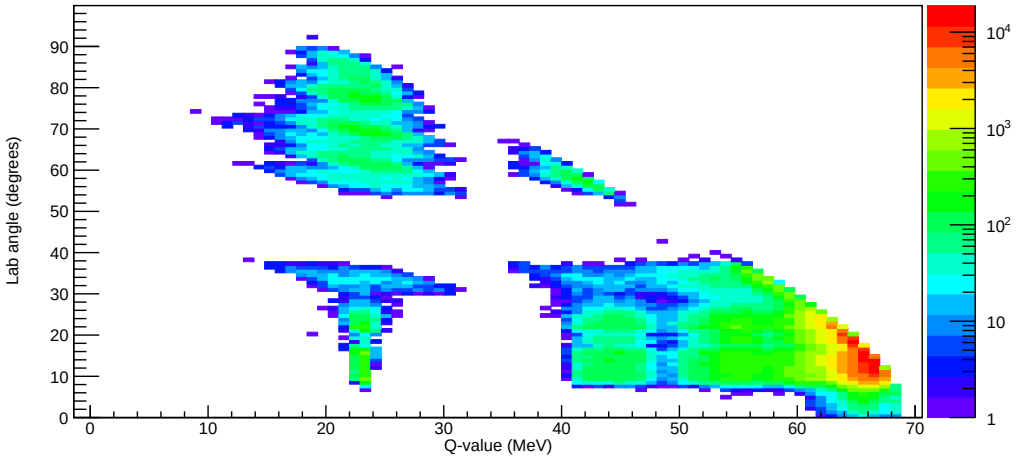

(a) Monte Carlo data for (negative) Q-value spectrum when reconstructing an unmeasured ^{20}Ne from the missing momentum from a measured ^{8}Be(g.s) against the angle of the detected ^{8}Be(g.s). $E_b = 160$ MeV.

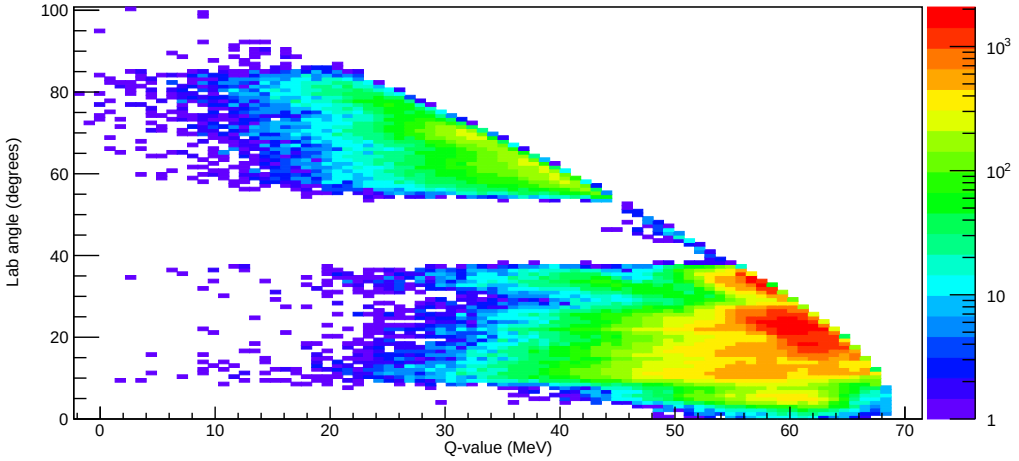

(b) Experimental data (negative) Q-value spectrum when reconstructing an unmeasured ^{20}Ne from the missing momentum from a measured ^{8}Be(g.s) against the angle of the detected ^{8}Be(g.s). $E_b = 160$ MeV.

Figure 5.78: Comparison of the MC and experimental data when examining the (negative) Q-value for the ^{20}Ne + ^{8}Be(g.s) path following the measurement of the ^{8}Be.

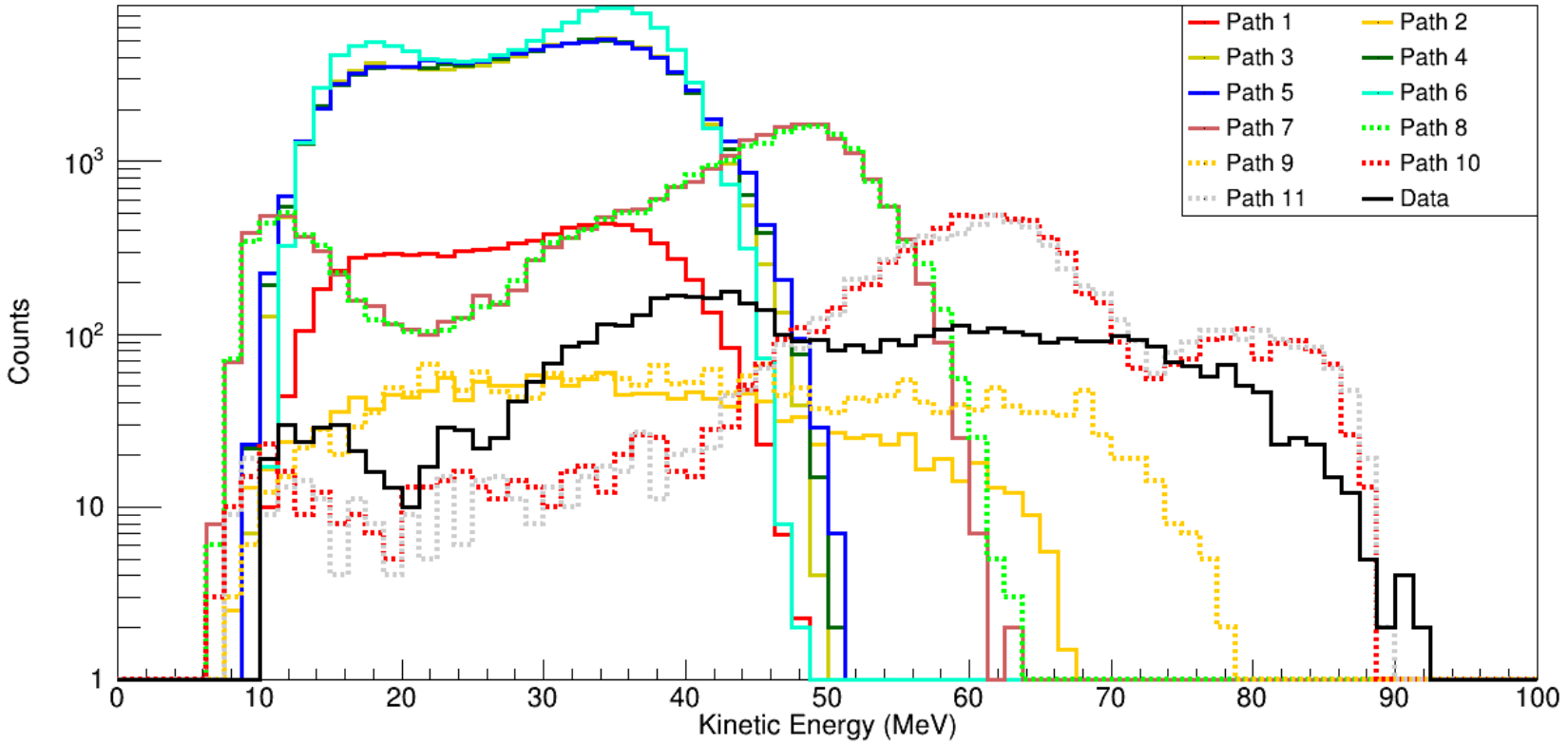

Figure 5.79: Kinetic energy of the reconstructed Hoyle state for the different MC modes and experimental data for E_b = 160 MeV.

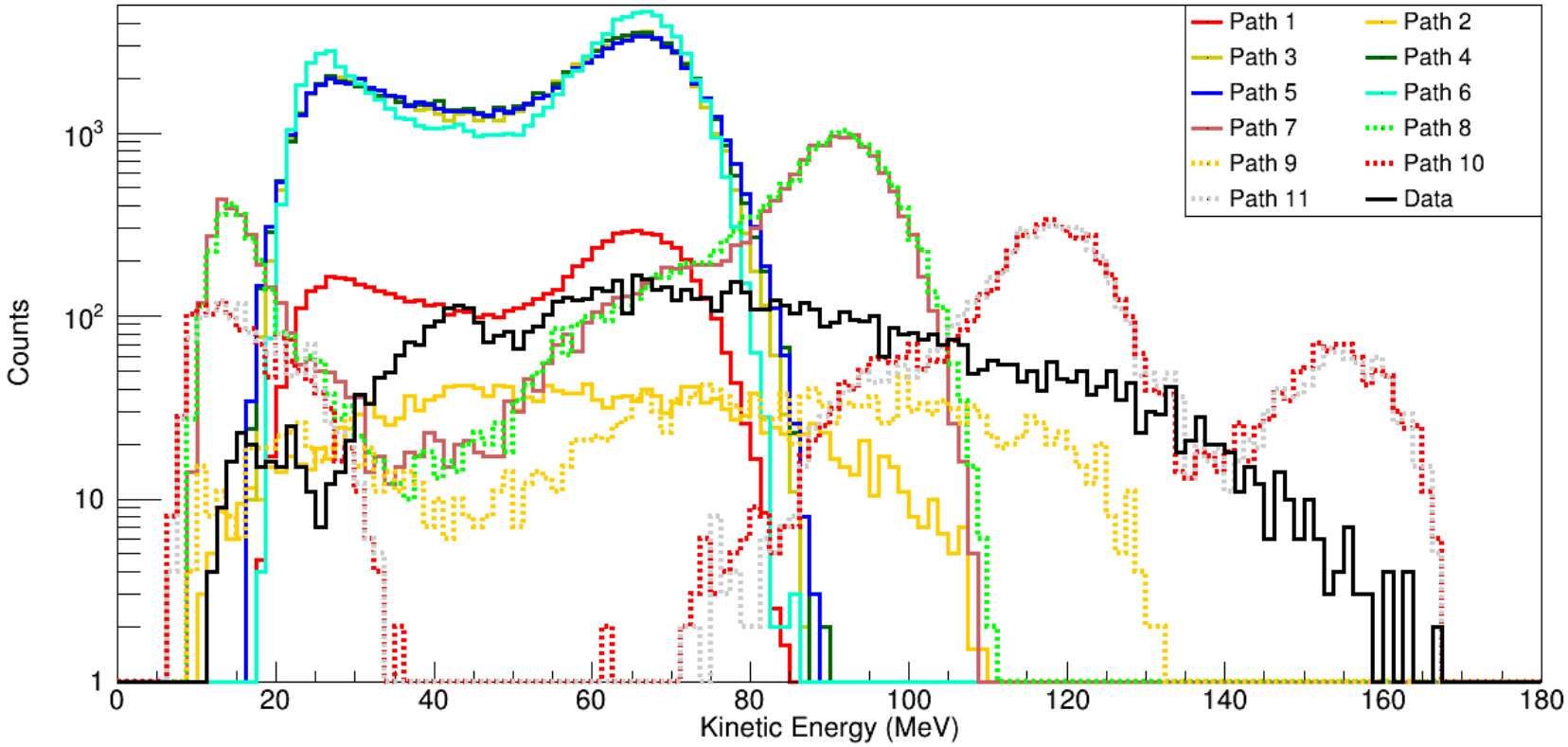

Figure 5.80: Kinetic energy of the reconstructed Hoyle state for the different MC modes and experimental data for E_b = 280 MeV.

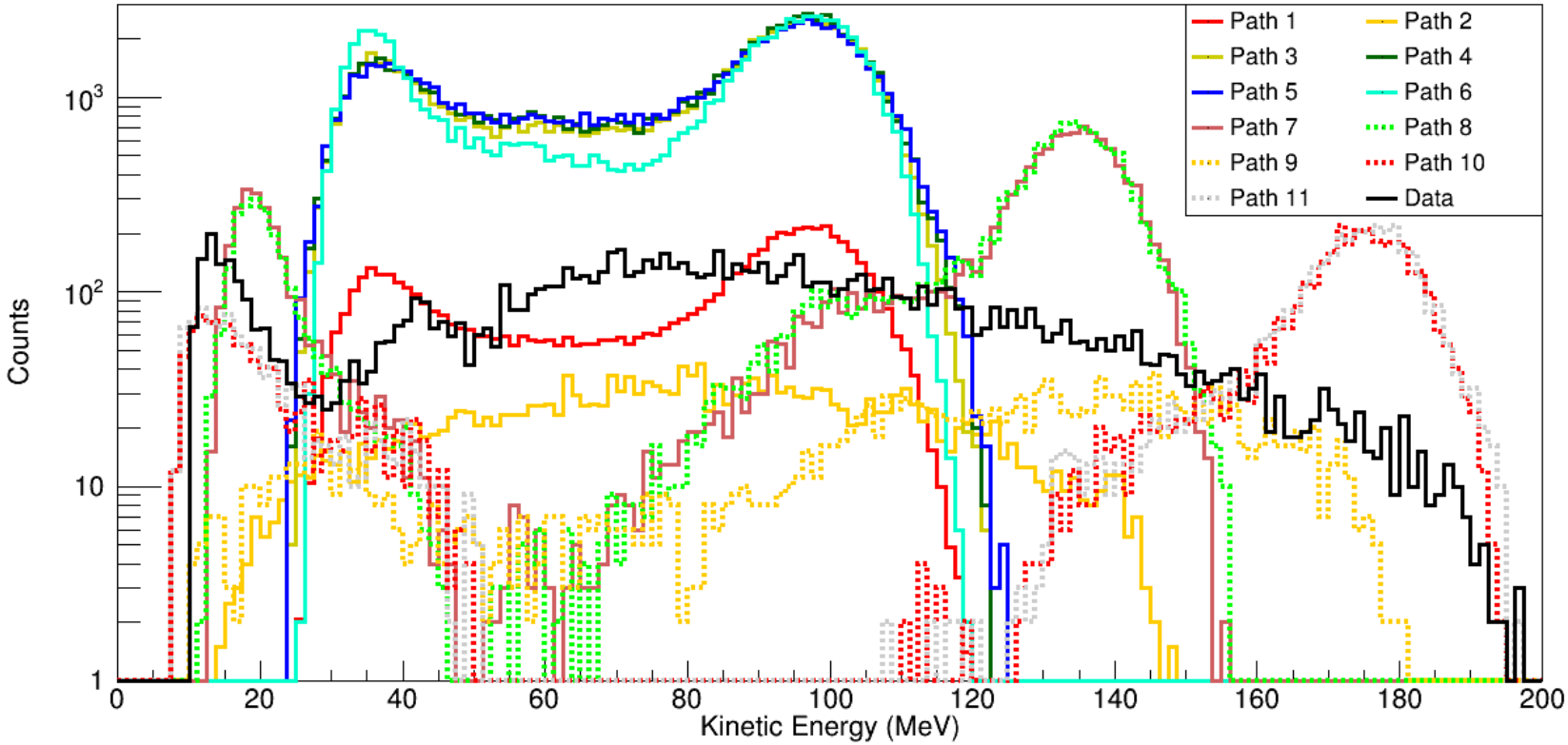

Figure 5.81: Kinetic energy of the reconstructed Hoyle state for the different MC modes and experimental data for E_b = 400 MeV.

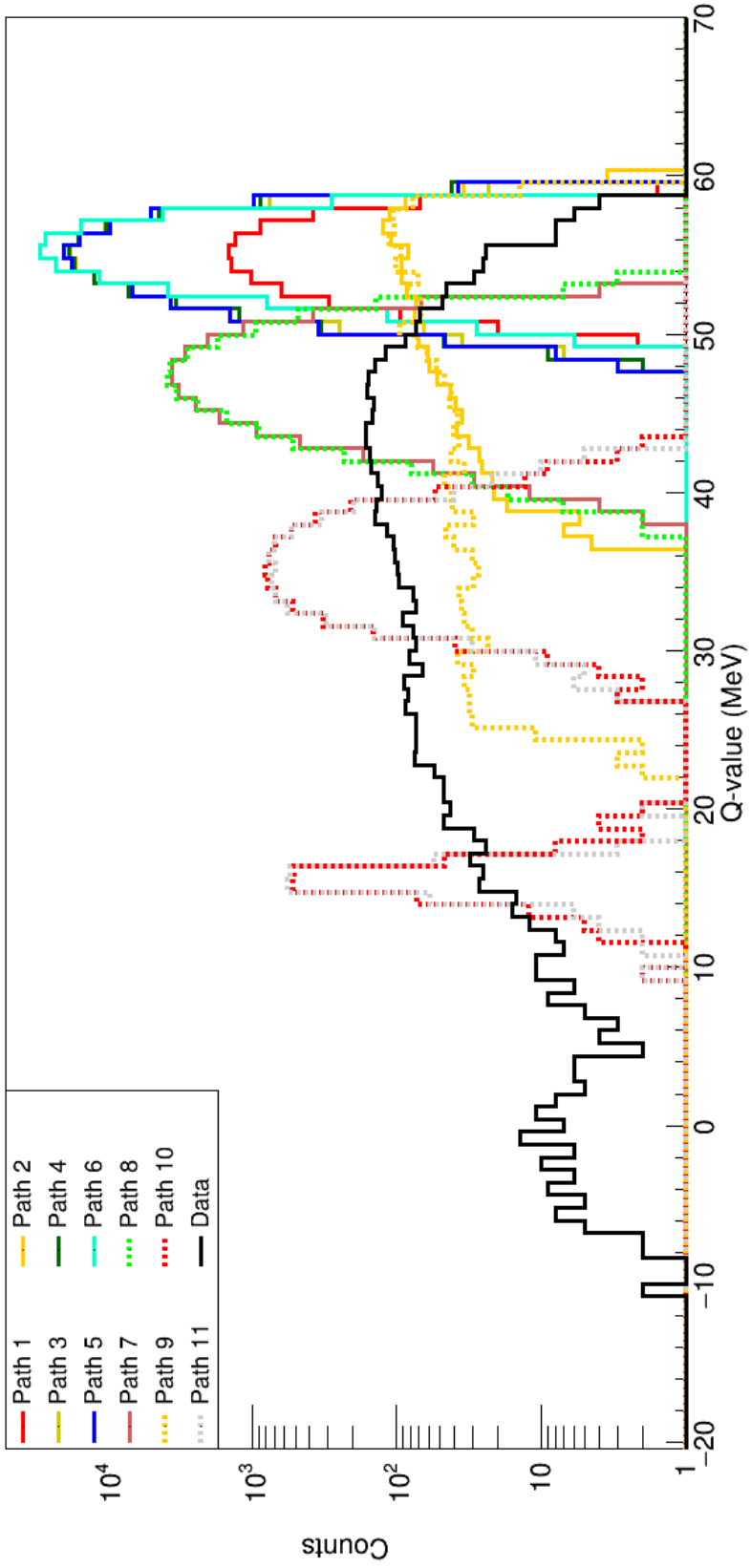

Figure 5.82: (Negative) Q-value for the reconstruction of ^{16}O from the measurement of the Hoyle decay comparing the experimental data to the MC decay paths for $E_b = 160$ MeV.

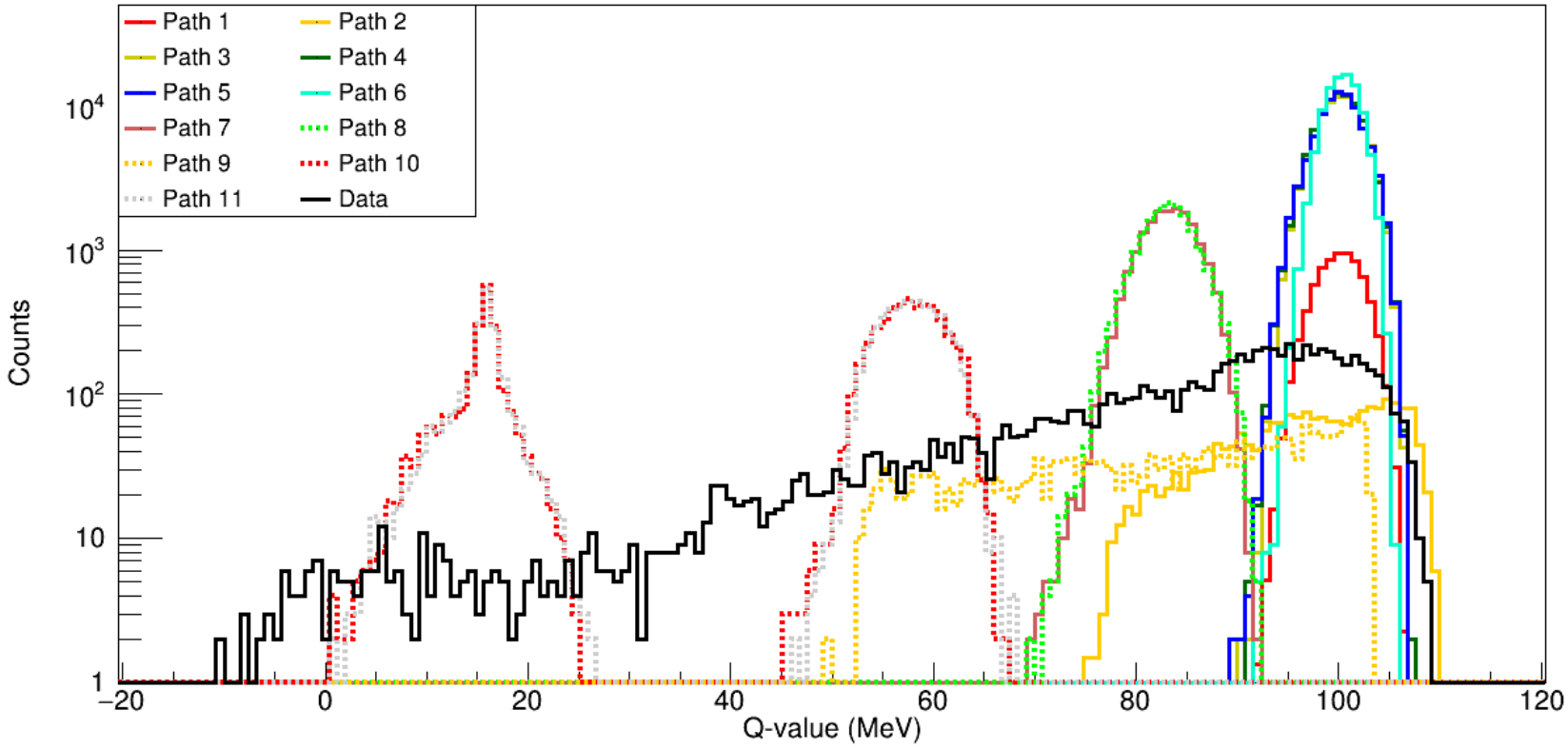

Figure 5.83: (Negative) Q-value for the reconstruction of ^{16}O from the measurement of the Hoyle decay comparing the experimental data to the MC decay paths for $E_b = 280$ MeV.

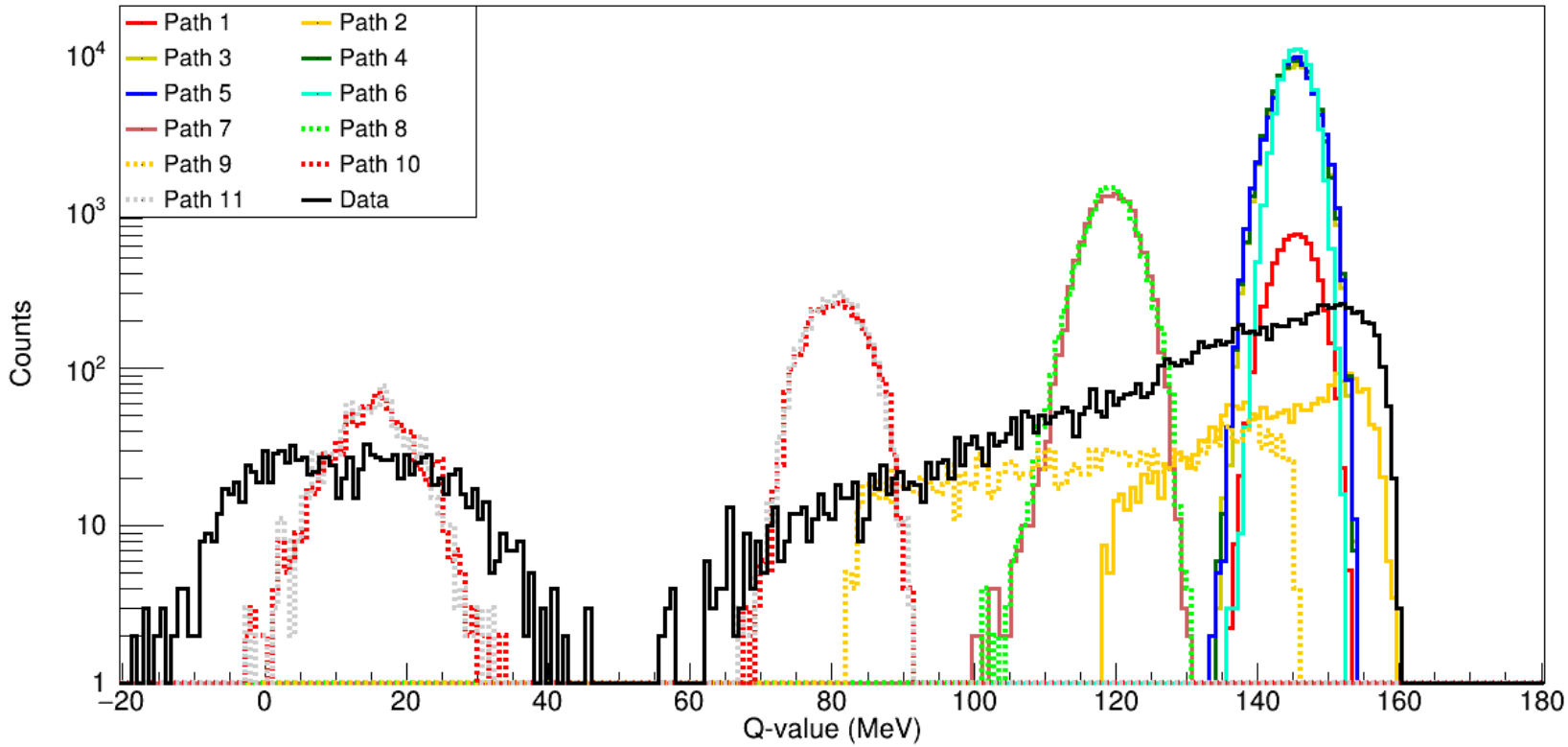

Figure 5.84: (Negative) Q-value for the reconstruction of ^{16}O from the measurement of the Hoyle decay comparing the experimental data to the MC decay paths for $E_b = 400$ MeV.

a width of around 1.2 MeV for $E_b = 160$ MeV but this massively increases to $\Gamma \sim 12$ MeV for $E_b = 400$ MeV. This is due to the large dependence of the resolution on the kinetic energy of the $^{12}C^{\star}$. At the high energies experienced for the $E_b = 400$ MeV data, the $^{12}C(0_2^+)$ has a kinetic energy of > 200 MeV. At this high incident energy, the constituent α-particles cannot be well identified as their energy deposited in the silicon stage is below/near threshold. Subsequently, the reconstruction from the Hoyle state can only occur when the level is detected at large angles where, as seen in Figure 5.78a for the ^{8}Be + ^{20}Ne Q-value spectrum, the angular resolution is drastically worse.

It can be demonstrated therefore that for the three beam energies, there is a **reasonable $^{12}C(0_2^+) + {}^{16}O$(g.s) contribution** although this decay mode is not dominant. As discussed previously, and shown in Figures 5.26, 5.28 and 5.30, the yield of the Hoyle state with angle is smooth and consistent with that arising from compound nucleus decay rather than via direct reaction mechanisms.

5.6.3 $^{12}C(3_1^-)$

As a comparison for the $^{12}C(0_2^+)$ break-up, one can also evaluate the Q-value while gating on the broader peak in ^{12}C at ~ 9.6 MeV. One must be careful to take into account the increased background this state sits on. Therefore, reconstructions of the background regions either side of this broad peak were performed. For the two backgrounds, cuts of $E_x = 8.5 \rightarrow 9.0$ and $E_x = 10.2 \rightarrow 10.7$ were taken to investigate the effect of this non-resonant contribution, where the contribution from the state is severely reduced. The results from applying these cuts can be seen in Figure 5.85 where the same features are shown for both the peak and the two background gates. Additionally, comparing the Q-value spectrum to that for the Hoyle state also shows the same features suggesting the two resonances occur via the same reaction mechanism which is also the same source as the uncorrelated α-particles. As demonstrated previously, the mechanisms seen are a combination of sequential decay and n-body break-up.

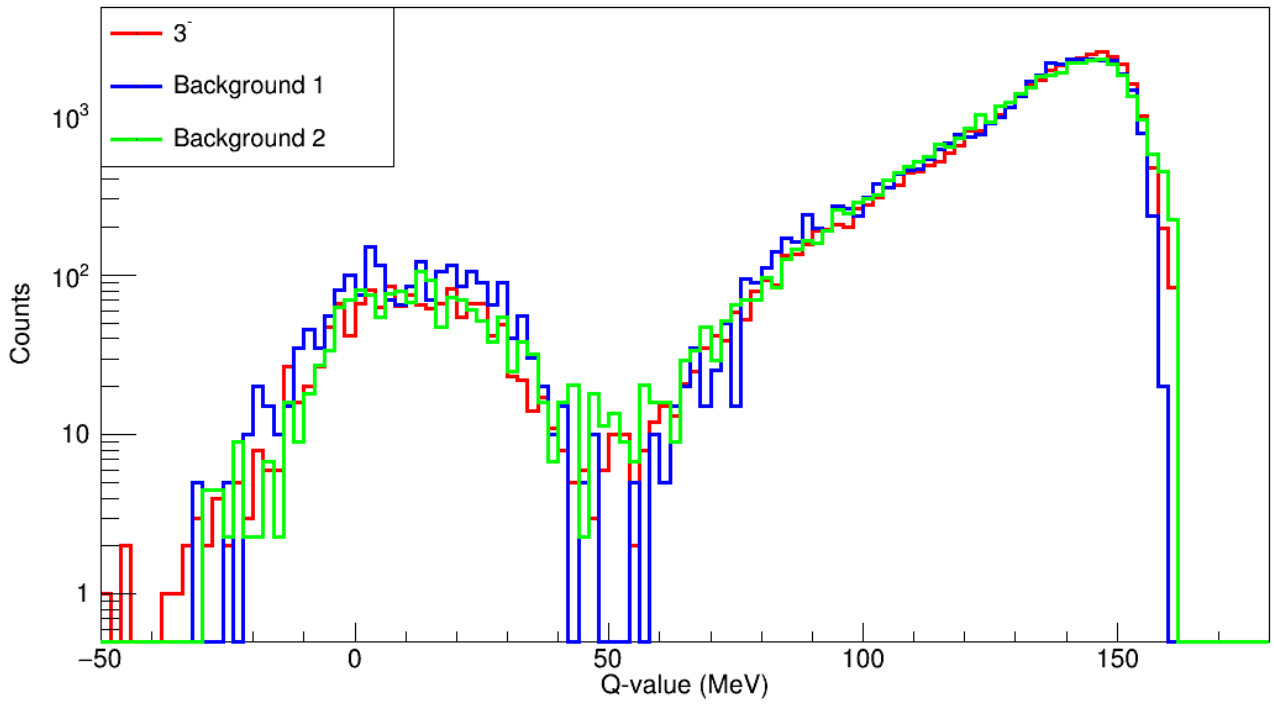

Figure 5.85: (Negative) Q-value spectrum for the 3-α excitation function at $E_b = 400$ MeV. The missing ^{16}O is reconstructed from momentum conservation. Data taken from the peak at 9.6 MeV (red) are shown in comparison to those from the background gates placed either side of the resonance (blue/green).

5.6.4 ^{16}O

While the 4-α excitation does not yield any clearly evident states, one can still reconstruct the missing momentum to gain information about the reaction mechanisms involved. This tool can also be used to introduce selectivity to the 4-α excitation spectrum by selecting regions in the Q-value spectra where the decay mode of interest is preferentially located. This can be understood by examining a 2D spectrum showing the excitation energy reconstructed in ^{16}O against the Q-value when reconstructing the missing ^{12}C. This is best typified by Figure 5.86, where one can see as the excitation energy becomes extremely large in ^{16}O (50 $\rightarrow$ 90 MeV), there becomes a small component in the Q-value spectrum, visible when plotting only events where the excitation energy lies in this range. This is seen in Figure 5.87 where two components can be seen at low energies (despite low statistics) which corresponds to 7.65 MeV and 14 MeV. These contributions correspond to the Hoyle state and a strongly populated state seen previously in the inelastic scattering data for 400 MeV. This region with a two-body component

corresponds well to the secondary bump seen previously in the 4-α excitation functions of Figure 5.63 which has a large Hoyle+α decay. This situation is mirrored for the 280 MeV data (visible in Figure 5.88 and 5.89) where above 40 MeV, one sees a similar contribution to the Q-value spectrum at the same energies although the statistics are limited here. This region also coincides with a secondary bump in the 4-α excitation function.

From these combined analyses one can therefore demonstrate **a reasonable ^{12}C($\mathbf{0_2^+}$) + ^{16}O* and ^{12}C(14 MeV) + ^{16}O* component in these data**. The possible interpretation of this 14 MeV state is discussed in Chapter 6.

5.6.5 ^{20}Ne

It was seen in Chapter 5.5.5 that in the 160 MeV there was a contribution from the ^{20}Ne spectrum that was incongrous with the event-mixing showing the effect of the uncorrelated α-particles. Figure 5.90 shows the results from reconstructing ^{8}Be from the measured 5-α events and plotting the negative Q-value to give an effective excitation spectrum in ^{8}Be. The data from the 160 MeV beam energy can be seen to comprise of a single peak although this does not correspond to the ^{20}Ne* + ^{8}Be(g.s) Q-value which is shown on the figure. This peak does not however correspond to the expected Q-value. The density of states in ^{8}Be is extremely small and therefore this contribution can be attributed to other population modes such as the ^{20}Ne + 2α which is predicted to be considerably stronger than the ^{20}Ne + ^{8}Be(g.s) mode in the EHF calculation. The 280 and 400 MeV similarly show no contribution that could correspond to the ^{20}Ne + ^{8}Be path suggesting these 5-α events also arise from the ^{20}Ne + 2α channel. Any contribution via mixing of 5 out of 6 α-particles from the decay of ^{24}Mg would also correspond to this same decay path as there is only a negligible contribution to the population of ^{24}Mg that isn't from the initial fission of the compound nucleus (i.e. nearly all ^{24}Mg is populated via (^{28}Si, α) rather than (^{25}Mg, n) or similar reactions).

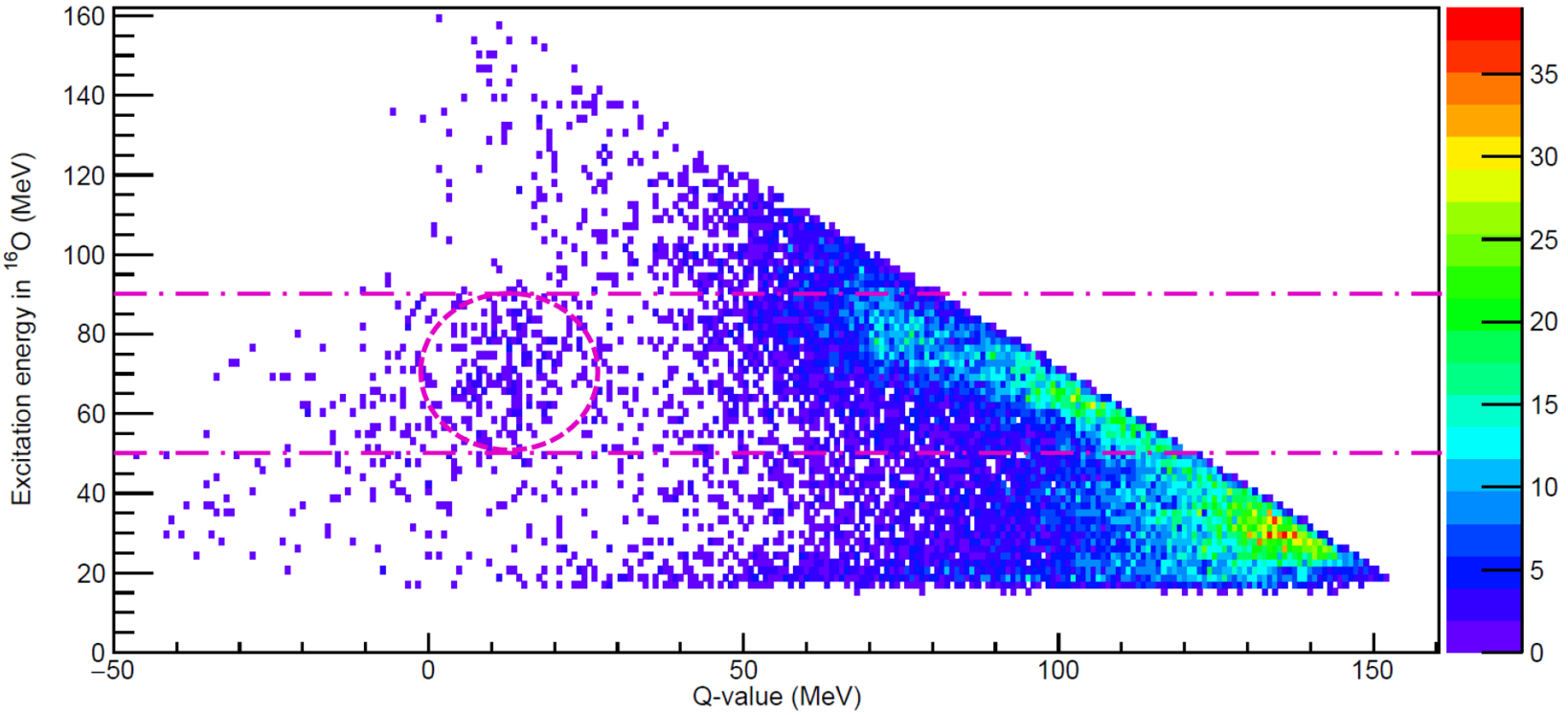

Figure 5.86: Excitation energy from 4-α against the (negative) Q-value for the reaction for a beam energy of 400 MeV. The area marked by a pink ellipse corresponds to the additional yield seen at lower excitation energies in Figure 5.87 where only events between the two pink dot-dashed lines are taken.

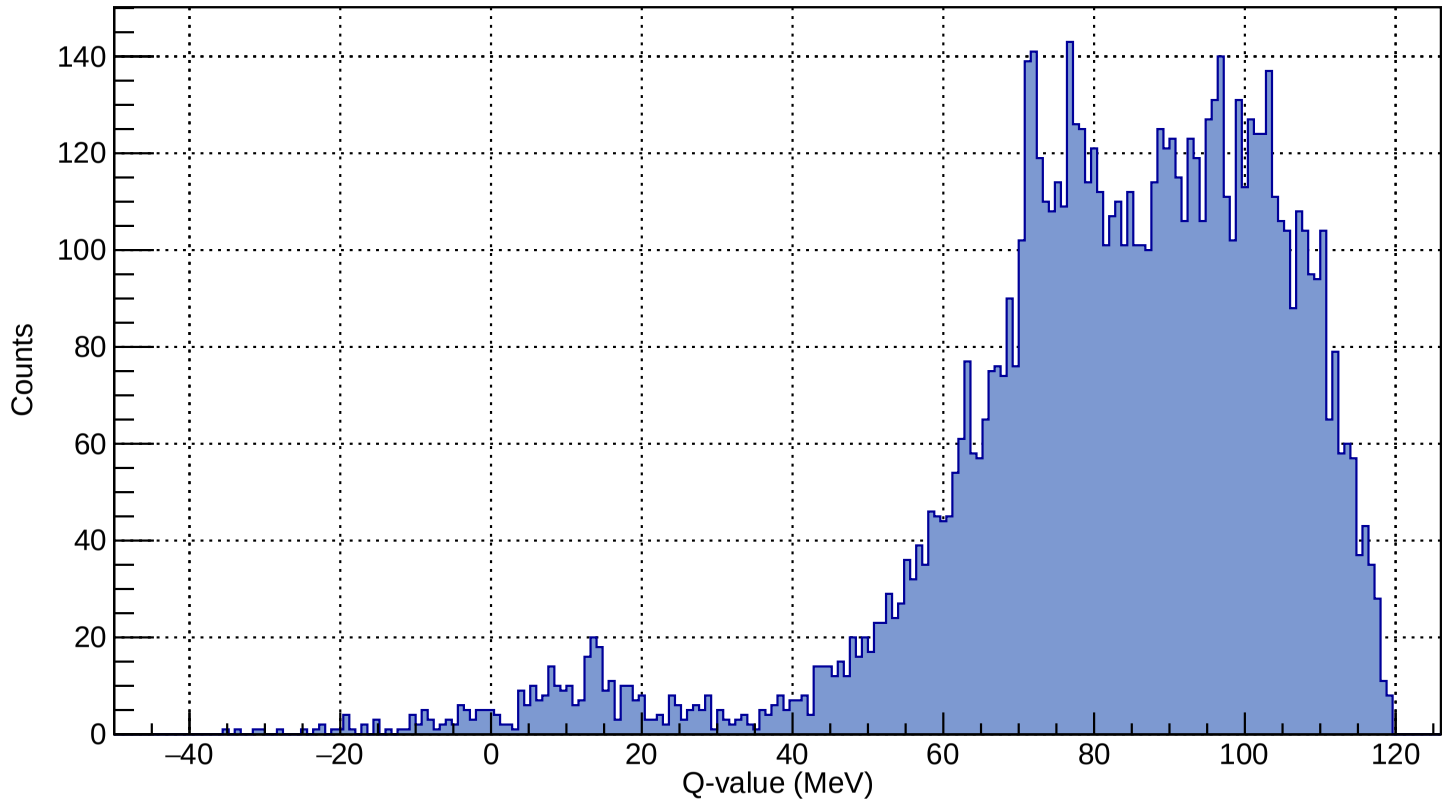

Figure 5.87: Projection from $E_x = 50 \rightarrow 90$ MeV in ^{16}O in Figure 5.86 showing the Q-value for $^{28}\mathrm{Si}^{\star} \rightarrow ^{12}\mathrm{C}^{\star} + ^{16}\mathrm{O}^{\star}$ for a beam energy of 400 MeV.

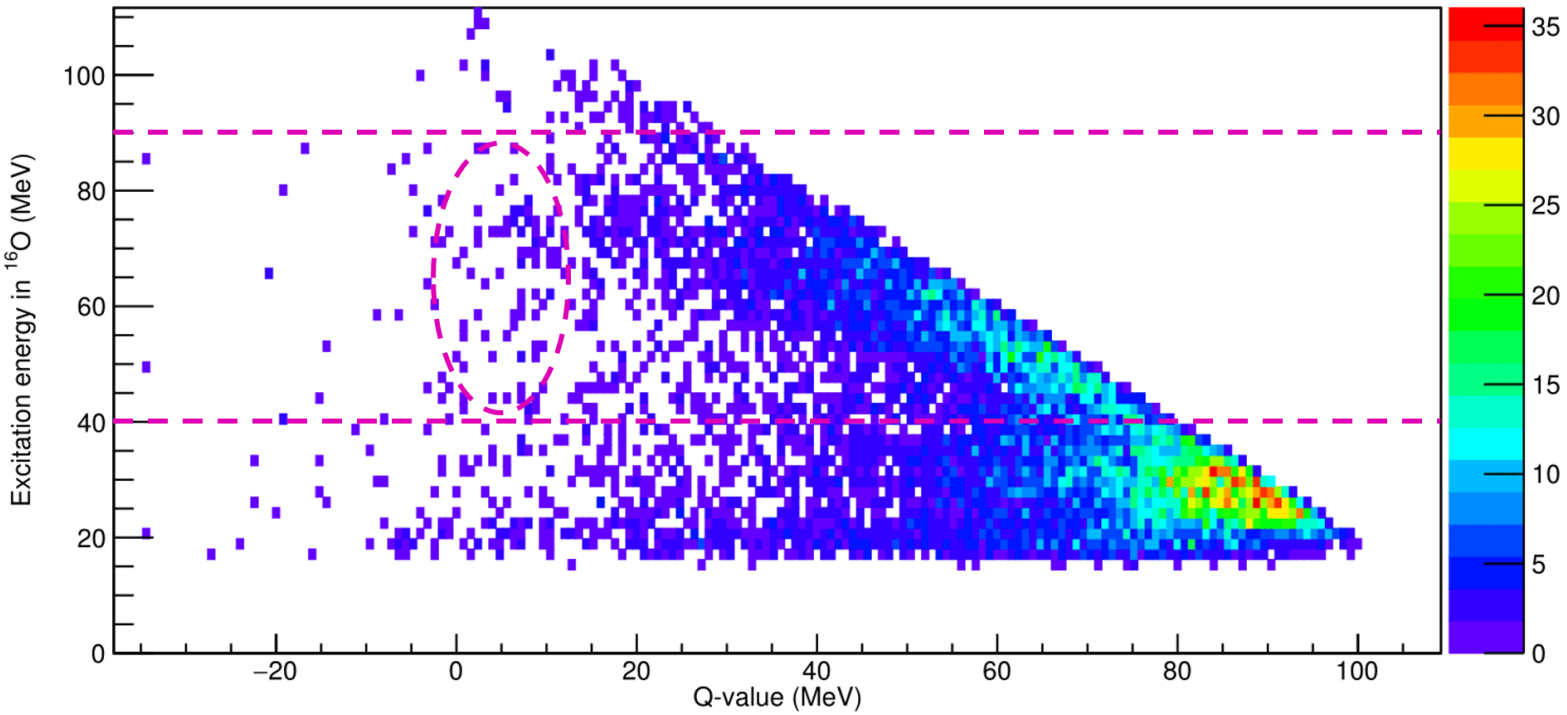

Figure 5.88: Excitation energy from 4-α against the (negative) Q-value for the reaction for a beam energy of 280 MeV. The area marked by a pink ellipse corresponds to the additional yield seen at lower excitation energies in Figure 5.89 where only events between the two pink dot-dashed lines are taken.

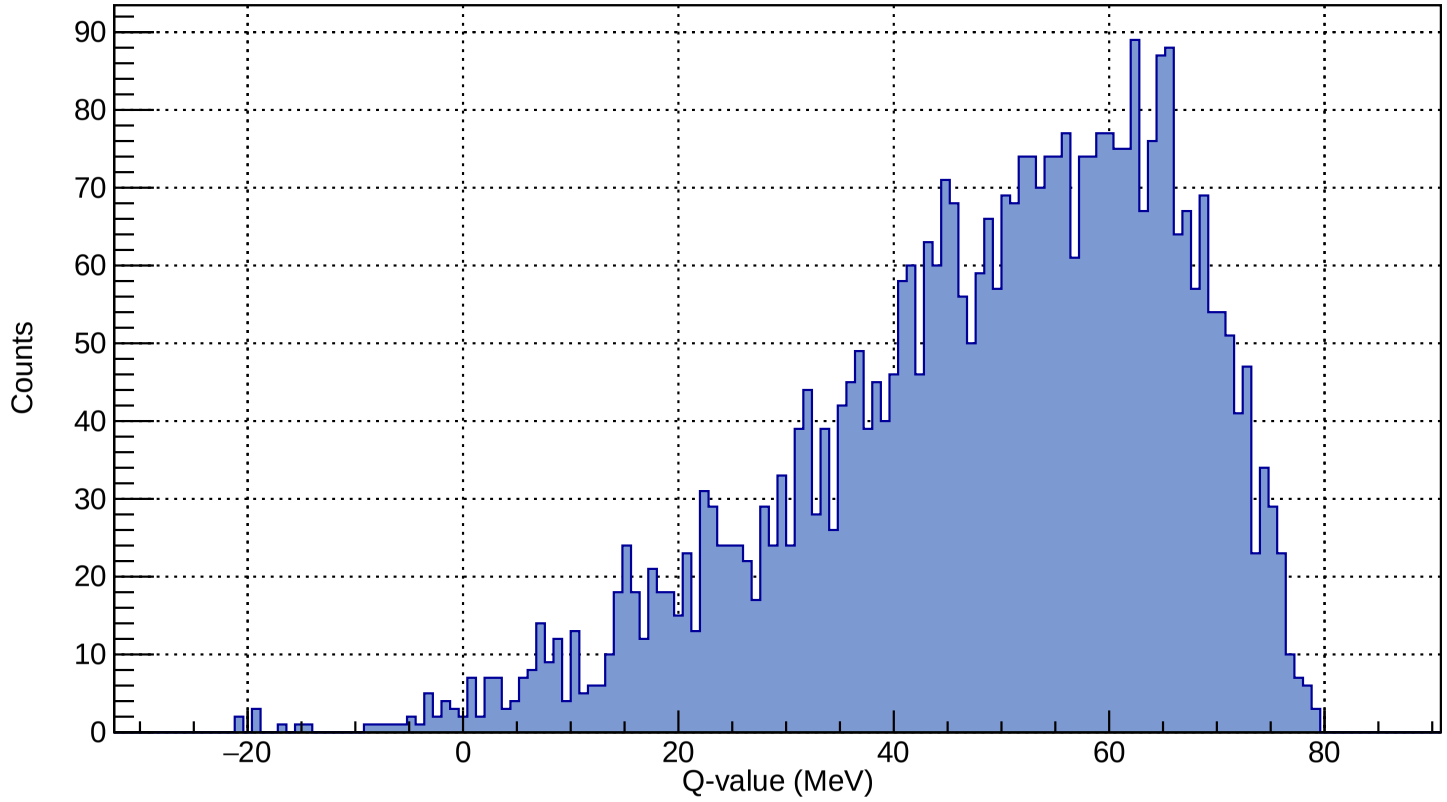

Figure 5.89: Projection from $E_x = 40 \rightarrow 90$ MeV in ^{16}O in Figure 5.88 showing the Q-value for $^{28}\mathrm{Si}^{\star} \rightarrow ^{12}\mathrm{C}^{\star} + ^{16}\mathrm{O}^{\star}$ for a beam energy of 280 MeV.

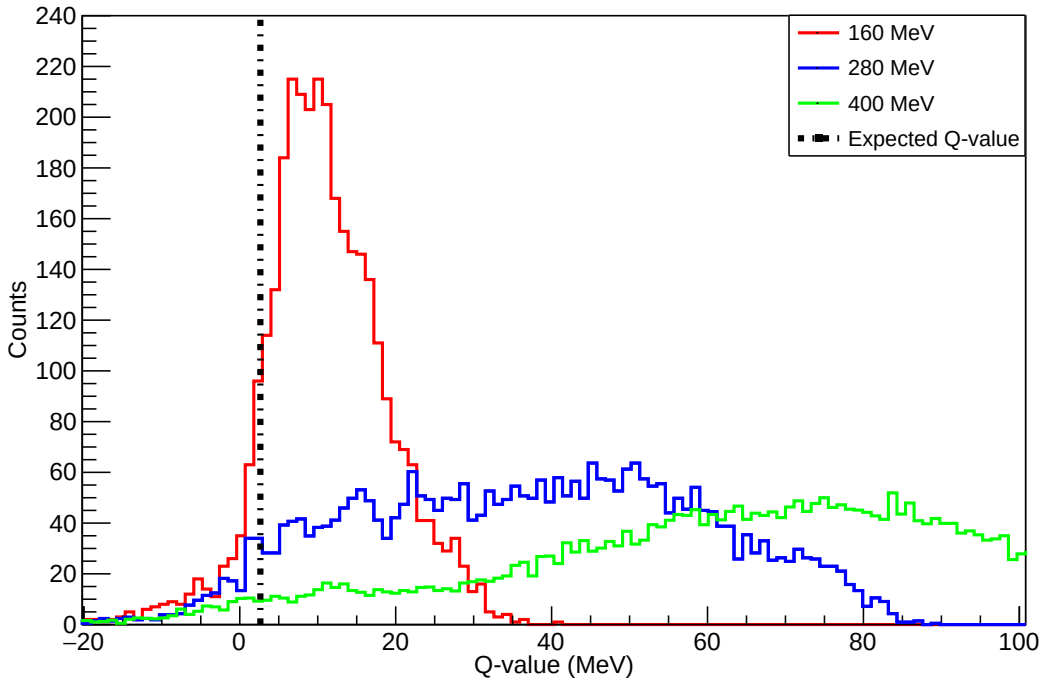

Figure 5.90: (Negative) Q-value for reconstruction of a missing ^{8}Be from all 5-α events for the three different beam energies. The expected Q-value for ^{12}C(^{16}O,^{20}Ne) is also shown by the black dashed line.

5.7 Comparison between the experimental and theoretical branching ratios for the 7-α channels

Given the results of reconstructing the states in the α-conjugate nuclei, the predictions detailed in Chapter 5.2.1 were compared to the experimental data, the values for both can be seen in Table 5.10.

As the beam energy increases in the Fermi break-up calculation, one can see the dominant decay modes change as the energy dependency becomes more important than the permutation for the $^{8}\mathrm{Be} + 5\alpha$ (VII) path. This decay mode is suppressed by a factor of 5! in comparison to the $^{12}\mathrm{C}(0_2^+) + ^{8}\mathrm{Be} + 2\alpha$ (III) path which only has a suppression factor of 2. A similar situation can be seen for the 7α-particle (VIII) decay which, while a 7-body decay has a high power dependence on the energy, is suppressed by a factor of 7!. The lower beam energies therefore correspondingly favour a small n-body decay.

It is apparent from Table 5.10 that the decay modes seen experimentally for $E_b = 160$ MeV heavily favour the $^{8}\mathrm{Be} + ^{8}\mathrm{Be}$ (VI), single $^{8}\mathrm{Be}$ (VII) and 7-α (VIII) decay modes far in excess of those predicted theoretically. Part of this discrepancy can be attributed to modelling additional excited states in $^{12}\mathrm{C}$ above 7.65 MeV. While these states will have an increasingly reduced phase space by virtue of the decrease in the kinematically available energy, these high-lying states may also have a large spin component which may partially compensate this effect. This angular momentum consideration (and all aspects of penetrability) are omitted in the Fermi break-up model. A large phase space to higher excitations in $^{12}\mathrm{C}$ would therefore manifest itself as replacing the $^{12}\mathrm{C}(0_2^+)$ strength with $^{8}\mathrm{Be} + \alpha$ and 3-α strength. Repositioning the branching ratio from the $^{12}\mathrm{C}(0_2^+) + ^{8}\mathrm{Be}$ and single-$^{12}\mathrm{C}(0_2^+)$ to these decay modes (i.e. III and IV move to VI and VII) then creates a greater agreement with the experimentally observed data. It is not possible to include these additional contributions in the calculations as one cannot be certain of the density and spin of states once one enters the continuum and additionally the transition matrix elements may start to deviate drastically from the constant value used under the assumption of an α-condensate [84].

An additional explanation for the discrepancy between the experimental and theoretical values is that the Hoyle state is not well described as an α-condensate and as such, the transition matrix to break-up into the Hoyle state and α-condensed systems is reduced or the mechanism is better described by a series of sequential decays rather than directly breaking-up into constituent α-particles. This latter explanation has been

demonstrated to be unlikely as the experimental data suggest a reaction mechanism which differs from the EHF calculations by virtue of the measured α-particle multiplicities and the disagreement over the strength of binary scission modes which were shown to be extremely weak experimentally. The reaction mechanism which describes the data well however has been demonstrated to be described well by aspects of both the Fermi break-up mode and the statistical decay model showing the importance of both of these decay paths.

The 280 and 400 MeV data show a very similar pattern to those at 160 MeV albeit with a movement of strength in the ^{8}Be+^{8}Be (VI) channel to the 7-α channel (VII). Even directly assigning the strength from the channels with excitations in ^{12}C to the 7-α path, the strength is still in excess of that expected. This suggests that some of the yield seen in the single-^{8}Be is therefore also sent to the 7-α channel. This could perhaps be by virtue of populating higher excitations in ^{8}Be (i.e. the ^{8}Be(2^{+}_{1}) where limited statistics and resolution mean this contribution is difficult to observe. Again, this channel is difficult to calculate as the assumption of an identical transition matrix is no longer valid.

Overall, the Fermi break-up description can be seen to show a reasonable agreement with the experimental data once the points above regarding modeling additional higher excitations is taken into consideration. In practicality, this is difficult to separate from the alternate postulate that the transition matrix to these disparate decay modes is different. The population of the seen $3^{-}/2^{+}$ contribution with the same characteristics of the Hoyle state however demonstrates that, as the 3^{-}_{1} state would have an impeded transition matrix, and the overall $3^{-}/2^{+}$ contribution is populated at a level consistent with that of the Hoyle state that perhaps the effect of the transition matrix is not of primary importance here or this 2^{+}_{2} state has an extremely similar wave function to the Hoyle state and is therefore suggestive of a rotational excitation.

Decay Path		Efficiency %		
Label	Constituents	160 MeV	280 MeV	400 MeV
I	$^{12}C(0_2^+) + {}^{12}C(0_2^+) + \alpha$	0.338	0.286	0.127
II	$^{12}C(0_2^+) + {}^{8}Be + {}^{8}Be$	0.030	0.156	0.133
III	$^{12}C(0_2^+) + {}^{8}Be + 2\alpha$	0.205	0.212	0.201
IV	$^{12}C(0_2^+) + 4\alpha$	0.180	0.223	0.152
V	$^{8}Be + {}^{8}Be + {}^{8}Be + \alpha$	0.187	0.186	0.177
VI	$^{8}Be + {}^{8}Be + 3\alpha$	0.034	0.036	0.021
VII	$^{8}Be + 5\alpha$	0.180	0.223	0.152
VIII	7α	0.052	0.054	0.025

Table 5.9: Efficiencies for the different Monte Carlo decay paths given in Table 5.10.

Decay Path		Exp. branching ratio %			Theor. branching ratio %		
Label	Constituents	160 MeV	280 MeV	400 MeV	160 MeV	280 MeV	400 MeV
I	$^{12}C(0_2^+) + {}^{12}C(0_2^+) + \alpha$	0.0(0.0)	0.0(0.0)	0.2(0.2)	7.1	0.3	0.0
II	$^{12}C(0_2^+) + {}^{8}Be + {}^{8}Be$	0.0(0.0)	0.0(0.0)	0.0(0.0)	1.0	0.3	0.1
III	$^{12}C(0_2^+) + {}^{8}Be + 2\alpha$	1.8(1.3)	2.8(1.1)	1.1(0.5)	43.3	11.5	5.0
IV	$^{12}C(0_2^+) + 4\alpha$	4.5(2.0)	2.8(1.1)	1.5(0.6)	11.7	16.7	10.8
V	$^{8}Be + {}^{8}Be + {}^{8}Be + \alpha$	3.6(1.8)	0.4(0.4)	0.4(0.3)	20.7	5.2	2.3
VI	$^{8}Be + {}^{8}Be + 3\alpha$	33.0(6.3)	13.8(2.5)	10.1(1.5)	7.0	8.4	4.6
VII	$^{8}Be + 5\alpha$	45.5(7.7)	37.8(4.5)	32.8(3.0)	9.2	57.3	76.7
VIII	7α	11.6(10.4)	42.5(5.4)	53.9(3.5)	0.0	0.3	0.5

Table 5.10: Experimental and theoretical branching ratios for the 7-α break-up modes for the different beam energies. The theoretical branching ratios for the 7-α break-up modes are calculated with the Fermi break-up model and efficiency corrected using the Monte Carlo simulations. The error on the theoretical values is estimated at $\sim 1\%$ of the total branching ratio from the uncertainty in the MC efficiency. Heavier shading of the cell corresponds to a larger branching ratio.

Chapter 6

Conclusions

In Chapter 3, the experimental observables for an α-condensate system were discussed. The results of the different probes of α-gas structure will be examined here.

Multiplicities

Previous experiments [147] [103] have investigated α-condensation although neither utilised the compound nucleus method, instead relying on inelastic scattering. These experiments described the mechanisms involved in a high multiplicity decay via statistical decay codes. It was seen in Chapter 5.2.1 from the extended Hauser Feshbach calculations that as the energy of the system was increased, the expected α-particle multiplicity was expected to decrease as additional decay channels became available.

The experimentally observed multiplicity distributions in Chapter 5.4.2 were seen to exceed those expected from this purely statistical description. After correcting for pileup events and the efficiency of detecting different multiplicities, high multiplicity decays were seen to contribute a large amount of the total branching ratio from the compound nucleus. Further investigation of the intermediate α-conjugate nuclei showed the population of these isotopes differed from that predicted via the EHF calculations.

In addition to describing the reaction via a series of sequential decays, the Fermi break-up model was used in Chapter 5.2.2 which utilises phase-space considerations to look at the expected breakup into n particles. These calculations showed the contribution from $n > 2$ decays is dominant and the system readily decays directly into 7-α particles. The plot for the number of break-up particles (Figure 5.20) peaks at a similar value to the experimental data (although this looks solely at α-particles) in Fig-

ure 5.42. By analysing the relative phase-space for different 7-α final states (limited to the expected α-gas states - α, ^{8}Be and ^{12}C(0_2^+)) and correcting for the efficiency of these different paths, a prediction of the expected 7-α branching ratios was achieved. These decay paths were seen to deviate from those expected which contain ^{12}C in the Hoyle state. While this reduced yield could be attributed to the Hoyle state not being well described as an α-gas state and therefore the transition matrix element being reduced, this is more easily explained by additional resonances in ^{12}C being populated. The spin of these states means they have an increased phase-space as afforded by the $(2J+1)$ spin dependency. These higher energy states therefore move strength from the Hoyle paths to the ^{8}Be(g.s)+α and 3α paths. A prediction of the α-particle multiplicity from the Fermi break-up model is much more consistent with the experimentally observed data.

Energy of particles

Figure 3.6 showed how the effect of a condensate state can modify the Coulomb barrier to modify the minimum energy spectrum. One can therefore examine the difference in the energy spectrum of α-particles from decays of the Hoyle state, the $3^-/2^+$ and those which do not correspond to any intermediate resonance (i.e. statistical uncorrelated α-particles). Figures 6.1-6.3 show the results of this comparison with the yields for each mode normalised to the total α-particle count to clearly show any differences. One can see the high energy tail events are absent in the events with Hoyle and $3^-/2^+$ decays. The features for the Hoyle and $3^-/2^+$ decays are very similar at high energies where they show the same drop off and general shape however at low energies, the two contributions are seen to differ. For the 160 MeV data, the $3^-/2^+$ decays exceed that of the Hoyle state at low energies. In the 280 MeV data, this difference is extremely small while at 400 MeV, a large enhancement is seen for the Hoyle decays near the energy-threshold. While this low-energy enhancement was suggested as a signature for α-particle condensation, one must also be careful that this signature cannot be explained by other methods. In Figures 5.79-5.81, it was shown from the MC simulations that this low energy enhancement for Hoyle state decays can be indicative of the ^{12}C(0_2^+) $+^{16}$ O* decay mode which has previously been shown to be strong in these data. This result is therefore consistent with originating from this binary fission mode.

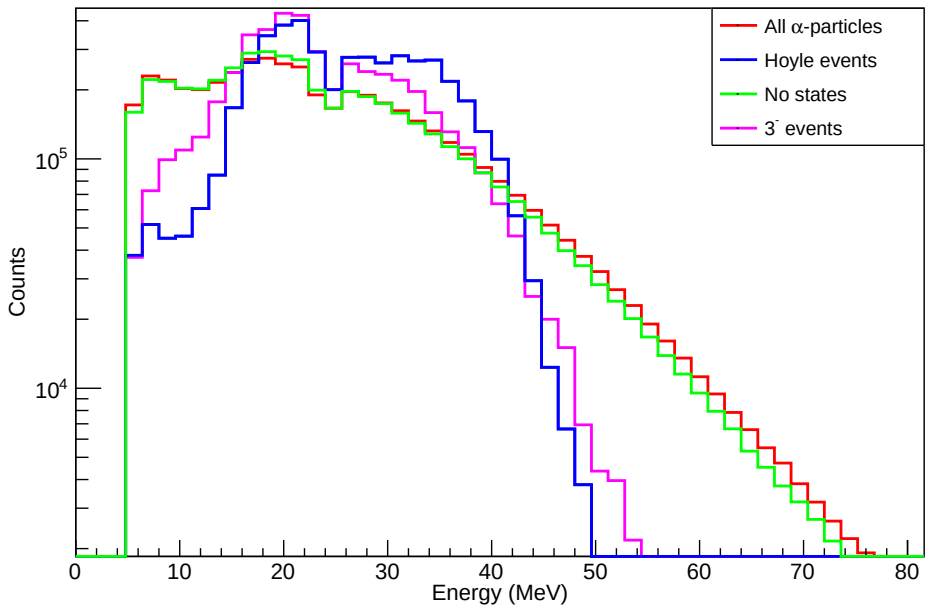

Figure 6.1: Comparison of the normalised kinetic energy distribution of α-particles with different conditions for $E_b = 160$ MeV.

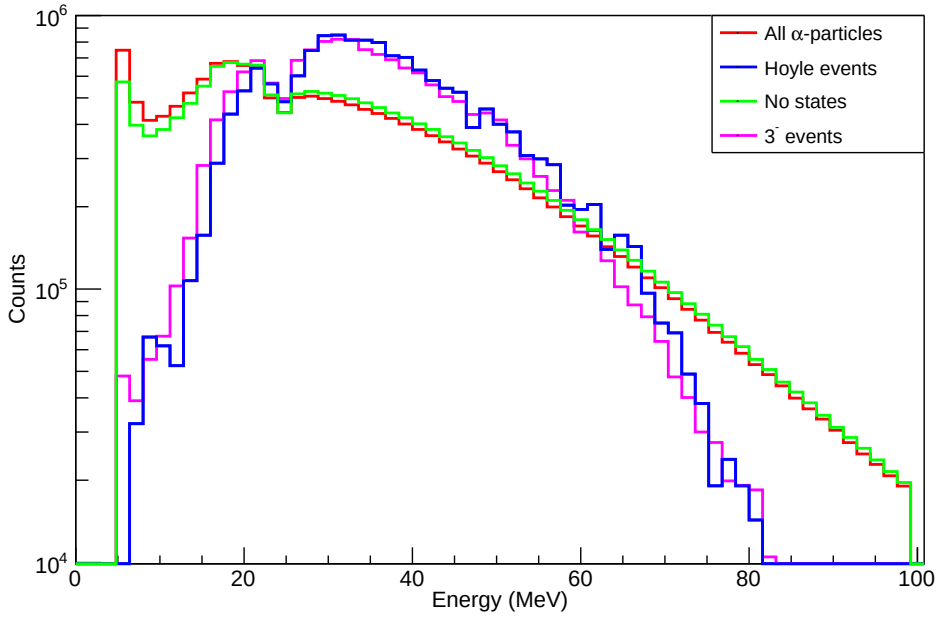

Figure 6.2: Comparison of the normalised kinetic energy distribution of α-particles with different conditions for $E_b = 280$ MeV.

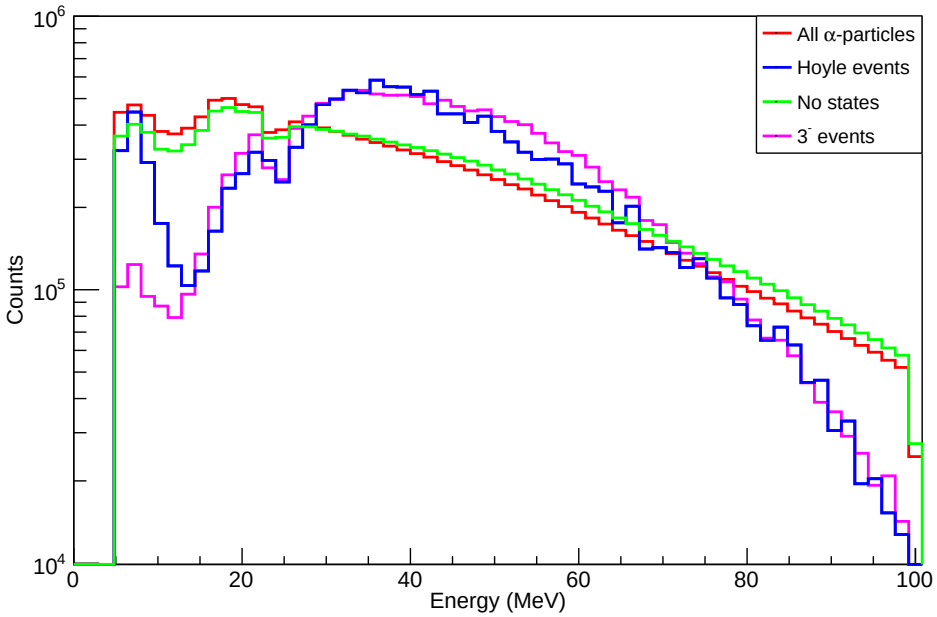

Figure 6.3: Comparison of the normalised kinetic energy distribution of α-particles with different conditions for $E_b = 400$ MeV.

N-α states

Reconstructing the α-particles to search for intermediate states also allowed for an insight into the reaction mechanisms involved. It also enabled a direct search for near-threshold resonances. Event-mixing between separate events showed a good description of the continuum associated with these excitation functions showing the large effect of uncorrelated α-particles. The conclusions from each α-conjugate nuclei will be briefly discussed.

^{8}Be

The ground-state in ^{8}Be is seen to be well populated however higher excitations (e.g. the broad 3 MeV state) are not seen to be well populated. This is perhaps surprising as the compound nucleus has a large angular momentum and high excitation energy, therefore (as mentioned above) a $(2J+1)$ factor means that this 2^{+}_{1} state should be preferentially populated. Analysing the origin of the ^{8}Be(g.s), one can observe the absence of a direct ^{8}Be(g.s)+^{20}Ne* breakup. The ^{8}Be is therefore easily demonstrated as being

largely generated by alternative paths (i.e. sequential decay processes or high multiplicity particle break-up where this spin dependence is offset by the reduced transition matrix) may explain why the ^{8}Be(2^{+}_{1}) is not populated.

^{12}C

A large number of the observed ^{8}Be(g.s) can be attributed to being from the decay of the Hoyle state and a broad component at 9.7 MeV which, by virtue of its anomalous width, is attributed to a combination of the 3^{-}_{1} state and the 2^{+}_{2} state. This 2^{+}_{2} is assigned as being the rotational excitation of the Hoyle state. This rotational excitation is not incongruous with an α-condensate description of the Hoyle state [148]. For all beam energies, a number of these Hoyle state decays can be demonstrated to arise from a direct ^{16}O + ^{12}C(0^{+}_{2}) path. These ^{12}C(0^{+}_{2}) decays correspond to those with an extremely low or high kinetic energy. These extremes correspond to the ^{12}C* being emitted parallel or antiparallel to the beam direction. This situation is mirrored with the $3^{-}/2^{+}$ decays where a component can be attributed to a two-body decay. These predictions are in agreement with the Hauser Feshbach results which show a reasonable ^{12}C + ^{16}O scission mode with the discrete levels in ^{12}C being well populated.

The predicted energy levels from the EHF for the ^{12}C however showed that as the beam energy increases, the discrete levels should rapidly become dwarfed by statistical α-particles from the continuum. For the three beam energies, the contribution to the Hoyle state and the $3^{-}/2^{+}$ is fairly constant in therefore in disagreement with the statistical decay model. This is indicative that the seen discrete levels are more readily ascribed to a multi-particle break-up. This agrees with the Q-value spectra seen where only a small fraction of the overall events can be seen to arise from a binary scission.

As well as a contribution from the Hoyle state and the 2^{+}_{2} which has been assigned to the Hoyle rotational band (although not yet unambiguously demonstrated experimentally), Chapter 5.6.4 showed that there was evidence of a resonance at 14 MeV. Two 4^{+} states have been previously measured at 13.3 [149] and 14.08 MeV [150] which can also be assigned to the Hoyle rotational band [50]. It is therefore possible that these contributions seen in the data are evidence of populating the 0^{+}, 2^{+} and 4^{+} resonances of a rotational band. All these states will have a similar wave function overlap therefore if the Hoyle state is well populated then so should the higher rotational excitations. As discussed in Chapter 5.2.2, there is also a $(2J+1)$ spin factor which increases the strength of higher spin states. This result requires further corroboration but represents

a good suggestion that these states may constitute a rotational band.

^{16}O

In contrast with the ^{12}C 3-α excitation function, there is no obvious near-threshold component. As mentioned in Chapter 3, the predicted α-gas state in ^{16}O is not expected to have a large 4-α branching ratio. Examination of the ^{12}C + α decay path also showed no evidence of a resonance at this expected energy. The large density of states combined with the poor resolution, by virtue of the large angular resolution, means that no resonances stick out above the continuum. By selecting paths more prone to α-clustering as well as reducing the effect of uncorrelated α-particles, the ^{12}C(0_2^+) + α and ^{8}Be + ^{8}Be decay modes were examined and two contributions were seen at 19 and 23 MeV. The lowest of these can be attributed to a previously measured 6^+ state with a measured 4-α structure.

In addition, the ^{16}O* excitation function was examined by reconstructing the missing ^{12}C to look for the ^{12}C* + ^{16}O* path. A broad peak was seen in all 3 data sets at 40, 55 and 67 MeV for the 160, 280 and 400 MeV data sets respectively. This peak was not well described by the event-mixing which demonstrated the contribution from uncorrelated α-particles. Looking at the excitation energy this corresponds to in ^{12}C, one sees a weak contribution for the Hoyle state and a state at 14 MeV, the latter of which is apparent in the inelastic scattering data but is submerged by background in the 3-α excitation function.

^{20}Ne

The results from the EHF calculations predicted a smaller initial population of ^{20}Ne than that seen for ^{12}C or ^{16}O. Additionally, the constraint for a 5-α final state also means the overall cross section for the complete break-up into a system of α-particles is reduced. Combined with the decreased experimental efficiency to detect 5 α-particles means the statistics were very limited for ^{20}Ne. There was a hint of high energy resonances for the 160 MeV where the event-mixing showed a description of the seen excitation function via uncorrelated α-particles was poor. As the beam energy was increased, one sees an increasingly accurate description via this event-mixing suggesting a transition towards a situation better described by the Fermi break-up model. This is backed up by the absence of the ^{8}Be(g.s)+^{20}Ne* seen either via measurement of the

^{8}Be or the ^{20}Ne in a manner consistent with previous experiments (e.g. [146]).

Chapter 7

Summary

A selection of different techniques were used to attempt to extract a signature of an α-condensed state. The physics at the three different beam energies appeared to be largely similar, that being a combination of compound nucleus decay via sequential decay and also via many-particle break-up which was modeled using the Fermi break-up model. This was demonstrated by the incongruity between the observed α-particle multiplicity and that predicted from the EHF calculations for sequential decay. Analysing the origin of the α-conjugate nuclei, particularly the observed resonances of ^{8}Be(g.s), ^{12}C(0^{+}_{2}) and ^{12}C($3^{+}_{1}/2^{+}_{2}$), showed only a small fraction of these resonances arose from a two-body decay. Event-mixing showed a remarkable description of the seen 4-α correlation function suggesting a large amount of the observed $m_{\alpha} = 4$ events seen were from uncorrelated α-particles which is better described by the Fermi break-up model. This inseparable contribution from the sequential and many-body decay modes, in combination with the limits of the Fermi break-up model meant the observed 7-α decay modes differed by a small fraction where the channels with a ^{8}Be present were enhanced and those with a ^{12}C(0^{+}_{2}) were suppressed. This mirrors the observed increased yield of ^{8}Be in comparison to the EHF predictions for all three beam energies. This disagreement of the data with the Fermi model can be attributed to additional contributions from the ^{12}C continuum, the unsuitability of treating the Hoyle state as an α-condensate or the omission of a sequential decay contribution is these equations. Finally, direct observation of α-condensed states (particularly the predicted 15.1 MeV 0^{+}_{6} state in ^{16}O) was also attempted. These data showed no evidence of a near-threshold enhancement above that which can be explained via event-mixing. The suppression of the total width in the 4-α channel is a possible explanation for this by virtue of the proximity of the state

to the 4-α threshold which limits the penetrability to such a degree that the dominant decay modes are α_0 and α_1. Reconstruction of the α_0 decay mode however showed no enhancement near the expected region.

In summary, the reaction mechanism of the ^{12}C(^{16}O,^{28} Si*) was studied at three beam energies of 160, 280 and 400 MeV. This experiment was performed to search for α-gas states in ^{12}C, ^{16}O, ^{20}Ne, ^{24}Mg and ^{28}Si. In the case of heavier isotopes, there were various reasons discussed in this work in detail which could have obscured the observation of those states. The Hoyle state (^{12}C(0_2^+)) is the best candidate for such a state (from theoretical predictions). Following other recent experiments (e.g. of the direct 3α-decay of the Hoyle state [87] [88]), we can conclude that although theoretically this state fits well with an α-gas description, experimentally it appears that the underlying fermionic structure of the α-particles is sufficient to prevent this α-gas nature and none of the expected signatures for α-condensation were seen in the current analysis.

Chapter 8

Future Work

A primary hurdle in the direct search for near-threshold α-gas states is the effect of the Coulomb barrier. As discussed using the $^{16}O(0_6^+)$ state, the Coulomb barrier here is so inhibitive that the α_2 decay path is suppressed by several orders of magnitude. The increased radius of such an α-gas state may reduce this tunneling as shown by Figure 3.6 however the lack of such a state in the 4-α channel in the data (despite the good efficiency up to the threshold as demonstrated in Chapter 5.5.6) and the prevalence of the ^{8}Be(g.s) and $^{12}C(0_2^+)$ states in the data heavily suggest the Coulomb barrier is to blame here. One must therefore find a way to overcome this inhibiting of the characteristic decay mode. To understand this, one can examine predictions for α-condensation in heavier systems.

Condensation size limits

The phenomena of α-condensation in light systems, particularly ^{8}Be,$^{12}C(0_2^+)$,$^{16}O(0_6^+)$ has been well studied theoretically. A potent question is then how far one can treat this idea in heavier systems. While with atomic BEC, there is a large number of bosons in the medium, in the nuclear realm one finds increasing the system decreases the stability overall. This is an area that has been previously studied by Yamada [72].

To examine this size dependence on the binding of a condensate system, one can think about the competition of the attractive and repulsive forces in the system. The repulsive force in the system, in addition to the PEP applying at small distances as already discussed which drives a lowering of the density, is the Coulomb force. This Coulomb repulsion between all α-particles naturally exists as a long range interaction

causing the system to become less bound. The magnitude of this unbinding scales as $N(N-1)$ with the size of the Nα system as each of the N α-particles repel $(N-1)$ others. The attractive force for the system is comprised of 2 and 3 body forces (although the 3 body force is repulsive). In the work of Yamada [72], two different potential systems were used with one phenomenological model chosen to well reproduce parameters such as the ^{8}Be ground state energy. The second potential is a density-dependent potential similar in form to an effective NN potential. Both sets of potentials were examined when applied to an increasingly heavy α-condensate system. Using the Gross-Pitaevskii equation, which treats the system as comprised of identical bosons with a pseudo interaction, the solution can be achieved with the Hartree-Fock approximation where the solution of the system is approximated as the symmetrised form of the product of individual α-particles. This gives a solution for the total energy of a system which demonstrates a quadratic dependence with N. This demonstrates the importance of the Coulomb repulsion in making the system less bound which we expected to follow a quadratic relationship.

One can also investigate the total potential exhibited in the system as felt by a single α-particle. This can be seen in Figure 8.1. It is apparent that as the size of the system increases, the effect of the Coulomb potential is such to raise the total barrier higher and higher above the α threshold. This raising also means that any state existing in this local minimum is made less and less bound. As N reaches the critical value (N_{cr}) of 10, the potential is left extremely flat and the Coulomb barrier effectively disappears. This is by virtue of the total raising of the barrier and is not indicative of the absence of the effect of the Coulomb repulsion.

This (albeit reasonably approximate) investigation into the systematics via the $\alpha-\alpha$ interaction demonstrate that the critical value whereby adding more α-particles no longer can yield a condensate is therefore $N_{cr} \sim 10$. In the ^{40}Ca system this state corresponds to, one is left with an interesting experimental opportunity. Due to the effective absence of the Coulomb barrier, populating a state which exists in the extremely small local minimum of the potential would be incredibly loosely bound such that the system would be allowed to freely expand into its constituent particles, in this case into a system of 10 α-particles. This idea has been termed "Coulomb explosion" to describe this coherent emission of α-particles. Measurement of such an enhancement of this decay mode would be the smoking gun for α-particle condensation as such a phenomenon would be extremely inhibited in a traditional clustered system and relies on the nucleons behaving as a gas of α-particles. This technique however requires careful population

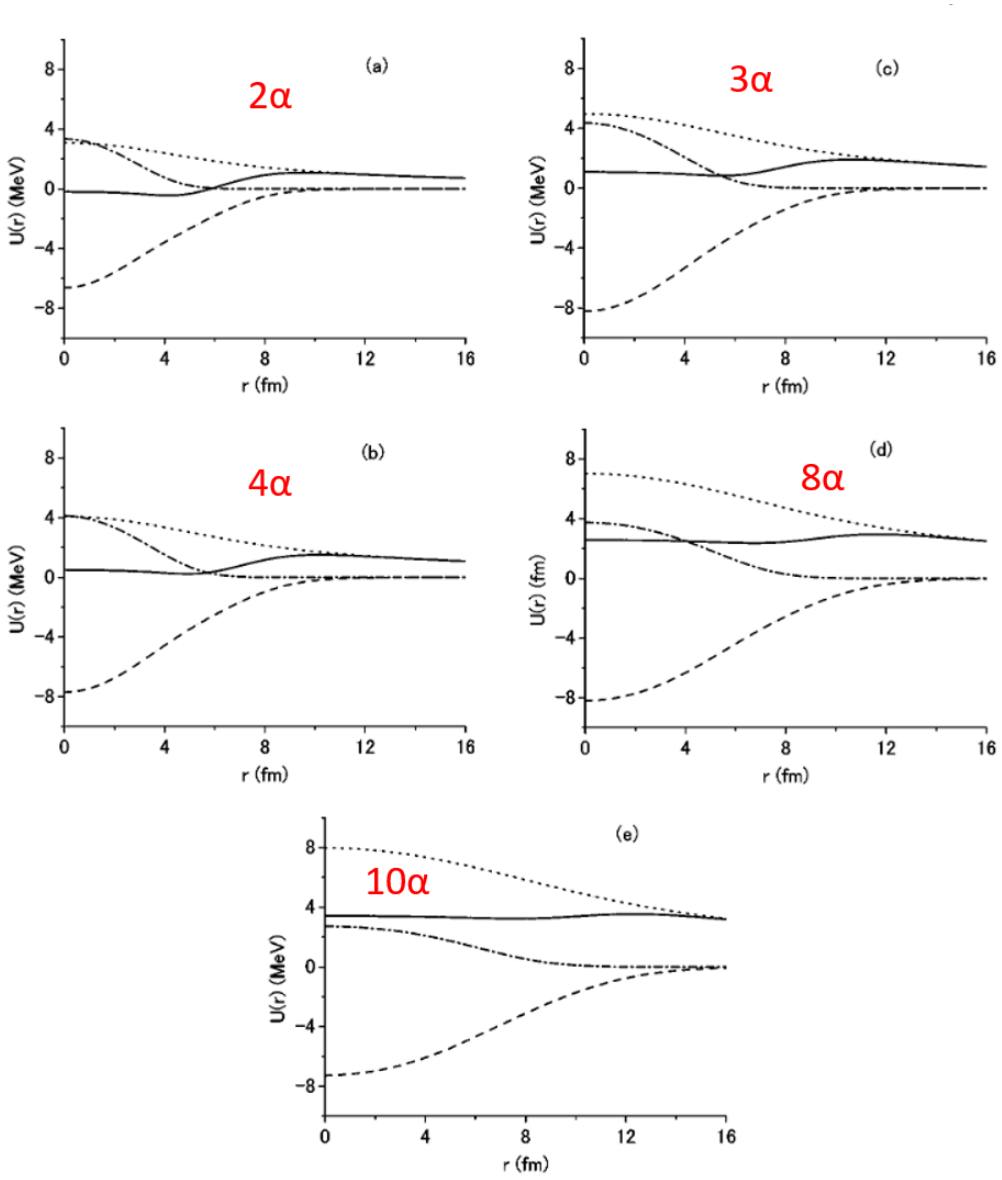

Figure 8.1: Single α-particle potential felt by different Nα systems. As N increases, the system becomes less bound overall until $N_{cr} > 10$, where the system is no longer quasibound. Figure taken from [72].

of this 0^+ at around 60-70 MeV, i.e. above the 10-α threshold in ^{40}Ca. Compound nucleus reactions whereby high excitation energies can be reached however will struggle to populate this state due to the high angular momentum in the compound system. Instead, one may utilise techniques such as Coulomb excitation whereby 0^+ population can be strongly and preferentially populated via phonon interactions.

Figure 8.2 shows how such a measurement can be achieved experimentally. To

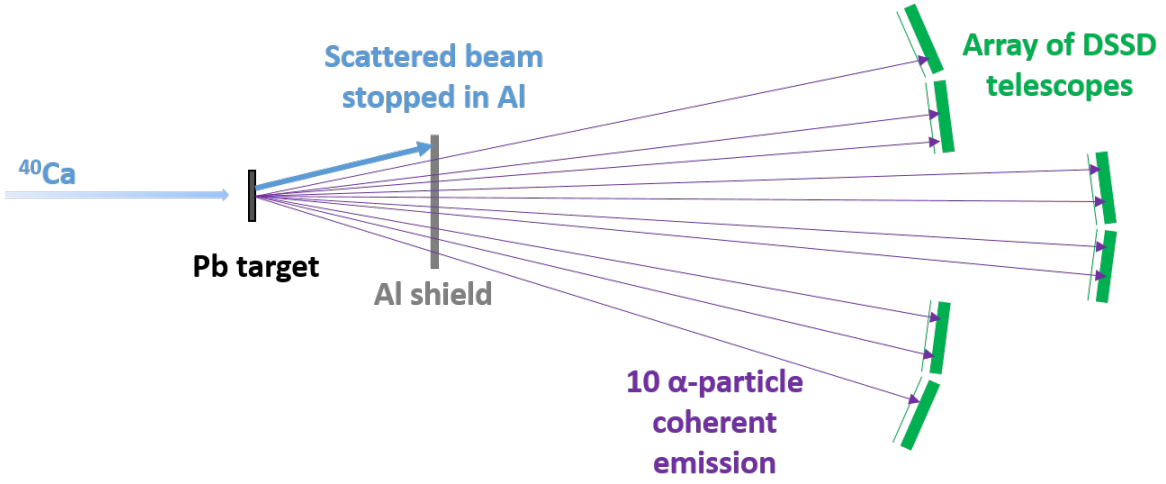

Figure 8.2: Possible experimental set-up for measuring the 10-α "Coulomb-explosion" of ^{40}Ca using Coulex techniques.

achieve the necessary energies to populate $\sim$ 60 MeV, one needs an extremely high energy beam of around 100 MeV/A. As such, one requires a protective shield over the detectors of $\sim$ 4 mm of aluminium which is sufficient to stop the beam but allows the α-particles which are produced to pass through while only losing $\sim$ 25 MeV. A large coverage array of DSSDs (focused at small lab angles) can then be placed to capture the 10 α-particles which are coherently emitted. Alternatively, one can increase the thickness of aluminium used to stop all nuclei heavier than ^{4}He which may make particle identification easier if there are multiple α-particles hitting the same detector (as discussed in Chapter 4.17), there can be no ambiguities if lithium and beryllium isotopes cannot make it to the detector. Alternatively, one may rely on methods more suited to high energy interactions such as nuclear track emulsion which has previously been used in Dubna [151] to show the dissociation of ^{20}Ne and ^{16}O into their constituent α-particles at energies of $>$ 1 GeV/A.

As discussed previously, one cannot solely rely on the dissociation of the ^{40}Ca system as a signature of α-condensation as this may be consistent with the Fermi break-up parameter. Reconstruction of the 10 α-particle system should show an enhancement in this cross section at the energy corresponding to the α-gas state. This measurement would provide the clearest experimental evidence for the phenomena of α-condensation. Further refining of this technique could then investigate increasingly heavy systems to find the N_{cr} value experimentally where no such state exists above the N-α threshold.

Chapter 9

Glossary

- Ground State - **g.s.**
- Pauli Exclusion Principle -**PEP**
- Simple Harmonic Oscillator - **SHO**
- Shell Mode - **SM**
- Nucleon nucleon - **NN**
- Interaction Boson Model - **IBM**
- Bose-Einstein Condensate - **BEC**
- Orthogonality Condition Model - **OCM**
- Branching Ratio - **BR**
- Time Projection Chamber - **TPC**
- Charge to Digital Converter - **QDC**
- Photomultiplier Tube - **PMT**
- Constant Fraction Discriminator - **CFD**
- Time Of Flight - **TOF**
- Particle Identification - **PID**
- Double-sided Silicon Strip Detector - **DSSD**
- (Application Specific Integrated Circuit) Analogue Digital Converter - **ASAD**
- Centre Of Mass - **COM**
- Beam energy - $\mathbf{E_b}$
- Monte Carlo - **MC**
- Extended Hauser Feshbach - **EHF**

Bibliography

[1] Y. Ne'eman, *Nucl. Phys.*, vol. 26, no. 2, pp. 222 –229, 1961, ISSN: 0029-5582. DOI: https://doi.org/10.1016/0029-5582(61)90134-1 (cit. on p. 1).

[2] D. J. Gross and F. Wilczek, *Phys. Rev. Lett.*, vol. 30, pp. 1343–1346, 26 1973. DOI: 10.1103/PhysRevLett.30.1343 (cit. on p. 1).

[3] H. D. Politzer, *Phys. Rev. Lett.*, vol. 30, pp. 1346–1349, 26 1973. DOI: 10.1103/PhysRevLett.30.1346 (cit. on p. 1).

[4] F. D. Aaron *et al.*, *Eur. Phys. Jour. C*, vol. 64, no. 4, pp. 561–587, 2009, ISSN: 1434-6052. DOI: 10.1140/epjc/s10052-009-1169-x (cit. on p. 1).

[5] R. Pohl *et al.*, *Nature*, vol. 466, 213 EP –, 2010 (cit. on p. 1).

[6] C. A. Aidala, S. D. Bass, D. Hasch, and G. K. Mallot, *Rev. Mod. Phys.*, vol. 85, pp. 655–691, 2 2013. DOI: 10.1103/RevModPhys.85.655 (cit. on p. 2).

[7] ESFRI, http://www.esfri.eu/esfri_roadmap2016/roadmap-2016.php; 2016 (cit. on p. 2).

[8] J. J. Thomson, *Lond. Edinb. Dubl. Phil. Mag.*, vol. 7, no. 39, pp. 237–265, 1904. DOI: 10.1080/14786440409463107. eprint: https://doi.org/10.1080/14786440409463107 (cit. on p. 2).

[9] H. Geiger and D. E. Marsden, *Proc. Royal Soc. Lond. A*, vol. 82, no. 557, pp. 495–500, 1909, ISSN: 0950-1207. DOI: 10.1098/rspa.1909.0054. eprint: http://rspa.royalsocietypublishing.org/content/82/557/495.full.pdf (cit. on p. 2).

[10] E. Rutherford, *Lond. Edinb. Dubl. Phil. Mag.*, vol. 21, no. 125, pp. 669–688, 1911. DOI: 10.1080/14786440508637080. eprint: https://doi.org/10.1080/14786440508637080 (cit. on p. 2).

[11] J. Chadwick, *Nature*, vol. 129, 312 EP –, 1932 (cit. on p. 2).

[12] C. F. v. Weizsäcker, *Z. Phys*, vol. 96, no. 7, pp. 431–458, 1935, ISSN: 0044-3328. DOI: 10.1007/BF01337700 (cit. on p. 2).

[13] R. D. Woods and D. S. Saxon, *Phys. Rev.*, vol. 95, pp. 577–578, 2 1954. DOI: 10.1103/PhysRev.95.577 (cit. on pp. 3, 14).

[14] M. G. Mayer, *Phys. Rev.*, vol. 75, pp. 1969–1970, 12 1949. DOI: 10.1103/PhysRev.75.1969 (cit. on p. 4).

[15] A. Koning, S. Hilarie, and M. Duijvestijn, TALYS Manual v1.4. Proceedings of the international Conference on Nuclear Data for Science and Technology - ND2007, April 22-27, 2007 http://www.talys.eu/fileadmin/talys/user/docs/talys1.4.pdf, 2011 (cit. on p. 7).

[16] N. Bohr, *Nature*, vol. 137, 344 EP –, 1936 (cit. on p. 9).

[17] M. J. Fluss, J. M. Miller, J. M. D'Auria, N. Dudey, B. M. Foreman, L. Kowalski, and R. C. Reedy, *Phys. Rev.*, vol. 187, pp. 1449–1465, 4 1969. DOI: 10.1103/PhysRev.187.1449 (cit. on p. 9).

[18] A. M. Lane and R. G. Thomas, *Rev. Mod. Phys.*, vol. 30, pp. 257–353, 2 1958. DOI: 10.1103/RevModPhys.30.257 (cit. on p. 9).

[19] I. J. Thompson and F. M. Nunes. Nuclear Reactions for Astrophysics: Principles, Calculation and Applications of Low-Energy Reactions, Cambridge University Press, 2009, ISBN: 0849385482 (cit. on pp. 9, 90).

[20] W. Zimmerman *et al.*, *Phys. Rev. Lett.*, vol. 110, p. 152 502, 15 2013. DOI: 10.1103/PhysRevLett.110.152502 (cit. on pp. 12, 155).

[21] D. Cline, *Ann. Rev. of Nucl. and Part. Sci.*, vol. 36, no. 1, pp. 683–716, 1986. DOI: 10.1146/annurev.ns.36.120186.003343. eprint: https://doi.org/10.1146/annurev.ns.36.120186.003343 (cit. on p. 13).

[22] E. Caurier, G. Martínez-Pinedo, F. Nowacki, A. Poves, and A. P. Zuker, *Rev. Mod. Phys.*, vol. 77, pp. 427–488, 2 2005. DOI: 10.1103/RevModPhys.77.427 (cit. on p. 13).

[23] P. Pyykk, *Mol. Phys.*, vol. 106, no. 16-18, pp. 1965–1974, 2008. DOI: 10.1080/00268970802018367. eprint: https://doi.org/10.1080/00268970802018367 (cit. on p. 15).

[24] R. B. Wiringa, V. G. J. Stoks, and R. Schiavilla, *Phys. Rev. C*, vol. 51, pp. 38–51, 1 1995. DOI: 10.1103/PhysRevC.51.38 (cit. on p. 15).

[25] A. Astier, P. Petkov, M.-G. Porquet, D. S. Delion, and P. Schuck, *Phys. Rev. Lett.*, vol. 104, p. 042 701, 4 2010. DOI: 10.1103/PhysRevLett.104.042701 (cit. on p. 18).

[26] E. M. Burbidge, G. R. Burbidge, W. A. Fowler, and F. Hoyle, *Rev. Mod. Phys.*, vol. 29, pp. 547–650, 4 1957. DOI: 10.1103/RevModPhys.29.547 (cit. on p. 18).

[27] W. von Oertzen, M. Freer, and Y. Kanada-Enyo, *Phys. Rep.*, vol. 432, no. 2, pp. 43 –113, 2006, ISSN: 0370-1573. DOI: https://doi.org/10.1016/j.physrep.2006.07.001 (cit. on p. 19).

[28] E. Epelbaum, H. Krebs, D. Lee, and U.-G. Meißner, *Phys. Rev. Lett.*, vol. 106, p. 192 501, 19 2011. DOI: 10.1103/PhysRevLett.106.192501 (cit. on p. 19).

[29] C. W. Cook, W. A. Fowler, C. C. Lauritsen, and T. Lauritsen, *Phys. Rev.*, vol. 107, pp. 508–515, 2 1957. DOI: 10.1103/PhysRev.107.508 (cit. on p. 19).

[30] H. Morinaga, *Phys. Rev.*, vol. 101, pp. 254–258, 1 1956. DOI: 10.1103/PhysRev.101.254 (cit. on p. 20).

[31] L. R. Hafstad and E. Teller, *Phys. Rev.*, vol. 54, pp. 681–692, 9 1938. DOI: 10.1103/PhysRev.54.681 (cit. on p. 20).

[32] F. Arickx, J. Broeckhove, and E. Deumens, *Nucl. Phys. A*, vol. 318, no. 3, pp. 269 –286, 1979, ISSN: 0375-9474. DOI: https://doi.org/10.1016/0375-9474(79)90648-1 (cit. on p. 20).

[33] R. Bijker and F. Iachello, *Ann. of Phys.*, vol. 298, no. 2, pp. 334 –360, 2002, ISSN: 0003-4916. DOI: http://dx.doi.org/10.1006/aphy.2002.6255 (cit. on p. 20).

[34] A. Tohsaki, H. Horiuchi, P. Schuck, and G. Röpke, *Phys. Rev. Lett.*, vol. 87, p. 192 501, 19 2001. DOI: 10.1103/PhysRevLett.87.192501 (cit. on pp. 20, 29–31).

[35] W. von Oertzen, *Eur. Phys. J. A*, vol. 11, no. 4, pp. 403–411, 2001. DOI: 10.1007/s100500170052 (cit. on p. 21).

[36] N. Itagaki, S. Okabe, K. Ikeda, and I. Tanihata, *Phys. Rev. C*, vol. 64, p. 014 301, 1 2001. DOI: 10.1103/PhysRevC.64.014301 (cit. on p. 21).

[37] T. Baba and M. Kimura, *Phys. Rev. C*, vol. 95, p. 064 318, 6 2017. DOI: 10.1103/PhysRevC.95.064318 (cit. on p. 21).

[38] W. von Oertzen, *Z. Phys A.*, vol. 357, no. 4, pp. 355–365, 1997, ISSN: 1431-5831. DOI: 10.1007/s002180050255 (cit. on p. 21).

[39] M. Freer *et al.*, *Phys. Rev. Lett.*, vol. 96, p. 042 501, 4 2006. DOI: 10.1103/PhysRevLett.96.042501 (cit. on p. 21).

[40] M. Freer, Online; 2010. DOI: 10.4249/scholarpedia.9652 (cit. on p. 22).

[41] M. Freer, *Rep. on Prog. in Phys.*, vol. 70, no. 12, p. 2149, 2007 (cit. on p. 23).

[42] Y. Kanada-En'yo, M. Kimura, and A. Ono, *Prog. Theor. Exp. Phys*, vol. 2012, no. 1, 01A202, 2012. DOI: 10.1093/ptep/pts001. eprint: /oup/backfile/content_public/journal/ptep/2012/1/10.1093_ptep_pts001/1/pts001.pdf (cit. on p. 23).

[43] M. Freer, H. Horiuchi, Y. Kanada-En'yo, D. Lee, and U.-G. Meiner, To appear in Reviews of Modern Physics, 2017. eprint: arXiv:1705.06192 (cit. on pp. 23, 33, 43).

[44] Y. Kanada-En'yo, *Prog. Theor. Phys*, vol. 117, no. 4, pp. 655–680, 2007. DOI: 10.1143/PTP.117.655. eprint: /oup/backfile/content_public/journal/ptp/117/4/10.1143/ptp.117.655/2/117-4-655.pdf (cit. on p. 24).

[45] T. W. B. Kibble, 2015. eprint: arXiv:1502.06276 (cit. on p. 24).

[46] A. Arima and F. Iachello, *Phys. Rev. Lett.*, vol. 35, pp. 1069–1072, 16 1975. DOI: 10.1103/PhysRevLett.35.1069 (cit. on p. 24).

[47] J. P. Elliott, *Proc. Royal Soc. Lond. A*, vol. 245, no. 1240, pp. 128–145, 1958, ISSN: 0080-4630. DOI: 10.1098/rspa.1958.0072. eprint: http://rspa.royalsocietypublishing.org/content/245/1240/128.full.pdf (cit. on p. 25).

[48] B. Bayman and A. Bohr, *Nucl. Phys.*, vol. 9, no. 4, pp. 596 –599, 1958, ISSN: 0029-5582. DOI: https://doi.org/10.1016/0029-5582(58)90343-2 (cit. on p. 25).

[49] R. Bijker and F. Iachello, *Phys. Rev. C*, vol. 61, p. 067 305, 6 2000. DOI: 10.1103/PhysRevC.61.067305 (cit. on p. 25).

[50] D. J. Marín-Lámbarri, R. Bijker, M. Freer, M. Gai, Tz. Kokalova, D. J. Parker, and C. Wheldon, *Phys. Rev. Lett.*, vol. 113, p. 012 502, 1 2014. DOI: 10.1103/PhysRevLett.113.012502 (cit. on pp. 25, 209).

[51] Wikipedia, the free encyclopedia, https://commons.wikimedia.org/wiki/File:Boron-trifluoride-3D-balls.png; 2007 (cit. on p. 26).

[52] D. J. Marín-Lámbarri, R. Bijker, M. Freer, M. Gai, Tz. Kokalova, D. J. Parker, and C. Wheldon, *Phys. Rev. Lett.*, vol. 113, p. 012 502, 1 2014. DOI: 10.1103/PhysRevLett.113.012502 (cit. on p. 27).

[53] D. J. Rowe and J. L. Wood. Fundamentals of nuclear models: foundational models, World Scientific, 2010, p. 51 (cit. on p. 25).

[54] G. Brown and A. Green, *Nucl. Phys.*, vol. 75, no. 2, pp. 401 –417, 1966, ISSN: 0029-5582. DOI: https://doi.org/10.1016/0029-5582(66)90771-1 (cit. on p. 25).

[55] H. Feshbach and F. Iachello, *Physics Letters B*, vol. 45, no. 1, pp. 7 –11, 1973, ISSN: 0370-2693. DOI: https://doi.org/10.1016/0370-2693(73)90239-6 (cit. on p. 25).

[56] E. Epelbaum, H. Krebs, T. A. Lähde, D. Lee, U.-G. Meißner, and G. Rupak, *Phys. Rev. Lett.*, vol. 112, p. 102 501, 10 2014. DOI: 10.1103/PhysRevLett.112.102501 (cit. on p. 25).

[57] R. Bijker and F. Iachello, *Phys. Rev. Lett.*, vol. 112, p. 152 501, 15 2014. DOI: 10.1103/PhysRevLett.112.152501 (cit. on p. 28).

[58] B. Flowers and M. Vujii, *Nucl. Phys.*, vol. 49, pp. 586 –604, 1963, ISSN: 0029-5582. DOI: https://doi.org/10.1016/0029-5582(63)90123-8 (cit. on p. 29).

[59] N. Sandulescu, D. Negrea, and C. W. Johnson, *Phys. Rev. C*, vol. 86, p. 041 302, 4 2012. DOI: 10.1103/PhysRevC.86.041302 (cit. on p. 29).

[60] Y. Kagan, A. E. Muryshev, and G. V. Shlyapnikov, *Phys. Rev. Lett.*, vol. 81, pp. 933–937, 5 1998. DOI: 10.1103/PhysRevLett.81.933 (cit. on p. 29).

[61] G. Röpke, A. Schnell, P. Schuck, and P. Nozières, *Phys. Rev. Lett.*, vol. 80, pp. 3177–3180, 15 1998. DOI: 10.1103/PhysRevLett.80.3177 (cit. on p. 29).

[62] T. Sogo, R. Lazauskas, G. Röpke, and P. Schuck, *Phys. Rev. C*, vol. 79, p. 051 301, 5 2009. DOI: 10.1103/PhysRevC.79.051301 (cit. on p. 29).

[63] T. Sogo, G. Röpke, and P. Schuck, *Phys. Rev. C*, vol. 82, p. 034 322, 3 2010. DOI: 10.1103/PhysRevC.82.034322 (cit. on p. 29).

[64] P. Schuck, *J. Phys. Conf. Ser.*, vol. 436, no. 1, p. 012 065, 2013 (cit. on p. 29).

[65] F. London, *Nature*, vol. 141, 643 EP –, 1938 (cit. on p. 29).

[66] P. Kapitza, *Nature*, vol. 141, 74 EP –, 1938 (cit. on p. 29).

[67] M. H. Anderson, J. R. Ensher, M. R. Matthews, C. E. Wieman, and E. A. Cornell, *Science*, vol. 269, no. 5221, pp. 198–201, 1995, ISSN: 0036-8075. DOI: 10.1126/science.269.5221.198. eprint: http://science.sciencemag.org/content/269/5221/198.full.pdf (cit. on p. 29).

[68] C. R. Cabrera, L. Tanzi, J. Sanz, B. Naylor, P. Thomas, P. Cheiney, and L. Tarruell, *Science*, 2017, ISSN: 0036-8075. DOI: 10.1126/science.aao5686. eprint: http://science.sciencemag.org/content/early/2017/12/13/science.aao5686.full.pdf (cit. on p. 29).

[69] D. D. Osheroff, R. C. Richardson, and D. M. Lee, *Phys. Rev. Lett.*, vol. 28, pp. 885–888, 14 1972. DOI: 10.1103/PhysRevLett.28.885 (cit. on p. 30).

[70] Nobel Media, https://www.nobelprize.org/nobel_prizes/physics/laureates/2001/advanced-physicsprize2001.pdf; 2001 (cit. on p. 30).

[71] J. E. Jones, *Proceedings of the Royal Society of London A: Mathematical, Physical and Engineering Sciences*, vol. 106, no. 738, pp. 463–477, 1924, ISSN: 0950-1207. DOI: 10.1098/rspa.1924.0082. eprint: http://rspa.royalsocietypublishing.org/content/106/738/463.full.pdf (cit. on p. 31).

[72] T. Yamada and P. Schuck, *Phys. Rev. C*, vol. 69, p. 024 309, 2 2004. DOI: 10.1103/PhysRevC.69.024309 (cit. on pp. 32, 214–216).

[73] Wikipedia, the free encyclopedia, https://commons.wikimedia.org/wiki/File:12-6-Lennard-Jones-Potential.svg; 2007 (cit. on p. 32).

[74] M. Beyer, S. Sofianos, C. Kuhrts, G. Röpke, and P. Schuck, *Physics Letters B*, vol. 488, no. 3, pp. 247 –253, 2000, ISSN: 0370-2693. DOI: https://doi.org/10.1016/S0370-2693(00)00908-4 (cit. on p. 33).

[75] D. Tilley, J. Kelley, J. Godwin, D. Millener, J. Purcell, C. Sheu, and H. Weller, *Nuclear Physics A*, vol. 745, no. 3, pp. 155 –362, 2004, ISSN: 0375-9474. DOI: https://doi.org/10.1016/j.nuclphysa.2004.09.059 (cit. on p. 34).

[76] A. Tohsaki, H. Horiuchi, P. Schuck, and G. Röpke, *Rev. Mod. Phys.*, vol. 89, p. 011 002, 1 2017. DOI: 10.1103/RevModPhys.89.011002 (cit. on p. 34).

[77] M. Chernykh, H. Feldmeier, T. Neff, P. von Neumann-Cosel, and A. Richter, *Phys. Rev. Lett.*, vol. 98, p. 032 501, 3 2007. DOI: 10.1103/PhysRevLett.98.032501 (cit. on p. 35).

[78] Y. Suzuki, *Prog. Theor. Phys*, vol. 55, no. 6, pp. 1751–1768, 1976. DOI: 10.1143/PTP.55.1751. eprint: /oup/backfile/content_public/journal/ptp/55/6/10.1143/ptp.55.1751/2/55-6-1751.pdf (cit. on p. 35).

[79] Y. Funaki *et al.*, *Phys. Rev. Lett.*, vol. 101, p. 082 502, 8 2008. DOI: 10.1103/PhysRevLett.101.082502 (cit. on p. 35).

[80] Y. Funaki, H. Horiuchi, W. von Oertzen, G. Röpke, P. Schuck, A. Tohsaki, and T. Yamada, *Phys. Rev. C*, vol. 80, p. 064 326, 6 2009. DOI: 10.1103/PhysRevC.80.064326 (cit. on p. 36).

[81] Y. Funaki *et al.*, *Phys. Rev. C*, vol. 82, p. 024 312, 2 2010. DOI: 10.1103/PhysRevC.82.024312 (cit. on p. 36).

[82] I. J. Thompson and F. M. Nunes. Nuclear Reactions for Astrophysics: Principles, Calculation and Applications of Low-Energy Reactions, Cambridge University Press, 2009, pp. 298–303, ISBN: 0849385482 (cit. on p. 37).

[83] Y. Funaki *et al.*, *J. Phys. Conf. Ser.*, vol. 436, no. 1, p. 012 004, 2013 (cit. on p. 38).

[84] Tz. Kokalova, N. Itagaki, W. von Oertzen, and C. Wheldon, *Phys. Rev. Lett.*, vol. 96, p. 192 502, 19 2006. DOI: 10.1103/PhysRevLett.96.192502 (cit. on pp. 38, 46, 47, 109, 202).

[85] Tz. Kokalova, Private communication (cit. on pp. 38, 46).

[86] D. J. Griffiths. Introduction to Quantum Mechanics, Cambridge University Press, 2016, ch. 8, ISBN: 1107179866 (cit. on p. 38).

[87] R. Smith *et al.*, *Phys. Rev. Lett.*, vol. 119, p. 132 502, 13 2017. DOI: 10.1103/PhysRevLett.119.132502 (cit. on pp. 41, 151, 213).

[88] D. Dell'Aquila *et al.*, *Phys. Rev. Lett.*, vol. 119, p. 132 501, 13 2017. DOI: 10.1103/PhysRevLett.119.132501 (cit. on pp. 41, 151, 213).

[89] H. Zheng, A. Bonasera, M. Huang, and S. Zhang, *Physics Letters B*, vol. 779, pp. 460 –463, 2018, ISSN: 0370-2693. DOI: https://doi.org/10.1016/j.physletb.2018.02.040 (cit. on p. 41).

[90] M. Freer *et al.*, *Phys. Rev. C*, vol. 83, p. 034 314, 3 2011. DOI: 10.1103/PhysRevC.83.034314 (cit. on p. 42).

[91] M. Itoh *et al.*, *Nucl. Phys. A*, vol. 738, no. Supplement C, pp. 268 –272, 2004, Proceedings of the 8th International Conference on Clustering Aspects of Nuclear Structure and Dynamics, ISSN: 0375-9474. DOI: https://doi.org/10.1016/j.nuclphysa.2004.04.044 (cit. on p. 42).

[92] M. Freer *et al.*, *Phys. Rev. C*, vol. 80, p. 041 303, 4 2009. DOI: 10.1103/PhysRevC.80.041303 (cit. on p. 42).

[93] M. Itoh *et al.*, *Phys. Rev. C*, vol. 84, p. 054 308, 5 2011. DOI: 10.1103/PhysRevC.84.054308 (cit. on p. 42).

[94] H. Fynbo, Private communication, 2017 (cit. on p. 42).

[95] M. Itoh *et al.*, *J. Phys. Conf. Ser.*, vol. 436, no. 1, p. 012 006, 2013 (cit. on p. 42).

[96] Y. Kanada-En'yo, *Prog. Theor. Phys*, vol. 117, no. 4, pp. 655–680, 2007. DOI: 10.1143/PTP.117.655. eprint: /oup/backfile/content_public/journal/ptp/117/4/10.1143/ptp.117.655/2/117-4-655.pdf (cit. on p. 42).

[97] G. Cardella *et al.*, http://www.ct.infn.it/home/cardella/images/PDF/proposals/hoyle-pac.pdf; 2017 (cit. on p. 42).

[98] P. Chevallier, F. Scheibling, G. Goldring, I. Plesser, and M. W. Sachs, *Phys. Rev.*, vol. 160, pp. 827–834, 4 1967. DOI: 10.1103/PhysRev.160.827 (cit. on p. 44).

[99] F. Brochard *et al.*, *Phys. Rev. C*, vol. 13, pp. 967–975, 3 1976. DOI: 10.1103/PhysRevC.13.967 (cit. on pp. 44, 171).

[100] N. Curtis *et al.*, *Phys. Rev. C*, vol. 88, p. 064 309, 6 2013. DOI: 10.1103/PhysRevC.88.064309 (cit. on pp. 44, 171).

[101] K. C. W. Li *et al.*, *Phys. Rev. C*, vol. 95, p. 031 302, 3 2017. DOI: 10.1103/PhysRevC.95.031302 (cit. on pp. 44, 45).

[102] Tz. Kokalova *et al.*, *Eur. Phys. Jour. A*, vol. 23, no. 1, pp. 19–31, 2005, ISSN: 1434-601X. DOI: 10.1140/epja/i2004-10071-3 (cit. on p. 46).

[103] H. Akimune *et al.*, *J. Phys. Conf. Ser.*, vol. 436, no. 1, p. 012 010, 2013 (cit. on pp. 46, 205).

[104] J. V. Kratz, http://tan11.jinr.ru/pdf/06_Sep/S_1/02_Kratz.pdf; 2011 (cit. on p. 50).

[105] A. Pagano *et al.*, *Nucl. Phys. A*, vol. 734, pp. 504 –511, 2004, ISSN: 0375-9474. DOI: https://doi.org/10.1016/j.nuclphysa.2004.01.093 (cit. on p. 53).

[106] E. Pagano *et al.*, *EPJ Web of Conferences*, vol. 117, p. 10 008, 2016. DOI: 10.1051/epjconf/201611710008 (cit. on pp. 53, 85).

[107] CHIMERAUNPACKER code, E. de Filippo, Private communication (cit. on p. 54).

[108] N. L. Neindre *et al.*, *Nucl. Instr. Meth. Phys. Res. A*, vol. 490, no. 1, pp. 251 –262, 2002, ISSN: 0168-9002. DOI: https://doi.org/10.1016/S0168-9002(02)01008-2 (cit. on pp. 59, 71).

[109] M. Alderighi *et al.*, *Nucl. Phys. A*, vol. 734, no. Supplement, E88 –E91, 2004, Proceedings of the Eighth International Conference on Nucleus-Nucleus Collisions (NN2003), ISSN: 0375-9474. DOI: https://doi.org/10.1016/j.nuclphysa.2004.03.027 (cit. on p. 59).

[110] G. Knoll. Radiation Detection And Measurement, 4th Edition Wiley India, 2011, p. 668, ISBN: 0470131489 (cit. on p. 62).

[111] L. Francalanza, PhD thesis, Universita Degli Studi Di Catania, 2007 (cit. on p. 62).

[112] NEWPED code, E. de Filippo, Private communication (cit. on p. 63).

[113] G. Knoll. Radiation Detection And Measurement, 4th Edition Wiley India, 2011, pp. 305–307, ISBN: 0470131489 (cit. on p. 65).

[114] G. Knoll. Radiation Detection And Measurement, 4th Edition Wiley India, 2011, p. 238, ISBN: 0470131489 (cit. on p. 66).

[115] G. Cardella *et al.*, *Nucl. Instr. Meth. Phys. Res. A*, vol. 799, no. Supplement C, pp. 64 –69, 2015, ISSN: 0168-9002. DOI: https://doi.org/10.1016/j.nima.2015.07.054 (cit. on p. 66).

[116] A. Wagner, W. P. Tan, K. Chalut, R. J. Charity, B. Davin, Y. Larochelle, M. D. Lennek, T. X. Liu, W. G. Lynch, A. M. Ramos, R. Shomin, L. G. Sobotka, R. T. de Souza, M. B. Tsang, G. Verde, and H. S. Xu, 2000. DOI: 10.1016/S0168-9002(00)00542-8. eprint: arXiv:nucl-ex/0004011 (cit. on p. 66).

[117] DEEFIT code, E. de Filippo, Private communication (cit. on p. 71).

[118] Pillbug code, M. Houck, Private communication (cit. on p. 76).

[119] O. Tarasov and D. Bazin, *Nucl. Instr. Meth. Phys. Res. B*, vol. 376, pp. 185 –187, 2016, Proceedings of the XVIIth International Conference on Electromagnetic Isotope Separators and Related Topics (EMIS2015), Grand Rapids, MI, U.S.A., 11-15 May 2015, ISSN: 0168-583X. DOI: https://doi.org/10.1016/j.nimb.2016.03.021 (cit. on pp. 79, 81).

[120] Private communication, Computer Program DEDX (University of Birmingham, UK) unpublished. Based on computer program SPAR - T.W. Armstrong, K.C. Chandler, NIM 113, 313 (1973) (cit. on p. 81).

[121] FARCOS Collaboration, Accessed January 2018, 2015 (cit. on p. 85).

[122] L. Quattrocchi *et al.*, *EPJ Web of Conferences*, vol. 66, p. 11 001, 2014. DOI: 10.1051/epjconf/20146611001 (cit. on p. 85).

[123] W. Hauser and H. Feshbach, *Phys. Rev.*, vol. 87, pp. 366–373, 2 1952. DOI: 10.1103/PhysRev.87.366 (cit. on p. 90).

[124] L. H. Thomas, *Math. Proc. Camb. Philos. Soc*, vol. 23, no. 5, 542548, 1927. DOI: 10.1017/S0305004100011683 (cit. on p. 90).

[125] E. Fermi, *Z. Phys*, vol. 48, no. 1, pp. 73–79, 1928, ISSN: 0044-3328. DOI: 10.1007/BF01351576 (cit. on p. 90).

[126] H. An and C. Cai, *Phys. Rev. C*, vol. 73, p. 054 605, 5 2006. DOI: 10.1103/PhysRevC.73.054605 (cit. on p. 90).

[127] A. Kumar, S. Kailas, S. Rathi, and K. Mahata, *Nucl. Phys. A*, vol. 776, no. 3, pp. 105 –117, 2006, ISSN: 0375-9474. DOI: https://doi.org/10.1016/j.nuclphysa.2006.07.032 (cit. on p. 90).

[128] T. Matsuse, C. Beck, R. Nouicer, and D. Mahboub, *Phys. Rev. C*, vol. 55, pp. 1380–1393, 3 1997. DOI: 10.1103/PhysRevC.55.1380 (cit. on p. 91).

[129] E. Fermi, *Prog. Theor. Phys*, vol. 5, no. 4, pp. 570–583, 1950. DOI: 10.1143/ptp/5.4.570. eprint: /oup/backfile/content_public/journal/ptp/5/4/10.1143/ptp/5.4.570/2/5-4-570.pdf (cit. on p. 107).

[130] M. Freer, Private communication, 2017 (cit. on p. 109).

[131] N. Curtis *et al.*, *Phys. Rev. C*, vol. 51, pp. 1554–1557, 3 1995. DOI: 10.1103/PhysRevC.51.1554 (cit. on p. 111).

[132] N. Curtis *et al.*, *Phys. Rev. C*, vol. 53, pp. 1804–1810, 4 1996. DOI: 10.1103/PhysRevC.53.1804 (cit. on p. 111).

[133] I. J. Thompson and F. M. Nunes. Nuclear Reactions for Astrophysics: Principles, Calculation and Applications of Low-Energy Reactions, Cambridge University Press, 2009, p. 384, ISBN: 0849385482 (cit. on p. 114).

[134] A. Gavron, *Phys. Rev. C*, vol. 21, pp. 230–236, 1 1980. DOI: 10.1103/PhysRevC.21.230 (cit. on p. 119).

[135] T. Kawano, R. Capote, S. Hilaire, and P. Chau Huu-Tai, *Phys. Rev. C*, vol. 94, p. 014 612, 1 2016. DOI: 10.1103/PhysRevC.94.014612 (cit. on p. 128).

[136] G. Knoll. Radiation Detection And Measurement, 4th Edition Wiley India, 2011, p. 642, ISBN: 0470131489 (cit. on p. 136).

[137] F. James, CERN, Minuit: Function Minimisation and Error Analysis : Reference Manual, Version 94.1, 1994 (cit. on p. 136).

[138] R. Brun and F. Rademakers, *Nucl. Instr. Meth. Phys. Res. A*, vol. 389, no. 1, pp. 81 –86, 1997, New Computing Techniques in Physics Research V, ISSN: 0168-9002. DOI: https://doi.org/10.1016/S0168-9002(97)00048-X (cit. on p. 136).

[139] R. J. Charity *et al.*, *Phys. Rev. C*, vol. 52, pp. 3126–3150, 6 1995. DOI: 10.1103/PhysRevC.52.3126 (cit. on p. 148).

[140] Tz. Kokalova *et al.*, *Phys. Rev. C*, vol. 87, p. 057 307, 5 2013. DOI: 10.1103/PhysRevC.87.057307 (cit. on p. 153).

[141] M. Freer *et al.*, *Phys. Rev. C*, vol. 86, p. 034 320, 3 2012. DOI: 10.1103/PhysRevC.86.034320 (cit. on p. 155).

[142] M. Itoh *et al.*, *Phys. Rev. C*, vol. 84, p. 054 308, 5 2011. DOI: 10.1103/PhysRevC.84.054308 (cit. on p. 155).

[143] R. H. Dalitz, *Phil. Mag. Ser. 7*, vol. 44, pp. 1068–1080, 1953. DOI: 10.1080/14786441008520365 (cit. on p. 158).

[144] N. Curtis *et al.*, *Phys. Rev. C*, vol. 94, p. 034 313, 3 2016. DOI: 10.1103/PhysRevC.94.034313 (cit. on p. 171).

[145] M. Freer *et al.*, *Phys. Rev. C*, vol. 71, p. 047 305, 4 2005. DOI: 10.1103/PhysRevC.71.047305 (cit. on p. 175).

[146] Tz. Kokalova *et al.*, *Phys. Rev. C*, vol. 87, p. 057 309, 5 2013. DOI: 10.1103/PhysRevC.87.057309 (cit. on pp. 175, 211).

[147] B. Borderie *et al.*, *Physics Letters B*, vol. 755, pp. 475 –480, 2016, ISSN: 0370-2693. DOI: https://doi.org/10.1016/j.physletb.2016.02.061 (cit. on p. 205).

[148] Y. Funaki, *Phys. Rev. C*, vol. 92, p. 021 302, 2 2015. DOI: 10.1103/PhysRevC.92.021302 (cit. on p. 209).

[149] M. Freer *et al.*, *Phys. Rev. C*, vol. 83, p. 034 314, 3 2011. DOI: 10.1103/PhysRevC.83.034314 (cit. on p. 209).

[150] O. S. Kirsebom *et al.*, *Phys. Rev. C*, vol. 81, p. 064 313, 6 2010. DOI: 10.1103/PhysRevC.81.064313 (cit. on p. 209).

[151] N. P. Andreeva *et al.*, *Eur. Phys. Jour. A*, vol. 27, no. 1, pp. 295–300, 2006, ISSN: 1434-601X. DOI: 10.1140/epja/i2006-08-045-2 (cit. on p. 217).